

11-43-2R
0382-5

SEMI-ANNUAL REPORT

(for January - June 1997)

Contract Number NAS5-31363

OCEAN OBSERVATIONS WITH EOS/MODIS:

Algorithm Development and Post Launch Studies

Howard R. Gordon
University of Miami
Department of Physics
Coral Gables, FL 33124

(Submitted July 1, 1997)

Abstract

Several significant accomplishments were made during the present reporting period.

- We expanded our new method, for identifying the presence of absorbing aerosols and simultaneously performing atmospheric correction, to the point where it could be added as a subroutine to the MODIS water-leaving radiance algorithm.
- We successfully acquired micro pulse lidar (MPL) data at sea during a cruise in February.
- We developed a water-leaving radiance algorithm module for an approximate correction of the MODIS instrument polarization sensitivity.
- We delivered a complete version of the water-leaving radiance algorithm to R. Evans for incorporation into the next version of MODIS software.
- We participated in one cruise to the Gulf of Maine, a well known region for mesoscale coccolithophore blooms. We measured coccolithophore abundance, production and optical properties.

Preamble

As in earlier reports, we will continue to break our effort into seven distinct units:

- Atmospheric Correction Algorithm Development
- Whitecap Correction Algorithm
- In-water Radiance Distribution
- Residual Instrument Polarization
- Pre-launch/Post-launch Atmospheric Correction Validation
- Detached Coccolith Algorithm and Post-launch Studies

This separation has been logical thus far; however, as launch of AM-1 approaches, it must be recognized that many of these activities will shift emphasis from algorithm development to validation. For example, the second, third, and fifth bullets will become almost totally validation-focussed activities in the post-launch era, providing the core of our experimental validation effort. Work under the first bullet will continue into the post-launch time frame, but will be driven in part by algorithm deficiencies revealed as a result of validation activities. We will continue to use this format for CY97.

1. Atmospheric Correction Algorithm Development.

a. Task Objectives:

During CY 1997 there are seven objectives under this task. Task (i) below is considered to be the most critical. If the work planned under this task is successful, a module that enables the algorithm to distinguish between weakly- and strongly-absorbing aerosols will be included in the atmospheric correction algorithm.

(i) We will continue the study of the "spectral matching" algorithm with the goal of having an algorithm ready for implementation by the end of CY 1997. As our work has shown that a knowledge of the vertical distribution of the aerosol is critical, if it is strongly absorbing, we have procured a micro pulse lidar (MPL) system for use at sea on validation cruises, and from islands (likely Barbados or the Canary Islands) in the Saharan dust zone, to begin to compile the climatology of the vertical distribution required to adopt candidate distributions for use in this region.

(ii) We need to test the basic atmospheric correction algorithm with actual ocean color imagery. We will do this by looking at SeaWiFS and OCTS imagery as they become available.

(iii) We must implement our strategy for adding the cirrus cloud correction into the existing atmospheric correction algorithm. Specific issues include (1) the phase function to be used for the cirrus clouds, (2) the details of making two passes through the correction algorithm, and (3) preparation of the required tables. However, in the light of the success of our spectral matching algorithm, we may have to make significant modifications in our original strategy. These issues will be addressed during CY 1997 with the goal of having a complete implementation strategy ready by the end of CY 1997.

(vi) The basic correction algorithm yields the product of the diffuse transmittance and the water-leaving reflectance. However, we have shown that the transmittance depends on the angular distribution of the reflectance only when the pigment concentration is very low and then only in the blue. We need to develop a method to include the effects of the subsurface BRDF for low-pigment waters in the blue.

(v) We will initiate a study to determine the efficacy of the present atmospheric correction algorithm on removal for the aerosol effect from the measurement of the fluorescence line height (MOD 20).

Semi-Annual Report (1 January – 30 June 1997) NAS5–31363

(vi) We will examine methods for efficiently including earth-curvature effects into the atmospheric correction algorithm. This will most likely be a modification of the look-up tables for the top-of-the-atmosphere contribution from Rayleigh scattering.

(vii) We will examine the necessity of implementing our out-of-band correction to MODIS.

b. Work Accomplished:

(i) We consider this task to be our most important atmospheric correction activity of 1997, and as such the major part of our effort on atmospheric correction will be focussed on it. During this CY, we have further tested our spectral matching algorithm that, although very slow, is capable of distinguishing between weakly- and strongly-absorbing aerosols. It is based on combining a model of the atmosphere with a water-leaving radiance model for the ocean, and effecting a variation of the relevant parameters until a satisfactory fit to the MODIS top-of-atmosphere radiance is achieved. In simulations it showed significant success in detecting the absorption properties of the aerosol, i.e., distinguishing between weakly- and strongly-absorbing aerosols. We demonstrated that, at least in the first approximation, it is also capable of functioning in the same manner when aerosol vertical structure is added as an additional parameter. (Note that vertical structure is only important when the aerosol is strongly absorbing.) We found ways to significantly increase the speed of the algorithm, and to enable it to operate using the same set of lookup tables that the basic algorithm uses. This will enable us to incorporate the spectral matching algorithm in the basic correction algorithm, to be called each $N \times N$ pixels (where $N \sim 10 - 100$) to insure that candidate aerosol models with the correct properties are being used by the basic algorithm. A complete report describing our progress on this task is provided in **Appendix 1**. Our goal is to be able to have this new algorithm functional by the end of this CY.

(ii) Some imagery has been acquired from the OCTS and we are preparing to test the performance of the algorithm in its present state.

(iii) None. This task has been put on hold to free resources for examination of task (i).

(iv) No work was carried out on this task.

(v) To study the efficacy of atmospheric correction of the fluorescence line height, we needed a set of lookup tables specific to the relevant spectral bands. These required about 14,000 radiative transfer simulations. These tables have been prepared for our basic aerosol models.

(vi) No work was carried out on this task.

Semi-Annual Report (1 January – 30 June 1997) NAS5-31363

(vii) The specifics on incorporating the out-of-band corrections in the MODIS algorithm have been worked out.

c. Data/Analysis/Interpretation: See item b above.

d. Anticipated Future Actions:

(i) We will continue work on the spectral matching algorithm. Of particular interest is to devise a way of performing the optimization that is more efficient and accurate than the “brute-force” method described in **Appendix 1**. Also, we need to know how closely the candidate aerosol models must be to the true aerosol in order to effect a good retrieval. To try to understand this we are attempting to use generic power-law size distributions of identical particles (a size-independent refractive index) as candidates for retrieving aerosol and ocean properties when the true aerosol is a combination of two log-normal distributions with the two components composed of different species. The initial results for this have been encouraging.

(ii) As more OCTS imagery is acquired, we shall continue testing the algorithm. In particular, we want to test the spectral matching algorithm with real ocean color data.

(iii) None. The cirrus cloud issue in the presence of our spectral matching method needs to be explored. We will resolve the spectral matching questions first, then devise a strategy to implement the cirrus correction.

(iv) None.

(v) We will perform a basic test of the efficacy of the correction algorithm for retrieving the fluorescence line height.

(vi) None.

(vii) None, until we are provided with the final MODIS spectral response functions.

f. Publications: Four papers are in various stages of the publication process. They are:

H.R. Gordon, T. Zhang, F. He, and K. Ding, Effects of stratospheric aerosols and thin cirrus clouds on atmospheric correction of ocean color imagery: Simulations, *Applied Optics*, **36**, 682–697 (1997).

H.R. Gordon, Atmospheric Correction of Ocean Color Imagery in the Earth Observing System Era, *Jour. Geophys. Res.* (In Press).

Semi-Annual Report (1 January – 30 June 1997) NAS5-31363

H. Yang and H.R. Gordon, Remote sensing of ocean color: Assessment of the water-leaving radiance bidirectional effects on the atmospheric diffuse transmittance, *Applied Optics* (Accepted).

H.R. Gordon, T. Du, and T. Zhang, Remote sensing ocean color and aerosol properties: resolving the issue of aerosol absorption, *Applied Optics* (Accepted).

2. Whitecap Correction Algorithm (with K.J. Voss).

As the basic objectives of this task have been realized, work is being suspended until the validation phase, except insofar as the radiometer will be operated at sea when sufficient number of personnel are available. Karl Moore, the post doctoral associate who was responsible for the operation of the instrument and the data analysis, has moved to the Scripps Institution of Oceanography. In his absence our goal is to maintain experience in operating and maintaining the instrumentation in preparation for the validation phase of the contract.

a. Task Objectives:

Operate the radiometer at sea to maintain experience in preparation for the validation phase.

b. Work Accomplished:

The radiometer was operated during a February cruise with Dennis Clark off Hawaii. From the standpoint of whitecaps this was a very good cruise (high winds). A large amount of whitecap data was collected.

c. Data/Analysis/Interpretation

At this time we have reduced the calibration data, but not the cruise data.

d. Anticipated Future Actions:

We will work to reduce the cruise data during this period, but it is a lower priority than the analysis of other data collected during this cruise.

e. Problems/Corrective Actions: None

f. Publications: Two papers on our whitecap work are still in the review process. They are:

K.D. Moore, K.J. Voss, and H.R. Gordon, Spectral reflectance of whitecaps: Instrumentation, calibration, and performance in coastal waters, *Jour. Atmos. Ocean. Tech.* (Submitted).

K.D. Moore, K.J. Voss, and H.R. Gordon, Spectral reflectance of whitecaps: Fractional coverage and the augmented spectral reflectance contribution to the water-leaving radiance, *Jour. Geophys. Res.* (Submitted).

3. In-water Radiance Distribution (with K.J. Voss).

a. Task Objectives:

The main objective in this task is to obtain upwelling radiance distribution data at sea for a variety of solar zenith angles to understand how the water-leaving radiance varies with viewing angle and sun angle.

b. Work accomplished:

The instrument failed just before use on a cruise in February. It was repaired and used during a short cruise in Florida Bay during May. On this cruise we obtained several upwelling radiance distributions in turbid Case 2 water. The instrument operated properly and was calibrated both before and after this cruise.

c. Data/Analysis/Interpretation: None.

d. Anticipated future actions:

We will operate this instrument during a cruise with Dennis Clark in July in Hawaii. We will also be reducing data from three cruises and their associated calibrations.

e. Problems/Corrective actions: None.

f. Publications: None.

4. Residual Instrument Polarization.

The basic question here is: if the MODIS responds to the state of polarization state of the incident radiance, given the polarization-sensitivity characteristics of the sensor, how much will this degrade the performance of the algorithm for atmospheric correction, and how can we correct for these effects?

a. Task Objectives:

Add a module to perform the correction for residual instrument polarization.

b. Work Accomplished:

A module was added to perform the correction for residual instrument polarization.

c. Data/Analysis/Interpretation: None.

d. Anticipated Future Actions:

Although this task is now basically complete. All that remains is incorporating the SBRS/MCST polarization-sensitivity data into the module.

e. Problems/Corrective Actions: None

f. Publications: The paper describing the polarization-sensitivity correction has been accepted for publication in *Applied Optics*.

H.R. Gordon, T. Du, and T. Zhang, Atmospheric correction of ocean color sensors: Analysis of the effects of residual instrument polarization sensitivity, *Applied Optics* (Accepted).

5. Pre-launch/Post-launch Atmospheric Correction Validation (with K.J. Voss).

a. Task Objectives:

The long-term objectives of this task are four-fold:

(i) First, we need to study aerosol optical properties over the ocean in order to verify the applicability of the aerosol models used in the atmospheric correction algorithm. Effecting this requires obtaining long-term time series in typical maritime environments. This will be achieved using a CIMEL sun/sky radiometer that can be operated in a remote environment and send data back to the laboratory via a satellite link. These are similar the radiometers used by B. Holben in the AERONET Network.

(ii) Second, we must be able to measure the aerosol optical properties from a ship during the initialization/calibration/validation cruises. The CIMEL-type instrumentation cannot be used (due to the motion of the ship) for this purpose. The required instrumentation consists of an all-sky camera (which can measure the entire sky radiance, with the exception of the solar aureole region) from a moving ship, an aureole camera (specifically designed for ship use) and a hand-held sun photometer. We had a suitable sky camera and sun photometer but had to construct an aureole camera. Our objective for this calendar year is to make measurements at sea with this instrumentation, both to collect a varied data set and to test the instrumentation and data reduction procedures.

In the case of strongly-absorbing aerosols, we have shown that knowledge of the aerosol vertical structure is critical. Thus, we need to be able to measure the vertical distribution of aerosols during validation exercises. This can be accomplished with ship-borne LIDAR. We have procured a Micro Pulse Lidar (MPL) system and modified it for ship operation. Our goal during this reporting period was to successfully operate it on a ship.

(iii) The third objective is to determine how accurately the radiance at the top of the atmosphere can be determined based on measurements of sky radiance and aerosol optical thickness at the sea surface. This requires a critical examination of the effect of radiative transfer on "vicarious" calibration exercises.

(iv) The forth objective is to utilize data from other sensors that have achieved orbit (OCTS, POLDER, MSX), or are expected to achieve orbit (SeaWiFS) prior to the launch of MODIS, to validate and fine-tune the correction algorithm.

b. Work Accomplished:

Semi-Annual Report (1 January – 30 June 1997) NAS5-31363

(i) During the last year we were operating the CIMEL in its location in the Dry Tortugas. In October this instrument was removed for recalibration. At the same time the AERONET network, run by B. Hobren, decided to upgrade the CIMEL instruments with more stable interference filters and small hardware changes. It was returned in June, just before we had the deployment for ACE-II. An attempt was made to install it in the short time before ACE-II; however it was unsuccessful as the instrument failed. It has been sent back to NASA and either they or we will install it during the next reporting period.

(ii) The sky camera system and aureole system was used on a cruise with Dennis Clark off of Hawaii (during February). Dennis Clark's group provided the sun photometer data. In addition to participating on the cruise we performed calibration of all the systems pre- and post-cruise. We have begun reducing sky radiance data obtained during several cruises in the last year. We have also reduced the aureole data from the first two cruises, and are currently evaluating this data. We are working on the data reduction procedures to allow measurements to be reduced in almost real time (each night) so that almucantor and principal plane measurements can be obtained quickly.

To try to extend the data base of aerosol optical properties, we examined the possibility of extending our sky radiance inversion algorithm for application over the land. The rationale for this is the simplicity of land-based compared to ship-based measurements in coastal areas. The results, as expected, show that as long as the land albedo is small, good inversions can be obtained in the red and near infrared regions of the spectrum. The complete results of this study are provided in **Appendix 2**.

To address the problem of vertical distribution of aerosols we have acquired a Micro Pulse Lidar from SSEI. We have constructed an air-conditioned weather-proof box for the instrument and this system was used for the first time during the February cruise with Dennis Clark. It performed well during this test, but a couple of modifications to its operation are being performed now. In particular the computer supplied with the system has had problems. These have been solved. We have made the following modifications to the MPL system to improve the reliability:

- Added tilted front window to the case to allow water to run off more easily and avoid retroreflection problems.
- Adding access panels to the Lidar box to enable us to check cabling and other system problems more easily.

Semi-Annual Report (1 January – 30 June 1997) NAS5-31363

- Replaced the computer supplied by SSEI with a notebook computer to allow more reliable operation. This will also significantly reduce the shipping costs required for the system.

(iii) We have completed a study of the accuracy with which one can compute the radiance at the top of the atmosphere from sky radiance measurements made at the sea surface. The results suggest that the bulk of the error is governed by the uncertainty in the sky radiance measurements. Furthermore, as it was shown that the largest error in the radiative transfer process was the error due to the use of scalar radiative transfer theory, we developed a an inversion/prediction method using vector theory. We find that it is possible to predict the polarization state of the top-of-atmosphere radiance quite accurately from surface measurements. This may be very important for validating the pre-launch polarization-sensitivity characterization of MODIS.

We completed definition of the requirements for the vicarious calibration of ocean color sensors in general. This has been submitted for publication and is included here as **Appendix 3**.

(iv) We have obtained small quantities of OCTS data and are working with R. Evans to test the MODIS algorithm with these data.

c. Data/Analysis/Interpretation:

(i) Since August 1993 we have been making aerosol optical depth measurements at three sites occupied by the Atmosphere/Ocean Chemistry Experiment (AEROCE) in Miami, Bermuda, and Barbados. Analysis of this data is complete. A draft paper describing the results of this analysis is provided here in **Appendix 4**.

(ii) We have described the design and operation of our sky camera (with the polarization feature) in two publications submitted to *Applied Optics*. These papers also provide samples of data acquired at Miami. They are included here as **Appendices 5 and 6**.

In addition, we have begun processing the MPL data from the February cruise. As an example we show two figures. Figure 1 shows the MPL return as a function of time between 0300 and 0400 GMT on February 25, 1997. In this figure the major aerosol is low, between 0 and 1 km. Between 1 and 2 kilometer some fairly thin clouds appear and disappear through the night. Figure 2 is an inverted LIDAR return. This is from the 6th minute of the hour shown in the time series. Obvious in this graph is the higher aerosol near the surface, falling off to 1 km, where a thin cloud appears (1-2 km). The signal very near the surface (0 - 200 m) is not available because of the instrument

Semi-Annual Report (1 January – 30 June 1997) NAS5-31363

self return. We are still learning how to process the data from the LIDAR, and will look at the data collected during the February cruise and ACE-II during the next reporting period.

d. Anticipated Future Actions:

(i) We will be reinstalling the CIMEL in the Dry Tortugas at the first opportunity after its return from NASA. We are also working on a better method of acquiring the data through NASA. This will enable us to look at the sky radiance data in a more timely manner.

(ii) We will finish the data reduction work with the sky camera system in the next reporting period. We are also reworking portions of this system to allow more automation of the data collection, and fix minor problems which developed during the last cruise (specifically overheating of the system computer and corrosion on the computer backplane). The reduced aureole data will be merged with the sky radiance data to provide a complete sky radiance distribution during this next period. We will also finish reducing all of the aureole data, and we will use the sky camera and aureole camera during a cruise in July with Dennis Clark.

Much effort in this reporting period has gone toward getting ready to deploy the MPL in Tenerife, Canary Islands during ACE-II. This will occur during June and July and will give us a chance to collect Lidar profiles along with CIMEL sun/sky radiometry and atmospheric chemistry measurements from airplanes, surface and ships. In addition, another MPL is being deployed by Dr. John Reagen at Univ. of Arizona so that simultaneous measurements will be obtained at the surface, near the ocean, and at Izania, a mountain observatory. This data set should help us determine the vertical structure of dust as it comes off of the Sahara. African Dust is an important absorbing aerosol over the Atlantic. One goal of this work for 1997 is to begin obtaining a data base of the thickness of the Saharan dust layer over the Tropical Atlantic.

(iii) We will apply our sky radiance inversion algorithm to actual data obtained at sea.

(iv) We will continue working with R. Evans on implementation of our atmospheric correction algorithm on our R10000 computer to facilitate fine-tuning the algorithm.

e. Problems/corrective actions: None.

MPL Signal Return on February 25, 1997 (0300 GMT)

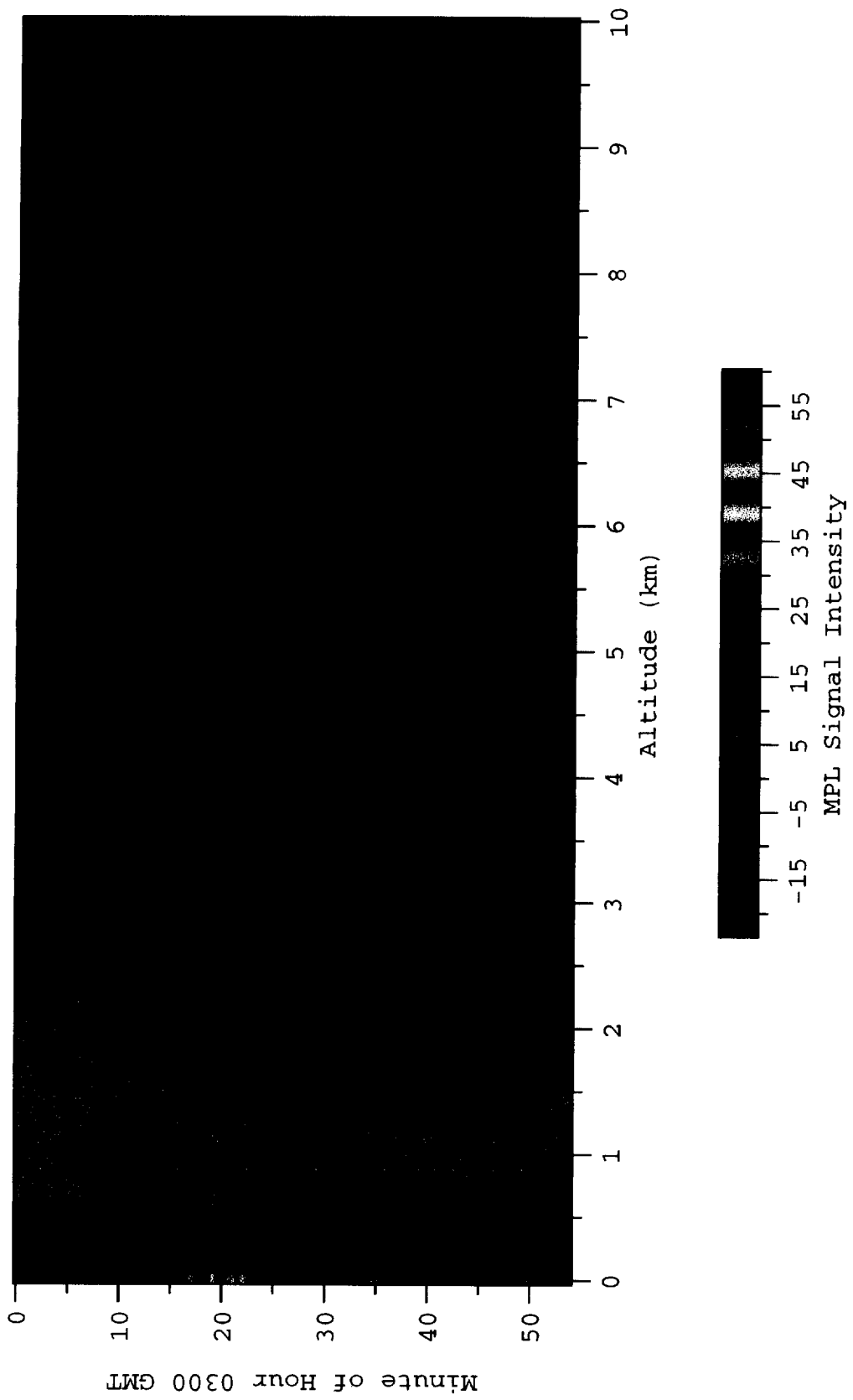
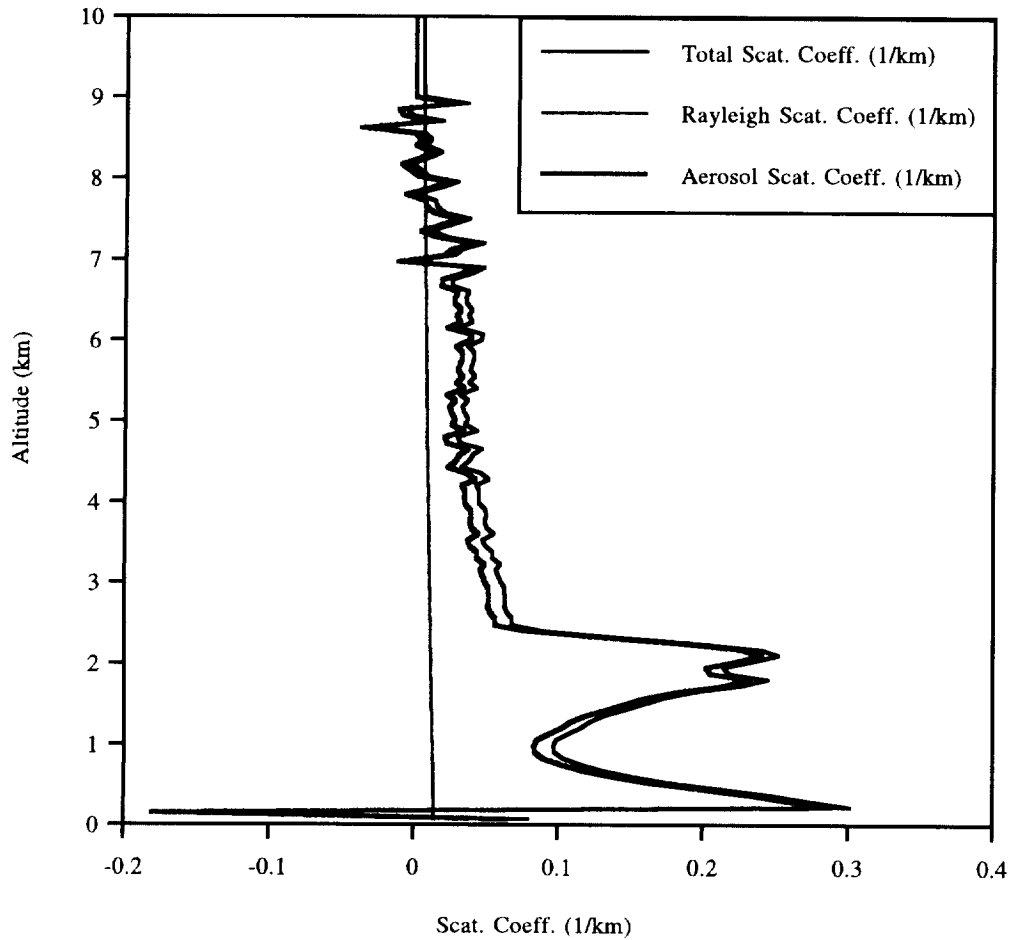


Fig 1

MPL Scattering Coeff. February 25, 1997 (0300 GMT)



```
(NasaHeader) unit_number: 50
Record Number: 12
month: 2 day: 25 year: 97
hour: 3 minute: 6 second: 20 hund_sec: 0
trigger_freq: 2500
energy_monitor: 6.199000
detect_temp: 25.890000
filter_temp: 0.000000
box_temp: 22.260000
laser_temp: 24.790000
ten_volt: 0.000000
five_volt: 0.000000
fifteen_volt: 0.000000
cbh: 0.000000
background: 0.318874
bintime: 500.000000
maxaltitude: 30.000000
deadtimecorrected: 0.000000
altitudeInt: 0.075000
numberBins: 400.000000
averageTime: 30.000000
numberRecords: 109.000000
```

Fig 2

Semi-Annual Report (1 January – 30 June 1997) NAS5-31363

f. Publications: Several papers in various stages of the publication process are listed below.

D.K. Clark, H.R. Gordon, K.J. Voss, Y. Ge, W. Broenkow, and C. Trees, Validation of Atmospheric Correction over the Oceans, *Jour. Geophys. Res.* (In press).

K.J. Voss and Y. Liu, Polarized radiance distribution measurements of skylight: Part 1, system description and characterization, *Applied Optics* (Accepted).

Y. Liu and K.J. Voss, Polarized radiance distribution measurements of skylight: Part 2, experiment and data, *Applied Optics* (Accepted).

H. Yang and H.R. Gordon, Retrieval of the Columnar Aerosol Phase Function and Single Scattering Albedo from Sky Radiance over Land: Simulations, *Applied Optics* (Submitted).

H.R. Gordon, In-orbit calibration strategy of ocean color sensors, *Remote Sensing of Environment* (Submitted).

6. Detached Coccolith Algorithm and Post Launch Studies (W.M. Balch).

a. Task Objectives:

The algorithm for retrieval of the detached coccolith concentration from the coccolithophorid, *E. huxleyi* is described in detail in our ATBD. The key is quantification of the backscattering coefficient of the detached coccoliths. Our earlier studies focussed on laboratory cultures to understand factors affecting the calcite-specific backscattering coefficient. A thorough understanding of the relationship between calcite abundance and light scatter, in situ, will provide the basis for a generic suspended calcite algorithm. As with algorithms for chlorophyll, and primary productivity, the natural variance between growth related parameters and optical properties needs to be understood before the accuracy of the algorithm can be determined. To this end, the objectives of our coccolith studies during this reporting period months have been:

- (1) Acquire optical field data on the distribution and abundance of coccolithophores in the Gulf of Maine.
- (2) Summarize our flow cytometer experiments for publication.
- (3) Publish earlier results from a 0.5 million square kilometer coccolithophore bloom.

For perspective on the directions of our work, we provide an overview of our previous activities. During 1995, we focussed on chemostat cultures (in which algal growth rate was precisely controlled) and we examined how the optical properties of these calcifying algae changed as a function of growth. During the latter half of 1995, our work focused on shipboard measurements of suspended calcite and estimates of optical backscattering as validation of the laboratory measurements. We participated on two month-long cruises to the Arabian sea, measuring coccolithophore abundance, production, and optical properties. During the first half of 1996, we focused again on field calcite distributions, during two Gulf of Maine cruises, one in March and one in June. During the second half of 1996, we participated on another cruise to the Gulf of Maine.

b. Work Accomplished:

1) We have processed samples for calcification rates and chlorophyll concentrations from our November 1996 Gulf of Maine cruise. We sampled for total and calcite-dependent backscattering (continuously), suspended calcite concentrations, calcification rates, chlorophyll concentrations, coccolithophore and coccolith counts, and particulate organic carbon. The microscope work is still ongoing.

Semi-Annual Report (1 January – 30 June 1997) NAS5-31363

2) We installed a new Argon-Ion laser in our Wyatt light scattering photometer and successfully re-calibrated the instrument. The new laser will provide us with 514 nm wavelength light which is more appropriate for the coccolithophore work.

3) We performed a pre-launch MODIS cruise in the Gulf of Maine aboard the RV Albatross under extremely bad weather conditions (up to 50 kt winds and 20 foot seas). We ran our underway system for the entire trip (~ 1500 nautical miles) without a problem. On this cruise, we provided sea truth radiance and irradiance data for the OCTS (with imagery coordinated with Dr. Gene Feldman). We visited 60 stations, 28 of which were full optical stations (with measurements of total backscattering, acid-labile backscattering, calcite concentrations, coccolithophore and coccolith counts). We had the Yentsch/Phinney group on board measuring spectral absorption, in situ absorption/attenuation (AC-9), upwelling and downwelling irradiance (SATLANTIC TSRB bio-optical sampler), dissolved organic matter absorption, and in situ backscattering (performed by Dr. Ajit Subramanian).

4) Suspended calcite samples from the Gulf of Maine have been run in the graphite furnace atomic absorption spectrometer at the University of Maine. We now only have samples from our most recent cruise in June '97.

5) All cell and coccolith counts from the Arabian Sea were completed and the data from process cruise 6 are being entered into spreadsheets at this time. We now are focussing on the several hundred cell count samples from our recent Gulf of Maine cruises. This will take many months to complete.

6) All calcification data from the March, June and November 1996 Gulf of Maine cruise have been processed to units of $\text{gC m}^{-3} \text{d}^{-1}$ and integrated over the water column at each station. They have been processed into complete sections.

c. Data/Analysis/Interpretation:

Single cell experiments

We have focussed on data analysis for our flow cytometer experiments. This work has entailed the processing of backscattering coefficients of 8 species of calcifying algae, plated-with or denuded-of coccoliths. We also sorted detached coccoliths of these different species for bulk analysis. Following measurements, the calcite was measured using graphite furnace atomic absorption spectrometry. These samples were run during the preceding 6 months at the University of Maine Darling Center. The other aspect of this work was to sort calcite particles from field samples, and

Semi-Annual Report (1 January – 30 June 1997) NAS5-31363

to measure their scattering and calcite composition. The atomic absorption samples, too, were processed in the last 6 months.

One of the interesting aspects of the flow cytometer analysis was comparing backscattering by particulate inorganic and organic matter to data by Morel. The results of organic carbon scattering shows strikingly good agreement with Morel's data. The consistent organic carbon results allow us to estimate both inorganic and organic carbon standing stock using our flow-through scattering detector. The first draft of a manuscript has been written which summarizes these results.

Cruise results

Calcite-dependent backscattering was quite high in the Gulf of Maine during June, 1997; chlorophyll levels were moderate. Calcite scattering commonly accounted for 10-20% of total backscattering. Interestingly, it was highest over Georges Bank and in coastal waters as opposed to Wilkinson Basin, a stratified basin in the middle of the Gulf of Maine. The underway data from the Gulf of Maine are being merged with our calibration measurements (calibrations are periodically made at sea and these data are being processed to verify instrument calibrations). Hydrographic plots of the Gulf of Maine data will be made in which light scattering and chlorophyll are plotted in temperature salinity space.

The March, June and November cruises to the Gulf of Maine were processed to show the aerial distribution and depth profiles of calcification. Interestingly, these results showed that the shelf waters near the tip of Cape Cod to be a "hot spot" for calcification. We have observed this before. Georges Bank also had higher-than-expected calcite concentrations in June.

d. Anticipated Future Actions:

Work in the next year will address several areas:

- 1) Processing of the suspended calcite samples from the June '97 cruise.
- 2) Final analysis and write-up of our fall flow cytometer experiments.
- 3) Continued microscope cell/coccolith counts for samples from the Gulf of Maine.
- 4) We will go to sea in November on another Gulf of Maine cruise.

e. Problems/Corrective Actions: None

Semi-Annual Report (1 January – 30 June 1997) NAS5-31363

f. Publications: During this time reporting period, two papers have been revised for publication. One dealing exclusively with the optics coccolithophores is included here as **Appendix 7**.

Voss, K., W. M. Balch, and K. A. Kilpatrick. Scattering and attenuation properties of *Emiliana huxleyi* cells and their detached coccoliths. Revised for *Limnol. Oceanogr.*

Balch, W. M. and B. Bowler. Sea surface temperature gradients, baroclinicity, and vegetation gradients in the sea. In revision for *J. Plank. Res.*

7. Other Activities.

The PI participated in the MOCEAN meeting in Miami in January, and met with A. Fleig and K. Yang of SDST regarding MODIS Ocean test data sets. The PI worked with MCST and SBRS to resolve the issue of proper measurement of the MODIS polarization sensitivity. The issue was successfully concluded in early May. The PI participated in the MODIS Science Team meeting in May, and reviewed the MSCT Level-1B processing algorithms.

Several papers were presented at the AGU Spring Meeting in Baltimore. They are provided below.

H. Yang and H.R. Gordon, Retrieval of aerosol properties over land, *EOS, Transactions*, AGU, S70 (1997).

E.J. Welton, K.J. Voss, and J.M. Prospero, Radiative characteristics of specific types and concentration of aerosols in the marine environment, *EOS, Transactions*, AGU, S88 (1997).

J.M. Ritter, K.J. Voss, and H.R. Gordon, A new instrument for shipborne radiometric measurements of the solar aureole, *EOS, Transactions*, AGU, S93 (1997).

8. Appendices

1. H.R. Gordon, T. Du, and T. Zhang, Remote sensing ocean color and aerosol properties: resolving the issue of aerosol absorption.
2. H. Yang and H.R. Gordon, Retrieval of the Columnar Aerosol Phase Function and Single Scattering Albedo from Sky Radiance over Land: Simulations.
3. H.R. Gordon, In-orbit calibration strategy for ocean color sensors.
4. E.J. Welton, K.J. Voss, and J.M. Prospero, Long term aerosol optical depth analysis, Program description and results (DRAFT).
5. K.J. Voss and Y. Liu, Polarized radiance distribution measurements of skylight: Part 1, system description and characterization.
6. Y. Liu and K.J. Voss, Polarized radiance distribution measurements of skylight: Part 2, experiment and data.
7. Voss, K., W. M. Balch, and K. A. Kilpatrick. Scattering and attenuation properties of *Emiliana huxleyi* cells and their detached coccoliths.

Appendix 1

**Remote sensing ocean color and aerosol properties:
resolving the issue of aerosol absorption**

**Remote sensing ocean color and aerosol properties:
resolving the issue of aerosol absorption**

By

Howard R. Gordon, Tao Du, and Tianming Zhang

Department of Physics

University of Miami

Coral Gables, FL 33124

Abstract

Present atmospheric-correction and aerosol-retrieval algorithms for ocean color sensors use measurements of the top-of-atmosphere reflectance in the near infrared, where the contribution from the ocean is known for Case 1 waters, to assess the aerosol optical properties. Such measurements are incapable of distinguishing between weakly- and strongly-absorbing aerosols, and the atmospheric correction and aerosol retrieval algorithms fail if the incorrect absorption properties of the aerosol are assumed. In this paper we present an algorithm that appears promising for the retrieval of in-water biophysical properties and aerosol optical properties in atmospheres containing both weakly- and strongly-absorbing aerosols. Using the entire spectrum available to most ocean color instruments (412–865 nm), we simultaneously recover the ocean’s bio-optical properties and a set of aerosol models that best describe the aerosol optical properties. The algorithm is applied to simulated situations that are likely to occur off the U.S. East Coast in summer, when the aerosols could be of the locally-generated weakly-absorbing Maritime type, or of the pollution-generated strongly-absorbing Urban type transported over the ocean by the winds. The simulations show that the algorithm behaves well in an atmosphere with either weakly- or strongly-absorbing aerosol. It successfully identifies absorbing aerosols and provides close values for the aerosol optical thickness. It also provides excellent retrievals of the ocean bio-optical properties. The algorithm uses a bio-optical model of Case 1 waters and a set of aerosol models for its operation. The relevant parameters of both the ocean and atmosphere are systematically varied to find the best (in an RMS sense) fit to the measured top-of-atmosphere spectral reflectance. Examples are provided showing the algorithm’s performance in the presence of errors, e.g., error in the contribution from whitecaps and error in radiometric calibration.

1. Introduction

The Coastal Zone Color Scanner (CZCS) demonstrated the feasibility of measuring marine phytoplankton concentrations from earth-orbiting sensors.^{1,2} Based on the success of the CZCS, several similar instruments with a higher radiometric sensitivity and a larger number of spectral bands, e.g., the sea-viewing wide-field-of-view sensor (SeaWiFS),³ the moderate resolution imaging spectroradiometer (MODIS),⁴ etc., will be launched in the near future. These ocean color instruments will actually measure the chlorophyll *a* concentration in the water as a surrogate for the phytoplankton concentration. In fact, the CZCS measured the sum of the concentrations of chlorophyll *a* and its degradation product phaeophytin *a*. This sum was referred to as the pigment concentration, *C*. Phytoplankton pigments have a broad absorption maximum in the blue (~ 435 nm) and a broad absorption minimum in the green (~ 565 nm), and the CZCS derived *C* from the ratio of the radiances backscattered out of the water (the water-leaving radiance, L_w) near these two wavelengths.^{5,6} Typically, L_w is at most 10% of the total radiance, L_t , exiting the top of the atmosphere (TOA) in the blue and $< 5\%$ in the green. Therefore, it is necessary to extract L_w from L_t to derive *C*. This process is called atmospheric correction.

The atmospheric correction algorithm developed for CZCS⁶⁻¹⁰ is not sufficiently accurate for the new generation of sensors with higher radiometric sensitivity. Atmospheric correction of these sensors requires incorporation of multiple-scattering effects. Gordon and Wang^{11,12} developed such an algorithm for SeaWiFS, and found that the multiple-scattering effects depended on the physical and chemical properties of the aerosol (size distribution and refractive index). Therefore, incorporation of multiple scattering into atmospheric correction required the introduction of aerosol models in the algorithm.

The Gordon and Wang algorithm is very simple to describe. The spectral variation in L_t in the near infrared (NIR) spectral region, where $L_w \approx 0$ in Case 1 waters, is used to provide information concerning the aerosol's optical properties, as L_t there is due principally to Rayleigh scattering (which is known) and to aerosol scattering. The Rayleigh scattering component is then removed, and the spectral variation of the remainder is compared to that produced by a set of candidate aerosol models in order to determine which two models of the candidate set are most

appropriate. These models are then used to estimate the multiple-scattering effects. Gordon¹² has shown that this algorithm can provide L_w with the desired accuracy as long as the aerosol is weakly absorbing (more accurately, the aerosol must be weakly absorbing and it must follow the relationship between size distribution and refractive index that is implicitly implied in the choice of the candidate aerosol models). Unfortunately, strongly-absorbing aerosols, e.g., aerosols from anthropogenic urban sources or mineral dust transported from desert areas to the ocean, can possess size distributions similar to the weakly-absorbing aerosols typically present over the oceans. As the spectral variation of aerosol scattering depends mostly on the aerosol size distribution, and only weakly on the index of refraction, the spectral variation of scattering in the NIR is not sufficient to distinguish between weakly- and strongly-absorbing aerosols. Furthermore, in the case of mineral dust an additional complication arises: the dust is colored, i.e., its absorption is a function of wavelength.^{13,14} Even if it were possible to estimate the absorption characteristics of mineral dust aerosol in the NIR, one would still not know the extent of the absorption in the visible. This is a particularly serious problem, as regions contaminated by mineral dust are often highly productive and thus important from a biogeochemical point of view. In fact, dust deposition may actually provide nutrients that enable the phytoplankton to bloom.¹⁵

The difficulty in detecting the presence of strongly-absorbing aerosols is that the effects of absorption become evident only in the multiple scattering regime. In the single scattering regime, the reflectance of the aerosol is proportional to the product of the single scattering albedo (ω_0) and the aerosol optical thickness (τ_a), i.e., at small τ_a there is no way to distinguish nonabsorbing aerosols ($\omega_0 = 1$) with a given τ_a from absorbing aerosols ($\omega_0 < 1$) and a larger τ_a . Retrieval of information concerning aerosol absorption requires multiple scattering; however, this multiple scattering need not be aerosol multiple scattering — when a low concentration of aerosol exists in the presence of strong Rayleigh scattering, e.g., in the blue, multiple Rayleigh scattering can increase the length of photon paths through the aerosol and enhance the chance of absorption. Also, if distributed vertically in the atmospheric column, the absorbing aerosol can reduce the Rayleigh-scattering component, which is otherwise large in the blue. Thus, the possibility of inferring aerosol absorption is increased as one progresses from the NIR into the visible, but unfortunately L_w is not known there (that is why atmospheric correction is required in the first place). The inescapable

conclusion is that the SeaWiFS algorithm¹¹ must fail when the aerosol is strongly absorbing unless the candidate aerosol models are restricted to those with similarly strong absorption properties.¹²

In addition to atmospheric correction, there is compelling interest in studying the global distribution and transport of aerosols because of their role in climate forcing and biogeochemical cycles.^{16,17} Furthermore, not only is the aerosol concentration required, it is also important to know their absorption properties to understand their climatic effects. There has been continuing interest in measuring aerosol concentration from earth-orbiting sensors.¹⁸⁻²⁴ Over the oceans these sensors generally utilize spectral bands for which the ocean can be assumed to be black ($L_w = 0$) or at least to have constant reflectance. In complete analogy to the atmospheric correction problem above, estimation of aerosol absorption properties from space fails for these sensors. The one exception is the retrieval of spatial distributions of an index indicating the presence of strongly-absorbing aerosols using the Total Ozone Mapping Spectrometer (TOMS) measurements in the ultraviolet.²⁵

In this paper, we describe an alternate approach to the problem of estimating oceanic biophysical properties for Case 1 waters, as well as the physical-chemical properties of the aerosol, using space-borne ocean color sensors. The approach is similar in spirit to that developed by Morel and coworkers^{26,27} for CZCS, and that proposed by Land and Haigh²⁸ for deriving Case-2 water properties using SeaWiFS. It utilizes all of the spectral bands of the sensor. This insures sufficient multiple-scattering (Rayleigh scattering in the blue) to enable identification of the aerosol absorption, even at low aerosol concentrations. In order to separate the effects of aerosols from radiance backscattered from beneath the sea surface (L_w), a Case-1 ocean-color model, in which the reflectance is related to the phytoplankton pigment concentration and the scattering properties of the phytoplankton and their associated detrital material, is used. As with the SeaWiFS algorithm, several candidate aerosol models are employed: nonabsorbing, weakly absorbing, and strongly absorbing. Through a systematic variation of the candidate aerosols, phytoplankton scattering, C , and τ_a , a "best" fit to simulated spectral L_t data is obtained. It is found that the algorithm can successfully discriminate between weakly- and strongly-absorbing aerosols, and can provide estimates of C , τ_a , and ω_0 with an accuracy that is nearly independent of ω_0 . For consistency with earlier work,¹² we specifically examine a situation that is likely to be encountered off the U.S. East

Coast in summer: polluted continental air transported by the winds to the Middle Atlantic Bight. However, this situation is used only as an example to demonstrate the approach. We believe the approach could be applied to oceanic regions subjected to mineral dust as well as aerosols resulting from biomass burning, given appropriate models for such aerosols.

We begin with a discussion of the approach and the modeling of the various quantities required for implementation. Next, we test the efficacy of the algorithm using simulated SeaWiFS³ data. Recall SeaWiFS has eight spectral bands centered at 412, 443, 490, 510, 555, 670, 765, and 865 nm. Finally, we examine the degradation of the performance of the algorithm in the presence of L_t -measurement error.

2. The algorithm approach and implementation

Rather than radiance L , we will use reflectance ρ defined as $\pi L / F_0 \cos \theta_0$, where F_0 is the extraterrestrial solar irradiance, and θ_0 is the solar zenith angle. Then, neglecting the influence of direct sun glitter, the total upwelling reflectance exiting the top of the atmosphere $\rho_t(\lambda)$ consists of the following components:^{11,12} the pure Rayleigh (molecular) scattering contribution $\rho_r(\lambda)$, the pure aerosol scattering contribution $\rho_a(\lambda)$, the contribution due to the interaction effect between air molecules and aerosols $\rho_{ra}(\lambda)$, the contribution from whitecaps $t(\lambda)\rho_{wc}(\lambda)$, and the desired water-leaving contribution $t(\lambda)\rho_w(\lambda)$, i.e.,

$$\rho_t(\lambda) = \rho_r(\lambda) + \rho_a(\lambda) + \rho_{ra}(\lambda) + t(\lambda)\rho_{wc}(\lambda) + t(\lambda)\rho_w(\lambda), \quad (1)$$

where $t(\lambda)$ is the diffuse transmittance of the atmosphere. From the satellite image, we have the spectrum of the upwelling reflectance $\rho_t(\lambda)$. As $\rho_r(\lambda)$ depends only on the surface atmospheric pressure,^{9,29} given an estimate of $t(\lambda)\rho_{wc}(\lambda)$ from a wind-speed estimate, it is not difficult to remove the pure Rayleigh scattering and whitecap contributions $\rho_r(\lambda) + t(\lambda)\rho_{wc}(\lambda)$ from the total reflectance $\rho_t(\lambda)$,

$$[\rho_t(\lambda) - \rho_r(\lambda) - t(\lambda)\rho_{wc}(\lambda)] = [\rho_a(\lambda) + \rho_{ra}(\lambda)] + [t(\lambda)\rho_w(\lambda)]. \quad (2)$$

The known reflectance spectrum of $[\rho_t(\lambda) - \rho_r(\lambda) - t(\lambda)\rho_{wc}(\lambda)]$ consists of two parts which are hard to separate, the water-leaving reflectance term $[t(\lambda)\rho_w(\lambda)]$ and the aerosol contribution $[\rho_a(\lambda) + \rho_{ra}(\lambda)]$ (which includes the interaction term between aerosols and air molecules). The goal of atmospheric correction is to retrieve the water-leaving reflectance $\rho_w(\lambda)$ from the known reflectance $[\rho_t(\lambda) - \rho_r(\lambda) - t(\lambda)\rho_{wc}(\lambda)]$. Because of the high spatial and temporal variability of the physical, chemical, and optical properties of aerosols, it is difficult to estimate the aerosol contribution $[\rho_a(\lambda) + \rho_{ra}(\lambda)]$ to the total upwelling reflectance.

The basic *assumption* of the proposed algorithm is that for each aerosol and pigment concentration there is a unique and distinctive spectrum characteristic of its upwelling reflectances $[\rho_a(\lambda) + \rho_{ra}(\lambda)]$ and $[t(\lambda)\rho_w(\lambda)]$. In a given sun-viewing geometry, similar (or close) spectra to $[\rho_t(\lambda) - \rho_r(\lambda) - t(\lambda)\rho_{wc}(\lambda)]$ can only be obtained from the atmosphere-ocean system by a combination of aerosols having similar optical properties to the actual aerosol, and a pigment concentration similar to that actually present in the ocean. That is, when we estimate $[t(\lambda)\rho_w(\lambda)]$ and $[\rho_a(\lambda) + \rho_{ra}(\lambda)]$ separately and form $[\rho_a(\lambda) + \rho_{ra}(\lambda)]'$ and $[t(\lambda)\rho_w(\lambda)]'$, where here and henceforth the primes will refer to computed or trial estimates, the computed reflectance spectrum

$$[\rho_t(\lambda) - \rho_r(\lambda) - t(\lambda)\rho_{wc}(\lambda)]' = [\rho_a(\lambda) + \rho_{ra}(\lambda)]' + [t(\lambda)\rho_w(\lambda)]',$$

will fit the true reflectance spectrum $[\rho_t(\lambda) - \rho_r(\lambda) - t(\lambda)\rho_{wc}(\lambda)]$ in the visible and near infrared only if the computed water-leaving reflectance $[t(\lambda)\rho_w(\lambda)]'$ and the computed aerosol contribution $[\rho_a(\lambda) + \rho_{ra}(\lambda)]'$ fit their true values *individually*. In order to implement this idea, we need to be able to obtain estimates of $[t(\lambda)\rho_w(\lambda)]'$ and $[\rho_a(\lambda) + \rho_{ra}(\lambda)]'$. We now describe how this is accomplished.

2.A The water component: $t\rho_w$

The prediction of the water-leaving reflectance, $\rho_w(\lambda)$, is effected using the semi-empirical bio-optical radiance model, developed by Gordon *et al.*³⁰ for Case 1 waters,^{5,31} i.e., waters for which the optical properties are controlled by the water itself and by the concentration of phytoplankton and

their decay products. Since we use the pigment concentration C as a surrogate for the phytoplankton concentration, one would expect that the absorption and scattering properties of the particles would depend only on C ; however, it is found for such waters that for a given C the total scattering coefficient varies by roughly a factor of two.⁵ Thus, a second scattering-related parameter b^0 , which ranges from 0.12 to 0.45 m^{-1} with a mean value of 0.30 m^{-1} (when C has units of mg/m^3), is introduced. Gordon *et al.*³⁰ found that by using such a model, the water-leaving radiance dependence on C in Case 1 waters could be explained. Similar results were also obtained by Bricaud and Morel.²⁶ This bio-optical ocean color model actually provides the *normalized* water-leaving reflectance,^{6,12} $[\rho_w(\lambda)]_N$, defined by

$$[\rho_w(\lambda)]_N \equiv \rho_w \exp[(\tau_r/2 + \tau_{Oz}) / \cos \theta_0],$$

where τ_r and τ_{Oz} are the Rayleigh and Ozone optical thicknesses of the atmosphere, respectively. Sample spectra of $[\rho_w(\lambda)]_N$ as a function of C and b^0 are shown in Figure 1. Clearly, the normalized water-leaving reflectance is very sensitive to the pigment concentration C for short wavelengths (412 and 443 nm) and small pigment concentration ($C \lesssim 0.4 \text{ mg}/\text{m}^3$). For longer wavelengths (555 and 670 nm) or large pigment concentrations ($C \gtrsim 0.8 \text{ mg}/\text{m}^3$), $[\rho_w(\lambda)]_N$ does not depend significantly on the pigment concentration C . It is taken to be zero at 765 and 865 nm.

It should be noted that the Gordon *et al.*³⁰ reflectance model above does not take into account the bidirectional effects of the sub-surface upwelled spectral radiance, i.e., it assumes that the upwelling radiance beneath the sea surface is totally diffuse. Morel and co-workers^{32–35} have demonstrated that this is not the case; however, as Morel and Gentili³⁵ have shown, bidirectional effects can be easily introduced into the model and described as a function of C (and, if necessary, b^0).

Once $\rho_w(\lambda)$ is determined, it is necessary to propagate it to the top of the atmosphere (TOA). As mentioned earlier, this is accomplished using the diffuse transmittance $t(\lambda)$. Tanre *et al.*³⁶ and Gordon *et al.*⁶ provided simple expressions for $t(\lambda)$ that include the effects of both aerosol and Rayleigh scattering. Later, Yang and Gordon³⁷ provided a detailed analysis of $t(\lambda)$ based on precise computations. They showed that (1) bidirectional effects play a role in t only in the blue and only at low C , (2) aerosols have a significant effect on t only if they are strongly absorbing, (3)

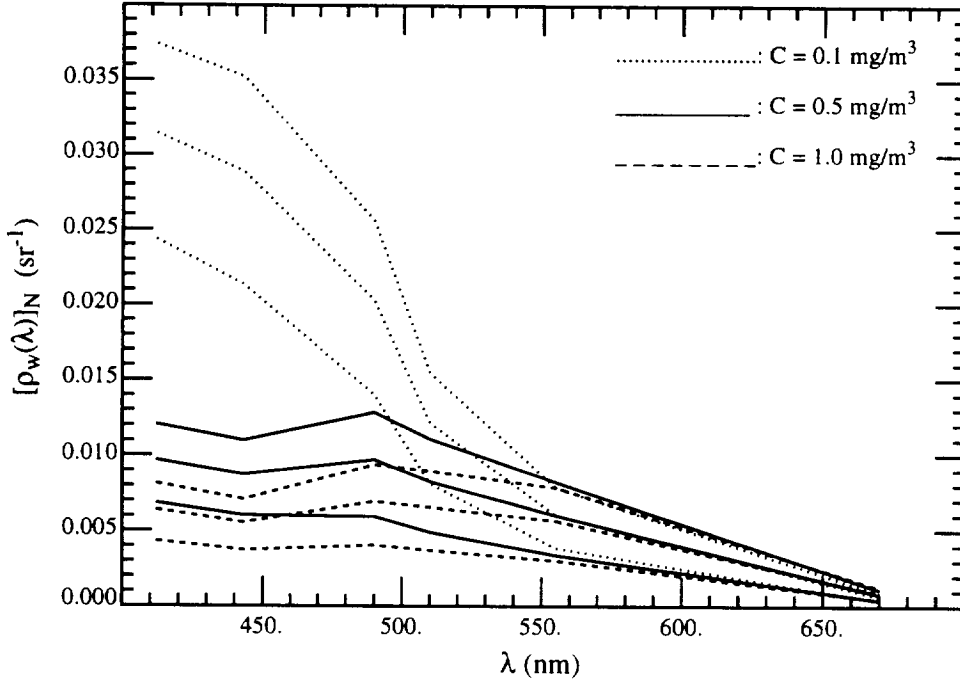


Figure 1 Spectrum of normalized water-leaving reflectance $[\rho_w(\lambda)]_N$ for pigment concentrations of 0.1, 0.5, and 1.0 mg/m^3 . For each pigment concentration, from the upper to the lower curves, the values of coefficient b^0 are 0.45, 0.30, and 0.12 m^{-1} , respectively.

t is independent of the aerosol vertical structure even if the aerosol is strongly absorbing, and (4) given an aerosol model it is simple to predict the correct value of t for any aerosol concentration and viewing geometry. The value of t can be computed precisely given C (to provide bidirectional effects), an aerosol model (to provide the aerosol properties), and the aerosol optical thickness $\tau_a(\lambda)$ (to provide the aerosol concentration). However, for the purposes of this paper, we will approximate t by assuming it is independent of the aerosol. In this case, $t(\lambda)$ is given by

$$t(\lambda) = \exp\left[-(\tau_r(\lambda)/2 + \tau_{Oz})/\cos\theta_v\right], \quad (3)$$

where θ_v is the angle between the zenith and a line from the sensor to the pixel under consideration.

Thus, the simulated $t(\lambda)\rho_w(\lambda)$ is given by

$$t(\lambda)\rho_w(\lambda) = [\rho_w(\lambda)]_N \exp\left[-(\tau_r(\lambda)/2 + \tau_{Oz})\left(\frac{1}{\cos\theta_0} + \frac{1}{\cos\theta_v}\right)\right]. \quad (4)$$

2.B The aerosol component: $\rho_a + \rho_{ra}$

Gordon and Wang¹¹ have shown that the multiple scattering effects in $\rho_a + \rho_{ra}$ depend significantly on the physical and chemical properties of the aerosol, i.e., their size distribution and their refractive index. Thus aerosol models have to be introduced to incorporate multiple scattering effects in atmospheric correction. Similarly, aerosol models are also required to retrieve aerosol properties from space observations.^{38,39} Gordon and Wang¹¹ used aerosol models that were developed by Shettle and Fenn⁴⁰ for LOWTRAN-6.⁴¹ These models consist of particles distributed in size according to combinations of two log-normal distributions, and are described in detail in Ref. 12. Briefly, four models at four different relative humidities are used here. These are the Maritime (M), the Coastal (C), the Tropospheric (T), and the Urban (U). The relative humidities used are 50%, 70%, 90%, and 99%. We denote a particular model by a letter and a number, e.g., M99 refers to the Maritime model at 99% relative humidity (RH). There is an increasing amount of absorption as one progresses through M,C,T, to U. For example, at 865 nm the aerosol single-scattering albedo, ω_0 , is 0.9934, 0.9884, and 0.9528, respectively, for the Maritime, Coastal, and Tropospheric models (RH = 80%), while in contrast, $\omega_0 = 0.7481$ for the Urban model. Here, the Urban model is intended to represent the strongly-absorbing aerosols that might be present over the oceans near areas with considerable urban pollution, e.g., the Middle Atlantic Bight off the U.S. East Coast in summer. Table 1 provides the absorption properties of the candidate aerosol models and the test aerosol models at 865 nm. Note the coarse resolution in ω_0 for the Urban models compared to the others.

We employ these sixteen aerosol models as candidates to test the algorithm. For a two-layer atmosphere, with the aerosol confined to the bottom layer, the scalar radiative transfer equation (polarization ignored) was solved for each of the 16 candidate aerosol models (M, C, T, U aerosols with RH = 50%, 70%, 90%, 99%) with eight values of $\tau_a(\lambda)$ in the range of 0.05 to 0.8 at each wavelength λ , for solar zenith angle $\theta_0 = 0^\circ$ to 80° in increments of 2.5° , and for 33 different viewing zenith angles with θ_v in the range of 0° to 90° . It is difficult to have this large computational set of values of $[\rho_a(\lambda) + \rho_{ra}(\lambda)]$ available for image processing for all of the aerosol candidates, aerosol optical thicknesses, sun-viewing geometries ($\theta_0, \theta_v, \phi_v$, where ϕ_v is the azimuth of the viewing

direction relative to the sun), and spectral bands; therefore, in a manner similar to the Gordon and Wang algorithm,¹² lookup tables (LUTs) are used to provide $[\rho_a(\lambda) + \rho_{ra}(\lambda)]$. In the Gordon and Wang algorithm the lookup tables related $[\rho_a(\lambda) + \rho_{ra}(\lambda)]$ to $\rho_{as}(\lambda)$, the single scattered aerosol reflectance. Equivalently, we relate the term $[\rho_a(\lambda) + \rho_{ra}(\lambda)]$ to the aerosol optical thickness τ_a ; our simulated values of $[\rho_a(\lambda) + \rho_{ra}(\lambda)]$ are fit to

$$[\rho_a(\lambda) + \rho_{ra}(\lambda)] = a(\lambda) \tau_a + b(\lambda) \tau_a^2 + c(\lambda) \tau_a^3 + d(\lambda) \tau_a^4 \quad (5)$$

using least-squares. To further reduce storage, coefficients $a(\lambda)$, $b(\lambda)$, $c(\lambda)$ and $d(\lambda)$ were expanded in Fourier series in the relative-azimuth view-angle ϕ_v , and only the Fourier coefficients were stored in the LUTs. Samples of the fit of $[\rho_a(\lambda) + \rho_{ra}(\lambda)]$ to the aerosol optical thickness are presented in Figure 2 for a sun-viewing geometry with $\theta_0 = 60^\circ$, $\theta_v \approx 46^\circ$, and $\phi_v \approx 93^\circ$. This geometry has relatively large errors in the fits compared to the other geometries used here. It can be seen that the method of using Eq. (5), and Fourier expanding its coefficients, is appropriate for computing $[\rho_a(\lambda) + \rho_{ra}(\lambda)]$ for any candidate aerosol model, at any sun-viewing geometry, aerosol optical thickness, and wavelength. The largest fitting errors occurred at the largest wavelength ($\lambda = 865$ nm) and small aerosol optical thickness ($\tau_a \approx 0.1$). They were of the order of 1% to 2%.

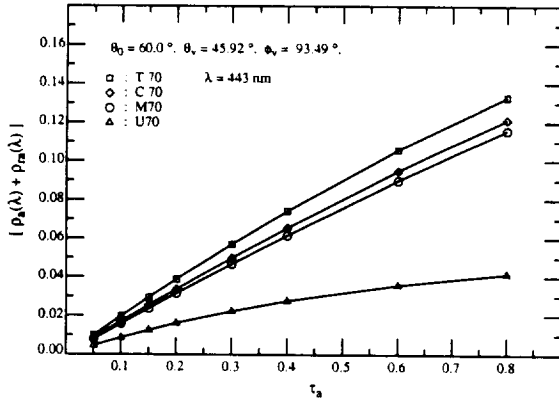


Figure 2(a) Curve fits of $[\rho_a(\lambda) + \rho_{ra}(\lambda)]$ vs. τ_a for aerosol models of M70, C70, T70 and U70 at $\lambda = 443$ nm with $\theta_0 = 60.0^\circ$, $\theta_v = 45.92^\circ$, and $\phi_v = 93.49^\circ$.

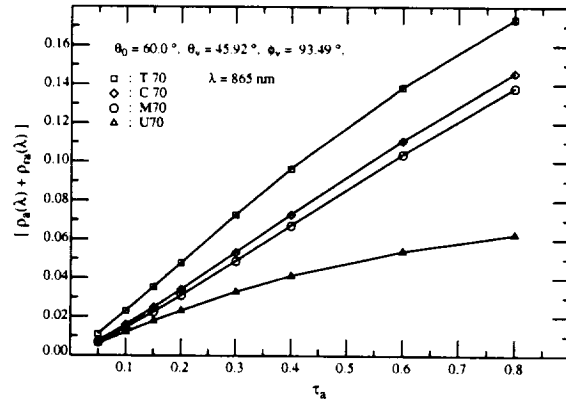


Figure 2(b) Curve fits of $[\rho_a(\lambda) + \rho_{ra}(\lambda)]$ vs. τ_a for aerosol models of M70, C70, T70 and U70 at $\lambda = 865$ nm with $\theta_0 = 60.0^\circ$, $\theta_v = 45.92^\circ$, and $\phi_v = 93.49^\circ$.

2.C The algorithm implementation

We experimented with several approaches for implementing the algorithm. The one we found most effective is summarized as follows:

First, for the given sun-viewing geometry $(\theta_0, \theta_v, \phi_v)$, we vary the value of aerosol optical thickness at 865 nm, $\tau_a(865)$, for each candidate aerosol model to provide the aerosol component $[\rho_a(\lambda) + \rho_{ra}(\lambda)]'$. We then vary the pigment concentration C and the scattering-related coefficient b^0 to provide the water-leaving reflectance $[t(\lambda)\rho_w(\lambda)]'$. These yield a trial upwelling reflectance $[\rho_t(\lambda) - \rho_r(\lambda) - t(\lambda)\rho_{wc}(\lambda)]'$ at each of N bands of the ocean color sensor.

Second, we compute the percent deviation δ' of this simulated spectrum $[\rho_t(\lambda) - \rho_r(\lambda) - t(\lambda)\rho_{wc}(\lambda)]'$ from the measured true spectrum $[\rho_t(\lambda) - \rho_r(\lambda) - t(\lambda)\rho_{wc}(\lambda)]$ over the N spectral bands for each test set $(A, \tau_a, C, b^0)'$, where A labels the candidate aerosol model. The percent deviation $\delta(A, \tau_a, C, b^0)'$ is defined in the sense of root-mean-squares,

$$\delta(A, \tau_a, C, b^0)' = 100\% \times \sqrt{\frac{1}{N-1} \sum_{i=1}^N \left[\frac{[\rho_t(\lambda_i) - \rho_r(\lambda_i) - t(\lambda_i)\rho_{wc}(\lambda_i)]' - [\rho_t(\lambda_i) - \rho_r(\lambda_i) - t(\lambda_i)\rho_{wc}(\lambda_i)]}{[\rho_t(\lambda_i) - \rho_r(\lambda_i) - t(\lambda_i)\rho_{wc}(\lambda_i)]} \right]^2}. \quad (6)$$

Third, we sort the deviations $\delta(A, \tau_a, C, b^0)'$ to find the best ten sets of $(A, \tau_a, C, b^0)'$ which yield the ten smallest percent deviations $\delta(A, \tau_a, C, b^0)'$.

Fourth, as the correct aerosol model is unlikely to be identical to one of the candidates, we assume the characteristics of aerosols and pigment concentration can be adequately described by these best ten sets of parameters $(A, \tau_a, C, b^0)'$. The retrieved single scattering albedo ω_0' and optical thickness τ_a' of the aerosols, and $b^{0'}$ and the pigment concentration C' in the ocean are then computed by averaging ω_0' , τ_a' , $b^{0'}$ and C' over the best ten sets of $(A, \tau_a, C, b^0)'$.

We considered applying standard multivariable minimization techniques⁴² to find the smallest δ' ; however, due to the discrete nature of the candidate models, this would have yielded at best the

minimum δ' for each test model A . Using the algorithm described above, we found that unless the actual aerosol was very close to one of the candidate models, the minimum of δ' was shallow, so the model yielding the minimum was not necessarily much better than other models with small changes in the parameters. Furthermore, we observed that it was rare that only one candidate model was chosen among the ten best, i.e., the n^{th} best for one A might be superior to the best for another A . Were the candidate models dense, in the sense that the actual aerosol would always be close to one of the candidates, multivariable minimization techniques would have been used.

3. The algorithm's performance

In this section, we examine the performance of the algorithm by applying it to simulated SeaWiFS³ data. The sun-viewing geometries are taken as those used in Refs. 11 and 12: viewing at the center of the scan (viewing zenith angle $\theta_v \approx 1^\circ$) for solar zenith angle $\theta_0 = 20^\circ, 40^\circ$ and 60° , and viewing at the edge of the scan ($\theta_v \approx 45^\circ$) near the perpendicular plane ($\phi_v = 90^\circ$) for $\theta_0 = 0^\circ, 20^\circ, 40^\circ$ and 60° . These cover much of the range of sun-viewing geometries available to SeaWiFS. Pseudodata are provided by solving the scalar radiative transfer equation for a two-layer atmosphere system with a specified aerosol confined in the lower layer. The pseudo water-leaving reflectance $\rho_w(\lambda)$ was provided for $b^0 = 0.30 \text{ m}^{-1}$ (the mean value for Case 1 waters)⁵ and pigment concentrations $C = 0.1, 0.5,$ and 1.0 mg/m^3 .

The algorithm attempts to match the pseudodata spectrum of $\rho_t(\lambda) - \rho_r(\lambda) - t(\lambda)\rho_{wc}(\lambda)$ by varying the aerosol model among the 16 candidates ($N_A = 16$), the aerosol optical thickness $\tau_a(865)$ from 0.01 to 0.40 in increments of 0.01 ($N_\tau = 40$), the pigment concentration from 0.05 to 1.50 mg/m^3 in increments of 0.05 mg/m^3 ($N_C = 30$), and finally, b^0 from 0.12 to 0.45 m^{-1} in increments of 0.03 m^{-1} ($N_b = 12$). The total number of elements in the test set $(A, \tau_a, C, b^0)'$ is $N = N_A \times N_\tau \times N_C \times N_b = 16 \times 40 \times 30 \times 12 = 230,400$.

For the first test of the algorithm we examined cases in which the aerosol optical properties of the pseudo atmosphere were included in the candidate aerosol models, i.e., the aerosol optical properties in the atmosphere system were taken from M70, C70, T70 and U70. The optical thickness

at 865 nm was taken to be $\tau_a(865) = 0.1, 0.2$ or 0.3 . The main purpose of this was to test the code for implementation of the algorithm. In all cases, for the best set (smallest δ') the correct aerosol model and the correct values of the parameters were chosen. In fact, δ' for the correct set was a small fraction of a percent and ~ 10 to 30 times smaller than the second best set. The residual error was due to small errors in the LUTs caused by the least-squares and Fourier analysis. Even the averages over the best ten sets were excellent, providing close values of $\tau_a(865)$, b^0 , and C . As the aerosol single scattering albedo ω_0 is a weak function of wavelength λ , we use the retrieved value at 865 nm, $\omega_0(865)$, (averaged over the best ten sets) as an indication of the algorithm's ability to distinguish between weakly- and strongly-absorbing aerosols. The derived values of $\omega_0(865)$ showed that weakly- and strongly-absorbing aerosols are easily recognized by the algorithm.

As it is unlikely for the aerosols in the atmosphere will have exactly the same optical properties as any one of candidate aerosol models, we tested more realistic cases in which the aerosol models were similar to, but not the same as any of, the sixteen candidate aerosol models. Following Gordon¹² the aerosol models M80, C80, T80 and U80 (Shettle and Fenn models with relative humidity 80%) were chosen for this purpose (Table 1). We begin by describing the results obtained from averaging the parameters from the sets with the ten smallest values of δ' . The averaged $\omega'_0(865)$, $\tau'_a(865)$, and C' for a given geometry are taken to be the retrieved values of these parameters. To estimate the performance on a more global scale, i.e., for the full range of sun-viewing geometries, we then average over all seven sun-viewing geometries and compute the mean and the standard deviation in the retrieved parameter values. The mean values of retrieved aerosol single scattering albedo $\omega'_0(865)$ are provided in Table 2 for a pseudo atmosphere characterized by the aerosol models M80, C80, T80 and U80. It can be seen from Table 2 that the retrieved results for ω_0 are very good for each of the four pseudo aerosol models. Large percent deviations (the standard deviation over the seven geometries divided by the mean) in the range of 3% to about 8%, are encountered for the strongly absorbing U80 aerosol model, because of the coarse resolution in the value of ω_0 for the candidates (Table 1). Nevertheless the algorithm can distinguish between the weakly absorbing aerosols (M80, C80, T80) and the strongly absorbing aerosol (U80) without difficulty.

Since the ultimate goal of ocean color remote sensing is to estimate the phytoplankton pigment concentration, we now examine the retrieval of C using the algorithm. Table 3 presents the mean values of retrieved C' , which are averaged over seven sun-viewing geometries and also over the four test aerosol models, M80, C80, T80, and U80 (28 cases in all). It can be observed that the retrieved results of pigment concentration are reasonable for all three tested aerosol optical thicknesses [$\tau_a(865) = 0.1, 0.2, \text{ and } 0.3$] and all three pigment concentrations [$C = 0.1, 0.5, \text{ and } 1.0 \text{ mg/m}^3$]. For the small pigment concentration, $C = 0.1 \text{ mg/m}^3$, or for small aerosol optical thickness, $\tau_a(865) = 0.1$, the spectrum-matching algorithm still works very well. With an increase in either pigment concentration or aerosol concentration, the percent deviations and percent errors in the retrieved C' become larger. For comparison, Table 4 provides similar results for the weakly-absorbing aerosols only, using the Gordon and Wang correction algorithm.¹² Note that the present algorithm behaves as well as the Gordon and Wang algorithm, even when strongly-absorbing aerosols are included. Had strongly-absorbing aerosols been included in Table 4, the results would have been significantly poorer, e.g., in many cases it would have been impossible even to compute C because one or both of the required $\rho_w(443)$ and $\rho_w(555)$ would be negative.

Detailed retrievals of the pigment concentration C are tabulated in Table 5, which gives percentages of cases with relative error in the retrieval, $|\Delta C|/C$, less than 5%, 10%, 20%, and 30%, respectively. For the smallest pigment concentration, in all of the 84 cases examined (three aerosol optical thicknesses, four aerosol models, and seven sun-viewing geometries), $|\Delta C|/C$ was always $< 20\%$, and even $< 5\%$ for about 90% of the cases. For a pigment concentration of $C = 0.5 \text{ mg/m}^3$, and for small aerosol optical thickness, $\tau_a(865) = 0.1$, all individual simulations have $|\Delta C|/C < 30\%$, while for $\tau_a(865) = 0.2$ there are about 89% of the cases having $|\Delta C|/C < 30\%$, and for $\tau_a(865) = 0.3$ about 75% of the cases having $|\Delta C|/C < 30\%$. At the highest pigment concentration examined (1.0 mg/m^3), for small aerosol optical thickness the algorithm still performs very well with only three cases with $|\Delta C|/C > 30\%$. However, as $\tau_a(865)$ increases, the errors become larger, and about 71% of the cases have $|\Delta C|/C < 30\%$ for $\tau_a(865) = 0.2$, and only about 60% for $\tau_a(865) = 0.3$.

The algorithm clearly works better in estimating C for smaller pigment concentrations. This is explained by the relationship between the (normalized) upwelling water-leaving reflectance and the pigment concentration (Figure 1). As we showed in Section 2, the water-leaving reflectance depends strongly on pigment concentration C when C is small ($C \lesssim 0.4 \text{ mg/m}^3$). At small C , a small change in C (0.05 mg/m^3 in the algorithm) will result in a significant change in the upwelling water-leaving reflectance. But when pigment concentration is as large as about 1.0 mg/m^3 , the upwelling water-leaving reflectance is only a weak function of pigment concentration, and a small change of 0.05 mg/m^3 in C does not result in a significant change in the upwelling water-leaving reflectance. This causes the larger percent deviation in C when the algorithm is applied to larger pigment concentrations.

Mean values of the retrieved aerosol optical thickness $\tau'_a(865)$ over the seven sun-viewing geometries and four testing aerosol models (M80, C80, T80 and U80) are presented in Table 6. The mean values are close to their corresponding “true” aerosol optical thicknesses, the percent deviations range from about 6% to about 11%.

Figure 3 provides samples of the three best sets (A, τ_a, C, b^0) determined by the algorithm for aerosol models of M80, C80, T80 and U80 with $\tau_a(865) = 0.2$ and $C = 0.5 \text{ mg/m}^3$, for a single sun-viewing geometry ($\theta_0 = 20^\circ$, $\theta_v = 45.92^\circ$, $\phi_v = 90^\circ$). As the pseudo aerosol models (M80, C80, T80 and U80) are similar to the candidate models used in the algorithm, (M, C, T, and U with RH = 50%, 70%, 90% and 99%), but are not identical to any of 16 candidates, there is no correct aerosol model for the algorithm to choose to match the upwelling reflectance $[\rho_a(\lambda) + \rho_{ra}(\lambda)] + [t(\lambda)\rho_w(\lambda)]$. The figure shows that the aerosol models which have similar optical properties to those of the test aerosol models are selected first by the algorithm. Even though there are some errors caused by picking the incorrect aerosol models, the pigment concentration chosen by the algorithm is close to its true value (0.5 mg/m^3 in Figure 3). For the four pseudo aerosol models tested, the percent deviations of the best match for whole spectrum $\delta(A, \tau_a, C, b^0)'$ varied from about 0.7% to 1.1%. Unlike the case when the test aerosol was one of the candidates, there was no significant increase in

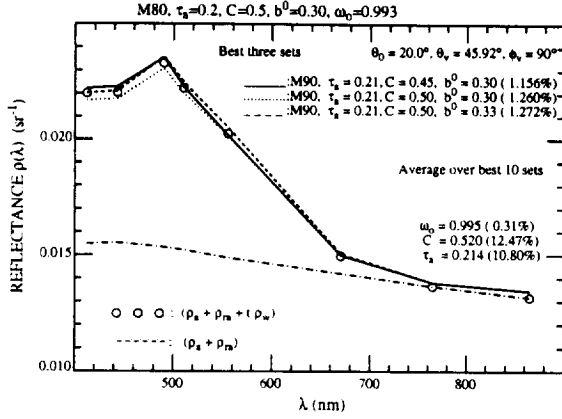


Figure 3(a) Reflectance spectrum matching for aerosol model M80 and pigment concentration $C = 0.50 \text{ mg/m}^3$ with sun-viewing geometry of $\theta_0 = 20.0^\circ$, $\theta_v = 45.92^\circ$, and $\phi_v = 90.0^\circ$.

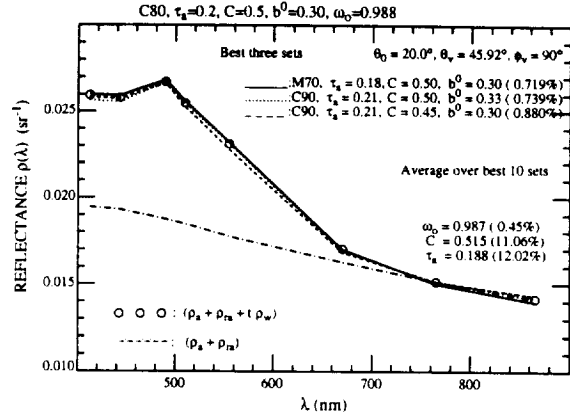


Figure 3(b) Reflectance spectrum matching for aerosol model C80 and pigment concentration $C = 0.50 \text{ mg/m}^3$ with sun-viewing geometry of $\theta_0 = 20.0^\circ$, $\theta_v = 45.92^\circ$, and $\phi_v = 90.0^\circ$.

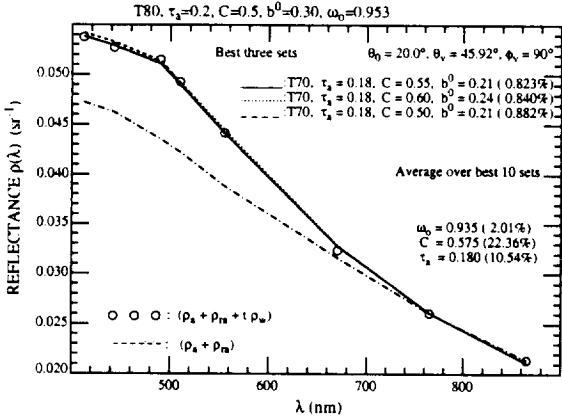


Figure 3(c) Reflectance spectrum matching for aerosol model T80 and pigment concentration $C = 0.50 \text{ mg/m}^3$ with sun-viewing geometry of $\theta_0 = 20.0^\circ$, $\theta_v = 45.92^\circ$, and $\phi_v = 90.0^\circ$.

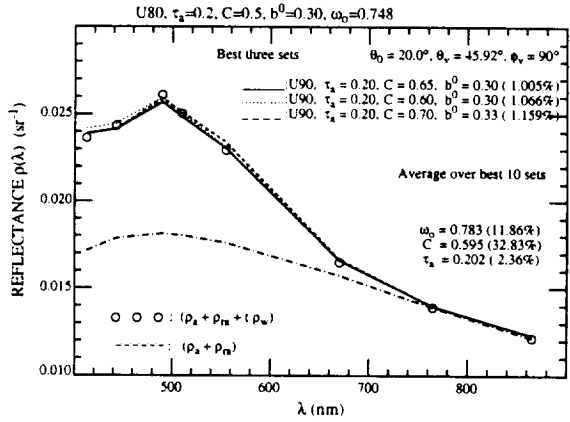


Figure 3(d) Reflectance spectrum matching for aerosol model U80 and pigment concentration $C = 0.50 \text{ mg/m}^3$ with sun-viewing geometry of $\theta_0 = 20.0^\circ$, $\theta_v = 45.92^\circ$, and $\phi_v = 90.0^\circ$.

δ' from the best set to the second best set, etc. For the best 10 sets, the largest percent deviation for $C = 0.5 \text{ mg/m}^3$ is about 1.5%.

Figure 3 also shows the reason for our basic *assumption* that a good fit is obtained only if the spectra of $t\rho'_w$ and $[\rho_a + \rho_{ra}]'$ individually fit $t\rho_w$ and $\rho_a + \rho_{ra}$: the spectral shapes of $\rho_a + \rho_{ra}$ (Figure 3, lower curves) and $t\rho_w$ (Figure 1) are usually quite different. This is particularly true for low values of C .

From these tests of the algorithm we conclude that it can detect the presence of strongly absorbing aerosols successfully. Whenever the optical properties of aerosol in the atmosphere are the same (or very close) to that of any of the 16 candidate aerosol models employed in the algorithm, the retrieved pigment concentration C will be excellent, meeting the requirements of SeaWiFS and MODIS. If the optical properties of the aerosol in the atmosphere are similar to that of any candidate aerosol model, the retrieval results for the pigment concentration C will still be good in the presence of small pigment concentration or small aerosol optical thickness. When both large aerosol optical thickness [$\tau_a(865)$ around 0.2 to 0.3] and large pigment concentration [C around 0.5 to 1.0 mg/m³] are present in the atmosphere-ocean system, the performance of the algorithm is degraded. Still, for the worst scenario examined here, $\tau_a(865) = 0.3$ and $C = 1.0$ mg/m³, about 60% of the individual simulations have $|\Delta C|/C < 30\%$. Note that when $\tau_a(865) = 0.3$, $\tau_a(443) = 0.347, 0.395, 0.745,$ and 0.620 , for M80, C80, T80, and U80, respectively, i.e., τ_a can be very large in the blue, particularly for T80 and U80.

These simulations suggest that the success of the algorithm depends on the appropriateness of candidate aerosol models and the bio-optical model employed in the algorithm. Although we will not be able to know the percent errors in the retrieved aerosol single scattering albedo $\omega'_0(865)$ and pigment concentration C' in processing a satellite image, i.e., we do not know the correct answer, we can compute $\delta(A, \tau_a, C, b^0)'$ over all bands which are used for ocean color remote sensing. This provides one measure of the quality of the retrievals. Also, we can compute the percent deviations for retrieved $\omega'_0(865)$ and C' over the ten best models. Our results suggest that when the deviation in a retrieved quantity is small, its retrieval is more accurate.

4. Inclusion of the aerosol vertical distribution

As mentioned in Section 1, when the aerosol is strongly absorbing, $\rho_a + \rho_{\tau_a}$ depends significantly on the aerosol's vertical distribution (Figure 4). In the simulations presented here, the correct vertical distribution was assumed, i.e., the pseudodata were created using the same vertical distribution as was assumed for the candidate aerosol models. It is reasonable to expect that the

vertical distribution can be introduced into the algorithm described in Section 2 simply as new candidate aerosol models, e.g., the U70 model with all of the aerosol in the marine boundary layer and the U70 aerosol model with the aerosol uniformly mixed with air throughout the entire atmosphere would represent two distinct candidate aerosol models. This hypothesis is tested next.

As the vertical distribution of the aerosol is important only if it is strongly absorbing, we will consider vertical structure only in the Urban models. In addition to the candidate Urban models

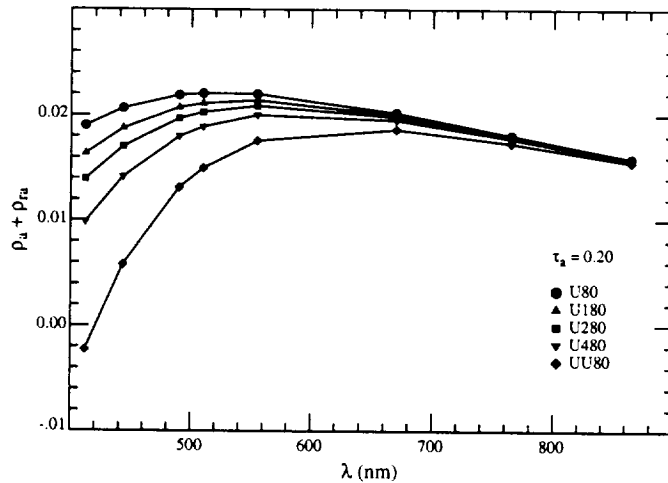


Figure 4. Influence of the physical thickness of the aerosol layer on the spectrum of $\rho_a + \rho_{ra}$. For U80 the aerosol is confined to a thin layer near the surface, while for U180, U280, U480, and UU80, the aerosol is uniformly mixed with air to a height of 1 km, 2 km, 4 km, and the whole atmosphere, respectively. Viewing is near nadir and $\theta_0 = 60^\circ$.

considered in Section 3, where the aerosol was all in the lower layer of a two layer atmosphere with all of the Rayleigh scattering confined to the upper layer, we now introduce three new vertical distributions: (1) the aerosol is uniformly mixed with air from the surface to an altitude of 2 km (21% of τ_r in the lower layer); (2) the aerosol is uniformly mixed with air from the surface to an altitude of 4 km (39% of τ_r in the lower layer); and (3) the aerosol is uniformly mixed with air throughout the entire atmosphere (all of τ_r accompanies the aerosol in a one-layer atmosphere). These distributions for aerosol optical models U50, U70, U90, and U99, constitute 12 candidate

aerosol models in addition to the 16 candidates in Section 3. Thus, for the algorithm tests described below in this section, there are a grand total of 28 candidate aerosol models.

To test the algorithm's ability to deal with aerosol vertical structure, we created pseudodata using the U80 aerosol optical model with vertical structures similar to the candidate aerosol models, i.e., the aerosol mixed uniformly with air to an altitude of 2 km (U280), 4km (U480), and uniformly mixed with air throughout the atmosphere (UU80). Figure 4 provides an example of the strong dependence of $\rho_a + \rho_{ra}$ on the vertical distribution of the aerosol for $\tau_a(865) = 0.2$ and the Urban aerosol models with RH = 80%. It is important to note from Figure 4 that an uncertainty of ± 1 km in the thickness of the aerosol layer results in an uncertainty of $\sim \mp 0.002$ in $\rho_a + \rho_{ra}$ at 443 nm, i.e., equal in magnitude to the maximum acceptable uncertainty in ρ_w . Also, measurement of $\rho_a + \rho_{ra}$ in the NIR provides virtually no indication of the aerosol vertical structure even when the physical-chemical properties of the aerosol are known. As in the earlier sections, seven sun-viewing geometries were investigated. The results of these tests can be summarized as follows:

(1) The algorithm had no difficulty in concluding that the aerosol was strongly absorbing; however, the range in the retrieved ω_0 was from 0.606 to 0.821 (i.e., pure U70 to pure U90) over the seven geometries, three vertical structures, and three values of $\tau_a(865)$, compared with the range 0.699-0.793 for U80 from Table 2. Thus, when vertical structure was included in the candidate aerosol models as described here, the actual value of ω_0 was not as accurate. The additional parameter (vertical distribution) provides an extra degree of freedom that allows ω_0 to take on a wider range of values, and still provide a small δ' .

(2) For $C = 0.1$ and 0.5 mg/m^3 , the aerosol models that were chosen in the ten best were nearly always all from the set with vertical structure, i.e., the candidates with the aerosol all at the bottom of the two-layer atmosphere were rarely chosen. The weakly-absorbing aerosol models were never among the best 10.

(3) For $C = 1 \text{ mg/m}^3$, many of the UU80 retrievals were very poor, e.g., the retrieved C' was $\sim 0.15 \text{ mg/m}^3$. In these cases, the UU70 candidate, which has too much absorption, was always chosen, requiring a smaller C to provide the additional reflectance needed in the blue. Similarly, for lower C , the UU80 cases tended to provide poorer results than the others; however, in all of these cases with poor retrievals, δ' tended to be ~ 5 -10 times larger than typical. These poor retrievals did not occur with the U280 and U480 cases, and probably could be avoided by using candidate models with a finer grid in ω_0 (Table 1).

(4) The mean values of the retrieved C over the seven geometries and three vertical distributions are shown in Table 7. The means are quite good (largest error $\sim 30\%$), but the deviations are larger than those in Table 3. However, note that this table includes the sometimes-very-poor results for UU80 described in (3).

(5) The distribution of $\Delta C/C$, as provided in Table 8 indicates that the error compares favorably with the corresponding error in Table 5. The fraction of retrievals with $|\Delta C/C|$ less than a specified amount is smaller when vertical structure is included; however, unlike Table 5, which also includes weakly-absorbing aerosols in the statistics, these statistics include *only* strongly-absorbing aerosols.

(6) The retrieved mean values of $\tau_a(865)$ show a small ($\sim +5\%$) bias; however, the dispersion of $\tau_a(865)$ over the seven geometries and three vertical structures is slightly less than those in Table 6.

These results all pertain to a situation in which the aerosol vertical structure was identical to that for some of the candidate models, although the aerosol optical model (size distribution and refractive index) was *not* among the candidate set. For completeness, we provide an additional example in which the pseudodata were created using the U80 aerosol optical model with the aerosol uniformly mixed to an altitude of 1 km. Thus, for this case, which we refer to as U180, neither the aerosol vertical structure nor the aerosol optical model are represented within the 28-member

candidate aerosol set. The results of these simulations are provided in Tables 9-12, and show that the algorithm performs very well in this particular situation.

The two tests presented in this section suggest that vertical structure for absorbing aerosols can be handled by including candidate vertical distributions within the candidate aerosol model set. In fact, considering that the results presented are for only strongly-absorbing aerosols, the performance of the algorithm is excellent.

5. Effects of error in $\rho_t - \rho_r - t\rho_{wc}$

In the absence of sun glint, there are two important errors that can influence the performance of the algorithm: (1) error in $\rho_t(\lambda)$ resulting from the sensor's radiometric calibration error; and (2) error in $\rho_{wc}(\lambda)$ resulting from natural "noise"⁴³ in the relationship between ρ_{wc} and the wind speed. Here, we examine the effects of these errors.

5.A Error in $\rho_t(\lambda)$

There will always be some error in the radiometric calibration of the sensor. The specifications for MODIS and SeaWiFS require that the uncertainty in the prelaunch calibration be less than 5% and 10% respectively. As the goal is to recover the water-leaving radiance (reflectance) with an error of $\lesssim \pm 5\%$ at 443 nm in clear ocean water, e.g., the Sargasso Sea in summer, where under such conditions the water-leaving radiance is expected to contribute $\sim 10\%$ to $L_t(443)$, a 5–10% error in L_t is clearly unacceptable. Thus, in-orbit calibration adjustments are required.⁴⁴ Evans and Gordon¹⁰ described methodology used to perform such adjustments for CZCS, and Gordon¹² sketched a possible procedure for SeaWiFS and MODIS. In principle, Gordon's SeaWiFS/MODIS procedure should be capable of reducing the calibration uncertainty in the blue to 0.5%. In fact, by simultaneously measuring $\rho_w(\lambda)$, $\rho_{wc}(\lambda)$, and $\tau_a(\lambda)$, Gordon⁴⁵ argued that for MODIS with a prelaunch calibration uncertainty of $\pm 5\%$, it should be possible in principle to reduce the calibration errors of the other bands to those shown in Table 13, and to insure that the residual calibration errors all have the same sign as the error at 865 nm. This is possible because of the known, and

rapidly increasing with decreasing wavelength, contribution of ρ_r to ρ_t . Here, we assume that this procedure has been effected and the sensor has the calibration errors of magnitude shown in Table 13.

We added positive and negative calibration errors to the ρ_t pseudodata described in Section 3 for the M80, C80, T80, and U80 aerosol models, and operated the algorithm. Generally, there were no large changes in the results. As before, the algorithm had no difficulty distinguishing between strongly- and weakly-absorbing aerosols. The statistics of the distribution in $\Delta C/C$ were similar to those in Table 5. The derived τ_a followed the expected trend, i.e., positive error led to greater values of τ_a . As an example of the retrieved pigment concentration statistics, Table 14 provides the mean C and its standard deviation over the 28 cases in the absence and presence of calibration errors. We see that the effect of the calibration error is to increase the dispersion with only minor changes in the mean values. This insensitivity to residual calibration errors results from the fact that they are small in the blue (Table 13).

5.B Error in $\rho_{wc}(\lambda)$

The whitecap reflectance contribution $t\rho_{wc}$ can be estimated given the wind speed.^{43,46} Gordon and Wang⁴³ show that $t\rho_{wc}$ is given by

$$t(\lambda)\rho_{wc}(\lambda) = [\rho_{wc}(\lambda)]_N t(\theta_0, \lambda) t(\theta_v, \lambda),$$

where $[\rho_{wc}(\lambda)]_N$ is the average increase in the reflectance of the ocean (over several pixels) at the sea surface, resulting from whitecaps in the absence of the atmosphere. It can be thought of as the product of the albedo of an individual whitecap and the fraction of the sea surface covered by whitecaps. $t(\theta_v, \lambda)$ is given in Eq. (3) and $t(\theta_0, \lambda)$ is also given by Eq. (3) with θ_v replaced by θ_0 . In the visible, for a wind speed of 10 m/s $[\rho_{wc}(\lambda)]_N$ varies from ~ 0 to 0.004 with a mean of ~ 0.002 .⁴³ Thus, given a wind speed of 10 m/s, the prediction of $[\rho_{wc}(\lambda)]_N$ would be 0.002 ± 0.002 in the visible. The spectrum of $[\rho_{wc}(\lambda)]_N$ was originally taken to be white;⁴³ however, measurements by Frouin et al.⁴⁷ in the surf zone suggest that the reflectance may decrease considerably in passing from the visible to the NIR. Using the Frouin et al.⁴⁷ whitecap spectrum, we investigated the

behavior of the algorithm for the M80, C80, T80, and U80 test models, given a ± 0.002 error in $[\rho_{wc}(\lambda)]_N$ in the visible when removing $t\rho_{wc}$ from ρ_t . The simulations showed that the presence of a strongly-absorbing aerosol could still be established with ease; however, ω_0 was larger (smaller) for a positive (negative) error in $t\rho_{wc}$. The variation in ω_0 was $\sim \pm 5\%$ for the U80 test. Conversely, τ_a was smaller (larger) for a positive (negative) error in $t\rho_{wc}$. The magnitude of the changes in τ_a was $\sim 10\text{-}15\%$ for all the test models. The variation in τ_a is easy to understand. If $[\rho_{wc}]_N$ is overestimated, then $\rho_a + \rho_{ra}$ will be too small, leading to a value of τ_a that is too small.

The average values of C' were not strongly influenced by the error in $[\rho_{wc}]_N$. This can be seen in Tables 15 and 16 for error in $[\rho_{wc}]_N$, $\Delta[\rho_{wc}]_N$, in the visible of $+0.002$ and -0.002 , respectively. These should be compared to Table 3 for $\Delta[\rho_{wc}]_N = 0$. The whitecap error causes a variation of $\pm 10\text{-}15\%$ in C' at the higher pigment concentrations, but has little effect at $C = 0.1 \text{ mg/m}^3$. The distributions of $|\Delta C|/C < \text{a given fraction}$ actually improve for $\Delta[\rho_{wc}]_N = +0.002$, e.g., for $C = 1 \text{ mg/m}^3$ and $\tau_a = 0.3$, the fraction with $|\Delta C|/C < 30\%$ was 53, 60, and 82% for $\Delta[\rho_{wc}]_N = -0.002$, 0, and $+0.002$, respectively.

Examination of the individual retrievals shows that in the case of the strongly-absorbing aerosols, the bias introduced by the whitecap error causes the same incorrect aerosol model to be always chosen among the best ten, e.g., either U70 or U90 was *always* chosen when the correct model was U80. This biases the individual retrievals of C , ω_0 and τ_a to be always too high or too low, and thus the averages are as well. This effect may be reduced by increased resolution in the model values of ω_0 . Similar effects were observed in the case of sensor calibration errors (Section 5.A)

These simulations suggest that the algorithm is not overly sensitive to error in removing the whitecap reflectance component from ρ_t .

6. Discussion

Present atmospheric correction algorithms for ocean color sensors operating over Case 1 waters use measurements of the TOA reflectance in the NIR, where the contribution for the ocean is

known, to assess the aerosol optical properties. Such measurements are incapable of distinguishing between weakly- and strongly-absorbing aerosols, and atmospheric correction fails if the incorrect absorption properties of the aerosol are assumed.¹² Similarly, algorithms for extracting aerosol properties from passive space-borne sensors operating in the red and NIR are also incapable of detecting absorption,⁴⁸ because the aerosol component of the TOA reflectance is proportional to the scattering optical thickness ($\omega_0\tau_a$), i.e., ω_0 cannot be separated from τ_a . However, it has been shown that it is possible to retrieve spatial distributions of an index indicating the presence of strongly-absorbing aerosols using the Total Ozone Mapping Spectrometer (TOMS) measurements in the ultraviolet,²⁵ where there is significant multiple scattering even in the absence of aerosols. The effect of aerosol absorption on the TOA reflectance becomes stronger as multiple scattering increases. This suggested to us that it would be possible to determine aerosol absorption using ocean color sensors only by utilizing observations in the blue, where unfortunately, the contribution to the TOA reflectance by the aerosol and by the radiance exiting the ocean are comparable. Thus, utilizing the blue portion of the spectrum requires simultaneous determination of the water-leaving reflectance and the aerosol's contribution to the TOA reflectance.

In this paper we have presented an algorithm that appears promising for the retrieval of in-water biophysical properties and aerosol optical properties in atmospheres containing both weakly- and strongly-absorbing aerosols. Using the entire spectrum available to most ocean color instruments (412–865 nm), we simultaneously recover the ocean's bio-optical properties and a set of aerosol models that best describe the aerosol optical properties. As an example, the algorithm has been applied to situations that are likely to occur off the U.S. East Coast in summer, when the aerosols could be of the locally-generated weakly-absorbing Maritime type, or of the pollution-generated strongly-absorbing Urban type transported over the ocean by the winds. Through simulations, we show that the algorithm behaves as well in an atmosphere with weakly- or strongly-absorbing aerosol as the Gordon and Wang¹¹ algorithm does in an atmosphere with only weakly-absorbing aerosols. In contrast to earlier algorithms,^{26–28} the present algorithm successfully identifies absorbing aerosols and provides close values for their optical thickness.

The algorithm requires a bio-optical model of the ocean³⁰ and a set of aerosol models for its operation. The parameters of the bio-optical model and the aerosol models are systematically varied to find the best (in an RMS sense) fit to the measured TOA spectral reflectance. It is critical that the aerosol models be representative of the aerosol expected to be present over the given area, e.g., the Urban models used here would not be expected to yield useful retrievals in a region subjected to absorbing mineral dust.¹⁴ Also it is necessary that aerosol models encompass the range of aerosol vertical distributions expected. As adequate bio-optical models are available only for Case 1 waters,^{5,26,30,49,50} the present algorithm would not operate successfully in Case 2 waters; however, given region specific models for Case 2 waters, comparable performance may be possible as long as the spectral variation of ρ_w and $\rho_a + \rho_{ra}$ are sufficiently different.²⁸ Fortunately, Case 1 waters include most of the open ocean.

A general observation from examining the individual retrievals (both weakly- and strongly-absorbing and vertically distributed) is that for low C , the algorithm will generally choose a value of C that is close to the correct value with very little dispersion over the ten best sets. This owes to the fact that the $\rho_w(\lambda)$ is a very strong function of C and λ for small C (Figure 1), and this provides a strong constraint on the range of values possible. Thus, using the nearly correct C , the algorithm apparently varies the aerosol model and τ_a seeking the optimum set. This results in a larger dispersion in τ_a and ω_0 than in C . In contrast, for large C , where $\rho_w(\lambda)$ depends weakly on both C and λ (Figure 1), and is small itself, the aerosol model typically provides the stronger constraint, and ω_0 along with τ_a are retrieved with small dispersions, while the algorithm optimizes δ' by varying C and b^0 . This causes a larger dispersion in C' . Generally, we find that the quantities with low dispersion over the ten best sets are retrieved more accurately than quantities with a large dispersion.

We intend to utilize this algorithm for processing SeaWiFS and MODIS imagery. In its present research implementation the algorithm is very slow because a brute-force determination of the best ten sets of parameters is employed. However, alternative formulations are faster. For example, as we know $\rho_w(865) = 0$, $\rho_a(865) + \rho_{ra}(865)$ can be retrieved unambiguously from the imagery. For a given aerosol model the value of $\tau_a(865)$ that yields the retrieved $\rho_a(865) + \rho_{ra}(865)$ can be found

directly. Thus, for each model there is really no reason to vary $\tau_a(865)$. When 16 aerosol models are used, this reduces the number of elements in the testing set from 230,000 to 5760. The resulting solution will not be identical to the method based on minimizing δ' in Eq. (6), because now for each set the residual error at 865 nm will be exactly zero, i.e., in Figure 3 every set would exactly pass through the point at $\lambda = 865$ nm. We have used this method to examine the test cases in Section 3 and, as expected, the results are not identical to those presented earlier (Tables 2, 3, 5, and 6), but there are no significant differences. To further reduce the number of test sets, we used the Gordon and Wang¹¹ algorithm to preselect models. Based on their spectral variation in the NIR, the Gordon and Wang algorithm operationally selects the best four models from the set of candidates. Employing this for the tests in Section 3 reduced the number of test sets by an additional factor of four to 1440. Again, there were no significant differences compared to the earlier results. We note, however, that as vertical structure is irrelevant to the spectral behavior in the NIR (Figure 4), if strongly-absorbing models are chosen by the Gordon and Wang algorithm, models with the same optical characteristics but different vertical structures should be included in the test set. For the examples in Section 4 there were a total of 28 models used as candidates, leading to 403,200 test sets; with the two improvements above, this would be reduced to 3600 assuming the Gordon and Wang algorithm would choose two strongly-absorbing and two weakly-absorbing aerosol models. This is the approach we intend to use for SeaWiFS and MODIS.

In reality, we see no need to apply the new algorithm on a pixel-by-pixel basis. We believe a viable strategy would be to employ it at the center of $N \times N$ pixel regions, where $N \sim 10 - 100$, to determine the best aerosol models, and then use the faster Gordon and Wang¹¹ algorithm, with a restricted set of models that are determined by the new algorithm. This strategy assumes that the only property of the aerosol that changes within the $N \times N$ region is the aerosol concentration.

A possible method for improving the algorithm is to use the linear-mixing model of Wang and Gordon,⁵¹ as improved by Abdou et al.,⁵² and vary the mixing ratios of a fixed set of aerosol components, rather than using a fixed set of aerosol models. This is similar in spirit to the Land and Haigh²⁸ approach. Wang and Gordon³⁹ have shown that such a method holds promise for

estimating the size distribution of weakly absorbing aerosols using simulated Multi-angle Imaging Spectroradiometer⁵³ data.

Acknowledgement

The authors are grateful for support from the National Aeronautics and Space Administration under Grant NAGW-273 Contracts NAS5-31363 and NAS5-31734.

References

1. W. A. Hovis, D. K. Clark, F. Anderson, R. W. Austin, W. H. Wilson, E. T. Baker, D. Ball, H. R. Gordon, J. L. Mueller, S. Y. E. Sayed, B. Strum, R. C. Wrigley and C. S. Yentsch, "Nimbus 7 coastal zone color scanner: system description and initial imagery," *Science* **210**, 60–63 (1980).
2. H. R. Gordon, D. K. Clark, J. L. Mueller and W. A. Hovis, "Phytoplankton pigments derived from the Nimbus-7 CZCS: initial comparisons with surface measurements," *Science* **210**, 63–66 (1980).
3. S. B. Hooker, W. E. Esaias, G. C. Feldman, W. W. Gregg and C. R. McClain, *SeaWiFS Technical Report Series: Volume 1, An Overview of SeaWiFS and Ocean Color* (NASA, Greenbelt, MD, Technical Memorandum 104566, July 1992).
4. V. V. Salomonson, W. L. Barnes, P. W. Maymon, H. E. Montgomery and H. Ostrow, "MODIS: Advanced Facility Instrument for Studies of the Earth as a System," *IEEE Geosci. Rem. Sens.* **27**, 145–152 (1989).
5. H. R. Gordon and A. Y. Morel, *Remote Assessment of Ocean Color for Interpretation of Satellite Visible Imagery: A Review* (Springer-Verlag, New York, 1983), 114 pp.
6. H. R. Gordon, D. K. Clark, J. W. Brown, O. B. Brown, R. H. Evans and W. W. Broenkow, "Phytoplankton pigment concentrations in the Middle Atlantic Bight: comparison between ship determinations and Coastal Zone Color Scanner estimates," *Applied Optics* **22**, 20–36 (1983).
7. H. R. Gordon, "Removal of Atmospheric Effects from Satellite Imagery of the Oceans," *Applied Optics* **17**, 1631–1636 (1978).

8. H. R. Gordon and D. K. Clark, "Atmospheric effects in the remote sensing of phytoplankton pigments," *Boundary-Layer Meteorology* **18**, 299–313 (1980).
9. H. R. Gordon, J. W. Brown and R. H. Evans, "Exact Rayleigh Scattering Calculations for use with the Nimbus-7 Coastal Zone Color Scanner," *Applied Optics* **27**, 862–871 (1988).
10. R. H. Evans and H. R. Gordon, "CZCS 'System Calibration:' A retrospective examination," *Jour. Geophys. Res.* **99C**, 7293–7307 (1994).
11. H. R. Gordon and M. Wang, "Retrieval of water-leaving radiance and aerosol optical thickness over the oceans with SeaWiFS: A preliminary algorithm," *Applied Optics* **33**, 443–452 (1994).
12. H. R. Gordon, 1997, Atmospheric Correction of Ocean Color Imagery in the Earth Observing System Era, *Jour. Geophys. Res.*, (In press).
13. G. A. d'Almeida, P. Koepke and E. P. Shettle, *Atmospheric Aerosols — Global Climatology and Radiative Characteristics* (A. Deepak Publishing, Hampton, VA, 1991).
14. T. Nakajima, M. Tanaka, M. Yamano, M. Shiobara, K. Arao and Y. Nakanishi, "Aerosol Optical Characteristics in the Yellow Sand Events Observed in May 1982 at Nagasaki – Part II Models," *Jour. Meteorological Soc. Japan* **67**, 279–291 (1989).
15. R. W. Young, K. L. Carder, P. R. Betzer, D. K. Costello, R. A. Duce, G. R. Ditullio, N. W. Tindale, E. A. Laws, M. Uematsu, J. T. Merrill and R. A. Feeley, "Atmospheric Iron Inputs and Primary Productivity: Phytoplankton Responses in the North Pacific," *Global Biogeochemical Cycles* **5**, 119–134 (1991).
16. R. J. Charlson, S. E. Schwartz, J. M. Hales, R. D. Cess, J. A. Coakley, J. E. Hansen and D. J. Hofmann, "Climate Forcing by Anthropogenic Aerosols," *Science* **255**, 423–430 (1992).

17. Y. J. Kaufman, "Remote Sensing of Direct and Indirect Aerosol Forcing," in *Aerosol Forcing of Climate*, edited by R. H. Charlson and J. Heintzenberg (Wiley, New York, NY, 1995) p. 297-332.
18. M. Griggs, "Measurements of the Aerosol Optical Thickness Over Water Using ERTS-1 Data," *Jour. Air Poll. Contr. Assoc.* **25**, 622-626 (1975).
19. Y. Mekler, H. Quenzel, G. Ohring and I. Marcus, "Relative Atmospheric Aerosol Content from ErtS Observations," *Jour. Geophys. Res.* **82**, 967-970 (1977).
20. R. S. Fraser, "Satellite measurement of mass of Sahara dust in the atmosphere," *Applied Optics* **15**, 2471-2479 (1976).
21. P. Koepke and H. Quenzel, "Turbidity of the Atmosphere Determined From Satellite: Calculation of Optimum Viewing Geometry," *Jour. Geophys. Res.* **84**, 7847-7856 (1979).
22. P. Koepke and H. Quenzel, "Turbidity of the Atmosphere Determined From Satellite: Calculation of Optimum Wavelength," *Jour. Geophys. Res.* **86**, 9801-9805 (1981).
23. P. A. Durkee, D. R. Jensen, E. E. Hindman and T. H. V. Haar, "The Relationship Between Marine Aerosol Particles and Satellite-Detected Radiance," *Jour. Geophys. Res.* **91D**, 4063-4072 (1986).
24. C. R. N. Rao, L. L. Stowe, E. P. McClain and J. Sapper, "Development and Application of Aerosol Remote Sensing with AVHRR Data from the NOAA Satellites," in *Aerosols and Climate*, edited by P. Hobbs and M. P. McCormick (Deepak, Hampton, VA, 1988) p. 69-80.
25. J. R. Herman, P. K. Bhartia, O. Torres, C. Hsu, C. Seftor and E. Celarier, "Global Distribution of Absorbing Aerosols from Nimbus-7/TOMS Data," 1996, *Jour. Geophys. Res.* (Submitted).

26. A. Bricaud and A. Morel, "Atmospheric Corrections and Interpretation of Marine Radiances in CZCS Imagery: Use of a Reflectance Model," *Oceanologica Acta* **7**, 33–50 (1987).
27. J. -M. André and A. Morel, "Atmospheric Corrections and Interpretation of Marine Radiances in CZCS Imagery, Revisited," *Oceanologica Acta* **14**, 3–22 (1991).
28. P. E. Land and J. D. Haigh, "Atmospheric correction over case 2 waters with an iterative fitting algorithm," *Applied Optics* **35**, 5443–5451 (1996).
29. J. E. Hansen and L. D. Travis, "Light Scattering in Planetary Atmospheres," *Space Science Reviews* **16**, 527–610 (1974).
30. H. R. Gordon, O. B. Brown, R. H. Evans, J. W. Brown, R. C. Smith, K. S. Baker and D. K. Clark, "A Semi-Analytic Radiance Model of Ocean Color," *Jour. Geophys. Res.* **93D**, 10909–10924 (1988).
31. A. Morel and L. Prieur, "Analysis of Variations in Ocean Color," *Limnology and Oceanography* **22**, 709–722 (1977).
32. A. Morel and B. Gentili, "Diffuse reflectance of oceanic waters: its dependence on Sun angle as influenced by the molecular scattering contribution," *Applied Optics* **30**, 4427–4438 (1991).
33. A. Morel and B. Gentili, "Diffuse reflectance of oceanic waters. II. Bidirectional aspects," *Applied Optics* **32**, 6864–6879 (1993).
34. A. Morel, K. J. Voss and B. Gentili, "Bidirectional reflectance of oceanic waters: A comparison of modeled and measured upward radiance fields," *Jour. Geophys. Res.* **100C**, 13,143–13,150 (1995).

35. A. Morel and B. Gentili, "Diffuse reflectance of oceanic waters. III. Implication of bidirectionality for the remote sensing problem," *Applied Optics* **35**, 4850–4862 (1996).
36. D. Tanre, M. Herman, P. Y. Deschamps and A. de Leffe, "Atmospheric modeling for space measurements of ground reflectances, including bidirectional properties," *Applied Optics* **18**, 3587–3594 (1979).
37. H. Yang and H. R. Gordon, 1997 , Remote sensing of ocean color: Assessment of the water-leaving radiance bidirectional effects on the atmospheric diffuse transmittance, *Applied Optics*, (Submitted).
38. M. Wang and H. R. Gordon, "Estimating aerosol optical properties over the oceans with the multiangle imaging spectroradiometer: Some preliminary studies," *Applied Optics* **33**, 4042–4057 (1994).
39. M. Wang and H. R. Gordon, "Estimation of aerosol columnar size distribution and optical thickness from the angular distribution of radiance exiting the atmosphere: simulations," *Applied Optics* **34**, 6989–7001 (1995).
40. E. P. Shettle and R. W. Fenn, *Models for the Aerosols of the Lower Atmosphere and the Effects of Humidity Variations on Their Optical Properties* (Air Force Geophysics Laboratory, Hanscomb AFB, MA 01731, AFGL-TR-79-0214, 1979).
41. F. X. Kenizys, E. P. Shettle, W. O. Gallery, J.H.Chetwynd, L. W. Abreu, J. E. A. Selby, S. A. Clough and R. W. Fenn, *Atmospheric Transmittance/Radiance: The LOWTRAN 6 Model* (Air Force Geophysics Laboratory, Hanscomb AFB, MA 01731, AFGL-TR-83-0187, 1983) NTIS AD A137796.
42. W. H. Press, B. P. Flannery, S. A. Teukolsky and W. T. Vetterling, *Numerical Recipes in FORTRAN* (Cambridge University Press, Cambridge, 1992), 963 pp.

43. H. R. Gordon and M. Wang, "Influence of Oceanic Whitecaps on Atmospheric Correction of SeaWiFS," *Applied Optics* **33**, 7754–7763 (1994).
44. H. R. Gordon, "Calibration Requirements and Methodology for Remote Sensors Viewing the Oceans in the Visible," *Remote Sensing of Environment* **22**, 103–126 (1987).
45. H. R. Gordon, On-orbit calibration strategy for vicarious calibration of ocean color sensors, *Applied Optics* (Submitted).
46. P. Koepke, "Effective Reflectance of Oceanic Whitecaps," *Applied Optics* **23**, 1816–1824 (1984).
47. R. Frouin, M. Schwindling and P. Y. Deschamps, "Spectral reflectance of sea foam in the visible and near-infrared: In-situ measurements and implications for remote sensing of ocean color and aerosols," *Jour. Geophys. Res.* **101C**, 14,361–14,371 (1996).
48. R. B. Husar, L. L. Stowe and J. M. Prospero, 1997, Satellite Sensing of Tropospheric Aerosols Over the Oceans with NOAA AVHRR, *Jour. Geophys. Res.* (In press).
49. A. Morel, "Optical Modeling of the Upper Ocean in Relation to Its Biogenous Matter Content (Case I Waters)," *Jour. Geophys. Res.* **93C**, 10,749–10,768 (1988).
50. Z. P. Lee, K. L. Carder, S. K. Hawes, R. G. Steward, T. G. Peacock and C. O. Davis, "Method to derive ocean absorption coefficients from remote sensing reflectance," *Applied Optics* **35**, 453–462 (1996).
51. M. Wang and H. R. Gordon, "Radiance reflected from the ocean-atmosphere system: Synthesis from individual components of the aerosol size distribution," *Applied Optics* **33**, 7088–7095 (1994).

52. W. A. Abdou, J. V. Martonchik, R. A. Kahn, R. A. West and D. J. Diner, 1997, A modified linear-mixing method for calculating atmospheric path radiances of aerosol mixtures, *Jour. Geophys. Res.* (In press).
53. D. J. Diner, C. J. Bruegge, J. V. Martonchik, T. P. Ackerman, R. Davies, S. A. W. Gerstl, H. R. Gordon, P. J. Sellers, J. Clark, J. A. Daniels, E. D. Danielson, V. G. Duval, K. P. Klaasen, G. W. L. A. D. I. Nakamoto, R. Pagano and T. H. Reilly, "MISR: A Multi-angle Imaging SpectroRadiometer for Geophysical and Climatological Research from EOS," *IEEE Transactions on Geoscience and Remote Sensing* **27**, 200–214 (1989).

Figure Captions

Figure 1. Spectrum of normalized water-leaving reflectance $[\rho_w(\lambda)]_N$ for pigment concentrations of 0.1, 0.5, and 1.0 mg/m³. For each pigment concentration, from the upper to the lower curves, the values of coefficient b^0 are 0.45, 0.30, and 0.12 m⁻¹, respectively.

Figure 2. Curve fits of $[\rho_a(\lambda) + \rho_{ra}(\lambda)]$ vs. τ_a for aerosol models of M70, C70, T70 and U70 with $\theta_0 = 60.0^\circ$, $\theta_v = 45.92^\circ$, and $\phi_v = 93.49^\circ$. Panel (a): 443 nm; panel (b): 865 nm.

Figure 3. Reflectance spectrum matching for pigment concentration $C = 0.50$ mg/m³ with sun-viewing geometry of $\theta_0 = 20.0^\circ$, $\theta_v = 45.92^\circ$, and $\phi_v = 90.0^\circ$. Panel (a): M80; panel (b): C80; panel (c): T80; panel (d) U80.

Figure 4. Influence of the physical thickness of the aerosol layer on the spectrum of $\rho_a + \rho_{ra}$. For U80 the aerosol is confined to a thin layer near the surface, while for U180, U280, U480, and UU80, the aerosol is uniformly mixed with air to a height of 1 km, 2 km, 4 km, and the whole atmosphere, respectively.

Table 1: Values of ω_0 at 865 nm for the candidate and test aerosol models.

	Candidate Models				Test Models
	RH=50%	RH=70%	RH=90%	RH=99%	RH=80%
M	0.9814	0.9859	0.9953	0.9986	0.9934
C	0.9705	0.9768	0.9919	0.9974	0.9884
T	0.9295	0.9346	0.9698	0.9870	0.9528
U	0.6026	0.6605	0.8206	0.9419	0.7481

Table 2: Mean values of retrieved $\omega'_0(865)$ for the seven sun-viewing geometries and each of four aerosol models (M80, C80, T80, U80). The standard deviation divided by the mean is listed in parenthesis.

	$C: \text{mg}/\text{m}^3$	0.100	0.500	1.000
M80 $\omega_0 = 0.993$	$\tau_a(865) = 0.100$	0.992 (0.43%)	0.996 (0.14%)	0.997 (0.10%)
	$\tau_a(865) = 0.200$	0.995 (0.10%)	0.995 (0.10%)	0.996 (0.05%)
	$\tau_a(865) = 0.300$	0.996 (0.05%)	0.996 (0.06%)	0.996 (0.10%)

	$C: \text{mg}/\text{m}^3$	0.100	0.500	1.000
C80 $\omega_0 = 0.988$	$\tau_a(865) = 0.100$	0.980 (0.97%)	0.972 (1.60%)	0.965 (2.26%)
	$\tau_a(865) = 0.200$	0.983 (0.53%)	0.988 (0.31%)	0.989 (0.41%)
	$\tau_a(865) = 0.300$	0.987 (0.25%)	0.987 (0.27%)	0.987 (0.37%)

	$C: \text{mg}/\text{m}^3$	0.100	0.500	1.000
T80 $\omega_0 = 0.953$	$\tau_a(865) = 0.100$	0.952 (0.78%)	0.935 (0.13%)	0.935 (0.00%)
	$\tau_a(865) = 0.200$	0.946 (0.34%)	0.936 (0.44%)	0.940 (1.41%)
	$\tau_a(865) = 0.300$	0.945 (0.31%)	0.934 (0.04%)	0.945 (1.82%)

	$C: \text{mg}/\text{m}^3$	0.100	0.500	1.000
U80 $\omega_0 = 0.748$	$\tau_a(865) = 0.100$	0.793 (4.21%)	0.761 (4.51%)	0.769 (3.36%)
	$\tau_a(865) = 0.200$	0.730 (4.76%)	0.750 (8.25%)	0.712 (7.44%)
	$\tau_a(865) = 0.300$	0.730 (5.14%)	0.784 (2.56%)	0.699 (7.34%)

Table 3: Mean values of retrieved C' for seven sun-viewing geometries and four aerosol models (M80, C80, T80, U80). The standard deviation divided by the mean is listed in parenthesis.

C : mg/m ³	0.100	0.500	1.000
$\tau_a(865) = 0.100$	0.100 (1.90%)	0.528 (7.30%)	1.098 (11.7%)
$\tau_a(865) = 0.200$	0.101 (4.56%)	0.547 (15.2%)	0.982 (23.9%)
$\tau_a(865) = 0.300$	0.101 (4.42%)	0.612 (24.1%)	0.947 (31.3%)

Table 4: Mean values of retrieved C' for seven sun-viewing geometries and three aerosol models (M80, C80, T80) derived using the Gordon and Wang¹¹ algorithm. The standard deviation divided by the mean is listed in parenthesis.

C : mg/m ³	0.10	0.47	0.91
$\tau_a(865) = 0.100$	0.101 (1.6%)	0.466 (3.4%)	0.912 (9.1%)
$\tau_a(865) = 0.200$	0.100 (3.1%)	0.470 (4.7%)	0.940 (12.8%)
$\tau_a(865) = 0.300$	0.098 (5.5%)	0.493 (15.3%)	0.936 (25.3%)

Table 5: Percentage of retrieved pigment concentration C' within certain error limits for aerosol models M80, C80, T80, and U80.

	$\Delta C/C :$	< 5%	< 10%	< 20%	< 30%
$C = 0.1 \text{ mg/m}^3$	$\tau_a(865) = 0.100$	96%	100%	100%	100%
	$\tau_a(865) = 0.200$	89%	92%	100%	100%
	$\tau_a(865) = 0.300$	89%	92%	100%	100%
	$\Delta C/C :$	< 5%	< 10%	< 20%	< 30%
$C = 0.5 \text{ mg/m}^3$	$\tau_a(865) = 0.100$	32%	75%	92%	100%
	$\tau_a(865) = 0.200$	32%	50%	75%	89%
	$\tau_a(865) = 0.300$	25%	35%	64%	75%
	$\Delta C/C :$	< 5%	< 10%	< 20%	< 30%
$C = 1.0 \text{ mg/m}^3$	$\tau_a(865) = 0.100$	21%	50%	71%	96%
	$\tau_a(865) = 0.200$	28%	39%	57%	71%
	$\tau_a(865) = 0.300$	14%	25%	50%	60%

Table 6: Mean values of retrieved $\tau'_a(865)$ for seven sun-viewing geometries and four aerosol models (M80, C80, T80, U80). The standard deviation divided by the mean is listed in parenthesis.

$C: \text{ mg/m}^3$	0.100	0.500	1.000
$\tau_a(865) = 0.100$	0.102 (8.94%)	0.101 (10.2%)	0.102 (11.6%)
$\tau_a(865) = 0.200$	0.201 (6.31%)	0.199 (8.53%)	0.199 (8.20%)
$\tau_a(865) = 0.300$	0.300 (6.22%)	0.294 (8.79%)	0.300 (9.93%)

Table 7: Mean values of retrieved C for seven sun-viewing geometries and three aerosol models (UU80, U280, U480). The standard deviation divided by the mean is listed in parenthesis.

C : mg/m ³	0.100	0.500	1.000
$\tau_a(865) = 0.100$	0.103 (8.74%)	0.600 (29.11%)	1.054 (19.27%)
$\tau_a(865) = 0.200$	0.114 (17.51%)	0.574 (39.12%)	1.026 (35.13%)
$\tau_a(865) = 0.300$	0.125 (32.93%)	0.644 (57.33%)	0.863 (52.53%)

Table 8: Percentage of retrieved pigment concentration C within certain error limits for aerosol models UU80, U280 and U480.

	$\Delta C/C$:	< 5%	< 10%	< 20%	< 30%
$C = 0.1 \text{ mg/m}^3$	$\tau_a(865) = 0.100$	85%	85%	95%	95%
	$\tau_a(865) = 0.200$	57%	57%	71%	80%
	$\tau_a(865) = 0.300$	57%	57%	61%	61%

	$\Delta C/C$:	< 5%	< 10%	< 20%	< 30%
$C = 0.5 \text{ mg/m}^3$	$\tau_a(865) = 0.100$	28%	52%	71%	90%
	$\tau_a(865) = 0.200$	38%	57%	66%	66%
	$\tau_a(865) = 0.300$	23%	38%	66%	66%

	$\Delta C/C$:	< 5%	< 10%	< 20%	< 30%
$C = 1.0 \text{ mg/m}^3$	$\tau_a(865) = 0.100$	47%	66%	71%	76%
	$\tau_a(865) = 0.200$	19%	38%	52%	61%
	$\tau_a(865) = 0.300$	4%	28%	52%	57%

Table 9: Mean values of retrieved $\omega_0(865)$ for seven sun-viewing geometries of aerosol model U180. The standard deviation divided by the mean is listed in parenthesis.

	$C: \text{mg/m}^3$	0.100	0.500	1.000
U180 $\omega_0 = 0.748$	$\tau_a(865) = 0.100$	0.764 (4.81%)	0.787 (6.82%)	0.787 (4.88%)
	$\tau_a(865) = 0.200$	0.737 (3.24%)	0.737 (8.84%)	0.723 (13.50%)
	$\tau_a(865) = 0.300$	0.736 (4.31%)	0.727 (4.39%)	0.714 (8.86%)

Table 10: Mean values of retrieved C for seven sun-viewing geometries of aerosol model U180. The standard deviation divided by the mean is listed in parenthesis.

$C: \text{mg/m}^3$	0.100	0.500	1.000
$\tau_a(865) = 0.100$	0.100 (0.00%)	0.556 (7.15%)	1.094 (8.53%)
$\tau_a(865) = 0.200$	0.100 (0.00%)	0.544 (8.74%)	1.101 (16.12%)
$\tau_a(865) = 0.300$	0.100 (0.00%)	0.566 (3.04%)	1.061 (15.11%)

Table 11: Percentage of retrieved pigment concentration C within certain error limits for the aerosol model U180.

	$\Delta C/C :$	< 5%	< 10%	< 20%	< 30%
$C = 0.1 \text{ mg/m}^3$	$\tau_a(865) = 0.100$	100%	100%	100%	100%
	$\tau_a(865) = 0.200$	100%	100%	100%	100%
	$\tau_a(865) = 0.300$	100%	100%	100%	100%
	$\Delta C/C :$	< 5%	< 10%	< 20%	< 30%
$C = 0.5 \text{ mg/m}^3$	$\tau_a(865) = 0.100$	28%	42%	71%	100%
	$\tau_a(865) = 0.200$	14%	42%	100%	100%
	$\tau_a(865) = 0.300$	0%	14%	100%	100%
	$\Delta C/C :$	< 5%	< 10%	< 20%	< 30%
$C = 1.0 \text{ mg/m}^3$	$\tau_a(865) = 0.100$	28%	57%	85%	100%
	$\tau_a(865) = 0.200$	0%	28%	57%	100%
	$\tau_a(865) = 0.300$	28%	28%	71%	100%

Table 12: Mean values of retrieved $\tau_a(865)$ for seven sun-viewing geometries of the aerosol model U180. The standard deviation divided by the mean is listed in parenthesis.

$C: \text{ mg/m}^3$	0.100	0.500	1.000
$\tau_a(865) = 0.100$	0.102 (1.68%)	0.101 (3.62%)	0.099 (3.83%)
$\tau_a(865) = 0.200$	0.206 (3.49%)	0.206 (2.89%)	0.209 (7.59%)
$\tau_a(865) = 0.300$	0.305 (3.32%)	0.307 (2.52%)	0.304 (7.36%)

Table 13: Values of the residual radiometric calibration uncertainty after effecting an in-orbit calibration adjustment.⁴⁵

λ_i (nm)	% Uncertainty
412	0.3
443	0.5
490	0.8
520	1.0
550	1.5
670	2.0
765	3.0
865	5.0

Table 14: Mean values of the retrieved C for the seven sun-viewing geometries and each of four aerosol models (M80, C80, T80, U80) for the indicated calibration error (Table 13). The standard deviation divided by the mean is listed in parenthesis. $\tau_a(865) = 0.2$.

Calibration Error	C (mg/m ³)		
	0.100	0.500	1.000
+ Error	0.102 (4.3%)	0.539 (15.1%)	0.976 (21.2%)
0 Error	0.100 (3.1%)	0.470 (4.7%)	0.940 (12.8%)
- Error	0.100 (5.7%)	0.534 (15.9%)	1.029 (23.3%)

Table 15: Mean values of retrieved C for seven sun-viewing geometries and four aerosol models (M80, C80, T80, U80) for $\Delta[\rho_{wc}] = +0.002$.

The standard deviation divided by the mean is listed in parenthesis.

$C: \text{mg/m}^3$	0.100	0.500	1.000
$\tau_a(865) = 0.100$	0.100 (0.00%)	0.455 (9.54%)	0.838 (19.89%)
$\tau_a(865) = 0.200$	0.101 (4.68%)	0.485 (15.72%)	0.891 (23.44%)
$\tau_a(865) = 0.300$	0.102 (6.97%)	0.526 (18.80%)	0.843 (25.55%)

Table 16: Mean values of retrieved C for seven sun-viewing geometries and four aerosol models (M80, C80, T80, U80) for $\Delta[\rho_{wc}] = -0.002$.

The standard deviation divided by the mean is listed in parenthesis.

$C: \text{mg/m}^3$	0.100	0.500	1.000
$\tau_a(865) = 0.100$	0.100 (0.94%)	0.647 (12.83%)	1.175 (18.21%)
$\tau_a(865) = 0.200$	0.100 (2.32%)	0.644 (17.53%)	1.030 (24.13%)
$\tau_a(865) = 0.300$	0.101 (4.96%)	0.699 (24.94%)	0.985 (31.03%)

Appendix 2

Columnar Aerosol Phase Function and Single Scattering Albedo from Sky Radiance over Land: Simulations

Retrieval of the Columnar Aerosol Phase Function and Single Scattering

Albedo from Sky Radiance over Land: Simulations

Haoyu Yang and Howard R. Gordon

Department of Physics

University of Miami

Coral Gables, FL 33124

Submitted to *Applied Optics*

Acknowledgment

The authors gratefully acknowledges support the of the National Aeronautics and Space Administration for support under Grant NAGW-273 and Contracts NAS5-31363 and NAS5-31734.

Abstract

This paper centers on a retrieval scheme which can be used to derive the aerosol phase function and single scattering albedo from the sky radiance over land. The retrieval algorithm iteratively corrects the aerosol volume scattering function, the product of the single scattering albedo and the phase function, based on the difference between the measured sky radiance and the radiance calculated by solving the radiative transfer equation. It is first tested under ideal conditions, i.e., the approximations made in the retrieval algorithm totally agree with actual conditions assumed in creating the pseudo data for sky radiance. It is then tested under more realistic conditions to assess its susceptibility to measurement errors and effects of conditions not recognized in the retrieval algorithm, i.e., surface horizontal inhomogeneity, departures of the surface from lambertian, and aerosol horizontal inhomogeneity. These simulations show that, in most cases, this scheme can retrieve the aerosol single scattering albedo with high accuracy (within 1%), and can therefore be used to identify absorbing aerosols. It can also produce meaningful retrievals of most aerosol phase functions: less than 5% error at 865 nm and less than 10% at 443 nm in most cases. Typically, the error in the volume scattering function is small for scattering angles $\lesssim 70^\circ - 80^\circ$, then increases for larger angles. Disappointing results in both the single scattering albedo and the scattering phase function occur at 443 nm, either when there are large calibration errors in the radiometer used to measure the sky radiance, or when the land reflection properties are significant inhomogeneous.

1. Introduction

Aerosols are of considerable interest today because of their role in biogeochemical cycling and climate.¹⁻³ Thus, several space-borne visible and near infrared (NIR) remote sensing systems have been planned that are capable of delineating their global distribution: the Moderate Resolution Imaging Spectrometer (MODIS),⁴ the Multi-angle Imaging SpectroRadiometer (MISR),⁵ the polarization and directionality of earth reflectance (POLDER),⁶ etc. However, interpretation of the remotely sensed top-of-atmosphere (TOA) radiance contributed by the aerosol in terms of its physical-chemical, or even optical, properties requires the use of aerosol models.^{7,8} These aerosol models can be physical-chemical, in which the size distribution and index of refraction of each aerosol component is specified (on the basis of direct measurements⁹), and the optical properties derived from Mie theory,^{10,11} completely optical, in which the aerosol phase function and single-scattering albedo are specified spectrally; or a combination of the two. Similarly, aerosol models are also required for atmospheric correction to enable remote sensing systems to retrieve the spectral reflectance of the earth's surface.^{12,13}

An aerosol network (AERONET)¹⁴ has been established for the purpose of obtaining the optical properties of aerosols under a wide variety of conditions. This network consists of robotic radiometers that measure the radiance of the direct sun and the angular distribution of the sky radiance. Thus far, analysis of this data has focused on the inversion of the aerosol optical thickness and solar aureole radiance, using methods developed by Nakajima,¹⁵ to study the aerosol size distribution.¹⁶ The resulting size distribution is then used with Mie theory to derive the aerosol phase function. One desirable advantage of this is that the *columnar* aerosol optical properties are obtained, quantities that would be very difficult to obtain by direct sampling.

In earlier papers, Gordon, Wang, and coworkers showed how the sky radiance,^{17,18} or a combination of the sky radiance and the TOA radiance,^{19,20} could be used to retrieve the columnar aerosol phase function and single-scattering albedo directly, without the necessity of Mie theory. The basic Wang and Gordon¹⁷ algorithm is an extension of the work of Wendisch and von Hoyningen-Huene.²¹ Briefly, the sky radiance is computed by solving the radiative transfer equation (RTE) with an initial input of an arbitrary aerosol volume scattering function (product of the phase function and single-scattering albedo). Recursive procedures are then applied to correct the trial volume scattering function based in the difference between the calculated and measured sky radiance. The RTE

is solved at each iteration, so the final solution contains all the effects of multiple scattering. Simulations show that the algorithm can successfully retrieve the single-scattering albedo and aerosol phase function even when the aerosol optical thickness is as high as 2.¹⁹

The Wang and Gordon algorithm was originally designed to facilitate the retrieval of the aerosol single scattering albedo and phase function over the ocean, and until now, has not been modified for operation over the land. There are intrinsic differences between ocean surfaces and land surfaces. First, land surfaces are much brighter than ocean surfaces. They more strongly influence the sky radiance; therefore, they are expected to have a negative impact on retrieval. Second, the bidirectional reflectance distribution functions (BRDF's) for land surfaces are much more complicated than those for ocean surfaces. The BRDF's for the ocean surface in the NIR can basically be described by a universal relationship, the only variable in which is the wind speed.²²⁻²⁴ No such relationship exists for land surfaces.

In this paper, the Wang and Gordon algorithm is modified for application over land for retrieving the aerosol single scattering albedo and volume scattering function. First, we illustrate the basic procedure of the retrieval algorithm. Next, we provide simulation results of the assuming measurements are made under ideal conditions and are error-free. Finally, we assess the effects on the retrievals of measurement errors and various conditions which may exist in practice, yet are not taken into account in the retrieval algorithm, including surface horizontal inhomogeneity, aerosol horizontal inhomogeneity, and a non-Lambertian surface.

2. Basic Procedure of the Retrieval Algorithm

The total optical thickness of the atmosphere includes the optical thickness of Rayleigh scattering, τ_r , the optical thickness of aerosol scattering, τ_a , the optical thickness of the ozone layer, τ_{O_z} , and the optical thickness of other absorbing gases, τ_g . τ_r is very stable, and given the surface pressure, can be computed at each wavelength.²⁵ τ_g , even though not so stable, is insignificant except in absorption bands. If one performs measurements between the absorption bands of absorbing gases, τ_g can generally be neglected.²⁶ Ozone absorption occurs throughout the visible and cannot be neglected. Also, τ_{O_z} is highly variable. However it can be measured with space-borne sensors, e.g., TOMS.²⁷ Therefore, it is possible to obtain the aerosol optical thickness by subtracting τ_r and τ_{O_z} from the measured total optical thickness. Thus, we will assume that τ_a can be obtained in this manner.

The basic procedure in the algorithm is as follows.

- 1) Measure the sky radiance, the aerosol optical thickness (Figure 1), and the land albedo.
- 2) Calculate the sky radiance by solving the RTE using an arbitrary aerosol volume scattering function, the measured aerosol optical thickness, and land albedo.
- 3) Adjust the aerosol volume scattering function based on the difference between the measured sky radiance and the calculated sky radiance.
- 4) Interpolate and extrapolate the adjusted volume scattering function and use it to recalculate the sky radiance.
- 5) Repeatedly apply Steps (2), (3) and (4).

The volume scattering function V is defined as follows:

$$V(\hat{\xi}_0 \rightarrow \hat{\xi}) = \frac{\omega_0}{4\pi} P(\hat{\xi}_0 \rightarrow \hat{\xi}), \quad (1)$$

where ω_0 is the single scattering albedo and P is the scattering phase function. (This definition differs from the ordinary definition of the volume scattering function,²⁸ β , the differential scattering cross section per unit volume, by a factor of c , which is the extinction coefficient: $\beta = cV$). The centerpieces of implementing the above algorithm are to (1) develop a computer code to solve the

radiative transfer equation (RTE) for radiance given an aerosol volume scattering function, and to (2) establish a relationship between the error in the volume scattering function, $\Delta V_a(\Theta)$, and $\Delta L_t(\hat{\xi})$, the difference between the calculated radiance and the measured sky radiance.

To solve the RTE, we make the following assumptions and approximations. First we assume that the aerosol and Rayleigh scattering are confined between parallel planes. Also, since in reality about 80% of the aerosols are confined to a layer extending approximately two kilometers above the ground or the ocean, and about 80%-90% of the Rayleigh scattering is distributed above the aerosol layer,²⁹ we assume that the atmosphere is divided into two layers. The upper layer is exclusively Rayleigh scattering and the lower layer contains only aerosols. The above atmospheric model is known as the two-layer plane-parallel model. The ozone layer and other absorbing gases have been neglected. The ozone layer can be conveniently treated as a fully absorptive layer above the top of the atmosphere, and therefore can be easily incorporated into the retrieval algorithm. As for other absorbing gases, one can generally choose the wavelength windows between strong absorption bands of absorbing gases, where the effect of absorbing gases are not significant. For these reasons, the omission is not regarded as significant. We further assume that the land surface as well as the atmosphere is horizontally homogeneous, and that the land surface is Lambertian. With the above approximations and assumptions, one can solve the RTE using the successive order method.²¹ The details of implementing this method are provided by Van de Hulst.³⁰

Now that we can solve the RTE, the next challenge is to find the relationship between ΔV_a and ΔL_t . It is sometimes desirable to distinguish between the radiance resulting from Rayleigh scattering and the radiance resulting from aerosol scattering. The total radiance may be divided into the following terms:

$$L_t = L_r e^{-\tau_a/\mu} + L_a e^{-\tau_r/\mu_0} + L_{ra}, \quad (2)$$

where L_r is the radiance contributed by Rayleigh scattering in the absence of aerosol scattering, L_a is the radiance contributed by aerosol scattering in the absence of Rayleigh scattering, and L_{ra} ³¹ is the radiance contributed by the interaction between aerosol scattering and Rayleigh scattering. μ and μ_0 are, respectively, the cosines of the viewing zenith angle and solar zenith angle.

Suppose the sky radiance is simulated with an aerosol volume scattering function different from the true one. The calculated sky radiance is naturally different from the measured sky radiance,

i.e.,

$$\Delta L_t(\hat{\xi}_i) \equiv L_t^{(m)}(\hat{\xi}_i) - L_t^{(c)}(\hat{\xi}_i), \quad (3)$$

where $L_t^{(m)}$ is the measured sky radiance, $L_t^{(c)}$ is the calculated sky radiance and $\hat{\xi}_i$ is the i^{th} viewing direction. None of $\Delta L_t(\hat{\xi}_i)$ results from pure Rayleigh scattering. Therefore,

$$\Delta L_t(\hat{\xi}_i) = \Delta L_a(\hat{\xi}_i)e^{-\tau_r/\mu_0} + \Delta L_{ra}(\hat{\xi}_i). \quad (4)$$

Divide L_a into single scattering radiance, L_{as} , and multiple scattering radiance, L_{am} , and further divide L_{as} into single scattering radiance in the absence of a surface, L_{as0} , and a surface contribution, L_{ass} . Since the interaction term is usually smaller than the other terms when the aerosol optical thickness is small, it is neglected:

$$\Delta L_t(\hat{\xi}_i) = \Delta[L_{as0}(\hat{\xi}_i) + L_{ass}(\hat{\xi}_i) + L_{am}(\hat{\xi}_i)]e^{-\tau_r/\mu_0} \quad (5)$$

Assume that the error in the total aerosol scattering is allocated to L_{as0} , L_{ass} , and L_{am} based on their values:

$$\frac{\Delta L_{as0}(\hat{\xi}_i)}{L_{as0}(\hat{\xi}_i)} = \frac{\Delta L_{ass}(\hat{\xi}_i)}{L_{ass}(\hat{\xi}_i)} = \frac{\Delta L_a(\hat{\xi}_i)}{L_a(\hat{\xi}_i)} = \frac{\Delta L_t(\hat{\xi}_i)}{L_a(\hat{\xi}_i)e^{-\tau_r/\mu_0}}. \quad (6)$$

Since

$$L_{as0}(\hat{\xi}_i) = \frac{F_0}{\mu} \tau_a V_a(\Theta_i), \quad (7)$$

we have

$$\frac{\Delta V_a(\Theta_i)}{V_a(\Theta_i)} = \frac{\Delta L_t(\hat{\xi}_i)}{L_a(\hat{\xi}_i)e^{-\tau_r/\mu_0}}, \quad (8)$$

where Θ_i is the scattering angle from the solar beam to the i^{th} viewing direction, $\hat{\xi}_i$.

The assumption made in Eq. (6) is not accurate. Indeed, usually more error is made in proportion to aerosol multiple scattering than to single scattering. Also, if the aerosol optical thickness is high, one cannot neglect the interaction term. Therefore, Eq. (8) is not precise. If it is used without modification in the iterative procedure illustrated at the beginning of this section, the calculated sky radiance often diverges instead of converging to the measured sky radiance. To solve this problem, we devised a self-adjusting constant C to ensure the convergence of the calculated radiance:

$$[V_a(\Theta_i)]_{new}^{(c)} = [V_a(\Theta_i)]_{old}^{(c)} - C\Delta[V_a(\Theta_i)]^{(c)}, \quad (9)$$

where $\Delta[V_a(\Theta_i)]^{(c)}$ is $\Delta V_a(\Theta_i)$ calculated in Eq. (8), $[V_a(\Theta_i)]_{old}^{(c)}$ is the volume scattering function used in the previous iteration, and $[V_a(\Theta_i)]_{new}^{(c)}$ is the new trial volume scattering function. The

initial value of C is set to one. In each iteration, the algorithm keeps track of the previous average value of $|\Delta L_t(\hat{\xi}_i)/[L_a^{(c)}(\hat{\xi}_i)e^{-\tau_r/\mu_0}]|$. If it increases, which suggests that the $|V_a^{(c)}(\Theta_i)|$ is over-corrected, C is decreased by half. When there are relatively large errors in the measurements, C may get too small. In this case C is reset to 1.

The retrieval algorithm is almost complete up to this point. However, it is necessary to define certain conditions to terminate the iteration. The conditions used in the retrieval algorithm are (1) the average absolute percentage difference between the measured sky radiance and the calculated radiance in all measurement directions is smaller than a certain threshold value (0.1%), and the *maximum* percentage difference is smaller than twice that value, or (2) the number of iterations exceed a certain value (100). Once the iteration stops, the single scattering albedo and phase function are obtained by applying the following equations:

$$\omega_0 = \int_{4\pi} V_a(\Theta) d\Omega, \quad (10)$$

$$P_a(\Theta) = 4\pi \frac{V_a(\Theta)}{\omega_0}. \quad (11)$$

Other than the fact that the lower boundary of the medium is a Lambertian reflector as opposed to a Fresnel reflector, there are a few differences between the above-illustrated retrieval algorithm and the original Wang and Gordon algorithm for use over the ocean. First, Eq. (8) is slightly different from the basic equation used in the Wang and Gordon algorithm. In the Wang and Gordon algorithm, the denominator on the right hand side of Eq. (8) is $L_t(\hat{\xi}_i) - L_r(\hat{\xi}_i)e^{-\tau_a/\mu_0}$. The difference is not regarded as significant. Second, the constant C remains the same in the Wang and Gordon algorithm. The value of C is determined empirically. The assignment of C as a self-adjusting variable not only reduces the number of iterations in each run, but also reduces the amount of testing necessary to determine an optimum C . Finally, the Wang and Gordon algorithm is terminated after a certain number of iterations. The design to terminate the iteration based on the relative error in the sky radiance also improves the efficiency of the retrieval algorithm.

3. Basic Simulation Results

3.1 Simulation of the Sky Radiance

To evaluate the performance of the retrieval algorithm, we used simulated measurements. However, we do take into consideration the practicality of these measurements so that they can be made in real situations. The radiance in the simulated measurements is obtained by solving the RTE. A variety of aerosol models with different aerosol optical thicknesses have been used to generate the pseudo data for the sky radiance. The performance of the retrieval algorithm is evaluated by comparing the retrieved volume scattering function with the aerosol volume scattering function used in creating the pseudo data, henceforth referred to as the true aerosol volume scattering function.

The proposed measurements of sky radiance include almucantar measurements and principal plane measurements. In the almucantar measurements, one first aims the detector directly at the sun ($\theta_v = \theta_0$, $\phi_v = 0$). While keeping the zenith angle of the detector fixed, one increases the azimuth angle, ϕ_v , of the detector by fixed increments until it reaches 180° . Subsequent to the almucantar measurements, one keeps the azimuth angle of the detector at 180° in the principal plane measurements, and increases the zenith angle of the detector by fixed increments until it is almost horizontal. Figure 1 shows the geometry of the measurements.

The solar zenith angle is fixed to be 60° in all cases. The increments in both the almucantar measurements and the principal plane measurements are set to 5° . The almucantar measurement at $\phi_v = 0$ is excluded, because it's impossible in actual measurements to separate the scattered light from the direct sun light when the detector points at the sun. Two additional measurements are taken in the almucantar measurements at $\phi_v = 3^\circ$ and $\phi_v = 7^\circ$ in order to obtain more information on the aerosol volume scattering function at small angles, since most aerosol phase functions are strongly forward peaked. At $\phi_v = 3^\circ$, ($\theta_v = 60^\circ$) the scattering angle from the sun to the detector is 2.59° .

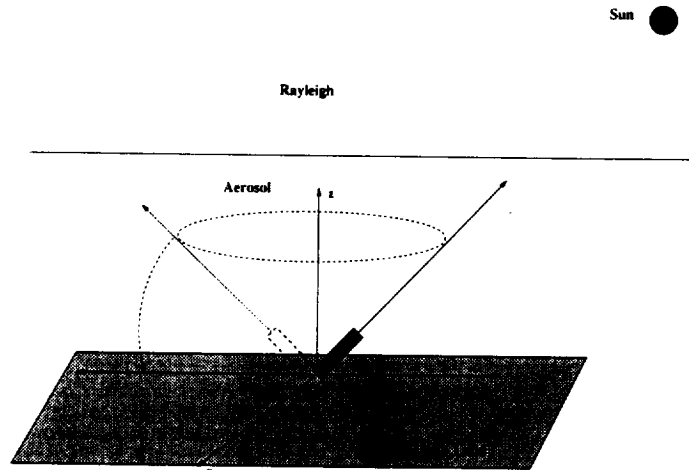


Figure 1. Downwelling radiance measurement.

This is the smallest angle at which a volume scattering function is obtained from measurements. The volume scattering function at scattering angles smaller than 2.59° has to be obtained through extrapolation. Note that presently, the smallest scattering angle from the sun to the detector at which the radiance can be measured accurately is about 2° .¹⁵ Therefore, it is practical to measure the sky radiance at $\Theta = 2.59^\circ$. In the principal plane measurements, the largest zenith angle of the detector is set at 85° . Therefore, in the sky radiance measurements, the largest single scattering angle achievable is $\Theta = \theta_0 + 85^\circ = 145^\circ$. At any scattering angle larger than 145° , the phase function has to be extrapolated. We extrapolate the phase function by assuming that it is the same beyond 145° as it is at 145° .

Throughout this section, it is assumed that no error is incurred in these measurements. In addition, it is assumed that these measurements are conducted under ideal conditions, i.e., the conditions under which the measured radiance is produced are identical to those in the retrieval algorithm. To be more specific, the two-layer plane-parallel atmosphere model and the horizontal homogeneity assumption of aerosols and land surfaces, along with the approximation of a Lambertian surface, all of which are used in the retrieval algorithm, are adopted in generating measured radiance. The same values of the land albedos and aerosol optical thicknesses were used in both the retrieval algorithm and the sky radiance simulation program.

3.2 The Retrieval Results

Rayleigh scattering can have significant influence on the total radiance, especially when the scattering angle from the solar beam to the detector is large. To assess possible effects of Rayleigh scattering on the retrieval results, we applied the retrieval algorithm at wavelengths of 865 nm and 443 nm. The optical thickness for Rayleigh scattering is 0.01554 at 865 nm and 0.2361 at 443 nm at standard surface pressure.²⁵ These values have been used throughout this paper.

We plan to use the algorithm described here to understand the properties of aerosols in coastal areas, therefore, we shall concentrate on aerosol models most likely to represent aerosols near the coast. For this purpose, we use the Gordon and Wang¹² coastal aerosol model at 80% relative humidity (RH), C80, in most computations. However, because we also wanted to examine the performance of the algorithm under more general conditions, we have also carried out tests using several aerosol models described by Shettle and Fenn.¹⁰ These include their urban models at $RH = 0\%$, $RH = 99\%$ (U00 and U99), and their tropospheric model at $RH = 80\%$ (T80). These aerosols

provide a range of shapes for the volume scattering function and a range of values for the single scattering albedo. The phase functions and values of the single scattering albedos for these models at 865 nm and 443 nm are provided in Figure 2. In this figure, the phase functions for Rayleigh scattering are represented by dash-and-dotted lines, and the phase functions of C80, U99, U00 and T80 are represented by solid lines, dotted lines, long-dashed lines and short-dashed lines, respectively.

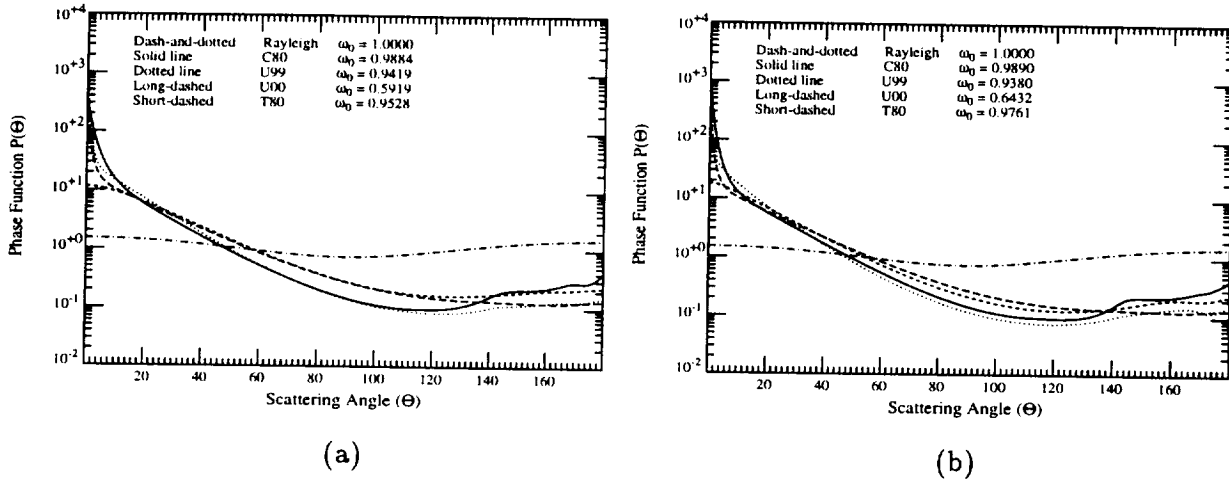


Figure 2: Phase functions and single scattering albedos for the aerosol models used in this study. (a) is for $\lambda=865$ nm and (b) is for $\lambda=443$ nm.

The coastal aerosol model is expected to be representative of aerosols found in coastal areas. They have a component of relatively large sea salt particles in addition to the aerosol in the T80 model. Beside the sharp peak at small scattering angles, the phase functions for C80 also have a significant backward structure. The tropospheric aerosol model is used for aerosols in the troposphere, which are the small-particle component of aerosols expected to be found in rural areas free of pollution. Compared to the C80 aerosol at both wavelengths, the phase functions for T80 are less forwardly peaked. Urban aerosols are normally found in heavily polluted urban areas. They are composed of both large and small particles. The phase functions for U99 are extremely sharp at near-zero scattering angles. The phase functions for U00 are milder in forward directions, but the aerosol is highly absorbing. The single scattering albedo for U00 at 865 nm and 443 nm are 0.5919 and 0.6432, respectively. In backward directions, the phase functions for both U99 and U00 are much smoother compared to those for C80. Thus, our models span a considerable range of shapes for $P(\Theta)$ and values of ω_0 .

Figure 3 shows the comparison of the true volume scattering functions and the retrieved volume scattering functions for the C80 aerosol at 865 nm and 443 nm. The true volume scattering functions are represented by solid lines and the retrieved volume scattering functions are represented by open circles. The land albedo is set to 1.0 at 865 nm and 0.5 at 443 nm, since most vegetated surfaces have a smaller albedo in the blue than in the near infrared (NIR). Note that these albedos are also larger than would be found in nature.^{32,33} We use these larger albedos to make the retrieval more difficult for the algorithm. The optical thickness of the aerosol is set to 0.2 in both figures for comparison purposes. (In reality, the optical thickness of the aerosol layer would be larger at 443 nm than at 865 nm). In both figures, the retrieved volume scattering functions are almost perfect at small angles. They start to deviate from the true volume scattering functions at large angles due to the inability to get data beyond $\Theta = 145^\circ$.

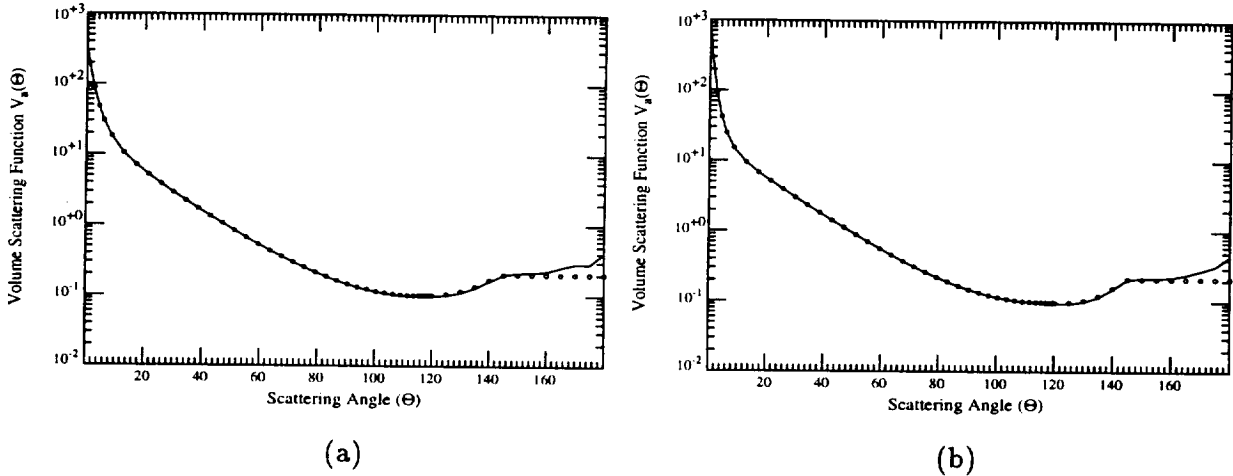


Figure 3. Comparison between the true (lines) and retrieval (circles) $V_a(\Theta)$ for the C80 aerosol model: (a) is for $\lambda = 865$ nm and (b) is for $\lambda = 443$ nm.

We define the error in the aerosol single scattering albedo $\Delta\omega_0$ as

$$\Delta\omega_0 = \frac{\omega_0^{(c)} - \omega_0^{(t)}}{\omega_0^{(t)}}, \quad (12)$$

where $\omega_0^{(c)}$ is the retrieved aerosol single scattering albedo and $\omega_0^{(t)}$ is the true single scattering albedo, and we define the average error in the volume scattering function $\Delta V_a/V_a$ as

$$\Delta V_a/V_a = \frac{1}{N} \sum_{i=1}^N \left| \frac{[V_a(\Theta_i)]^{(c)} - [V_a(\Theta_i)]^{(t)}}{[V_a(\Theta_i)]^{(t)}} \right|, \quad (13)$$

where N is the number of measurements of L_t in a data set. Note that the definition of $\Delta V_a/V_a$ does not include the error in the volume scattering function for scattering angles smaller than 2.59° or larger than 145° . For the inversions shown in Figure 3, $\Delta\omega_0 = -0.004\%$, $\Delta V_a/V_a = 1.29\%$ at 865 nm; $\Delta\omega_0 = -0.004\%$, $\Delta V_a/V_a = 1.29\%$ at 443 nm.

Figure 4 shows the retrieval errors for C80, T80, U99, and U00 at 865 nm and 443 nm as a function of τ_a . The land albedo is set to 1.0 at 865 nm and 0.5 at 443 nm.

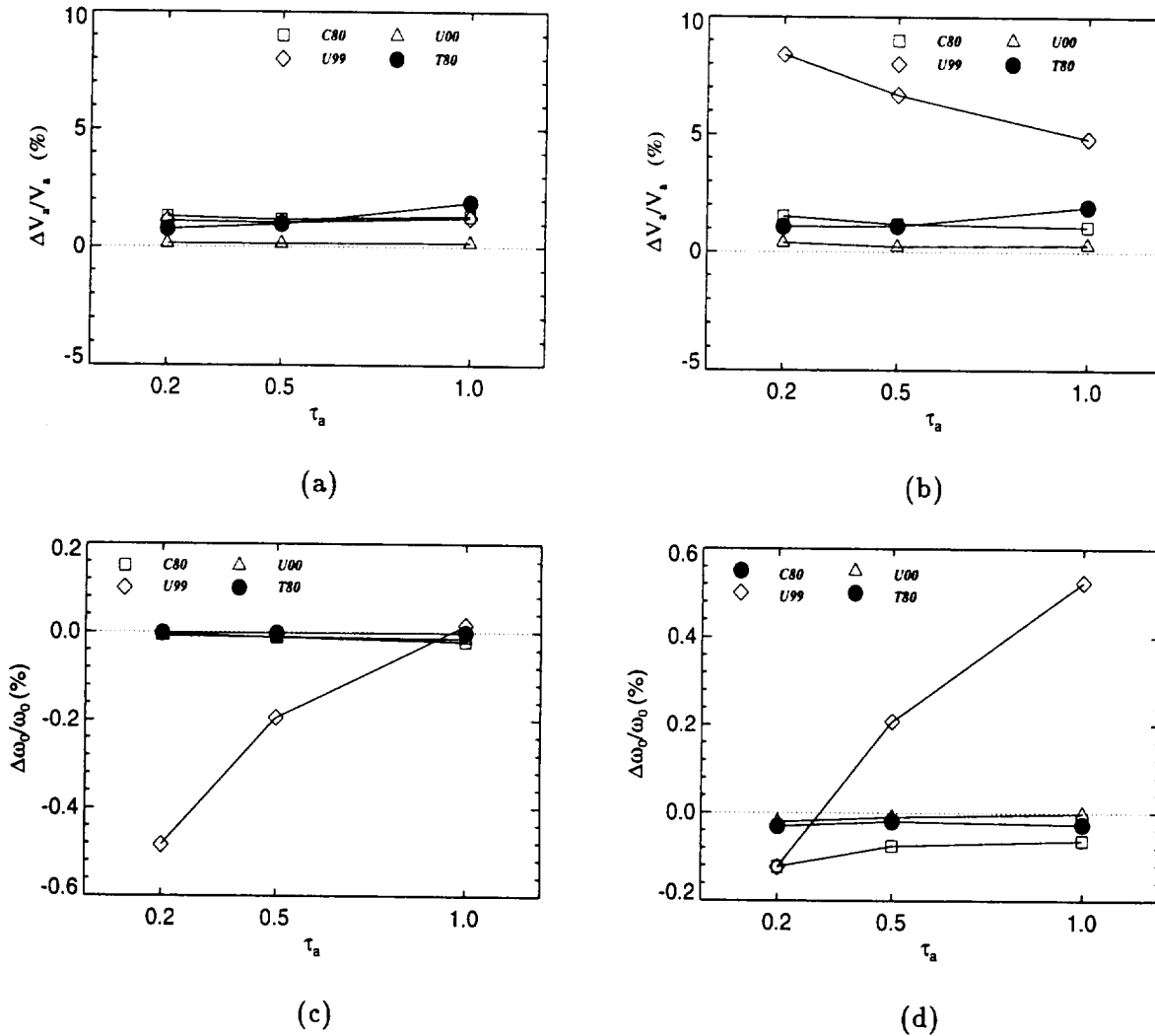


Figure 4: Retrieval errors as a function of τ_a under ideal conditions. (a) and (b) show the error in the aerosol volume scattering function at $\lambda=865$ nm and $\lambda=443$ nm, respectively. (c) and (d) show the error in the aerosol single scattering albedo at $\lambda=865$ nm and $\lambda=443$ nm, respectively.

The overall retrieval results are excellent. For most aerosols, retrieval errors in the volume scattering functions are within 2%, and retrieval errors in the single scattering albedo are within 0.1%. It is worthy of mentioning that the retrieval results for U00, the absorbing aerosol, are extremely good, which suggests that the retrieval algorithm may be used to identify absorbing aerosols. This is in agreement with the conclusions of King and Herman.³⁴ The retrieval results for U99 are somewhat disappointing. The errors in the single scattering albedo and the volume scattering function are significantly larger than for the other aerosol models. The explanation of the disappointing result is provided in the last part of this section.

Multiple scattering increases as the aerosol optical thickness increases. The more significantly multiple scattering contributes to the total radiance, the more diffuse the total radiance becomes. Generally speaking, the more diffuse the radiance is, the harder it is to retrieve the volume scattering function. However, this assertion is not manifest in the figures so far shown. The aerosol optical thickness does not, in the region of interest, have significant negative effect on the retrieval results. This may be due to the special design of the retrieval algorithm. Recall that iteration terminates after the average error in the volume scattering function is smaller than a certain value. (The error in the volume scattering function is approximated by $\Delta L/L_a e^{-\tau_r/\mu}$, Eq. (8)). Therefore, the accuracy of the retrieved volume scattering function is not the ultimate accuracy that the retrieval algorithm could achieve, but rather the accuracy specified by the retrieval algorithm. Had the retrieval algorithm been designed to obtain the maximum accuracy, the accuracy at a lower optical thickness could have been higher than that at a higher optical thickness. For instance, we did observe that for a lower optical thickness, a shorter time was taken for the retrieval algorithm to obtain the aerosol volume scattering function with the same accuracy. Even though the retrieval algorithm did not show the ultimate accuracy achievable at different aerosol optical thicknesses, it did show that the retrieval algorithm is successful even when the aerosol optical thickness is fairly high.

The presence of a thick Rayleigh scattering layer has a significant influence on the total radiance in directions where the scattering angles from the solar beam to the detector are large. However, inasmuch as it is shown in the retrieval results, Rayleigh scattering, despite having significant influence on the sky radiance, does not have much impact on the retrieval accuracy of either the single scattering albedo or the volume scattering function. Even though the retrieval results for U99 are much worse at 443 nm than at 865 nm, the poorer performance at 443 nm is believed

to be caused by the extrapolation error resulting from a much sharper phase function at 443 nm, rather than from Rayleigh scattering itself. This outcome is surprising but understandable. Since Rayleigh scattering can be calculated accurately, it does not contribute to the difference between the measured radiance and the calculated radiance, as long as the measured radiance is error-free. The conclusion would be totally different if there are slight errors in measurements.

In most of our simulations, relatively large errors are found in the volume scattering function at small angles. Especially for U99, the errors in the volume scattering function at 0° are about -50% at 865 nm and about -93% at 443 nm, which means that the real volume scattering function at 0° is more than 12 times as big as the retrieved function. The results are not surprising. Close observation (Figure 2) finds that the phase functions for U99 take an abrupt upward turn at around 2° , and increases dramatically as the scattering angle decreases. Therefore, the extrapolation of the phase functions at near-zero scattering angles is not likely to yield accurate results. However, notwithstanding the large errors at near-zero angles made in extrapolation, the retrieval results for U99 at 865 nm are surprisingly good. Errors in the volume scattering function are slightly over 1% at each optical thickness. The error in the single scattering albedo is -0.5% for $\tau_a = 0.2$, slightly larger than for other models, but as τ_a increases, the error becomes smaller. The retrieval results at 443 nm are significantly poorer. The average errors in the volume scattering function are 8.40%, 6.68% and 4.81% for $\tau_a = 0.2, 0.5, \text{ and } 1.0$, respectively. They are significantly larger than for other models. The larger errors in the volume scattering function are due to inaccurate extrapolation at near-zero angles.

To understand the effect of extrapolation, one has to consider multiple scattering. In this section, we only consider multiple scattering up to the second order. Higher order scatterings and the second order surface contribution are neglected. We believe the omission of these terms does not affect qualitative assertions. In this case, the total radiance L_t may be expressed as

$$L_t = L_{s0} + L_{ss} + L_{20}, \quad (14)$$

where L_{20} is the second order scattering without surface contribution. Suppose the aerosol optical thickness is low. If Rayleigh scattering is neglected, the downwelling single scattering radiance at any aerosol optical thickness τ may be written as

$$L_{s0}^{(d)}(\hat{\xi}') = F_0 \frac{\tau}{|\hat{\xi}' \cdot \hat{n}|} V_a(\hat{\xi}_0 \rightarrow \hat{\xi}'). \quad (15)$$

The upwelling single scattering radiance may be written as

$$L_{s0}^{(u)}(\hat{\xi}') = F_0 \frac{\tau_a - \tau}{|\hat{\xi}' \cdot \hat{n}|} V_a(\hat{\xi}_0 \rightarrow \hat{\xi}'), \quad (16)$$

where τ is defined such that at the top of the atmosphere $\tau = 0$ and $\tau = \tau_a$ at the surface.

One can obtain the second order scattering by applying the single scattering formula twice and integrating it over the whole range of aerosol optical thickness and over all solid angles. Neglecting higher orders of τ_a , one has

$$L_{20}(\hat{\xi}) = F_0 \frac{\tau_a^2}{2} \int_{4\pi} \frac{V_a(\hat{\xi}_0 \rightarrow \hat{\xi}') V_a(\hat{\xi}' \rightarrow \hat{\xi})}{|\hat{\xi}' \cdot \hat{n}| |\hat{\xi} \cdot \hat{n}|} d\Omega(\hat{\xi}'). \quad (17)$$

Notice that the integral does not converge. This is due to the fact that the formula used for single scattering without a surface contribution is an approximate formula where attenuation is neglected. Indeed, when the solar zenith angle is close to 90° , even if the aerosol optical thickness is low, attenuation is still significant. Had the accurate single scattering formula been used, the integral would converge. A more accurate formula may be derived for the second order scattering based on the accurate single scattering formula; however, our interest here is in the qualitative rather than quantitative aspects of the second order scattering. A more accurate formula would not differ from the formula as shown in Eq. (17) in this regard, therefore, we continue to use Eq. (17) and simply ignore the convergence problem.

Suppose the retrieved volume scattering function is exact except at near-zero angles. Approximate the extrapolation errors at near-zero solid angles with a delta function:

$$V_a'(\hat{\xi} \rightarrow \hat{\xi}') = V_a(\Theta) - C\delta(\hat{\xi} - \hat{\xi}'), \quad (18)$$

where $V_a(\Theta)$ is the real volume scattering function, C is a positive constant much smaller than one, and $\mu = \cos \Theta$. Note that C is simply the error in the single scattering albedo. It is easy to prove that if Eq. (18) is used, the radiance is exact for single scattering. The error in the second order scattering is obtained by combining Eqs. (17) and (18):

$$\Delta L_t(\hat{\xi}) = C F_0 \tau_a^2 \frac{V_a(\hat{\xi}_0 \rightarrow \hat{\xi})}{|\hat{\xi}_0 \cdot \hat{n}| |\hat{\xi} \cdot \hat{n}|}. \quad (19)$$

Comparing it with the single scattering formula L_{s0} , Eq. (19) can be expressed as

$$\Delta L_t(\hat{\xi}) = C \frac{\tau_a L_{s0}(\hat{\xi})}{|\hat{\xi}_0 \cdot \hat{n}|}. \quad (20)$$

Equation (20) reveals that the error in the radiance in any given direction is proportional to the error in the single scattering albedo (C) and single scattering radiance. If Rayleigh scattering is included, one can prove that Eq. (20) is still valid except that Rayleigh scattering has to be included in the single scattering formula:

$$\Delta L_t(\hat{\xi}) = \frac{C\tau_a}{|\hat{\xi}_0 \cdot \hat{n}|} (L_{a,s0}(\hat{\xi}) + L_{r,s0}(\hat{\xi})), \quad (21)$$

where L_{s0} has been expressed as a combination of Rayleigh scattering and aerosol scattering. Recall that the relative error in the volume scattering function was approximated by

$$\frac{\Delta V_a(\Theta)}{V_a(\Theta)} = \frac{\Delta L_t}{L_a e^{-\tau_r/\hat{\xi}_0 \cdot \hat{n}}}, \quad (22)$$

where L_a is the radiance in the absence of Rayleigh scattering. Substituting ΔL_t in Eq. (21) into Eq. (22), we have

$$\frac{\Delta V_a(\Theta)}{V_a(\Theta)} = C \frac{\tau_a}{\mu_0} \left[\frac{L_{a,s0} + L_{r,s0}}{L_a e^{-\tau_r/\mu_0}} \right], \quad (23)$$

where μ_0 is the cosine of the solar zenith angle. In the absence of Rayleigh scattering, it is obvious that $L_{a,s0}/L_a$ is always smaller than one. Therefore the maximum relative error in the volume scattering function is roughly limited to $C\tau_a/\mu_0$. This explains why the error in the retrieved volume scattering function of urban aerosol at 865 nm is not influenced by the extrapolation error at near-zero angles. However, if the optical thickness of Rayleigh scattering is relatively large, $L_{r,s0}$ can be much larger than L_a at larger scattering angles. In this case, while the small-angle scattering is not influenced by Rayleigh scattering since aerosol scattering is much more significant than Rayleigh scattering, errors at large scattering angles are magnified by Rayleigh scattering.

Examining Eq. (23) closely, we find that on the right-hand side of Eq. (23) the dominant term in the numerator is $L_{r,s0}$ at large scattering angles. It is independent of τ_a . On the other hand, as τ_a increases beyond the single scattering limit and double scattering needs to be considered, L_a is approximately proportional to τ_a^2 according to Eq. (17). It is not difficult to derive from Eq. (23) that, to the extent that $L_{r,s0}$ is much larger than $L_{a,s0}$,

$$\frac{\Delta V_a(\Theta)}{V_a(\Theta)} \propto \frac{1}{a + b\tau_a}, \quad (24)$$

where a and b are constants. This explains the result that when the aerosol optical thickness increases, the overall error in the volume scattering function becomes smaller.

4. The Effects of Approximations and Measurement Errors

In the previous section, we evaluated the performance of the retrieval algorithm based on the assumption that measurements are taken under ideal conditions and are error-free. However, in reality, the measurements will contain errors and the conditions assumed in the retrieval algorithm to calculate the sky radiance, e.g., the surface will usually not be Lambertian. The effects of measurement error and approximations may be quite significant. Therefore, an understanding of these effects is necessary.

4.1 Effect of a Non-Lambertian Surface

In the retrieval algorithm, we assumed the land surface to be lambertian, i.e., the surface reflectance is independent of the directions of the incident light and reflected light. In reality, the reflectance varies not only with the direction of the reflected light, but also with the direction of the incident light. Sometimes, it may not even be symmetric about the principal plane,³⁵ the plane determined by the incident light and the direction normal to the surface. Accordingly, the Lambertian surface approximation used in the retrieval algorithm might cause significant error when applied to non-Lambertian surfaces.

The surface reflectance can be represented by the bidirectional reflectance distribution function (BRDF), $R(\hat{\xi}_0 \rightarrow \hat{\xi})$, where $\hat{\xi}_0$ and $\hat{\xi}$ are the directions of the incident light and reflected light, respectively. The definition of R is as follows. If a beam of parallel light, with irradiance $E_0(\hat{\xi}_0)$ on a surface normal to the beam, is incident on a flat surface in a direction $\hat{\xi}_0$, and the radiance of the reflected beam in the viewing direction $\hat{\xi}$ is $L_{ref}(\hat{\xi})$, then the BRDF of the surface is

$$R(\hat{\xi}_0 \rightarrow \hat{\xi}) = \frac{\pi L_{ref}(\hat{\xi})}{E_0(\hat{\xi}_0) |\hat{\xi}_0 \cdot \hat{n}|}, \quad (25)$$

where \hat{n} is the surface normal. For a Lambertian surface, the surface reflectance function is reduced to a simple form:

$$R(\hat{\xi}_0 \rightarrow \hat{\xi}) = \omega_{land}, \quad (26)$$

where ω_{land} is the surface albedo. The BRDF for geophysical surfaces is difficult to measure, as both $\hat{\xi}_0$ and $\hat{\xi}$ must be varied. Most observations of the directional reflection properties of such surfaces involve measurement of the reflectance factor $R_L(\hat{\xi}, \hat{\xi}_s)$ defined by

$$R_L(\hat{\xi}, \hat{\xi}_s) \equiv \frac{\pi L_{ref}}{E_{Total}(\hat{\xi}_s)},$$

where $E_{Total}(\hat{\xi}_s)$ is the total irradiance (sun plus sky) falling on the surface ($\hat{\xi}_s$ is the direction of propagation of the solar beam). As both L_{ref} and $E_{Total}(\hat{\xi}_s)$ contain the influence of the sky irradiance, it is clear that $R(\hat{\xi}_0 \rightarrow \hat{\xi})$ cannot be derived from $R_L(\hat{\xi}, \hat{\xi}_s)$ unless the sky contribution to E_{Total} is much less than the sun's contribution. This is a good approximation in the red and near infrared portion of the spectrum if the measurements are made on relatively clear days (low aerosol concentration). We assume here that $R_L(\hat{\xi}, \hat{\xi}_s) = R(\hat{\xi}_0 \rightarrow \hat{\xi})$. Kimes has measured $R_L(\hat{\xi}, \hat{\xi}_s)$ for several geophysical surfaces.³⁶ For this work, we examined the stepped grass and an irrigated wheat surfaces. Kimes' measurements were performed in two wavelength bands, the 580 – 680 nm band and the 710 – 1100 nm band, at 3 different solar zenith angles, 27°, 35° and 63° for the stepped grass surface, and 28°, 42° and 59° for the irrigated wheat surface. At each solar zenith angle, measurements were taken at 6 viewing (reflected) zenith angles from 0° to 75° at intervals of 15°, and for each zenith angle, 5 viewing azimuth angles from 0° to 180° at intervals of 45°.

These measurements confirm that the BRDF depends not only on the viewing direction but also on the solar direction. Furthermore, if we calculate the albedo by integrating the extrapolated and interpolated BRDF:

$$\omega_{land}(\hat{\xi}_0) = \frac{1}{\pi} \int_{\hat{\xi} \cdot \hat{n} > 0} R(\hat{\xi}_0 \rightarrow \hat{\xi}) |\hat{\xi} \cdot \hat{n}| d\Omega(\hat{\xi}) \quad (27),$$

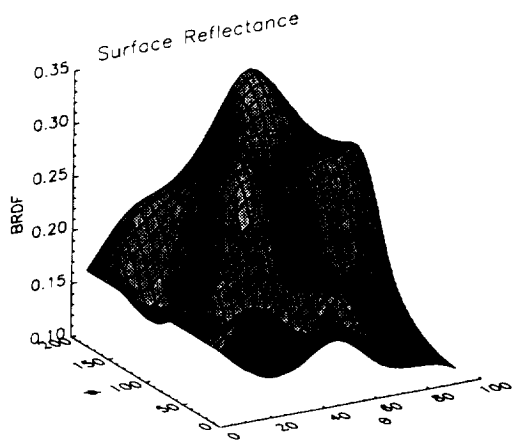
where \hat{n} is a unit vector normal to the surface pointing upward, the resulting albedos are different at different sun angles. For the stepped grass surface at the solar zenith angles of 27°, 35° and 63°, the albedos are 0.2334, 0.2254 and 0.1948, respectively, in the 580 – 680 nm band, and 0.3113, 0.3253 and 0.2917 in the 730 – 1100 nm band. The albedos for the irrigated wheat surface at the solar zenith angles of 28°, 42° and 59° are, respectively, 0.0467, 0.0522, 0.0819 in the 580 – 680 nm band, and 0.4107, 0.4785, and 0.5857 in the 730 – 1100 nm band.

To test the performance of the retrieval algorithm, we applied it to both the stepped grass surface and the irrigated wheat surface. In order to calculate the sky radiance, we have to know the value of the BRDF for all incident and reflected directions. Assuming $R_L = R$, at the solar zenith angles at which the measurements were taken, the BRDF for any viewing directions other than those measured can be either interpolated or extrapolated. However, interpolation and extrapolation of the BRDF with respect to the solar zenith angle is not likely to produce any meaningful results as we only have three solar zenith angles available. Therefore, we assumed that the BRDF is independent of the zenith angle of the incident direction, even though the data clearly indicate

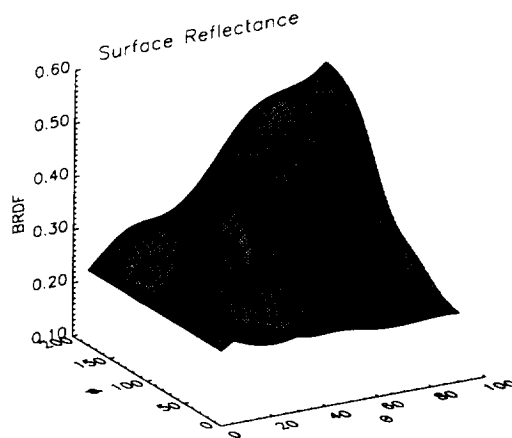
otherwise. Thus, we assume that $R_L(\hat{\xi}, \hat{\xi}_s) = R(\hat{\xi}_0 \rightarrow \hat{\xi})$ is independent of the zenith (but not the azimuth) angle of $\hat{\xi}_0$.

Figures 5a and 5b display the BRDF's, $R(\hat{\xi}_0 \rightarrow \hat{\xi})$, for the stepped grass surface in the 580–680 nm band and 730–1100 nm band, respectively, for a solar zenith angle of 63° . Figures 5c and 5d display the BRDF's for the irrigated wheat surface for a solar zenith angle of 59° in the 580–680 nm band and the 730–1100 nm band, respectively. The θ axis is the viewing zenith angle and the ϕ axis is the viewing azimuth angle. The vertical axis is the BRDF. The viewing angles are defined such that when the reflected light travels in the direction opposite to the solar beam, the viewing zenith angle is the same as the solar zenith angle and the viewing azimuth angle is 180° . (The solar azimuth angle, ϕ_s is 0 by definition.) Although measured for a specific solar zenith angle, these BRDF surfaces are taken to represent the BRDF for *any* zenith angle of an incident photon. In this case, ϕ in the figures is the difference in azimuth between the incident and reflected directions.

These graphs share the feature that the BRDF increases as the viewing zenith angle and azimuth angle increase. In other words, the BRDF's are larger in directions close to the direction opposite to the solar beam. This is true for most natural surfaces.³⁷ However, the BRDF's for the stepped grass surface show much less total variation than for the irrigated wheat surface.



(a)



(b)

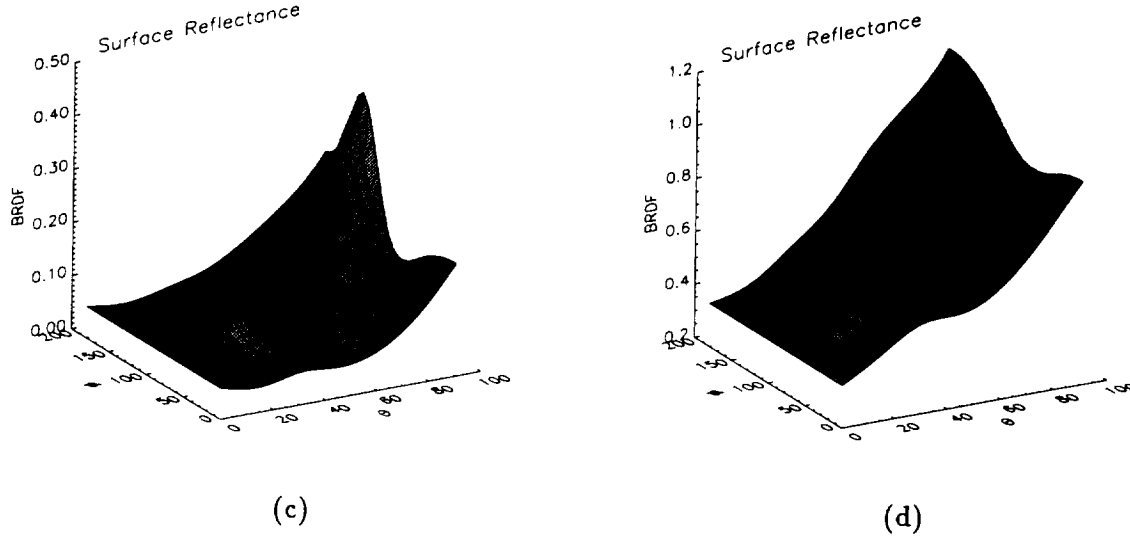
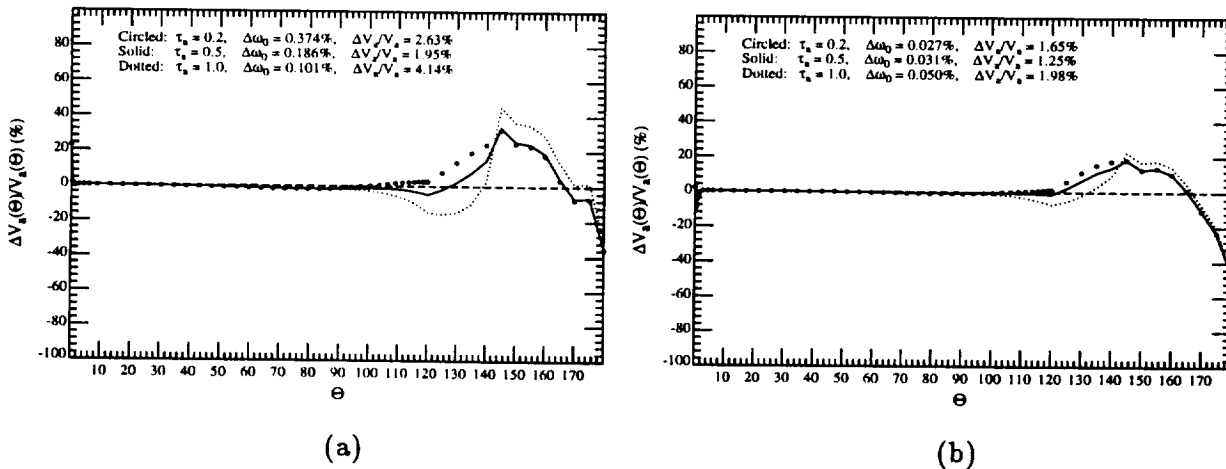


Figure 5: BRDF for two surfaces. (a) and (b) are for the stepped grass surface in Bands 580-680 nm and 730-1100 nm, respectively, at $\theta_0 = 63^\circ$. (c) and (d) are for the irrigated wheat surface in Bands 580-680 nm and 730-1100 nm, respectively, at $\theta_0 = 59^\circ$.

In the calculation of the sky radiance pseudo data, the presence of a non-Lambertian BRDF replaces the Lambertian surface. The solar zenith angle is set to 60° as usual. We choose the BRDF's measured at 63° and 59° to be the BRDF's for the stepped grass surface (Figures 5a and 5b) and the irrigated wheat surface (Figures 5c and 5d), respectively. The sky radiance is calculated at two wavelengths, 443 nm and 865 nm. Since we do not have information on the BRDF's at these wavelengths, the BRDF's in the 580 – 680 nm band and the 710 – 1100 nm band were used at 443 nm and 865 nm, respectively. The retrieval algorithm assumes a Lambertian surface and used the true values of the surface albedo which were obtained by integrating the BRDF. Figure 6 shows the retrieval results using the C80 aerosol model.



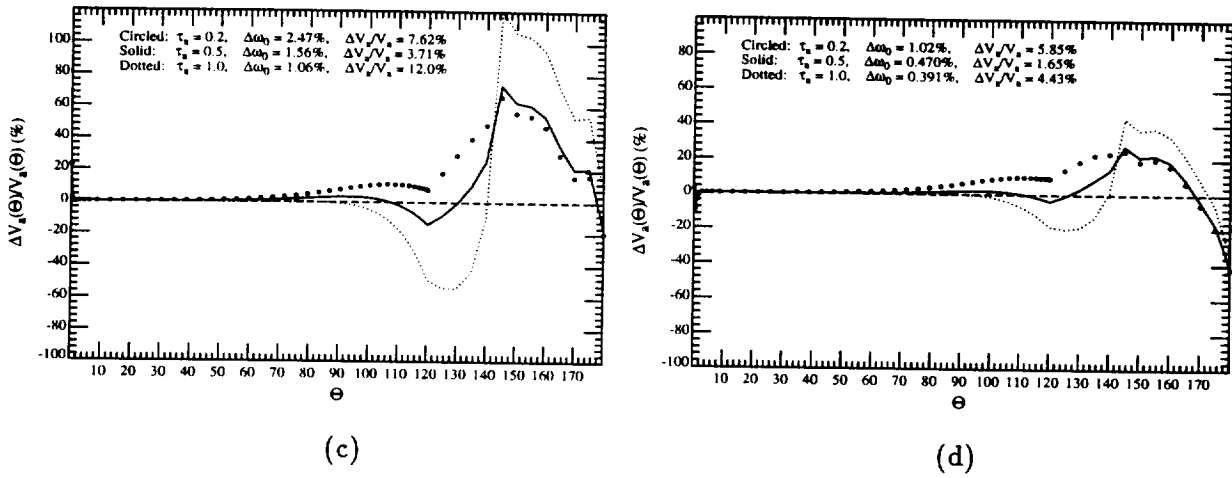


Figure 6 Retrieval errors for non-Lambertian surfaces: (a) and (b) are for the stepped grass surface at 865 nm and 443 nm, respectively; (c) and (d) are for the irrigated wheat surface at 865 nm and 443 nm, respectively.

The results for the stepped grass surface are fairly good. At 865 nm, the largest error in the single scattering albedo is less than 0.4%, and the largest average error in the volume scattering function is less than 5%. The results for the irrigated wheat surface are significantly poorer at 865 nm. The largest error in the single scattering albedo is more than 2% and the largest average error in the volume scattering function is more than 12.0%.

4.2 Effect of Horizontally Inhomogeneity in the Surface Albedo

In addition to the fact that land is usually not Lambertian, it is usually covered with different surfaces having different albedos. In urban areas, the land is covered with highways, roads, buildings, houses, lawns, trees, etc. Even in rural areas, where the landscape is much simpler, the land is usually covered by a mixture of crops, grasses, and bare soils. In these cases, the land is not horizontally homogeneous.

The following table lists the measured albedos of different types of surfaces obtained from the Kimes measurements.^{35,36,38} The albedos vary with the solar zenith angle, but to simplify the table, we list only the albedos for solar zenith angles near 60°.

Table 1. Albedos of different types of land surfaces

Surface Type	(580nm-680nm)	(730nm-1100nm)
Soil	0.1885	0.2246
Grass Land	0.3225	0.4307
Lawn Grass	0.0841	0.5056
Orchard Grass	0.0847	0.3424
Stepped Grass	0.1948	0.2917
Soybeans	0.0544	0.5743
Corn	0.0693	0.3224
Irrigated Wheat	0.0819	0.5857
Hard Wheat	0.2310	0.4334
Pine Forest	0.0655	0.2923
Hard Wood Forest	0.0467	0.3694

To simulate the inhomogeneity in land surfaces, we created a very simple model — the checker board model. In the checker board model, as the name suggests, the land is equally divided into square patches. Two types of surfaces are randomly assigned to each patch. To create the maximum contrast, we used the approximate albedos of the hard wood forest and the grass land surface at 443 nm ($\omega_{land} = 0.05$ and 0.35 , respectively), and soil and irrigated wheat at 865 nm ($\omega_{land} = 0.20$ and 0.60 , respectively). In this case, the pseudo data were created using a Monte Carlo code. In the retrieval algorithm we used the average albedo as the albedo of the homogeneous Lambertian surface. That is, $\omega_{land} = 0.20$ at 443 nm and $\omega_{land} = 0.40$ at 865 nm. The Lambertian surface approximation was used in the sky radiance pseudo data calculation as well as in the retrieval algorithm.

To assess the effect of the size of each individual patch on the retrieval, we vary the size from $0.1 \times 0.1 \text{ km}^2$ to $1.0 \times 1.0 \text{ km}^2$. For each size, we generate 10 independent random patterns. Figure 7 demonstrates the standard deviation of retrieved $\omega_0^{(i)}$, $\delta\omega_0$, and the average value of $|\Delta V_a/V_a|^{(i)}$, $\overline{\Delta V_a/V_a}$, for each size. The x axis is the length (km) of each individual square patch. $|\Delta V_a/V_a|$ and $\delta\omega_0$ are represented by squares and triangles, respectively at both wavelengths. In our calculation, we assume that aerosol and Rayleigh scattering are vertically homogeneous. The upper boundary of the aerosol and the lower boundary of Rayleigh scattering is 1 km above the ground. The upper boundary of Rayleigh scattering is 20 km above the ground. $\tau_a = 0.20$ in all of these cases. These results indicate that the size of the individual patch is crucial. The larger each individual patch is, the larger the fluctuations are in the retrieved volume scattering function and single scattering

albedo. When the land is divided into $0.1 \times 0.1 \text{ km}^2$ patches, there is little effect resulting from the randomness of the land surface albedo. As the size of the patch increases, so does the fluctuation in the volume scattering function and the single scattering albedo. Comparing the results at 443 nm with those at 865 nm, we found that Rayleigh scattering at 443 nm does not have significant influence on retrieval.

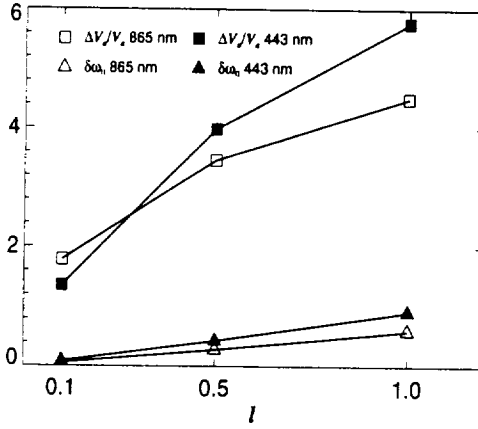


Figure 7: $|\overline{\Delta V_a/V_a}|$ and $\delta\omega_0$ for the checker board model.

These results can be understood through the following analysis. In the single scattering approach the surface contribution is represented by the following integral:

$$L_{ss}(\hat{\xi}) = F_0 \frac{|\hat{\xi}_0 \cdot \hat{n}|}{\pi} \int_{z_0}^{z_1} \int_{-\infty}^{+\infty} \int_{-\infty}^{+\infty} c_a \omega_{land}(x, y) \frac{V_a(\hat{\xi} \rightarrow \hat{\xi}')}{|\hat{\xi} \cdot \hat{n}|^2} \frac{|\hat{\xi}' \cdot \hat{n}|}{r^2(\hat{\xi}, z; x, y)} dx dy dz. \quad (28)$$

In Figure 8, z_1 is the altitude of the upper boundary of the aerosol layer, z_0 ($z_0 = 0$) is the altitude of the lower boundary of the aerosol layer, and z is any altitude in between. c_a is the extinction coefficient of the aerosol, $dx dy$ is an infinitesimal area of the land surface, and ω_{land} , which is a function of x and y , is the surface albedo. $\hat{\xi}_0$ is the direction in which the solar beam propagates, $\hat{\xi}$ is the viewing direction, $r(\hat{\xi}, z; x, y)$ is the distance from the infinitesimal area to any position along the viewing direction $\hat{\xi}$, and $\hat{\xi}'$ is the unit vector along r .

The contribution to the radiance from a unit area is proportional to $|\hat{\xi}' \cdot \hat{n}|/r^2$. Therefore, the closer the area is to the detector, the larger the influence it has on the radiance. Calculations show that more than 75% of the surface contribution from aerosol scattering is attributable to an area within 3 km radius of the detector. When the length of each patch is 1.0 km, the fluctuation in the surface term is extremely large.

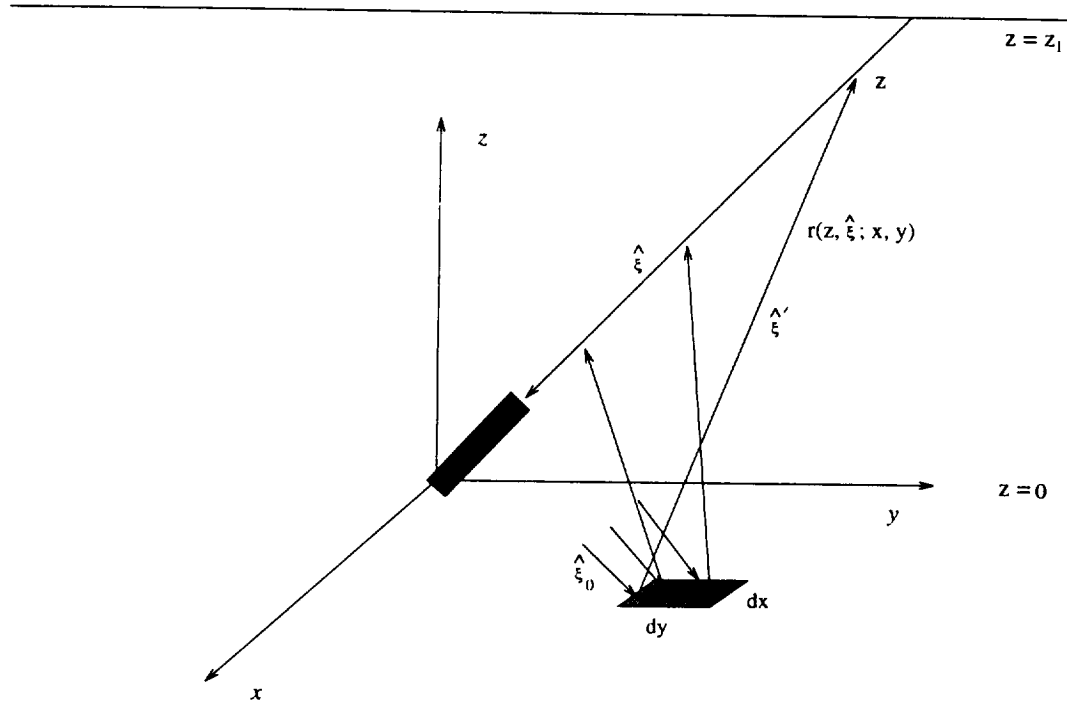


Figure 8 Illustration of the surface integral in Eq. (28).

Equation (28) can be easily modified to include Rayleigh scattering. All that is needed is to add a similar integral which contains Rayleigh scattering. Since Rayleigh scattering molecules are distributed from 1 to 20 km above the ground, a wide area of surface contributes significantly to total sky radiance. The wide area contains a large number of patches of land. Consequently the fluctuation in the surface contribution from Rayleigh scattering is small. This explains why the retrieval results did not seem to be influenced very much by Rayleigh scattering, i.e., were independent of wavelength.

4.3 Effect of Aerosol Horizontal Inhomogeneity

In the previous calculations, we assumed homogeneous aerosol density. In reality, the aerosol density varies both horizontally and vertically. In assessing the effect of aerosol horizontal inhomogeneity, we take an extreme approach. In the downwelling radiance calculation, we assume that all aerosols are confined in a square box. A detector is situated at the center of the bottom of the

box. Aerosols are uniform within the box, but no aerosol exists outside of the box. In the retrieval program, the aerosol density is assumed to be homogeneous over the entire horizontal range. The value of the optical thickness within the box in the radiance calculation program is used in the retrieval algorithm. The C80 aerosol is used to generate the sky radiance in a Monte Carlo code. A Lambertian surface with the surface albedo being 1.00 at 865 nm and 0.5 at 443 nm was used in both the sky radiance calculation and the retrieval algorithm. The height of the box (h_{box}) is 1 km. The length of the square box (l_{box}) varies from 10 km to 100 km. Figure 9 shows the retrieval results of the inhomogeneous aerosol at 865 nm and 443 nm, with box lengths of 10 km, 20 km, 50 km and 100km.

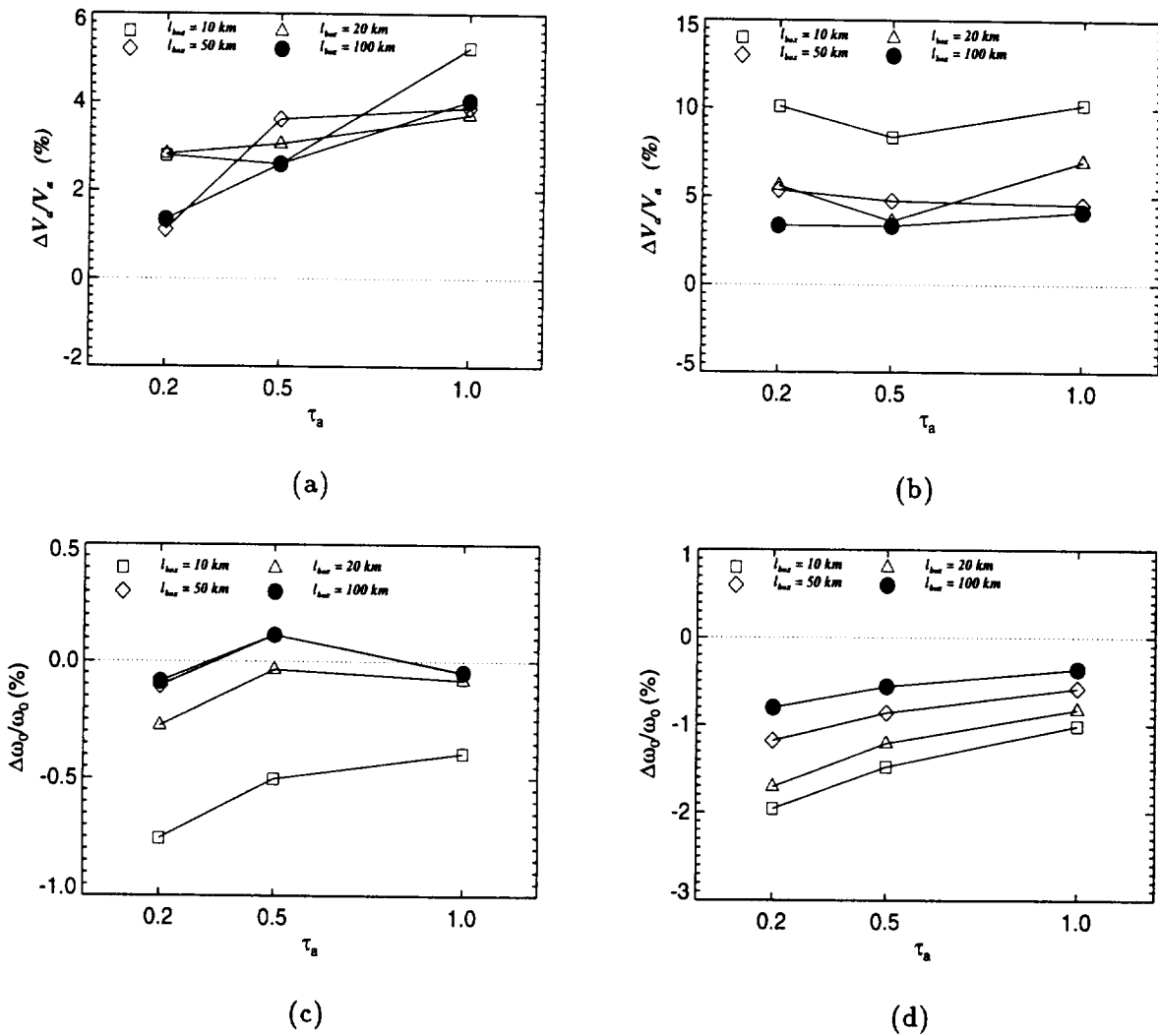


Figure 9: Errors in V_a and w_0 . (a) and (b) show the error in V_a at 865 nm and 443 nm respectively, (c) and (d) are show the error in w_0 at 865 nm and 443 nm respectively,

At 865 nm, when the length of the box is 10 km, errors are relatively large compared with the results when the aerosol is homogeneous, yet they are still acceptable. They become smaller as the length of homogeneity increases. When the length of homogeneity is 50 km, there is no significant error in either the single scattering albedo or the volume scattering function resulting from aerosol inhomogeneity. By comparison, the results at 443 nm are much poorer. For instance, when the length of homogeneity is 10 km, errors in the single scattering albedo at aerosol optical thicknesses of 0.2, 0.5 and 1.0 are, respectively -1.96% , -1.48% , and -1.01% , and average errors in the volume scattering function are 10.1% , 8.36% , and 10.2% , respectively. Even when the length of homogeneity increases to 100 km, error is still observed. For instance, when the aerosol optical thickness is 0.2, the error in the retrieved single scattering albedo is -0.804% . Errors caused by aerosol inhomogeneity seem to be magnified by Rayleigh scattering at 443 nm. This may be understood through the following analysis.

In order for a photon to contribute to the radiance, it has to enter the cone determined by the lens and the area of the detector. If there is no Rayleigh scattering, photons have to be scattered toward the detector within the segment of the cone that is inside the aerosol layer. Since the aerosol is distributed within 1 km above the ground, most photons entering the cone are those scattered near the detector. As a result, the radiance is determined mostly by the part of aerosols that are near the detector. Aerosols far away from the detector have virtually no effect on the sky radiance. In the presence of a thick Rayleigh layer at 443 nm, the segment of cone within which photons have to enter in order to contribute to the sky radiance includes not only the segment within the aerosol layer but also the segment within the Rayleigh layer. Since Rayleigh scattering molecules are distributed from the ground up to 20 km above the ground, photons far away from the detector now have much better chances of entering the cone and subsequently being scattered into the detector. Consequently, the sky radiance is determined not only by aerosols near the detector but also by aerosols far away. In this case, a larger range of aerosol homogeneity is required.

In conclusion, at 865 nm, the retrieval algorithm does not place a strict requirement on aerosol horizontal homogeneity. When the range of horizontal homogeneity is 50 km, in other words, when the aerosol is homogeneous within 25 km of the detector, it is safe to treat the aerosol as a horizontally homogeneous aerosol. On the other hand, the prevalence of Rayleigh scattering at 443 nm places a much stricter requirement on the aerosol homogeneity. One should carefully consider the effect of aerosol inhomogeneity when applying the retrieval algorithm at 443 nm.

4.4 Effects of Errors in the Sky Radiance

We examine two types of errors in the sky radiance measurements, random errors and systematic errors. Random errors are due to random noise in the instrument. The random noise is usually considered to have a gaussian distribution usually having a standard deviation of 1% of the mean. Systematic errors are due to the uncertainty in the conversion of electronic signals to radiance resulting in calibration uncertainty. They are usually less than 5%.

Simulating systematic errors is straightforward. We can simply add a fixed percentage to the true radiance in all viewing directions, i.e.,

$$L^{(m)}(\hat{\xi}_i) = L^{(t)}(\hat{\xi}_i) + \rho_0 L^{(t)}(\hat{\xi}_i) \quad (29)$$

where $L^{(m)}$ is the measured radiance, $L^{(t)}$ is the true radiance and ρ_0 is the systematic error. Simulating random errors is somewhat more complicated. One needs to create random errors according to the gaussian distribution, and then add them to the sky radiance in different directions.

$$L^{(m)}(\hat{\xi}_i) = L^{(t)}(\hat{\xi}_i) + \rho_i L^{(t)}(\hat{\xi}_i), \quad (30)$$

where

$$P(\rho_i) = \frac{1}{\sqrt{2\pi\sigma^2}} e^{-\rho_i^2/2\sigma^2} \quad (31)$$

ρ_i is the noise and $P(\rho_i)$ is the normalized distribution of ρ_i and σ^2 is the variance of the noise. In the radiance calculation, we assumed a Lambertian surface, the albedo of which is 1.0 at 865 nm and 0.5 at 443 nm.

4.4.1 Systematic errors

Figure 10 shows the retrieval results at 865 nm and 443 nm for the C80 aerosol when there are +5% systematic errors in the sky radiance, but no random errors. We observed that, in all of the curves, errors in the aerosol volume scattering function increase as the scattering angle increases. The retrieval results at 865 nm are acceptable. The largest error in the single scattering albedo is less than 4% and the largest average error in the volume scattering function is less than 7%. In comparison, the retrieval results at 443 nm are much worse. At $\tau_a = 0.2$, the error in the single scattering albedo is 4.66% and the average error in the volume scattering function is 12.4%.

Rayleigh scattering is believed to be largely responsible for the foregoing result. In the single

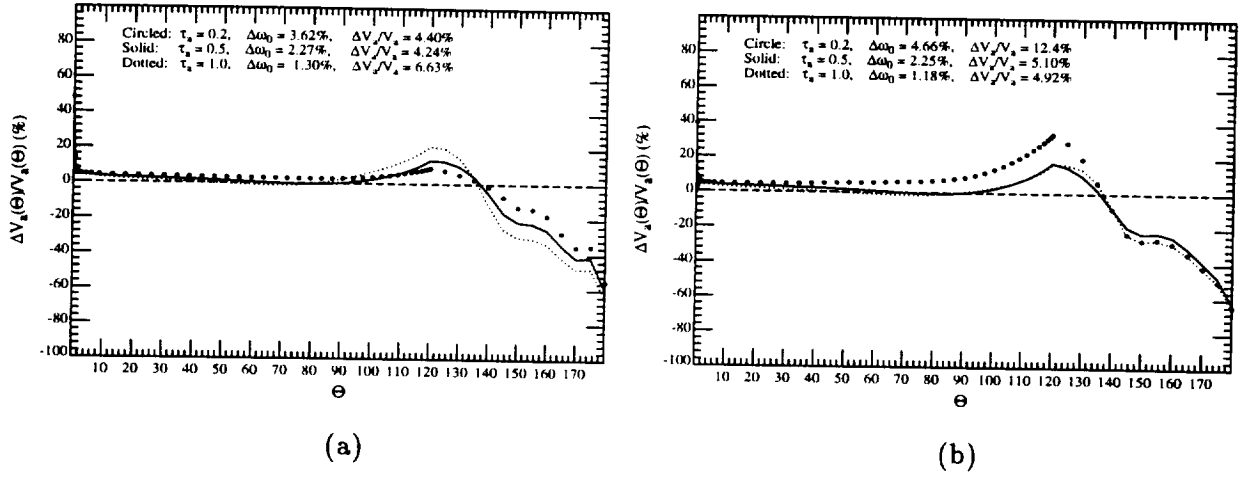


Figure 10: Retrieval errors when there is a +5% systematic error in the sky radiance. (a) is for $\lambda = 865$ nm and (b) is for $\lambda = 443$ nm.

scattering approach, the sky radiance is given by

$$L^{(t)}(\hat{\xi}) = \frac{\tau_a}{|\hat{\xi} \cdot \hat{n}|} V_a(\hat{\xi}_0 \rightarrow \hat{\xi}) + \frac{\tau_r}{|\hat{\xi} \cdot \hat{n}|} V_r(\hat{\xi}_0 \rightarrow \hat{\xi}), \quad (32)$$

where τ_a and τ_r are the Rayleigh optical thickness and aerosol optical thickness respectively, V_a is the aerosol volume scattering function and V_r is the Rayleigh volume scattering function. Rearranging Eq. (32), one can obtain the aerosol volume scattering function:

$$V_a(\hat{\xi}_0 \rightarrow \hat{\xi}) = \frac{L^{(t)}(\hat{\xi})|\hat{\xi} \cdot \hat{n}| - \tau_r V_r(\hat{\xi}_0 \rightarrow \hat{\xi})}{\tau_a}. \quad (33)$$

It is easy to prove that if the systematic error in $L^{(t)}$ is ρ_0 , the error in the aerosol volume scattering function, $\Delta V_a/V_a$, is

$$\frac{\Delta V_a(\hat{\xi}_0 \rightarrow \hat{\xi})}{V_a(\hat{\xi}_0 \rightarrow \hat{\xi})} = \rho_0 \frac{\tau_a V_a(\hat{\xi}_0 \rightarrow \hat{\xi}) + \tau_r V_r(\hat{\xi}_0 \rightarrow \hat{\xi})}{\tau_a V_a(\hat{\xi}_0 \rightarrow \hat{\xi})}. \quad (34)$$

It is evident in Eq. (34) that the error in the volume scattering function increases as τ_r increases. Also, the error is larger in the viewing directions where the aerosol volume scattering function is smaller. In other words, errors at large scattering angles are much larger than those at small scattering angles, since the aerosol volume scattering function is forwardly peaked and is usually very small at large scattering angles.

4.4.2 Random errors

Figure 11 shows the retrieval results at 865 nm and 443 nm, respectively, when there are 1% random errors in the sky radiance, i.e., the noise is gaussian with a standard deviation of 1%. No systematic error was assumed. The error in the volume scattering function increases as the aerosol

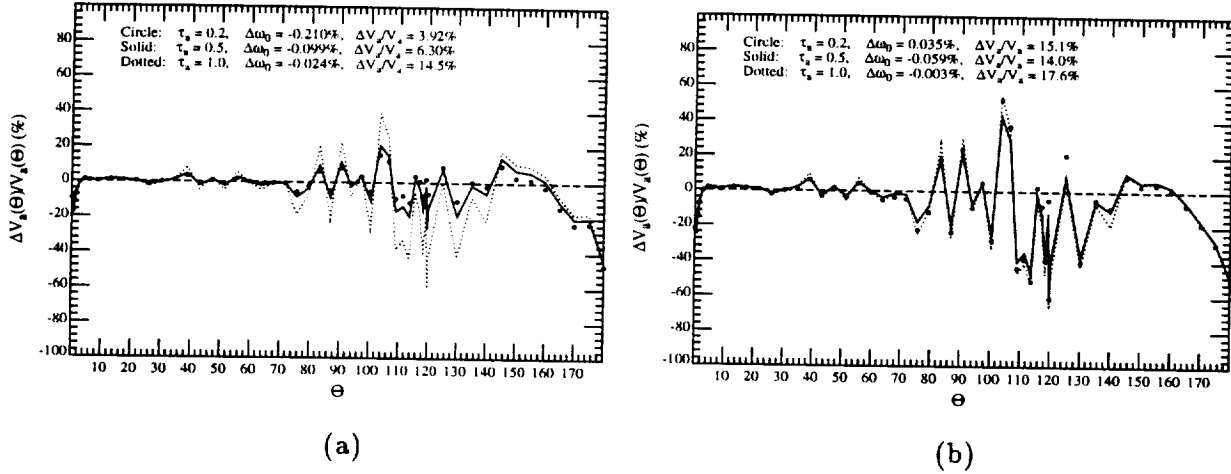


Figure 11: Retrieval errors when there is a 1% random error in the sky radiance. (a) is for $\lambda = 865$ nm and (b) is for $\lambda = 443$ nm.

optical thickness increases. Errors become extremely large at large scattering angles at 865 nm and even larger at 443 nm. However, errors in the single scattering albedo are not significant. The largest error in the single scattering albedo is only -0.21% . This is easily understandable. The single scattering albedo is simply the integral of the volume scattering function over all solid angles. Since errors in the volume scattering function at different angles have different signs due to the random nature of noise, they offset each other in the integral.

The large errors in the volume scattering functions result from the combined effects of multiple scattering and the surface contribution. Recall that, in the absence of Rayleigh scattering, if we only consider multiple scattering up to the second order and the surface contribution up to the first order, the sky radiance may be expressed as follows:

$$L_t(\hat{\xi}) = L_{s0}(\hat{\xi}) + L_{ss}(\hat{\xi}) + L_{20}(\hat{\xi}), \quad (35)$$

where

$$L_{s0}(\hat{\xi}) = F_0 \frac{\tau_a}{|\hat{\xi} \cdot \hat{n}|} V_a(\hat{\xi}_0 \rightarrow \hat{\xi}), \quad (36)$$

$$L_{ss}(\hat{\xi}) = F_0 \tau_a \frac{\omega_{land} |\hat{\xi}_0 \cdot \hat{n}|}{|\hat{\xi} \cdot \hat{n}|} \int_{\hat{\xi}' \cdot \hat{n} > 0} V_a(\hat{\xi} \rightarrow \hat{\xi}') d\Omega(\hat{\xi}'), \quad (37)$$

and

$$L_{20}(\hat{\xi}) = F_0 \frac{\tau_a^2}{2} \int_{4\pi} \frac{V_a(\hat{\xi}_0 \rightarrow \hat{\xi}') V_a(\hat{\xi}' \rightarrow \hat{\xi})}{|\hat{\xi}' \cdot \hat{n}| |\hat{\xi} \cdot \hat{n}|} d\Omega(\hat{\xi}'). \quad (38)$$

In these expressions, L_{s0} is single scattering radiance in the absence of a surface, L_{ss} is the surface contribution to single scattering radiance, L_{20} is double scattering contribution to radiance in the absence of a surface, θ_0 is the solar zenith angle, and Θ is the scattering angle from the sun to the detector.

Suppose the random error in the volume scattering function at a given scattering angle Θ_i is δ_i as a result of the noise in the radiance. The error in the single scattering radiance is

$$\Delta L_{s0}(\hat{\xi}_i) = \delta_i L_{s0}(\hat{\xi}_i). \quad (39)$$

Double scattering L_{20} and the surface contribution L_{ss} involve integrals of the volume scattering function. The errors in the volume scattering function offset each other in the integrals. Consequently, little error is incurred in the surface term and the multiple scattering term. The total error in the radiance is simply the error in L_{s0} .

$$\Delta L_t(\hat{\xi}_i) = \delta_i L_{s0}. \quad (40)$$

If we divide both sides of Eq. (40) by L_t and rearrange it, we have

$$\delta_i = \frac{L_t(\hat{\xi}_i)}{L_{s0}(\hat{\xi}_i)} \times \frac{\Delta L_t(\hat{\xi}_i)}{L_t(\hat{\xi}_i)}, \quad (41)$$

where $\Delta L_t(\hat{\xi}_i)/L_t(\hat{\xi}_i)$ is the random error in the radiance, simply what we called ρ_i . Equation (41) shows the error in the radiance is magnified by the ratio of total radiance to the single scattering radiance. The more insignificant single scattering is, or in other words, the more significant multiple scattering and the surface contribution are in the total radiance, the larger the error in the volume scattering function becomes. At large scattering angles from the sun to the detector, multiple scattering and the surface contribution constitute the major part of the radiance. Consequently, errors in the volume scattering function are very large.

Equation (41) was derived in the absence of Rayleigh scattering. However, it is not difficult to derive that it is still valid if Rayleigh scattering is included, except L_{s0} has to be replaced by $L_{a,s0}$, which is the single scattering radiance from aerosol scattering in the absence of a surface. In this

case, multiple scattering and the surface contribution become even more significant. Consequently, errors in the volume scattering function become even larger.

The preceding retrieval results and analysis show that the effect of random errors can be serious. However, in reality, one can successfully reduce them by averaging the measurement data over a period of time or the retrieved volume scattering function over a range of angles, therefore, they don't present a real threat to retrieval.

4.5 Effect of errors in land albedo

For a land surface with a BRDF that varies over a large range, it is very difficult to measure the surface albedo with high accuracy. Even for a land surface that is very close to Lambertian, significant errors may still be incurred in actual measurements of the surface albedo. Figure 5 shows the retrieval results at 865 nm and 443 nm for the C80 aerosol when incorrect surface albedos are used. The true land albedos are 1.0 at 865 nm and 0.5 at 443 nm. The albedos of 0.9 at 865 nm and 0.45 at 443 nm were used in the retrieval. A Lambertian surface was assumed in all simulations.

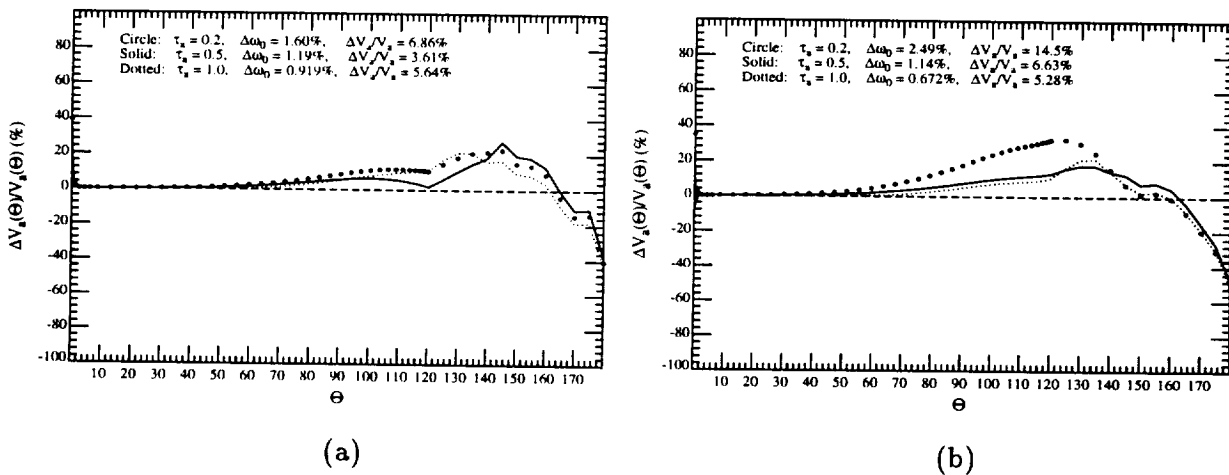


Figure 12: Retrieval errors when there is a -10% error in the land albedo. (a) is for $\lambda = 865$ nm and (b) is for $\lambda = 443$ nm.

The retrieval results at 865 nm are acceptable. The largest errors in the single scattering albedo (1.60%) and volume scattering function (6.86%) both occur at the optical thickness of 0.2. They decrease as the aerosol optical thickness increases. The results at 443 nm demonstrate the same trend. However, they are significantly poorer than the results at 865 nm. The largest error

in the aerosol volume scattering function and the single scattering albedo are 14.5% and 2.49% respectively, which occur at $\tau_a = 0.2$.

These results can be explained as follows. Rayleigh scattering dominates back scattering. A thick Rayleigh layer at 443 nm increases back scattering thereby increasing the surface contribution to sky radiance. These errors induced by the biased land albedo are much larger at 443 nm than those at 865 nm. Since all of the errors resulting from the biased land albedos are allocated to aerosol volume scattering function, errors in the aerosol volume scattering function and consequently the error in the single scattering albedo are much larger at 443 nm than those at 865 nm. At the same wavelength, as the aerosol optical thickness increases, the error in the surface contribution does not increase significantly, since the major part of the surface contribution comes from Rayleigh scattering. The implication thereof is that the errors become less significant in relation to the radiance caused by aerosol scattering. Consequently, the error in the aerosol volume scattering function and the single scattering albedo decrease as the aerosol optical thickness increases.

5 Conclusion

This paper illustrated a scheme which applies recursive procedures to retrieve columnar properties of aerosols, i.e., the scattering phase function and single scattering albedo, from the sky radiance.

When measurements are performed under ideal conditions, i.e., actual conditions are in total agreement with the approximations made in the retrieval algorithm, the overall retrieval results are excellent. The error in the single scattering albedo is usually within a fraction of 1%. The average error in the volume scattering function is usually well within 3%. However, we did find that, because of the inability to measure the sky radiance in directions close to the direct solar beam, relatively large errors in the retrieved aerosol volume scattering function (8.4% at $\tau_a = 0.2$) occurred at 443 nm when the true aerosol phase function was extremely sharp (U99).

Subsequent studies concentrated on the susceptibility of the retrieval algorithm to measurement errors and conditions deviating from the approximations made in the retrieval algorithm. These conditions include non-Lambertian reflectance of a land surface (the BRDF effect), surface inhomogeneity, as well as horizontal aerosol inhomogeneity. These studies reveal that the retrieval algorithm places certain restrictions on the land BRDF. When the land deviates significantly from the Lambertian approximation, e.g., the irrigated wheat surface, significant errors are found in the single scattering albedo (2.47% at 865 nm at $\tau_a = 0.2$) and, particularly, in the volume scattering function ($\Delta V/V_a = 12\%$ at 865 nm for $\tau_a = 1.0$)

These studies also reveal that a certain degree of horizontal aerosol homogeneity is required at 865 nm to ensure accurate retrieval. At 443 nm, a much higher degree is required as Rayleigh scattering is more significant. The effects of measurement errors in the aerosol optical thickness, surface albedo, as well as in the sky radiance on the retrieval results have been discussed in this paper. Aside from the error in surface albedo, the most serious effect is from the systematic error in sky radiance. Serious error would result from this when the aerosol optical thickness is low and simultaneously the Rayleigh optical thickness is high. Generally, one has to avoid such circumstances unless measurements of higher accuracy are available.

In summary, the retrieval error in the single scattering albedo is usually small. Even when actual conditions deviate significantly from the approximations made in the retrieval program, the

error in the single scattering albedo is usually $\leq 1\%$. This suggests that the retrieval algorithm, without any further adjustment, can be successfully applied quantitatively to identify absorbing aerosols. The retrieval results for the phase function are not quite as good. Generally, errors are usually quite small at small scattering angles, but they may get quite large for large scattering angles. However, in most of our calculations, the average errors in the volume scattering function are less than 5.0% at 865 nm and less than 10.0% at 443 nm.

Overall, the retrieval results at 443 nm, with the exception of the BRDF effect, are much less satisfactory than those at 865 nm. At 443 nm, the retrieval results are more susceptible to land inhomogeneity, vertical and horizontal aerosol inhomogeneity, systematic error in the sky radiance, etc., especially for low aerosol optical thickness. Simulations show that when there is large systematic (calibration) error in the sky radiance measurements, or when the land is strongly inhomogeneous on large (~ 1 km) scales, the error in the single scattering albedo can be as large as 10% or even higher at very low aerosol optical thickness (≤ 0.05). Error in the aerosol volume scattering function may be as large as 40%.

References

- [1] R. J. Charlson, J. E. Lovelock, M. O. Andreae and S. G. Warren, "Oceanic Phytoplankton, Atmospheric Sulphur, Cloud Albedo and Climate," *Nature* **326**, 655–661 (1987).
- [2] R. J. Charlson, S. E. Schwartz, J. M. Hales, R. D. Cess, J. A. Coakley, J. E. Hansen and D. J. Hofmann, "Climate Forcing by Anthropogenic Aerosols," *Science* **255**, 423–430 (1992).
- [3] Y. J. Kaufman, "Remote Sensing of Direct and Indirect Aerosol Forcing," in *Aerosol Forcing of Climate*, edited by R. H. Charlson and J. Heintzenberg (Wiley, New York, NY, 1995) p. 297–332.
- [4] V. V. Salomonson, W. L. Barnes, P. W. Maymon, H. E. Montgomery and H. Ostrow, "MODIS: Advanced Facility Instrument for Studies of the Earth as a System," *IEEE Geosci. Rem. Sens.* **27**, 145–152 (1989).
- [5] D. J. Diner, C. J. Bruegge, J. V. Martonchik, T. P. Ackerman, R. Davies, S. A. W. Gerstl, H. R. Gordon, P. J. Sellers, J. Clark, J. A. Daniels, E. D. Danielson, V. G. Duval, K. P. Klaasen, G. W. L. A. D. I. Nakamoto, R. Pagano and T. H. Reilly, "MISR: A Multi-angle Imaging Spectroradiometer for Geophysical and Climatological Research from EOS," *IEEE Transactions on Geoscience and Remote Sensing* **27**, 200–214 (1989).
- [6] P. Y. Deschamps, F. M. Bréon, M. Leroy, A. Podaire, A. Bricaud, J. C. Buriez and G. Sèze, "The POLDER Mission: Instrument characteristics and scientific objectives," *IEEE Trans. Geoscience and Remote Sensing* **32**, 598–615 (1994).
- [7] M. Wang and H. R. Gordon, "Estimating aerosol optical properties over the oceans with the multiangle imaging spectroradiometer: Some preliminary studies," *Applied Optics* **33**, 4042–4057 (1994).

- [8] M. Wang and H. R. Gordon, "Estimation of aerosol columnar size distribution and optical thickness from the angular distribution of radiance exiting the atmosphere: simulations," *Applied Optics* **34**, 6989–7001 (1995).
- [9] W. A. Hoppel, J. W. Fitzgerald, G. M. Frick, R. E. Larson and E. J. Mack, "Aerosol Size Distributions and Optical Properties Found in the Marine Boundary Layer Over the Atlantic Ocean," *J. Geophys Res.* **95D**, 3659–3686 (1990).
- [10] E. P. Shettle and R. W. Fenn, *Models for the Aerosols of the Lower Atmosphere and the Effects of Humidity Variations on Their Optical Properties* (Air Force Geophysics Laboratory, Hanscomb AFB, MA 01731, AFGL-TR-79-0214, 1979).
- [11] G. A. d'Almeida, P. Koepke and E. P. Shettle, *Atmospheric Aerosols — Global Climatology and Radiative Characteristics* (A. Deepak Publishing, Hampton, VA, 1991).
- [12] H. R. Gordon and M. Wang, "Retrieval of water-leaving radiance and aerosol optical thickness over the oceans with SeaWiFS: A preliminary algorithm," *Applied Optics* **33**, 443–452 (1994).
- [13] H. R. Gordon, 1997, Atmospheric Correction of Ocean Color Imagery in the Earth Observing System Era, *Jour. Geophys. Res.* (In press).
- [14] B. N. Holben, T. F. Eck, I. Slutsker, D. Tanre, J. P. Buis, A. Setzer, E. Vermote, J. Reagan, Y. Kaufman, T. Nakajima, F. Lavenu and I. Jankowiak, 1997, Automatic Sun and Sky Scanning Radiometer System for Network Aerosol Monitoring, *Remote Sensing of Environment* (In press)
- [15] T. Nakajima, M. Tanaka and T. Yamauchi, "Retrieval of the Optical Properties of Aerosols from Aureole and Extinction Data," *Applied Optics* **22**, 2951–2959 (1983).
- [16] Y. J. Kaufman, A. Gitelson, A. Karnieli, E. Ganor, R. S. Fraser, T. Nakajima, S. Mattoo and B. N. Holben, "Size Distribution and Scattering Phase Functions of Aerosol Particles Retrieved From Sky Brightness Measurements," *Jour. Geophys. Res.* **99D**, 10341–10356 (1994).

- [17] M. Wang and H. R. Gordon, "Retrieval of the Columnar Aerosol Phase Function and Single Scattering Albedo from Sky Radiance over the Ocean: Simulations," *Applied Optics* **32**, 4598–4609 (1993).
- [18] H. R. Gordon and T. Zhang, "How well can radiance reflected from the ocean-atmosphere system be predicted from measurements at the sea surface?," *Applied Optics* **35**, 6527–6543 (1996).
- [19] H. R. Gordon and T. Zhang, "Columnar Aerosol Properties Over Oceans by Combining Surface and Aircraft Measurements: Simulations," *Applied Optics* **34**, 5552–5555 (1995).
- [20] T. Zhang and H. R. Gordon, 1997, Columnar aerosol properties over oceans by combining surface and aircraft measurements: sensitivity analysis, *Applied Optics* (In press).
- [21] M. Wendisch and W. von Hoyningen-Huene, "High Speed Version of the Method of 'Successive Order of Scattering' and its Application to Remote Sensing," *Beitr. Phys. Atmosph.* **64**, 83–91 (1991).
- [22] T. Nakajima and M. Tanaka, "Effect of Wind-Generated Waves on the Transfer of Solar Radiation in the Atmosphere-Ocean System," *Jour. Quant. Spectr. Rad. Trans.* **29**, 521–537 (1983).
- [23] C. Cox and W. Munk, "Measurements of the Roughness of the Sea Surface from Photographs of the Sun's Glitter," *Jour. Opt. Soc. of Am.* **44**, 838–850 (1954).
- [24] H. R. Gordon and M. Wang, "Influence of Oceanic Whitecaps on Atmospheric Correction of SeaWiFS," *Applied Optics* **33**, 7754–7763 (1994).
- [25] J. E. Hansen and L. D. Travis, "Light Scattering in Planetary Atmospheres," *Space Science Reviews* **16**, 527–610 (1974).

- [26] F. X. Kenizys, E. P. Shettle, W. O. Gallery, J.H.Chetwynd, L. W. Abreu, J. E. A. Selby, S. A. Clough and R. W. Fenn, *Atmospheric Transmittance/Radiance: The LOWTRAN 6 Model* (Air Force Geophysics Laboratory, Hanscomb AFB, MA 01731, AFGL-TR-83-0187, 1983) NTIS AD A137796.
- [27] K. P. Bowman and A. J. Krueger, "A Global Climatology of Total Ozone From the Nimbus 7 Total Ozone Mapping Spectrometer," *J. Geophys. Res.* **90(D5)**, 7967-7976 (1985).
- [28] R. W. Preisendorfer and C. D. Mobley, "Direct and Inverse Irradiance Models in Hydrologic Optics," *Limnology and Oceanography* **29**, 903-929 (1984).
- [29] H. R. Gordon and D. J. Castaño, "Aerosol Analysis with the Coastal Zone Color Scanner: A Simple Method for Including Multiple Scattering Effects," *Applied Optics* **28**, 1320-1326 (1989).
- [30] H. C. van de Hulst, *Multiple Light Scattering* (Academic Press, New York, 1980), 739 pp.
- [31] P. Y. Deschamps, M. Herman and D. Tanre, "Modeling of the atmospheric effects and its application to the remote sensing of ocean color," *Applied Optics* **22**, 3751-3758 (1983).
- [32] D. T. Lindgren, "Land Use Planning and Remote Sensing," in *Remote Sensing of Earth Resources and Environment* (Dordrecht, Boston, MA, 1985) , p. 176.
- [33] C. Elachi, "Introduction to the Physics and Techniques of Remote Sensing," in *Remote Sensing* (Wiley, New York, 1987) , p. 413.
- [34] M. D. King and B. M. Herman, "Determination of the Ground Albedo and the Index of Absorption of Atmospheric Particulates by Remote Sensing. Part I: Theory," *Jour. Atmos. Sci.* **36**, 163-173 (1979).
- [35] D. S. Kimes, "Dynamics of Directional Reflectance Factor Distributions for Vegetation Canopies ," *Applied Optics* **22**, 1364-1372 (1983).

- [36] D. S. Kimes, W. W. Newcomb and C. J. Tucker, "Directional Reflectance Factor Distributions for Cover Types of Northern Africa," *Remote Sensing of Environment* **18**, 1-19 (1985).
- [37] J. A. Kirchner, D. S. Kimes and J. E. MM. III, "Variation of direction reflectance factor with structural changes of a developing alfafa canopy," *Applied Optics* **21**, 3766 (1982).
- [38] D. S. Kimes, W. W. Newcomb, R. F. Nelson and J. B. Schutt, "Directional Reflectance Factor Distributions of a Hardwood and Pine Forest Canopy," *IEEE Trans. Geoscience and Remote Sensing* **24**, 281-293 (1986).
- [39] F. X. Kenizys, E. P. Shettle, L. W. Abreu, G. P. Anderson, J.H.Chetwynd, W. O. Gallery, J. E. A. Selby and S. A. Clough, *Atmospheric Transmittance/Radiance: The LOWTRAN 7 Model* (Air Force Geophysics Laboratory, Hanscomb AFB, MA 01731, 1989), In Preparation.
- [40] T. Zhang, "Remote Sensing of Aerosol Properties over the Ocean by Combining Surface and Aircraft Measurements," 1995, Ph.D. Dissertation, University of Miami, Coral Gables FL, 95 pp.

Appendix 3

In-orbit calibration strategy for ocean color sensors

In-orbit calibration strategy for ocean color sensors

by

Howard R. Gordon
Department of Physics
University of Miami
Coral Gables, FL 33124

Submitted to *Remote Sensing of Environment*

The author is grateful for support from the National Aeronautics and Space Administration under Grant NAGW-273 Contracts NAS5-31363 and NAS5-31734.

Abstract

To recover the ocean water-leaving radiance and derive biophysical parameters from observations of space-borne ocean color sensors, the required uncertainty in the measured top-of-atmosphere radiance is at present impossible to achieve prior to launch. A methodology and strategy for achieving the required uncertainty in the post-launch era is presented here. The method consists of combining direct measurements of the water-leaving radiance, whitecap radiance, and aerosol optical thickness made simultaneously with satellite overpasses, with radiative transfer theory to reduce the calibration uncertainty of the visible bands with respect to the near-infrared (NIR). This procedure is possible over the open ocean where, in the absence of aerosol transported from land over long distances by the wind, the atmosphere can be very clear with most of the aerosol generated by local processes such as breaking waves, e.g., the aerosol optical thickness in the visible ~ 0.05 – 0.10 . In this case, the radiative transfer process is considerably simplified and molecular scattering is the dominant atmospheric component in the visible. It is shown that such a procedure alone is sufficient to reduce the calibration uncertainty to required levels. Further reduction is possible by reducing the uncertainty in the NIR calibration by measuring sky radiance from island locations (or a ship), and using these to predict the at-sensor radiance. For the most part, this NIR calibration is limited by the uncertainty in the calibration of the radiometer used to measure the sky radiance. Finally, the sensor calibration is maintained by monitoring the actual water-leaving radiance continuously at a single location, where the atmosphere is sufficiently clear that atmospheric correction introduces only a small error, and directly comparing the true and the sensor-derived water-leaving radiances.

1. Introduction

Several ocean color sensors are expected to be launched within the next few years, e.g., SeaWiFS [Hooker *et al.*, 1992] and MODIS [Salomonson *et al.*, 1989], for the purpose of understanding oceanic primary production on a global scale. As the information-containing radiance backscattered out of the water and transmitted to the top of the atmosphere (TOA) is only a small portion of the radiance that they measure, these sensors require an accuracy in radiometry that cannot be achieved pre-launch. There are several issues concerning radiometric calibration that must be addressed for each ocean color sensor. For example, when there are bright clouds in a scene, how close to the clouds will the radiometry be valid, i.e., not corrupted by the presence of the clouds? If sensors employ array detectors (MODIS), do all of the individual detectors in a given spectral band in the array record the same radiance when viewing a uniform scene? Most issues such as these can be resolved through a systematic examination of the imagery, or through small radiometric calibration adjustments of one detector relative to another in an array. However, in the latter case, even if all detectors provide the same values for the radiance when viewing a uniform scene, what is the uncertainty in that value? In this paper, we provide the methodology and the measurement requirements for reducing this latter uncertainty to acceptable levels in the post-launch era.

The radiance reflected from the ocean itself consists of two components (1) the radiance reflected from the sea surface (diffuse reflection from whitecaps and direct Fresnel-reflection from the interface), and (2) radiance backscattered *out* of the water from beneath the surface. The latter is referred to as the water-leaving radiance, L_w . It contains the desired information [Gordon and Morel, 1983]. In what follows, we will replace radiance L by reflectance ρ defined through $\rho = \pi L / F_0 \cos \theta_0$, where θ_0 is the solar zenith angle, and F_0 is the extraterrestrial solar irradiance. At a given wavelength, λ , the water-leaving reflectance is related to the reflectance observed at the sensor (ρ_t) through

$$\rho_t(\lambda) = \rho_r(\lambda) + \rho_a(\lambda) + \rho_{ra}(\lambda) + t(\lambda)\rho_w(\lambda) + t(\lambda)\rho_{wc}(\lambda) + T(\lambda)\rho_g(\lambda), \quad (1)$$

where $\rho_r(\lambda)$ is the contribution from pure Rayleigh (molecular) scattering, $\rho_a(\lambda)$ the contribution from pure aerosol scattering, $\rho_{ra}(\lambda)$ the contribution due to the interaction effect between air molecules and aerosols, $t(\lambda)\rho_{wc}(\lambda)$ the contribution from whitecaps, $T(\lambda)\rho_g(\lambda)$ the contribution from direct sun glitter, and $t(\lambda)\rho_w(\lambda)$ the desired water-leaving reflectance propagated to the TOA. T is the direct transmittance and t is the diffuse transmittance of the atmosphere. In Eq. (1), ρ_r ,

ρ_a , and ρ_{ra} are understood to include the interactions with the sea surface, e.g., ρ_r is the reflectance of a Rayleigh-scattering atmosphere bounded by a Fresnel-reflecting ocean that absorbs all photons penetrating through its interface. Typically, in clear water, the contribution of $t\rho_w$ to ρ_t is $\sim 10\%$ in the blue ($\lambda \sim 440$ nm), 5% in the green ($\lambda \sim 550$ nm) and negligible in the near infrared (NIR, $\lambda \gtrsim 750$ nm).

In Eq. (1) ρ_r can be precisely computed given the surface atmospheric pressure [Gordon, Brown and Evans, 1988], and ρ_{wc} can be estimated given the wind speed [Frouin, Schwindling and Deschamps, 1996; Gordon and Wang, 1994a; Moore, Voss and Gordon, 1997]. As ρ_g is very large near the specular image of the sun, it is required that viewing directions be chosen such that it is negligible. The terms involving aerosols, $\rho_a + \rho_{ra}$, are highly variable, and in the blue are comparable in magnitude to $t\rho_w$ [Gordon, 1997]. Thus, the principal difficulty in retrieving $t\rho_w$ from ρ_t is assessing the aerosol contribution.

Gordon and Wang [1994b] have developed an algorithm for retrieving $t\rho_w$ from ρ_t assuming that ρ_r is computed from an estimate of the surface pressure, ρ_{wc} has been determined from an estimate of the wind speed, and ρ_g is negligible. This algorithm has been shown to be capable of retrieving $t\rho_w$ at 443 nm with an uncertainty $\lesssim \pm 0.002$, when the aerosol over the ocean is nonabsorbing or only weakly absorbing [Gordon, 1997]. This uncertainty meets the goal of both SeaWiFS and MODIS: a 5% uncertainty in the water leaving reflectance in the blue in very clear ocean water [Hooker et al., 1992]. In the Gordon and Wang algorithm, the aerosol contribution and its spectral variation are assessed utilizing bands in the NIR, where ρ_w can be assumed to be ~ 0 due to the strong absorption of liquid water there. Aerosol models are used to extrapolate the aerosol contribution from the NIR to the visible, and also to account for the effects of multiple scattering.

2. Effect of calibration errors

Since the desired water-leaving reflectance is only a small part of ρ_t , accurate calibration of the sensor is critical [Gordon, 1987]. For example, if $t\rho_w$ is 10% of ρ_t , and we want ρ_w with an uncertainty of $\pm 5\%$, one would expect that it would be necessary to know ρ_t with an uncertainty of no more than $\pm 0.5\%$. However, as several bands are used in the atmospheric correction of a single

band, the variation of the calibration error from band to band is also important. We now describe simulations to estimate the magnitude of the effect of the radiometric calibration error.

To assess the effect of calibration errors, ρ_t pseudo data were simulated using the *Shettle and Fenn* [1979] maritime aerosol model with 80% relative humidity (M80). In the absence of calibration errors, the performance of the Gordon and Wang algorithm is excellent for this aerosol model. An error was then added to each of the pseudo measured reflectances, i.e.,

$$\rho'_t(\lambda) = \rho_t(\lambda)[1 + \alpha(\lambda)], \quad (2)$$

where $\alpha(\lambda)$ is the fractional error in $\rho_t(\lambda)$, and $\rho'_t(\lambda)$ is the value of $\rho_t(\lambda)$ that the incorrect sensor calibration would indicate. The Gordon and Wang correction algorithm was then operated using the incorrect $\rho'_t(\lambda)$ as the measured value, rather than the correct $\rho_t(\lambda)$, and the error in the retrieved $t\rho_w(\lambda)$, was computed.

The resulting error at 443 nm is presented in Figures 1a–1d, for a sensor viewing near the edge of the scan (viewing nadir angle $\sim 45^\circ$) in the perpendicular plane, as a function of θ_0 . The y -axis in these figures is the error in the retrieved $t\rho_w$, indicated by $\Delta\rho(\theta_0)$. Figures 1a and 1b are for $\alpha(765) = \alpha(865)$ with $\alpha(443) = 0$ (Figure 1a) and $\alpha(443) = \alpha(765) = \alpha(865)$ (Figure 1b). These show the effect of a calibration error that has the same magnitude and sign at both 765 and 865 nm. In contrast, Figures 1c and 1d show the effect of having calibration errors that have a much smaller magnitude but opposite signs at 765 and 865 nm. In this case even a small calibration error (1%) can have an effect similar to a large calibration error (5%) when the signs are all the same. As we shall see later, the reason the error is so much larger when it is of opposite sign at 765 and 865 nm is that it will cause an error in the estimated spectral variation of the aerosol component that will propagate through the atmospheric correction algorithm.

The goal for the pre-launch calibration of the relevant ocean color bands on SeaWiFS and MODIS is that L_t have an uncertainty of $< \pm 10\%$ and 5% , respectively. Figure 1 demonstrates that such an error would cause the error in the retrieved $\rho_w(443)$ to be far outside the acceptable range (± 0.002). A method for overcoming these calibration difficulties is provided below.

3. Radiative transfer in the aerosol single-scattering approximation

Over the open ocean the atmosphere can be very clear with most of the aerosol generated by local processes such as breaking waves. Such an aerosol is almost nonabsorbing and the aerosol optical thickness at 550 nm is often in the range 0.05–0.10 [Korotaev *et al.*, 1993; Reddy *et al.*, 1990; Villevalde *et al.*, 1994]. Under such conditions, a simple atmospheric correction algorithm that employs a multiply-scattered Rayleigh component and a singly-scattered aerosol component can be used to retrieve ρ_w [Gordon, 1997]. In this section we review the relevant radiative transfer for such an approximation.

When the aerosol concentration is small, it is possible to approximate the path reflectance $\rho_r + \rho_a + \rho_{ra}$ by $\rho_r + \rho_{as}$, where ρ_r is the multiple-scattering reflectance of a pure Rayleigh-scattering atmosphere bounded by a totally-absorbing Fresnel-reflecting interface, and ρ_{as} is the aerosol contribution computed to first order in the aerosol optical thickness τ_a . The aerosol contribution in this approximation is given by

$$\begin{aligned} \rho_{as}(\lambda) &= \omega_a(\lambda)\tau_a(\lambda)p_a(\theta_v, \phi_v; \theta_0, \phi_0; \lambda)/4 \cos \theta_v \cos \theta_0, \\ p_a(\theta_v, \phi_v; \theta_0, \phi_0; \lambda) &= P_a(\Theta_-, \lambda) + \left(\tau(\theta_v) + \tau(\theta_0) \right) P_a(\Theta_+, \lambda), \\ \cos \Theta_{\pm} &= \pm \cos \theta_0 \cos \theta_v - \sin \theta_0 \sin \theta_v \cos(\phi_v - \phi_0), \end{aligned} \quad (3)$$

where $P_a(\Theta, \lambda)$ is the aerosol scattering phase function for a scattering angle Θ , ω_a is the aerosol single scattering albedo, and $\tau(\alpha)$ is the Fresnel reflectance of the interface for an incident angle α . The angles θ_0 and ϕ_0 are, respectively, the zenith and azimuth angles of a vector from the point on the sea surface under examination (pixel) to the sun, and likewise, θ_v and ϕ_v are the zenith and azimuth angles of a vector from the pixel to the sensor. The zenith angles are measured with respect to the *upward* normal.

Thus, in the single-scattered aerosol approximation to the radiative transfer in the atmosphere, and ignoring whitecaps and sun glitter, we have

$$\rho_t(\lambda) = \rho_r(\lambda) + \rho_{as}(\lambda) + t(\lambda)\rho_w(\lambda). \quad (4)$$

Using this equation it is easy to devise an atmospheric correction algorithm [Wang and Gordon, 1994]. Consider two spectral bands in the near infrared (NIR) at λ_s and λ_l , where the subscript “s” stands for short and “l” for long. These bands are assumed to possess the attribute that $\rho_w \approx 0$,

because of the strong absorption by liquid water in the NIR. For MODIS $\lambda_s = 750$ nm and $\lambda_l = 865$ nm, while for SeaWiFS $\lambda_s = 765$ and $\lambda_l = 865$. Then Eq. (4) provides $\rho_r + \rho_{as}$ at both λ_s and λ_l . The quantity $\rho_r(\lambda)$ can be computed accurately, so $\rho_{as}(\lambda_s)$ and $\rho_{as}(\lambda_l)$ can be determined from the values of $\rho_t - \rho_r$ at λ_s and λ_l , allowing estimation of the parameter $\varepsilon(\lambda_s, \lambda_l)$:

$$\varepsilon(\lambda_s, \lambda_l) \equiv \frac{\rho_{as}(\lambda_s)}{\rho_{as}(\lambda_l)} = \frac{\omega_a(\lambda_s)\tau_a(\lambda_s)p_a(\theta_v, \phi_v; \theta_0, \phi_0; \lambda_s)}{\omega_a(\lambda_l)\tau_a(\lambda_l)p_a(\theta_v, \phi_v; \theta_0, \phi_0; \lambda_l)}. \quad (5)$$

If we can find a way to compute the value of $\varepsilon(\lambda_i, \lambda_l)$ for the band at $\lambda_i < \lambda_s$ from the measured value of $\varepsilon(\lambda_s, \lambda_l)$, we can compute $\rho_{as}(\lambda_i)$, which, when combined with $\rho_t(\lambda_i)$ and $\rho_r(\lambda_i)$, provides $\rho_w(\lambda_i)$:

$$t(\lambda_i)\rho_w(\lambda_i) = \rho_t(\lambda_i) - \rho_r(\lambda_i) - \varepsilon(\lambda_i, \lambda_l)\rho_{as}(\lambda_l). \quad (6)$$

The key to utilizing this procedure is to be able to estimate $\varepsilon(\lambda_i, \lambda_l)$ from the measured $\varepsilon(\lambda_s, \lambda_l)$. Using a set of aerosol models developed by *Shettle and Fenn* [1979], *Wang and Gordon* [1994] showed that to a good approximation

$$\varepsilon(\lambda_i, \lambda_l) = \exp[c(\lambda_l - \lambda_i)]. \quad (7)$$

Further examples of the validity of this approximation are provided in *Gordon* [1997]. Using this it is easy to complete the retrieval of $t(\lambda_i)\rho_w(\lambda_i)$:

$$t(\lambda_i)\rho_w(\lambda_i) = \rho_t(\lambda_i) - \rho_r(\lambda_i) - \varepsilon^{(e)}(\lambda_i, \lambda_l)\rho_{as}(\lambda_l). \quad (8)$$

In Eq. (8), $\varepsilon^{(e)}(\lambda_i, \lambda_l)$ is the estimated value of $\varepsilon(\lambda_i, \lambda_l)$ assuming the exponential variation with λ_i , i.e.,

$$\varepsilon^{(e)}(\lambda_i, \lambda_l) \equiv \exp[c(\lambda_l - \lambda_i)] = \exp\left[\left(\frac{\lambda_l - \lambda_i}{\lambda_l - \lambda_s}\right) \log_e\left(\frac{\rho_{as}(\lambda_s)}{\rho_{as}(\lambda_l)}\right)\right].$$

Gordon [1997] shows that excellent results can be obtained with this simple algorithm when the aerosol is nonabsorbing or weakly absorbing, and the aerosol optical thickness at λ_l (865 nm) is $\lesssim 0.10$. In the case of SeaWiFS, correction for the effect of the O₂ "A" absorption band are necessary at λ_s [*Ding and Gordon*, 1995].

We now use this aerosol single-scattering approximation to understand analytically the effects of the calibration errors that are shown in Figure 1. Assuming the aerosol single-scattering formulation of the radiative transfer process is exact, and using Eq. (7), to first order in $\alpha(\lambda)$ the error in the retrieved ρ_w is [*Gordon*, 1997]

$$\begin{aligned} t(\lambda_i)\Delta\rho_w(\lambda_i) &= \alpha(\lambda_i)\rho_t(\lambda_i) - \varepsilon(\lambda_i, \lambda_l)\alpha(\lambda_l)\rho_t(\lambda_l) \\ &\quad - \left(\frac{\lambda_l - \lambda_i}{\lambda_l - \lambda_s}\right) \left[\frac{\varepsilon(\lambda_i, \lambda_l)}{\varepsilon(\lambda_s, \lambda_l)} \alpha(\lambda_s)\rho_t(\lambda_s) - \varepsilon(\lambda_i, \lambda_l)\alpha(\lambda_l)\rho_t(\lambda_l) \right]. \end{aligned} \quad (9)$$

In Eq. (9), the first term, $\alpha(\lambda_i)\rho_t(\lambda_i)$, represents the direct effect of any calibration error at λ_i on the retrieved $\rho_w(\lambda_i)$. The remaining terms represent the indirect effect resulting from calibration error at λ_s and λ_l . Note that if λ_s and λ_l have calibration errors with the same sign, the second term will subtract from the first, and cancelation in the terms in the square brackets will also occur. In contrast, if $\alpha(\lambda_s)$ and $\alpha(\lambda_l)$ have different signs, the error is magnified as the two terms in the square brackets in Eq. (9) will add. This explains the behavior of the error in $t\rho_w$ in Figures 1c and 1d.

4. Calibration initialization

In Section 2 examples were provided to show the sensitivity of the algorithm to sensor calibration errors (Figure 1). It was demonstrated that calibration errors of the order of $\pm 5\%$, the absolute radiometric calibration uncertainty specified for the MODIS visible bands, would lead to excessive error in ρ_w , even if the calibration error in the two NIR bands were of the same sign. When errors in these bands are small ($\sim \pm 1\%$) but have opposite signs (Figures 1c and 1d), the error in the water-leaving reflectance becomes large because of the extrapolation of ϵ into the visible [Eq. (9)]. Thus, it is clear that the calibration uncertainty of SeaWiFS and MODIS must be reduced in order to provide acceptable ρ_w , retrievals.

Although the calibration requirement is difficult if not impossible to meet using standard laboratory methods, we show here that it should be possible to perform an adequate calibration in orbit using surface measurements to deduce the true water-leaving radiance and the optical properties of the aerosol. This is normally referred to as *vicarious* calibration [Evans and Gordon, 1994; Fraser and Kaufman, 1986; Gordon, 1987; Koepke, 1982; Slater et al., 1987]. We now outline a methodology for effecting such calibration, the process of which we refer to as *initialization*. This calibration is *not* radiometric, rather, it is a calibration of the entire system — the sensor *plus* the algorithms. As will be seen below, the sensor calibration will be adjusted to force the algorithm to conform to surface measurements of water-leaving radiance and atmospheric (aerosol) properties. A similar procedure was carried out for CZCS [Evans and Gordon, 1994], but without surface-based atmospheric measurements. It was only moderately successful because the calibration of that instrument varied in time, and there was no independent way of determining the temporal variation. Here, we make the assumption that any change in the sensitivity of the instrument with

time can be determined by other methods, e.g., using an on-board solar diffuser or imaging the moon.

Upon initial operation of the sensor, one expects that the $\alpha(\lambda_i)$ in Eq. (2) will be of the order of $\pm 5\%$ (MODIS), with $\alpha(\lambda_i)$ being positive for some of the λ_i 's and negative for others. We acquire imagery over ships measuring $L_w(\lambda_i)$ for a variety of (clear sky) aerosol concentrations. Given $\rho_w(\lambda_i)$, and assuming the atmospheric correction algorithm [Eq. (6)] is exact, we operate it backward, i.e., compute $\varepsilon(\lambda_i, \lambda_l)$ using $\rho_w(\lambda_i)$ at each wavelength λ_i . This provides the behavior of $\varepsilon(\lambda_i, \lambda_l)$ with λ_i . It is expected to be a smooth, nearly exponential [Gordon, 1997; Wang and Gordon, 1994], function of λ_i . If the $\alpha(\lambda_i)$'s differ significantly in magnitude (or in sign), $\varepsilon(\lambda_i, \lambda_l)$ will vary with λ_i in a repeatable (from day-to-day) but unrealistic manner, and this will be magnified when the aerosol optical thickness is small.

To understand this magnification, we assume that the aerosol single-scattering version of the radiative transfer is exact. In that case,

$$\rho_t(\lambda) = \rho_r(\lambda) + \rho_{as}(\lambda) + t(\lambda)\rho_w(\lambda),$$

and from its definition

$$\varepsilon(\lambda_i, \lambda_l) = \frac{\rho_{as}(\lambda_i)}{\rho_{as}(\lambda_l)} = \frac{\rho_t(\lambda_i) - \rho_r(\lambda_i) - t(\lambda_i)\rho_w(\lambda_i)}{\rho_t(\lambda_l) - \rho_r(\lambda_l) - t(\lambda_l)\rho_w(\lambda_l)}.$$

Inserting ρ'_t from Eq. (2) in place of ρ_t , we have the apparent value of $\varepsilon(\lambda_i, \lambda_l)$:

$$\varepsilon'(\lambda_i, \lambda_l) = \frac{\alpha(\lambda_i)\rho_t(\lambda_i) + \rho_{as}(\lambda_i)}{\alpha(\lambda_l)\rho_t(\lambda_l) + \rho_{as}(\lambda_l)}. \quad (10)$$

For very small $\alpha(\lambda)$'s this provides an approximately correct $\varepsilon(\lambda_i, \lambda_l)$, i.e., $\rho_{as}(\lambda_i)/\rho_{as}(\lambda_l)$; however, if the $\alpha(\lambda_i)$'s are not small, very significant errors in the computed $\varepsilon(\lambda_i, \lambda_l)$ are possible. This error will be particularly large for bands for which $\rho_t \gg \rho_{as}$, e.g., in the blue. To illustrate this, a numerical example is useful. Consider two error scenarios: (1) the $\alpha(\lambda_i)$'s alternate in sign from band to band; and (2) the $\alpha(\lambda_i)$'s all have the same sign. In each case we assume for simplicity that the $\alpha(\lambda_i)$ all have the same magnitude, and employ a viewing geometry specified by $\theta_0 \approx 32^\circ$, $\theta_v \approx 33^\circ$, and $\phi_v \approx 100^\circ$. We take the "aerosol radiance" L_a defined as $L_t - L_r - tL_w$ at 670 nm to be 0.2, 0.4, and 0.6 mW/cm²μm sr. These values correspond to $\rho_{as} \approx 0.005, 0.010, \text{ and } 0.015$, or $\tau_a \approx 0.04, 0.08, \text{ and } 0.12$ at 670 nm, respectively. For reference, from CZCS imagery, the mean L_a for the Arabian Sea in winter (the low aerosol season) is ~ 0.6 mW/cm²μm sr, with a

standard deviation of about $0.2 \text{ mW/cm}^2 \mu\text{m sr}$ (C.R. McClain, GSFC, personal communication). Thus, L_a values in this range are easily found over the oceans. The results of computing $\varepsilon'(\lambda_i, \lambda_l)$ with Eq. (10) as a function of the magnitude and the sign of the calibration error are provided in Figures 2a–2d. In preparing the figures it has been assumed that the correct value of $\varepsilon(\lambda_i, \lambda_l)$ is unity for all λ_i , i.e., what would be expected for a maritime aerosol at high relative humidity [Shettle and Fenn, 1979; Wang and Gordon, 1994]. The figures clearly show that the apparent value of $\varepsilon(\lambda_i, \lambda_l)$ is strongly influenced by the calibration error, and that the influence increases as the aerosol optical thickness decreases. If the true value of $\varepsilon(\lambda_i, \lambda_l)$ were known, the calibration for the band at λ_i could be adjusted to bring the apparent value into equality with the true value. That is, replacing ε' by the known ε in Eq. (10) shows that the residual value of $\alpha(\lambda_i)$ is related to $\alpha(\lambda_l)$ by

$$\alpha(\lambda_i) = \frac{\rho_t(\lambda_l)}{\rho_t(\lambda_i)} \varepsilon(\lambda_i, \lambda_l) \alpha(\lambda_l). \quad (11)$$

Thus, with this calibration adjustment, the residual error $\alpha(\lambda_i)$ will be $< \alpha(\lambda_l)$, since $\rho_t(\lambda_l) < \rho_t(\lambda_i)$ because of the strong spectral variation of ρ_r . We see that this form of calibration adjustment automatically reduces the error in the short-wave bands to a value below $\alpha(\lambda_l)$ and assures that all of the α 's have the same sign as $\alpha(\lambda_l)$.

In practice Eq. (11) is useless because $\alpha(\lambda_l)$ is unknown. Thus, given $\varepsilon(\lambda_i, \lambda_l)$ one must actually adjust the calibration by trial and error until $\varepsilon'(\lambda_i, \lambda_l)$ agrees with the correct value. This is equivalent to (1) solving Eq. (8) for $\rho_t(\lambda_i)$, given $t(\lambda_i)\rho_w(\lambda_i)$ and replacing $\varepsilon^{(e)}(\lambda_i, \lambda_l)$ by $\varepsilon(\lambda_i, \lambda_l)$, and (2) adjusting the sensor calibration to force $\rho_t'(\lambda_i)$ into agreement with the computed $\rho_t(\lambda_i)$. This was done for the example in Figures 2a and 2b, where $\alpha(865) = +0.05$. The resulting residual α 's are presented in Table 1. The residual α 's follow the expected pattern, i.e., Eq. (11), and in the first three bands are reduced to less than 1%. As mentioned above, this reduction is due to the increase in Rayleigh scattering with decreased λ_i . In fact, the Rayleigh optical thickness at 412 nm is approximately 12 times that at 765 nm, similar to the decrease in $\alpha(412)$ compared to $\alpha(765)$. Note, however, that this method cannot even detect the error at λ_l .

The residual errors in Table 1 were added to the ρ_t pseudo data used to prepare Figure 1, and the Gordon and Wang correction algorithm was applied. The resulting error in $t\rho_w$ at 443 nm is shown in Figure 3a. The error after this calibration adjustment is significantly reduced. In fact, it is similar to the error obtained when $\alpha \approx +0.02$ in all bands. Figure 3b shows the further

improvement that would be possible if $\alpha(\lambda_l)$ could be reduced to 0.025, half of its assumed initial value.

It is clear that the above method of calibration adjustment has the potential for reducing the effects of calibration errors; however, to effect the adjustment we need a method of determining the correct value of $\varepsilon(\lambda_i, \lambda_l)$. In addition, a method for reducing the error at the long wave band, λ_l , would further improve the retrieval of $t\rho_w$ (Figure 3b).

Gordon [1997] studied the properties of a wide variety of aerosol models with both log-normal and power-law size distributions. That study suggested that measurement of $\tau_a(\lambda_i)$, for all λ_i , would allow a reasonable estimate of $\varepsilon(\lambda_i, \lambda_l)$. Figure 4 from *Gordon* [1997] provides examples showing the existence of a rough relationship between $\tau_a(443)/\tau_a(865)$ and $\varepsilon(443, 865)$ for several aerosol models. These models include nonabsorbing aerosols (open symbols) as well as weakly- and strongly-absorbing aerosols (solid symbols). Far from terrigenous and anthropogenic aerosol sources, where the aerosol over the ocean is locally generated, one expects nonabsorbing aerosols. Figure 4 suggests that $\varepsilon(443, 865)$ in such cases can be estimated from $\tau_a(443)/\tau_a(865)$ with an uncertainty $\sim \pm 0.06$, when it is near unity, i.e., for a pure maritime aerosol at high relative humidity [*Gordon and Wang*, 1994b]. Figures 2c and 2d show that if $\varepsilon(443, 865)$ is known to within ± 0.1 , it should be possible to reduce $|\alpha(443)|$ to $\lesssim 0.01$.

To reduce $\alpha(\lambda_l)$ the full optical properties of the aerosol must be measured. *Wang and Gordon* [1993] have shown how to combine measurements of τ_a and sky radiance over the oceans to obtain the aerosol phase function and single scattering albedo. Furthermore, the derived P_a and ω_a can be inserted into the RTE to predict ρ_t . Predicting ρ_t in the visible requires measurement of ρ_w ; however, in the NIR $\rho_w \approx 0$, so $\rho_t(\lambda_l)$ can be predicted without ρ_w measurements. *Gordon and Zhang* [1996] performed a complete sensitivity analysis of this procedure for predicting ρ_t and, as expected, under the most favorable conditions the error in the predicted ρ_t would be approximately the calibration uncertainty of the radiometer used in the measurement of the sky radiance, i.e., the accuracy of the procedure is limited by the accuracy of the surface-based radiometer, *not* the radiative transfer process. It is now possible to calibrate a radiometer relative to a standard lamp to within $\pm 2.5\%$ [*Biggar, Slater and Gellman*, 1994], although it is believed that detector-based calibration could reduce the uncertainty to $\pm 1\%$ [*Slater et al.*, 1996]. The *Gordon and Zhang* [1996] study suggests that the radiative transfer process would introduce an uncertainty in the prediction of ρ_t that is $\lesssim \pm 1\%$ for error-free sky radiance measurements. Thus, assuming that the sky

radiance can be measured with an uncertainty of $\pm 2.5\%$, the *Gordon and Zhang* [1996] results suggest that the error in the predicted ρ_t should be $\lesssim \pm 2.7\%$ in an RMS sense.

On the basis of the above discussion, we believe that it should be possible to reduce the $\alpha(\lambda_i)$'s to $\lesssim 0.02 - 0.03$ in the NIR, and to significantly smaller values in the visible. Also, the residual $\alpha(\lambda_i)$'s will all have the same sign.

It is important to stress again that the calibration described here is *not* radiometric, but rather a calibration of the entire system — sensor *plus* algorithms. Also, since we use F_0 to compute ρ_t in the procedure, the calibration is also relative to this quantity. An error in $F_0(\lambda_i)$ will influence the resulting value of $\alpha(\lambda_i)$; however, it will change in a very simple manner. The measured *radiance* L'_i is related to the true value L_t by $L'_i = L_t(1 + \alpha_L)$. This is converted to reflectance by multiplying by $\pi/F_0 \cos \theta_0$. If the extraterrestrial solar irradiance used in the conversion (F'_0) is in error by a fraction α_F , i.e., $F'_0 = F_0(1 + \alpha_F)$, where F_0 is the true value, then ρ'_t and ρ_t are related by

$$\rho'_t = \frac{(1 + \alpha_L)}{(1 + \alpha_F)} \rho_t \approx (1 + \alpha_L - \alpha_F) \rho_t.$$

Comparing with Eq. (2) we see that the value of $\alpha(\lambda_i)$ resulting from the procedure is really $\alpha_L(\lambda_i) - \alpha_F(\lambda_i)$, i.e., it includes the effect of *both* the sensor radiometric calibration error and any error in the extraterrestrial the solar irradiance. Thus, our approach is pragmatic, no attempt is made to determine or understand the source of the error. The error in F_0 (corrected for the variation in the earth-sun distance) is independent of time, and as long as the radiometric sensitivity of the instrument is independent of time (or its variation is monitored by other means), the algorithms should perform as suggested by the analysis provided for Figures 1 and 3.

Summarizing, by combining the correction algorithm, measurements of ρ_w , and an estimate of $\varepsilon(\lambda_i, \lambda_l)$, it is possible to reduce the F_0 -sensor calibration error significantly in the visible, even with a rather large error ($\sim 5\%$) at λ_l . *This alone could provide a calibration that will yield atmospheric correction to nearly the desired accuracy* (Figure 3a). Further reduction of the error requires reducing the uncertainty at λ_l . This can be accomplished by making atmospheric measurements sufficient to characterize the aerosol, and then predicting $\rho_t(\lambda_l)$. The final calibration accuracy at λ_l will be approximately the same as the accuracy of the surface-based radiometer used to characterize the aerosols.

5. Out-of-band response

We have implicitly assumed that the sensor's spectral response is a Dirac delta function. In reality, each spectral band will respond to radiance in a range of wavelengths, some even far from the nominal band width. If $S_i(\lambda) d\lambda$ provides the electronic output (current or voltage) from the detector for unit input radiance in a narrow band $d\lambda$ around λ_i , then the band radiance measured by the sensor in orbit will be

$$\langle L(\lambda) \rangle_{S_i} \equiv \frac{\int L(\lambda) S_i(\lambda) d\lambda}{\int S_i(\lambda) d\lambda},$$

i.e., the electronic output will be $\propto \langle L(\lambda) \rangle_{S_i}$. In an earlier paper [Gordon, 1995], I provided methodology for including the out-of-band response in the analysis of ocean color imagery, e.g., applying atmospheric correction to $\langle L_t(\lambda) \rangle_{S_i}$. It is straightforward to apply my analysis here, where the aerosol single scattering formulation of radiative transfer is believed to be valid. All that is necessary is to convert the radiance to reflectance through

$$\langle L(\lambda) \rangle_{S_i} = \frac{\cos \theta_0}{\pi} \langle \rho(\lambda) \rangle_{F_0 S_i},$$

where

$$\langle \rho(\lambda) \rangle_{F_0 S_i} \equiv \frac{\int \rho(\lambda) F_0(\lambda) S_i(\lambda) d\lambda}{\int F_0(\lambda) S_i(\lambda) d\lambda},$$

rewrite Eq. (4) for the band radiance $\langle \rho(\lambda) \rangle_{F_0 S_i}$, and then treat each term in a manner identical to Gordon [1995]. In the case of sensors with spectral bands that overlap a water vapor absorption band, e.g., SeaWiFS, the total column water vapor concentration is required. This can be obtained from the surface through sun photometry [Thome *et al.*, 1993].

6. Effect of multiple scattering and measurement error

In essence, the calibration adjustment used to reduce $\alpha(\lambda_i)$ with respect to $\alpha(\lambda_l)$ involves estimating $\rho_t(\lambda_i)$ and then adjusting the sensor calibration so that it provides a value of $\rho'_t(\lambda_i)$ in agreement with the estimate. The estimated $\rho_t(\lambda_i)$ is given by

$$[\rho_t(\lambda_i)]_{\text{Est}} = \rho_r(\lambda_i) + t(\lambda_i)\rho_w(\lambda_i) + t(\lambda_i)\rho_{wc}(\lambda_i) + \varepsilon(\lambda_i, \lambda_l) \left[\rho_t(\lambda_l) - \rho_r(\lambda_l) - t(\lambda_l)\rho_{wc}(\lambda_l) \right], \quad (12)$$

where, if $\alpha(\lambda_l) = 0$, the term in the square brackets is $\rho_a(\lambda_l) + \rho_{ra}(\lambda_l)$, and was called $\rho_{as}(\lambda_l)$ earlier (in the aerosol single-scattering approximation). This estimated $\rho_t(\lambda_i)$ can be in error for several reasons: (1) error in the measured $t(\lambda_i)\rho_w(\lambda_i)$ and/or $t(\lambda_i)\rho_{wc}(\lambda_i)$; (2) error in $\varepsilon(\lambda_i, \lambda_l)$ by

virtue of its estimation from $\tau_a(\lambda_i)/\tau_a(\lambda_l)$; and error in the term in the square brackets [$\alpha(\lambda_l) \neq 0$ and/or error in $t(\lambda_l)\rho_{wc}(\lambda_l)$]. However, there is an additional error due to the fact that $\epsilon(\lambda_i, \lambda_l)$ is a single-scattering quantity, i.e., it is not equal to

$$\epsilon_{MS}(\lambda_i, \lambda_l) \equiv \frac{\rho_a(\lambda_i) + \rho_{ra}(\lambda_i)}{\rho_a(\lambda_l) + \rho_{ra}(\lambda_l)},$$

which includes multiple scattering, and which must replace $\epsilon(\lambda_i, \lambda_l)$ in Eq. (12) in order for the equation to provide the correct value of $\rho_t(\lambda_i)$ in the absence of errors in any of the measured reflectances or in $\rho_t(\lambda_l)$. In fact, the difference between $\epsilon(\lambda_i, \lambda_l)$ and $\epsilon_{MS}(\lambda_i, \lambda_l)$ is at the core of the *Gordon and Wang* [1994b] atmospheric correction algorithm. Fortunately, given $\epsilon(\lambda_i, \lambda_l)$ and $\tau_a(\lambda_i)$, computation of $\epsilon_{MS}(\lambda_i, \lambda_l)$ is not difficult. One need only employ a nonabsorbing aerosol model (the aerosol expected at any suitable initialization site) that has a similar $\epsilon(\lambda_i, \lambda_l)$, and solve the radiative transfer equation to simulate the multiple scattering. As we are close to the single-scattering regime, error in the estimate of ϵ_{MS} from ϵ should be small.

With so many possible sources of error (four), it is difficult to assess the overall accuracy to be expected, as the errors may combine in many different ways. The approach we take here is to examine each error separately in the absence of the others. For simplicity we provide a numerical example. Consider a situation in which the aerosol at the initialization site is characterized by the *Shettle and Fenn* [1979] Maritime aerosol with 80% relative humidity (M80). Assume $\theta_0 = 60^\circ$, and the sensor views the ocean in the near-nadir direction. The oceanic site is oligotrophic with a pigment concentration (the sum of chlorophyll *a* and phaeophytin *a*) ~ 0.03 mg/m³. The whitcap reflectance is characteristic of a wind speed of ~ 8 -9 m/s, and possesses the spectral variation prescribed by *Frouin, Schwindling and Deschamps* [1996]. Under these conditions, the computed individual TOA reflectances (including multiple scattering) are provided in Table 2 for four spectral bands. The values provided for $\rho_a + \rho_{ra}$ are for $\tau_a(865) = 0.1$. Given these values, we examined the error in the predicted $\rho_t(\lambda_i)$ induced by a $\pm 5\%$ error in $t(\lambda_i)\rho_w(\lambda_i)$, a $\pm 50\%$ error in $t(\lambda_i)\rho_{wc}(\lambda_i)$, and a $\pm 5\%$ (or $\pm 2.5\%$) error in the measured $\rho'_t(\lambda_l)$ ($\alpha(\lambda_l) \neq 0$). The results of this exercise are provided in Table 3 for predictions made using both $\epsilon(\lambda_i, \lambda_l)$ and $\epsilon_{MS}(\lambda_i, \lambda_l)$ (the correct value). For the four bands in the chosen geometry with $\tau_a(865) = 0.1$, $\epsilon(\lambda_i, \lambda_l) = 1.124, 1.085, 1.027$, and $\epsilon_{MS}(\lambda_i, \lambda_l) = 1.247, 1.201$, and 1.054 , respectively for $\lambda_i = 443, 555$, and 765 nm. Note that at 443 nm the difference between ϵ_{MS} and ϵ is ~ 0.1 , i.e., a little larger than the expected uncertainty (Figure 4) in $\epsilon(443, 865)$ derived from $\tau_a(443)/\tau_a(865)$, so the difference in two identical cases using ϵ_{MS} and ϵ provides an estimate of the error induced by error in ϵ or ϵ_{MS} . From Table 3 we see

that for a very clear atmosphere [$\tau_a(\lambda_i) = 0$] error in $\rho_{wc}(\lambda)$ produces very little error $\rho_t(\lambda)$. In contrast, error in $\rho_w(\lambda)$ produces significant error in ρ_t at 443 nm ($\sim 1\%$); however, notice that error in $\rho_w(\lambda_i)$ produces a much smaller error in $\rho_t(\lambda_i)$. For $\tau_a(\lambda_i) = 0.1$, using the correct ϵ_{MS} , error in ρ_w , ρ_{wc} , and $\rho_t(\lambda_i)$, lead to errors in $\rho_t(\lambda_i)$ that are similar to those with $\tau_a(\lambda_i) = 0$. When the incorrect ϵ is used the errors are generally larger, and error in $\rho'_t(\lambda_i)$, especially when it is too small, can lead to rather large error in $\rho_t(555)$; however, the effects at 443 nm are considerably less. As in the case when measurement errors are absent, typically the resulting $\alpha(\lambda_i)$'s all have the same sign (or when one has a different sign from the rest it has an insignificant magnitude). With the exception of the combination of a -5% error in $\rho_t(\lambda_i)$ and the incorrect ϵ_{MS} , $\alpha(555)$ and $\alpha(765)$ are similar to those in Table 1. In contrast, $\alpha(443)$ is often larger, usually when there is error in $\rho_w(443)$. The message from Table 3 is clear: a high priority should be placed on reducing error in $\rho_w(443)$, and on finding the value of $\epsilon_{MS}(\lambda_i, \lambda_i)$. It is believed that $\rho_w(\lambda_i)$ measurements can be carried out with an uncertainty $< 5\%$, indeed this is required to verify that the accuracy goal for $\rho_w(443)$ is met. However, it would be possible to reduce further the effect of ρ_w uncertainty by choosing a mesotrophic initialization site, for which the value of ρ_w in the blue would be considerably reduced. As error in $\rho_t(\lambda_i)$ can be important (especially in the presence of ϵ_{MS} error), reduction of $\alpha(\lambda_i)$ relative to $\alpha(\lambda_i)$ should be effected *after* reduction $\alpha(\lambda_i)$. The entries in Table 3 for $\alpha(865) = \pm 2.5\%$ show a concomitant improvement in $\alpha(\lambda_i)$.

As it is difficult to appreciate the effects of the residual errors shown in Table 3, we provide two examples of the quality of the atmospheric correction following a hypothetical initialization exercise. We assume that the atmosphere is very clear and use the $\tau_a = 0$ residuals from Table 3. We ignore whitecaps error under the assumption that it will be $\ll \pm 50\%$ (it is already almost insignificant at $\pm 50\%$). The uncertainties due to $\rho_w(443)$ and $\rho_t(865)$ are assumed to add, i.e., the worst-case scenario. Figures 5a and 5b provide the resulting error in $t(443)\rho_w(443)$ for $\alpha(865) = +5\%$ and $+2.5\%$, respectively. In both cases the correction is within the desired ± 0.002 range. Comparing these figures with Figures 3a and 3b underscores the importance of reducing the uncertainty in the measurement of $\rho_w(\lambda_i)$ if the measurements are carried out in oligotrophic waters.

7. Implementation Strategy

On the basis of Sections 3-6, we can enumerate the quantities that must be measured to implement the in-orbit calibration adjustment.

7A. Reduction of $\alpha(\lambda_i)$ relative to $\alpha(\lambda_l)$

In order to effect the reduction of $\alpha(\lambda_i)$ relative to $\alpha(\lambda_l)$, i.e., Eq. (11), we require $t(\lambda_i)$ and $\rho_w(\lambda_i)$ to provide $t\rho_w$, $\tau_a(\lambda_i)/\tau_a(\lambda_l)$ to provide $\varepsilon(\lambda_i, \lambda_l)$, surface atmospheric pressure (P) to provide $\rho_r(\lambda_i)$, and an assessment of $\rho_{wc}(\lambda_i)$ if whitecaps are present. These quantities must be measured in an oceanic area for which $\tau_a(\lambda)$ in the visible is $\lesssim 0.10$. The water-leaving reflectance $\rho_w(\lambda)$ should be horizontally uniform (or its variability assessed) over the scale of a few pixels around the measurement location. The water-leaving reflectance is deduced from measurement of ρ_u , the subsurface upwelled reflectance distribution. With the exception of $t(\lambda_i)$, the instrumentation required to effect these measurements is described in *Clark et al.* [1997]. In the clear atmospheres required for this exercise, computation of $t(\lambda_i)$ is easily effected [*Yang and Gordon, 1997*].

The desirable attributes of the calibration initialization site are (1) a very clear atmosphere ($\tau_a \lesssim 0.1$ in the visible), (2) horizontally uniform ρ_w over spatial scales of a few pixels (a few km), and (3) mesotrophic waters to reduce the effect of ρ_w measurement error in the blue. It is usually not possible to find a site possessing all three attributes. For example, the central gyres of the oceans usually possess attributes (1) and (2), except under situations when desert dust is transported to them by the winds. However, they become mesotrophic only episodically, e.g., during spring bloom conditions. Mesotrophic conditions often occur closer to land (shelf and slope regions); however, in these regions $\tau_a(\lambda)$ is not likely to be low. Because assessing the aerosol contribution under high aerosol loads is difficult, we drop attribute (3) in favor of (1) and (2). An apparently suitable site that possess attributes (1) and (2) is windward (~ 100 km) of the Hawaiian Islands. This site is logistically attractive (see Section 8) and should meet the requirements; however, the accuracy requirement on the ρ_w measurement will be challenging.

7B. Reduction of $\alpha(\lambda_l)$

In order to effect a reduction of $\alpha(\lambda_l)$, measurement of the normalized sky radiance ρ_{sky} , and aerosol optical thickness at λ_l , either at sea or from a small island, are required to utilize the methods of *Gordon and Zhang* [1996]. *Clark et al.* [1997] describe instrumentation currently available for such measurements. These measurements should be made close to the time of the satellite overpass; however, there are geometrical constraints. Using the *Gordon and Zhang* [1996] ρ_t inversion-prediction approach, the aerosol scattering phase function can be retrieved only for

scattering angles Θ for which the direct solar beam can be singly scattered into the sky radiometer. The maximum angle for which this is possible, Θ_{Max} , is $\theta_0 + 90^\circ$, and so $P_a(\Theta, \lambda)$ can be determined only for $0 \leq \Theta < \Theta_{\text{Max}} = \theta_0 + 90^\circ$. As Θ_{Max} corresponds to viewing in the horizontal direction, practically, the maximum Θ will be $\sim 5^\circ$ less than Θ_{Max} . Accurate predictions of the TOA reflectance ρ_t are possible only for those directions for which the solar beam can be singly scattered into the sensor through a scattering angle $< \Theta_{\text{Max}}$. For nadir viewing, the required scattering angle is $\Theta_N = 180^\circ - \theta_0$. For viewing at the scan edge (taken here to be $\theta_v = 45^\circ$, $\phi_v - \phi_0 = 90^\circ$), the required scattering angle Θ_E is given by $\cos \Theta_E = -0.707 \cos \theta_0$. Figure 6 provides Θ_{Max} , Θ_N , and Θ_E as functions of θ_0 . Noting that Θ must be $< \Theta_{\text{Max}}$ to effect a vicarious calibration, Figure 6 shows that this is possible only for $\theta_0 \gtrsim 35^\circ$ at the scan edge, and $\theta_0 > 45^\circ$ at the scan center (nadir viewing). When the practical limit on Θ_{Max} is considered (Θ_{Max} reduced by $\sim 5^\circ$), we find that $\theta_0 \gtrsim 47^\circ$ at the scan center, and $\theta_0 \gtrsim 38^\circ$ near the scan edge.

These geometrical constraints, coupled with the fact that ocean color sensors are typically in orbits for which the satellite overpass is within 1.5 hr of local noon, generally means that for simultaneous surface and satellite measurements to be possible in the northern hemisphere, the measurements must be carried out at mid latitudes near the winter solstice. Note that, although the reduction of $\alpha(\lambda_l)$ will be attempted at sea simultaneously with the reduction of $\alpha(\lambda_i)$, $\lambda_i < \lambda_l$, it can be carried out in a separate experiment at a different location and time if necessary, i.e., independently of the reduction of $\alpha(\lambda_i)$, $\lambda_i < \lambda_l$.

Although several sites are under consideration for an independent $\alpha(\lambda_l)$ reduction exercise, one that appears to possess the desirable attributes is the area surrounding the Dry Tortugas ($\sim 24^\circ 38' \text{N}$, $82^\circ 53' \text{W}$) in the Southern Gulf of Mexico. Presently, this site is part of the AERONET network [Holben *et al.*, 1997] and is equipped with instrumentation for measuring $\rho_{\text{sky}}(\lambda)$ and $\tau_a(\lambda)$. The island is sufficiently small that no corrections for its perturbation to the sky radiance should be required [Yang, Gordon and Zhang, 1995]. Although the waters in the vicinity of the island are shallow (\sim few meters), the strong absorption of liquid water at λ_l ($\sim 5 \text{ m}^{-1}$ at 865 nm) should prevent any bottom contribution to $\rho_w(\lambda_l)$, so the assumption that $\rho_w(\lambda_l) = 0$ should still be valid. (This can be verified by direct measurements.) During the winter, the passage of cold fronts at \sim 5-10 day intervals produce exceptionally clear atmospheres (τ_a as low as 0.04 at 670 nm). In this season, solar zenith angles $\sim 40^\circ - 50^\circ$ occur near solar noon, the approximate time of a SeaWiFS overpass. Solar zenith angles at the time of a MODIS overpass (\sim 1.5 hours before local noon)

can be as large as 56° (Figure 7). Noting that in practice we require $\theta_0 \gtrsim 47^\circ$ at the scan center and 38° at the scan edge, we see that in the case of MODIS, vicarious calibration is possible for a considerable number of days around the solstice irrespective of the scan angle. In contrast, for SeaWiFS (equator crossing at local noon) calibration can be effected at the scan center only near the solstice, but near the scan edge, it could be effected for several weeks on either side of the solstice. In the year 2000 a second MODIS instrument is planned to be launched with an equator crossing 1.5 hours after local noon. Figure 7 shows that the above comments regarding SeaWiFS would apply equally well to this second MODIS.

Our definition of the scan edge (45° viewing angle) is somewhat arbitrary. In fact, SeaWiFS will acquire data for θ_v as large as 58° (although the atmospheric correction for $\theta_v \gtrsim 45^\circ$ is not expected to be accurate). At $\theta_v = 58^\circ$ the minimum θ_0 is $\sim 30^\circ$, and this vicarious calibration technique could be extended to about 75 days on either side of the solstice.

Finally, it should be noted that the *Gordon and Zhang* [1996] technique works best when θ_0 is large, e.g., 60° , in which case one need guess at only a small portion of the scattering phase function at large angles. One way to achieve this is to measure the sky radiance at large θ_0 and use this data to retrieve the scattering phase function, and then predict ρ_t later in the day when the satellite overpass occurs. This would allow its application in situations where $\Theta_{\text{Max}} < \Theta_N$ or Θ_E , e.g., during at-sea exercises for reducing $\alpha(\lambda_t)$ relative to $\alpha(\lambda_l)$, should such exercises occur during summer. For SeaWiFS the sky radiance to be inverted would have to be acquired $\sim 1.5 - 2$ hours prior to the overpass at the Dry Tortugas site. As the AERONET sky radiometer/photometer operates in a nearly continuous mode, any change in the aerosol optical properties over the 1.5-2 hour period should be evident in the aerosol optical thickness spectral data. *Gordon and Zhang* [1996] provide examples of the expected accuracy in the predicted $\rho_t(\lambda_l)$ under conditions for which ρ_{sky} is obtained when $\theta_0 = 60^\circ$, but ρ_t is predicted for $\theta_0 = 45^\circ$ and 50° .

The basic approach to the reduction of $\alpha(\lambda_l)$ will be to continuously acquire sky radiance data throughout the winter months and use only those data acquired under optimum conditions to predict $\rho_t(\lambda_l)$. The main challenge will be the radiometric calibration of the sky radiometer. Presently, these radiometers are calibrated using an integrating sphere at Goddard Space Flight Center. This sphere has been part of the SeaWiFS Intercalibration Round-Robin Experiments (SIRREX) [*Johnson et al.*, 1996; *Mueller*, 1993; *Mueller et al.*, 1994; *Mueller et al.*, 1996], and as such the sky radiometer is calibrated with the same standards and protocols as the radiometers

used to measure ρ_w in Subsection 7A. However, maintaining the calibration of such unattended instruments is difficult.

7C. Summary of Required Measurements

The surface measurements required for the two vicarious calibration exercises described in this section are summarized in Table 4. Note that both exercises can be carried out at the same location if desired; however, it is not necessary. It is important to note that effecting the reduction of $\alpha(\lambda_i)$ in the summer, when θ_0 is small at the time of the sensor overpass, will require that ρ_{sky} is measured several hours prior to the overpass and that the stability of the atmosphere be monitored continuously between the times of the measurement and the overpass. Column H_2O is required only for sensors for which $S_i(\lambda)$ overlaps water vapor absorption bands.

8. Maintenance of Calibration

The strategy of maintaining the sensor calibration involves utilizing the on-board solar diffusers to monitor short-term variations in the calibration. However, as the reflectance of such diffusers may gradually decay, it is necessary to assess the long-term stability by other means. The strategy we plan to monitor long-term variations is the use of an unattended measurement of ρ_w at a single site where atmospheric correction of the satellite data is simple enough that it will not introduce significant error in the retrieval of ρ_w . Comparison of the satellite-retrieved and directly-measured ρ_w over long time periods (\sim several months to years) will provide a measure of the long-term variation in the calibration of the sensor. In addition, periodic observation of the moon can also provide a measure of the long-term stability (SeaWiFS) [Kieffer and Wildey, 1996].

To provide knowledge of the long-term stability of the calibration as well as a quality measure of the performance of the sensor and the algorithms, Clark has developed a marine optical buoy system (MOBY) for continuous and unattended measurement of $\rho_w(\lambda)$ near the nadir direction (radiance exiting the ocean propagating toward the zenith). A description of this system and its planned operation is provided in Clark *et al.* [1997]. Briefly, this buoy is moored \sim 11.3 nautical miles east of the island of Lanai in the Hawaiian chain, and provides nearly real time estimates of $\rho_w(\lambda)$ near the nadir direction on a continuous basis. As the sensor will not usually be looking at the site in the nadir direction, corrections to the radiance are required to account for the bidirectional

effects of the upwelling subsurface spectral radiance [Morel and Gentili, 1991; Morel and Gentili, 1993; Morel and Gentili, 1996; Morel, Voss and Gentili, 1995]. The magnitude of these effects can be assessed and corrected through a combination of models and direct measurements of the angular distribution of upwelling subsurface radiance in the vicinity of the site under a variety of conditions [Voss, 1989]. Although this data will be of somewhat lower quality than ship-acquired ρ_w data it should be sufficiently accurate for monitoring the long-term performance of the instrument.

9. Concluding remarks

As described in the introduction, it is not possible to calibrate ocean color sensors in the laboratory with the required accuracy prior to launch. In this paper we have summarized methodology to effect in-orbit calibration adjustment of ocean color sensors with an accuracy sufficient to provide ρ_w with the required uncertainty. The “vicarious” calibration uses a combination of surface measurements and the atmospheric radiative transfer process to predict the values of the spectral radiance that the sensor is measuring. As such, this work is an extension (to the ocean) of the methodology used earlier to calibrate principally land-viewing sensors [Fraser and Kaufman, 1986; Koepke, 1982; Slater et al., 1987; Slater et al., 1996].

Conditions are chosen (very clear atmospheres with nonabsorbing aerosols) so that the radiative transfer process introduces very little error into the estimates, i.e., conditions under which the atmospheric correction algorithm should provide excellent retrievals of ρ_w , and for which error in sensor calibration are particularly evident (especially in the blue).

The calibration adjustment is in three parts. First, the calibration error in the visible bands is reduced relative to that at λ_l by using surface measurements of $\rho_w(\lambda)$, $\tau_a(\lambda)$, and $\rho_{wc}(\lambda)$. This in itself can provide a calibration that enables retrieval of $\rho_w(\lambda)$ from $\rho_t(\lambda)$ with nearly the required accuracy (Figure 3). Next, the error at λ_l is reduced by making measurements of the sky radiance and τ_a from a ship, or an island location, simultaneously (or contemporaneously) with the satellite overpass. Inversion of the sky radiance provides the radiative properties of the aerosol, and these can be used to estimate the desired $\rho_t(\lambda_l)$ [Gordon and Zhang, 1996]. Finally, as solar diffusers on SeaWiFS and MODIS provide the capability of monitoring the short-term radiometric sensitivity, $\rho_w(\lambda)$ is continuously measured at a fixed location and compared with its retrieved counterpart to monitor variations in the long-term radiometric sensitivity of the sensor.

References

- Biggar, S. F., P. N. Slater and D. I. Gellman, Uncertainties in the in-flight calibration of sensors with reference to measured ground sites in the 0.4 to 1.1 μm range, *Remote Sensing of Environment*, 48, 245–252, 1994.
- Clark, D. K., H. R. Gordon, K. J. Voss, Y. Ge, W. Broenkow and C. Trees, 1997, Validation of Atmospheric Correction over the Oceans, *Jour. Geophys. Res.*, (In press).
- Ding, K. and H. R. Gordon, Analysis of the influence of O_2 A-band absorption on atmospheric correction of ocean color imagery, *Applied Optics*, 34, 2068–2080, 1995.
- Evans, R. H. and H. R. Gordon, CZCS 'System Calibration:' A retrospective examination, *Jour. Geophys. Res.*, 99C, 7293–7307, 1994.
- Fraser, R. S. and Y. J. Kaufman, Calibration of satellite sensors after launch, *Applied Optics*, 25, 1177–1185, 1986.
- Frouin, R., M. Schwindling and P. Y. Deschamps, Spectral reflectance of sea foam in the visible and near-infrared: In-situ measurements and implications for remote sensing of ocean color and aerosols, *Jour. Geophys. Res.*, 101C, 14,361–14,371, 1996.
- Gordon, H. R., Calibration Requirements and Methodology for Remote Sensors Viewing the Oceans in the Visible, *Remote Sensing of Environment*, 22, 103–126, 1987.
- Gordon, H. R., Remote sensing of ocean color: a methodology for dealing with broad spectral bands and significant out-of-band response, *Applied Optics*, 34, 8363–8374, 1995.
- Gordon, H. R., 1997, Atmospheric Correction of Ocean Color Imagery in the Earth Observing System Era, *Jour. Geophys. Res.*, (In press).
- Gordon, H. R., J. W. Brown and R. H. Evans, Exact Rayleigh Scattering Calculations for use with the Nimbus-7 Coastal Zone Color Scanner, *Applied Optics*, 27, 862–871, 1988.

- Gordon, H. R. and A. Y. Morel, *Remote Assessment of Ocean Color for Interpretation of Satellite Visible Imagery: A Review*, Springer-Verlag, New York, 1983, 114 pp.
- Gordon, H. R. and M. Wang, Influence of Oceanic Whitecaps on Atmospheric Correction of SeaWiFS, *Applied Optics*, 33, 7754–7763, 1994a.
- Gordon, H. R. and M. Wang, Retrieval of water-leaving radiance and aerosol optical thickness over the oceans with SeaWiFS: A preliminary algorithm, *Applied Optics*, 33, 443–452, 1994b.
- Gordon, H. R. and T. Zhang, How well can radiance reflected from the ocean-atmosphere system be predicted from measurements at the sea surface?, *Applied Optics*, 35, 6527–6543, 1996.
- Holben, B. N., T. F. Eck, I. Slutsker, D. Tanre, J. P. Buis, A. Setzer, E. Vermote, J. Reagan, Y. Kaufman, T. Nakajima, F. Lavenu and I. Jankowiak, 1997, Automatic Sun and Sky Scanning Radiometer System for Network Aerosol Monitoring, *Remote Sensing of Environment* (In press) .
- Hooker, S. B., W. E. Esaias, G. C. Feldman, W. W. Gregg and C. R. McClain, *SeaWiFS Technical Report Series: Volume 1, An Overview of SeaWiFS and Ocean Color*, NASA, Greenbelt, MD, Technical Memorandum 104566, July 1992.
- Johnson, B. C., S. S. Bruce, E. A. Early, J. M. Houston, T. R. O'Brian, A. Thompson, S. B. Hooker and J. L. Mueller, *SeaWiFS Technical Report Series: Volume 37, The Fourth SeaWiFS Intercalibration Round-Robin Experiment, SIRREX-4, May 1995*, NASA, Greenbelt, MD, Technical Memorandum 104566, May 1996.
- Kieffer, H. H. and R. L. Wildey, Establishing the Moon as a Spectral Radiance Standard, *Jour. Atmos. Oceanic Tech.*, 13, 360–375, 1996.
- Koepke, P., Vicarious Satellite Calibration in the Solar Spectral Range by Means of Calculated Radiances and its Application to Meteosat, *Applied Optics*, 21, 2845–2854, 1982.

- Korotaev, G. K., S. M. Sakerin, A. M. Ignatov, L. L. Stowe and E. P. McClain, Sun-Photometer Observations of Aerosol Optical Thickness over the North Atlantic from a Soviet Research Vessel for Validation of Satellite Measurements, *Jour. Atmos. Oceanic Technol.*, 10, 725–735, 1993.
- Moore, K. D., K. J. Voss and H. R. Gordon, 1997, Spectral Reflectance of Whitecaps: Fractional Coverage and the Augmented Spectral Reflectance Contribution to Water-Leaving Radiance, *Jour. Geophys. Res.*, (Submitted).
- Morel, A. and B. Gentili, Diffuse reflectance of oceanic waters: its dependence on Sun angle as influenced by the molecular scattering contribution, *Applied Optics*, 30, 4427–4438, 1991.
- Morel, A. and B. Gentili, Diffuse reflectance of oceanic waters. II. Bidirectional aspects, *Applied Optics*, 32, 6864–6879, 1993.
- Morel, A. and B. Gentili, Diffuse reflectance of oceanic waters. III. Implication of bidirectionality for the remote sensing problem, *Applied Optics*, 35, 4850–4862, 1996.
- Morel, A., K. J. Voss and B. Gentili, Bidirectional reflectance of oceanic waters: A comparison of modeled and measured upward radiance fields, *Jour. Geophys. Res.*, 100C, 13,143–13,150, 1995.
- Mueller, J. L., *SeaWiFS Technical Report Series: Volume 14, The First SeaWiFS Intercalibration Round-Robin Experiment, SIRREX-1, July 1992*, NASA, Greenbelt, MD, Technical Memorandum 104566, September 1993.
- Mueller, J. L., B. C. Johnson, C. L. Cromer, J. W. Cooper, J. T. McLean, S. B. Hooker and T. L. Westphal, *SeaWiFS Technical Report Series: Volume 16, The Second SeaWiFS Intercalibration Round-Robin Experiment, SIRREX-2, June 1993*, NASA, Greenbelt, MD, Technical Memorandum 104566, May 1994.

- Mueller, J. L., B. C. Johnson, C. L. Cromer, S. B. Hooker, J. T. McLean and S. F. Biggar, *SeaWiFS Technical Report Series: Volume 34, The Third SeaWiFS Intercalibration Round-Robin Experiment, SIRREX-3, September 1994*, NASA, Greenbelt, MD, Technical Memorandum 104566, March 1996.
- Reddy, P. J., F. W. Kreiner, J. J. Deluisi and Y. Kim, Aerosol Optical Depths Over the Atlantic Derived From Shipboard Sunphotometer Observations During the 1988 Global Change Expedition, *Global Biogeochemical Cycles*, 4, 225–240, 1990.
- Salomonson, V. V., W. L. Barnes, P. W. Maymon, H. E. Montgomery and H. Ostrow, MODIS: Advanced Facility Instrument for Studies of the Earth as a System, *IEEE Geosci. Rem. Sens.*, 27, 145–152, 1989.
- Shettle, E. P. and R. W. Fenn, Models for the Aerosols of the Lower Atmosphere and the Effects of Humidity Variations on Their Optical Properties, Air Force Geophysics Laboratory, Hanscomb AFB, MA 01731, AFGL-TR-79-0214, 1979.
- Slater, P. N., S. F. Biggar, R. G. Holm, R. D. Jackson, Y. Mao, M. S. Moran, J. M. Palmer and B. Yuan, Reflectance- and Radiance-Based Methods for the In-Flight Absolute Calibration of Multispectral Sensors, *Remote Sensing of Environment*, 22, 11–37, 1987.
- Slater, P. N., S. F. Biggar, K. J. Thome, D. I. Gellman and P. R. Spyak, Vicarious radiometric calibration of EOS sensors, *Jour. Atmos. Oceanic Tech.*, 13, 349–359, 1996.
- Thome, K. J., M. W. Smith, J. M. Palmer and J. A. Reagan, Method and instrument for retrieving total columnar water vapor from solar transmittance, *Proceedings, Society of Photo-Optical Instrumentation Engineers*, 1968, 856–861, 1993.
- Villevalde, Y. V., A. V. Smirnov, N. T. O'Neill, S. P. Smyshlyaev and V. V. Yakovlev, Measurement of Aerosol Optical Depth in the Pacific Ocean and North Atlantic, *Jour. Geophys. Res.*, 99D, 20983–20988, 1994.
- Voss, K. J., Electro-optic Camera System for Measurement of the Underwater Radiance Distribution, *Optical Engineering*, 28, 241–247, 1989.

- Wang, M. and H. R. Gordon, Retrieval of the Columnar Aerosol Phase Function and Single Scattering Albedo from Sky Radiance over the Ocean: Simulations, *Applied Optics*, 32, 4598–4609, 1993.
- Wang, M. and H. R. Gordon, A Simple, Moderately Accurate, Atmospheric Correction Algorithm for SeaWiFS, *Remote Sensing of Environment*, 50, 231–239, 1994.
- Yang, H. and H. R. Gordon, 1997, Remote sensing of ocean color: Assessment of the water-leaving radiance bidirectional effects on the atmospheric diffuse transmittance, *Applied Optics*, (Submitted).
- Yang, H., H. R. Gordon and T. Zhang, Island perturbation to the sky radiance over the ocean: Simulations, *Applied Optics*, 34, 8354–8362, 1995.

Table 1: Values of $\alpha(\lambda_i)$ required to produce a nearly correct $\varepsilon(\lambda_i, \lambda_i)$ for the examples in Figures 2a and 2b.

λ_i (nm)	$\alpha(\lambda_i)$
412	0.003
443	0.005
490	0.008
520	0.01
550	0.015
670	0.02
765	0.03

Table 2: Reflectance for M80 model near nadir.

($\theta_0 = 60^\circ$, $\tau_a(865) = 0.1$, λ in nm)

λ	$\rho_r(\lambda)$	$t\rho_w(\lambda)$	$t\rho_{wc}(\lambda)$	$\rho_a(\lambda) + \rho_{ra}(\lambda)$
443	0.11948	0.02667	0.00140	0.00939
555	0.04923	0.00348	0.00174	0.00905
765	0.01331	0	0.00173	0.00793
443	0.00806	0	0.00156	0.00752

Table 3: Summary of residual errors $\alpha(\lambda_i)$ after calibration adjustment.

τ_a	$\delta\rho_w(\lambda)$ (%)	$\delta\rho_{wc}(\lambda)$ (%)	ε	ε_{MS}	$\alpha(443)$ (%)	$\alpha(555)$ (%)	$\alpha(765)$ (%)	$\alpha(865)$ (%)
0	0	0			0	0	0	0
0	0	0			± 0.18	± 0.48	± 1.64	± 2.5
0	0	0			± 0.38	± 0.97	± 3.27	± 5.0
0	± 5	0			± 0.90	± 0.32	0	0
0	0	± 50			∓ 0.14	± 0.02	± 0.43	0
0.1	0	0		✓	0	0	0	0
0.1	0	0		✓	± 0.34	± 0.81	± 1.97	± 2.5
0.1	0	0		✓	± 0.68	± 1.62	± 3.93	± 5.0
0.1	± 5	0		✓	± 0.85	± 0.27	0	0
0.1	0	± 50		✓	± 0.17	± 0.11	± 0.19	0
0.1	0	0	✓		-0.59	-1.38	-0.85	0
0.1	0	0	✓		-0.28	-0.64	+1.07	+2.5
0.1	0	0	✓		+0.02	+0.09	+2.99	+5.0
0.1	0	0	✓		-0.90	-2.11	-2.77	-2.5
0.1	0	0	✓		-1.21	-2.84	-4.68	-5.0
0.1	+5	0	✓		+0.26	-1.10	-0.85	0
0.1	-5	0	✓		-1.44	-1.65	-0.85	0
0.1	0	+50	✓		-0.70	-1.34	-0.57	0
0.1	0	-50	✓		-0.48	-1.41	-1.12	0

Table 4: Measurements required for vicarious calibration.

Reduction of $\alpha(\lambda_i)$, $\lambda_i < \lambda_l$	Reduction of $\alpha(\lambda_l)$
$\rho_u(\lambda_i)$ angular distribution	$\rho_{sky}(\lambda_l)$
$\tau_a(\lambda_i)/\tau_a(\lambda_l)$	$\tau_a(\lambda_l)$
$\rho_{wc}(\lambda_i)$	
Assess horizontal variation of $\rho_w(\lambda_i)$	
Column H ₂ O	Column H ₂ O

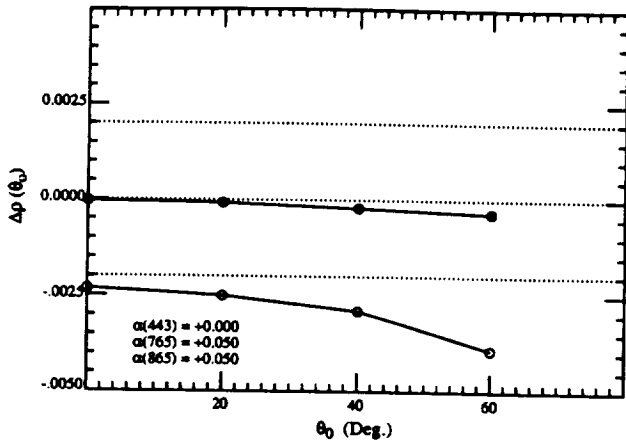


Figure 1a. Error in the retrieved $t(443)\rho_w(443)$ for viewing near the edge of the scan with a Maritime aerosol at RH = 80% as a function of the solar zenith angle with $\tau_a(865) = 0.2$ and calibration errors $\alpha(443)$, $\alpha(765)$, and $\alpha(865)$ in Eq. (2) (open circles). Solid circles are for $\alpha(\lambda_i) = 0$ for all λ_i .

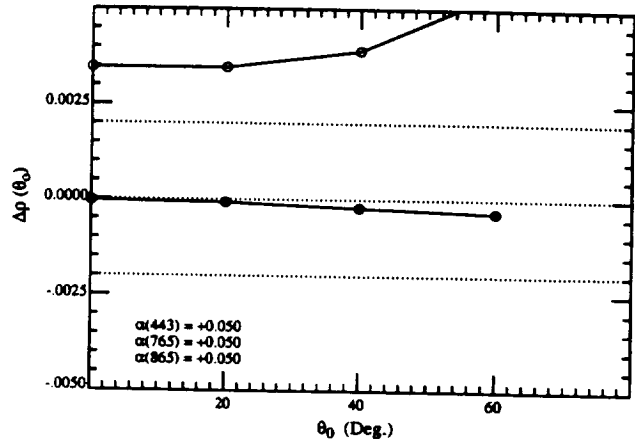


Figure 1b. Error in the retrieved $t(443)\rho_w(443)$ for viewing near the edge of the scan with a Maritime aerosol at RH = 80% as a function of the solar zenith angle with $\tau_a(865) = 0.2$ and calibration errors $\alpha(443)$, $\alpha(765)$, and $\alpha(865)$ in Eq. (2) (open circles). Solid circles are for $\alpha(\lambda_i) = 0$ for all λ_i .

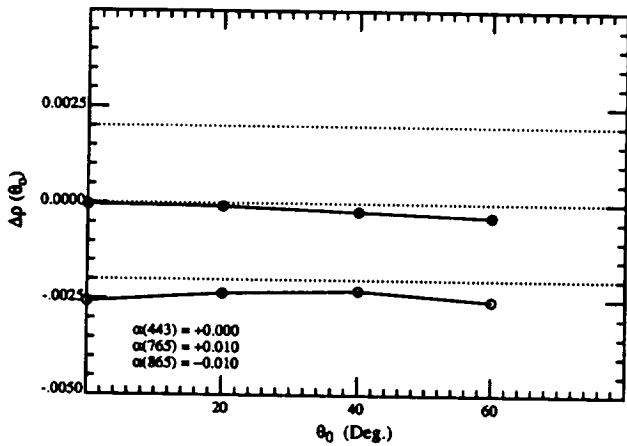


Figure 1c. Error in the retrieved $t(443)\rho_w(443)$ for viewing near the edge of the scan with a Maritime aerosol at RH = 80% as a function of the solar zenith angle with $\tau_a(865) = 0.2$ and calibration errors $\alpha(443)$, $\alpha(765)$, and $\alpha(865)$ in Eq. (2) (open circles). Solid circles are for $\alpha(\lambda_i) = 0$ for all λ_i .

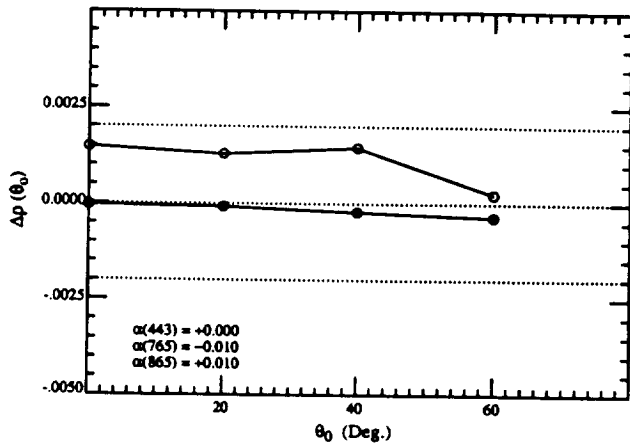


Figure 1d. Error in the retrieved $t(443)\rho_w(443)$ for viewing near the edge of the scan with a Maritime aerosol at RH = 80% as a function of the solar zenith angle with $\tau_a(865) = 0.2$ and calibration errors $\alpha(443)$, $\alpha(765)$, and $\alpha(865)$ in Eq. (2) (open circles). Solid circles are for $\alpha(\lambda_i) = 0$ for all λ_i .

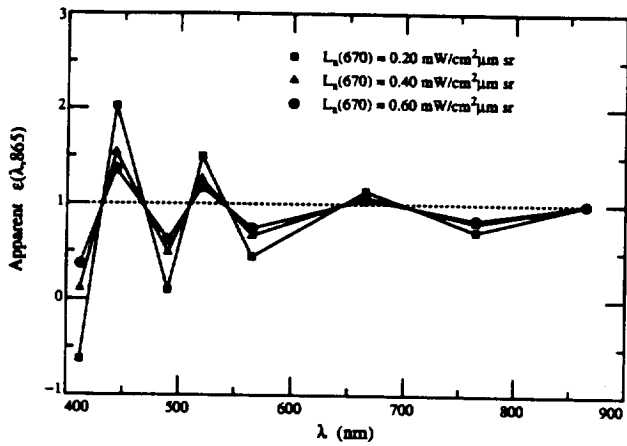


Figure 2a. Apparent value of $\epsilon(\lambda, 865)$ for three values of $L_s(670)$. $\alpha(\lambda)$ alternates in sign from band to band and $|\alpha(\lambda)| = 0.05$.

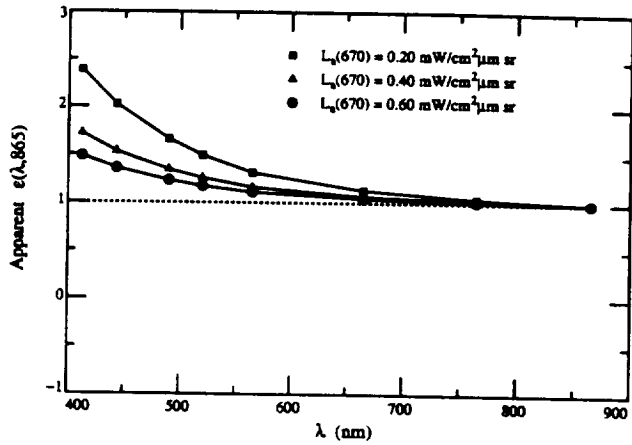


Figure 2b. Apparent value of $\epsilon(\lambda, 865)$ for three values of $L_s(670)$. $\alpha(\lambda) = 0.05$ for all bands.

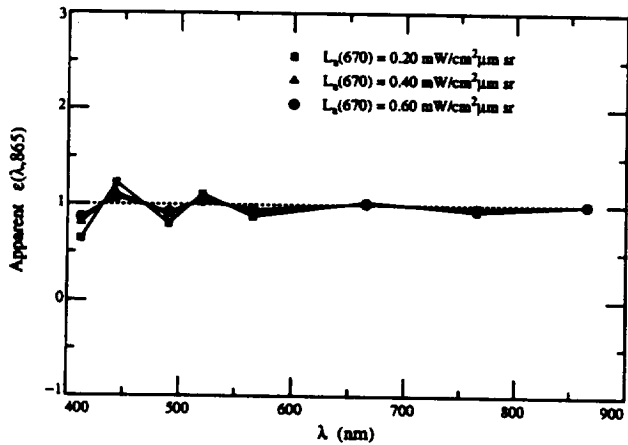


Figure 2c. Apparent value of $\epsilon(\lambda, 865)$ for three values of $L_s(670)$. $\alpha(\lambda)$ alternates in sign from band to band and $|\alpha(\lambda)| = 0.01$.

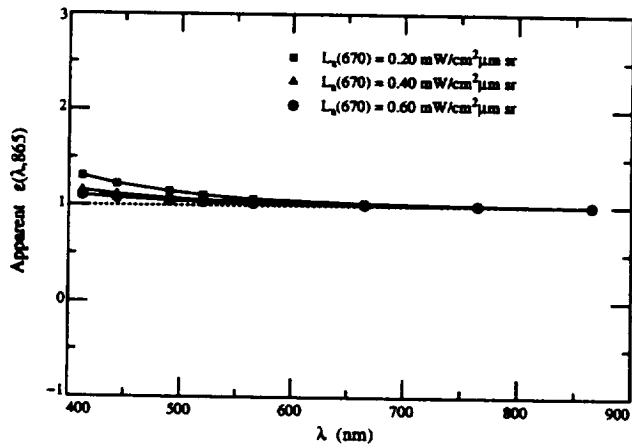


Figure 2d. Apparent value of $\epsilon(\lambda, 865)$ for three values of $L_s(670)$. $\alpha(\lambda) = 0.01$ for all bands.

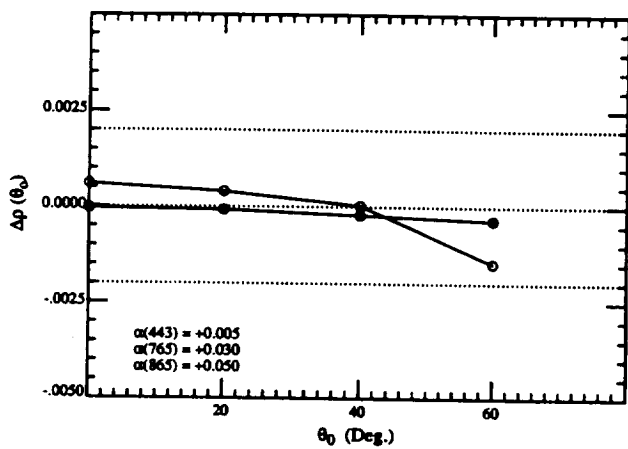


Figure 3a. Error in the retrieved $t(443)\rho_w(443)$ for viewing near the edge of the scan with a Maritime aerosol at RH = 80% as a function of the solar zenith angle with $\tau_a(865) = 0.2$ and calibration errors $\alpha(443)$, $\alpha(765)$, and $\alpha(865)$ in Eq. (2) (open circles). Solid circles are for $\alpha(\lambda_i) = 0$ for all λ_i .

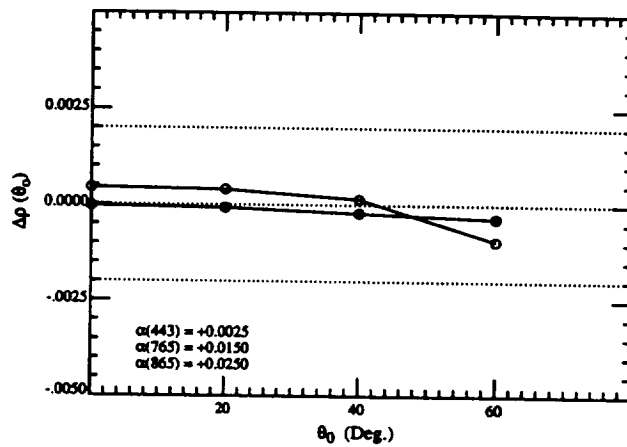


Figure 3b. Error in the retrieved $t(443)\rho_w(443)$ for viewing near the edge of the scan with a Maritime aerosol at RH = 80% as a function of the solar zenith angle with $\tau_a(865) = 0.2$ and calibration errors $\alpha(443)$, $\alpha(765)$, and $\alpha(865)$ in Eq. (2) (open circles). Solid circles are for $\alpha(\lambda_i) = 0$ for all λ_i .

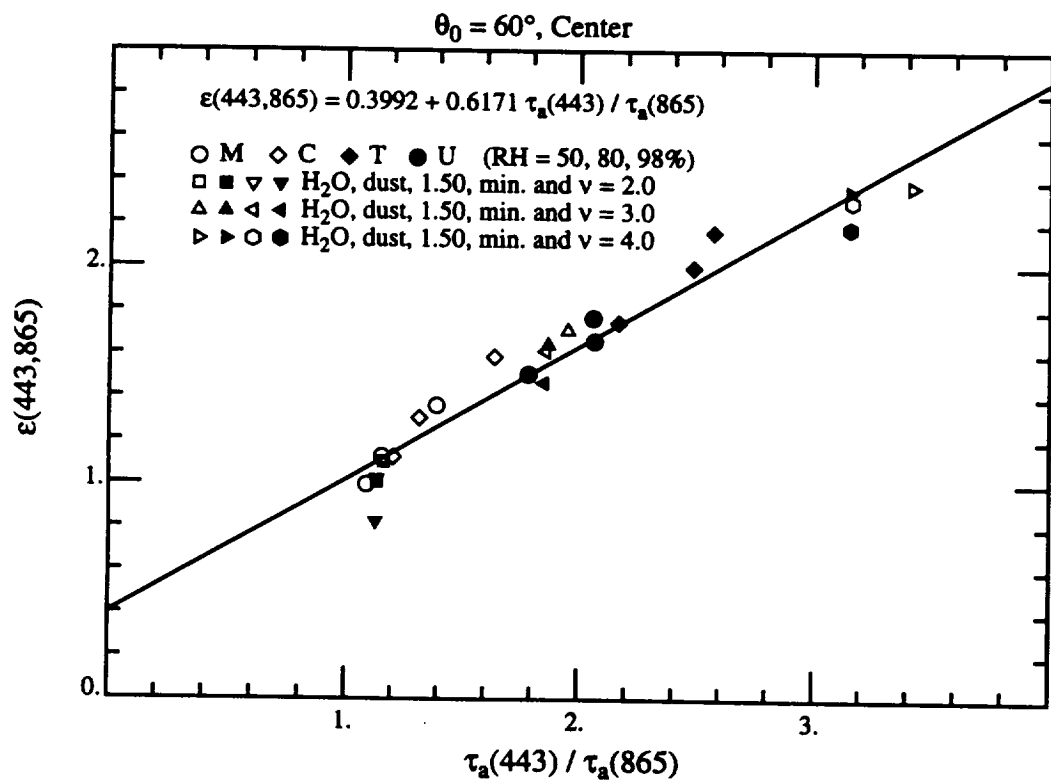


Figure 4. Relationship between $\tau_a(443)/\tau_a(865)$ and $\epsilon(443,865)$ at the scan center with $\theta_0 = 60^\circ$ for several aerosol models. From Gordon [1997].

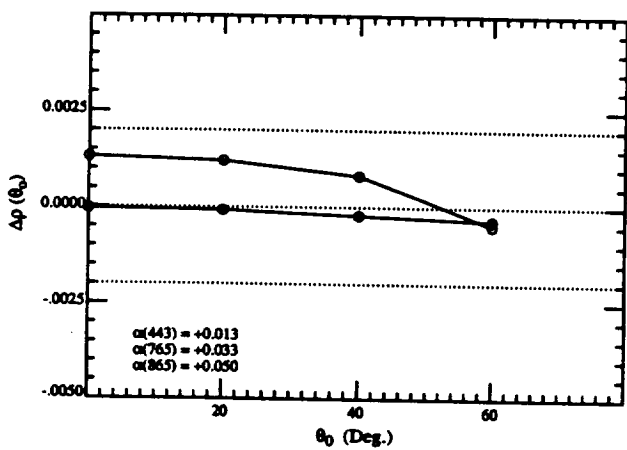


Figure 5a. Error in the retrieved $t(443)\rho_w(443)$ for viewing near the edge of the scan with a Maritime aerosol at RH = 80% as a function of the solar zenith angle with $\tau_a(865) = 0.2$ and calibration errors $\alpha(443)$, $\alpha(765)$, and $\alpha(865)$ in Eq. (2) (open circles). Solid circles are for $\alpha(\lambda_i) = 0$ for all λ_i .

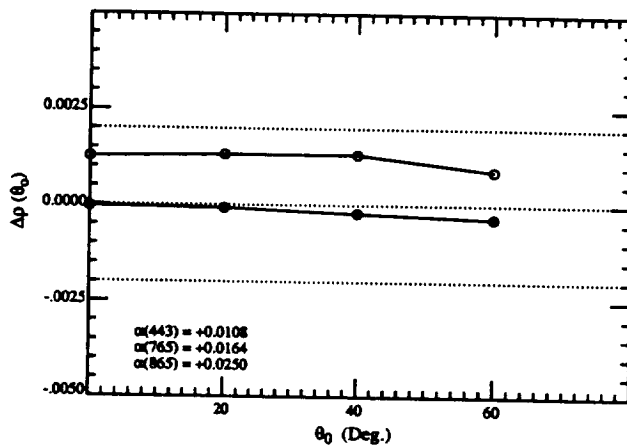


Figure 5b. Error in the retrieved $t(443)\rho_w(443)$ for viewing near the edge of the scan with a Maritime aerosol at RH = 80% as a function of the solar zenith angle with $\tau_a(865) = 0.2$ and calibration errors $\alpha(443)$, $\alpha(765)$, and $\alpha(865)$ in Eq. (2) (open circles). Solid circles are for $\alpha(\lambda_i) = 0$ for all λ_i .

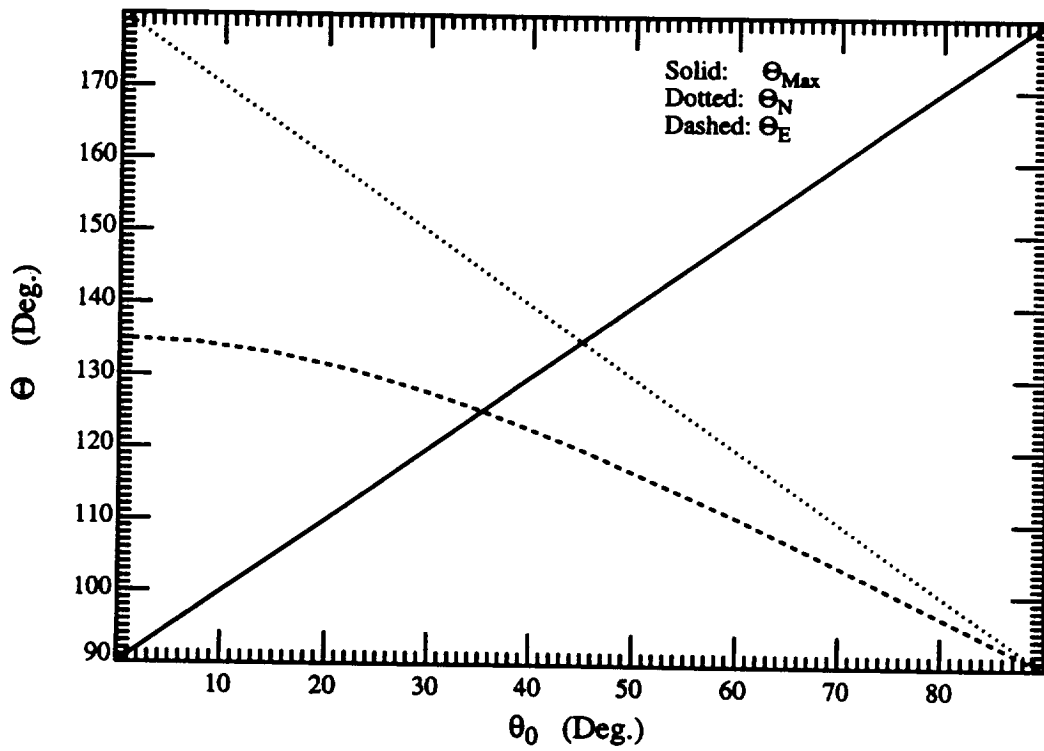


Figure 6. Θ_{Max} , Θ_N and Θ_E as functions of θ_0 .

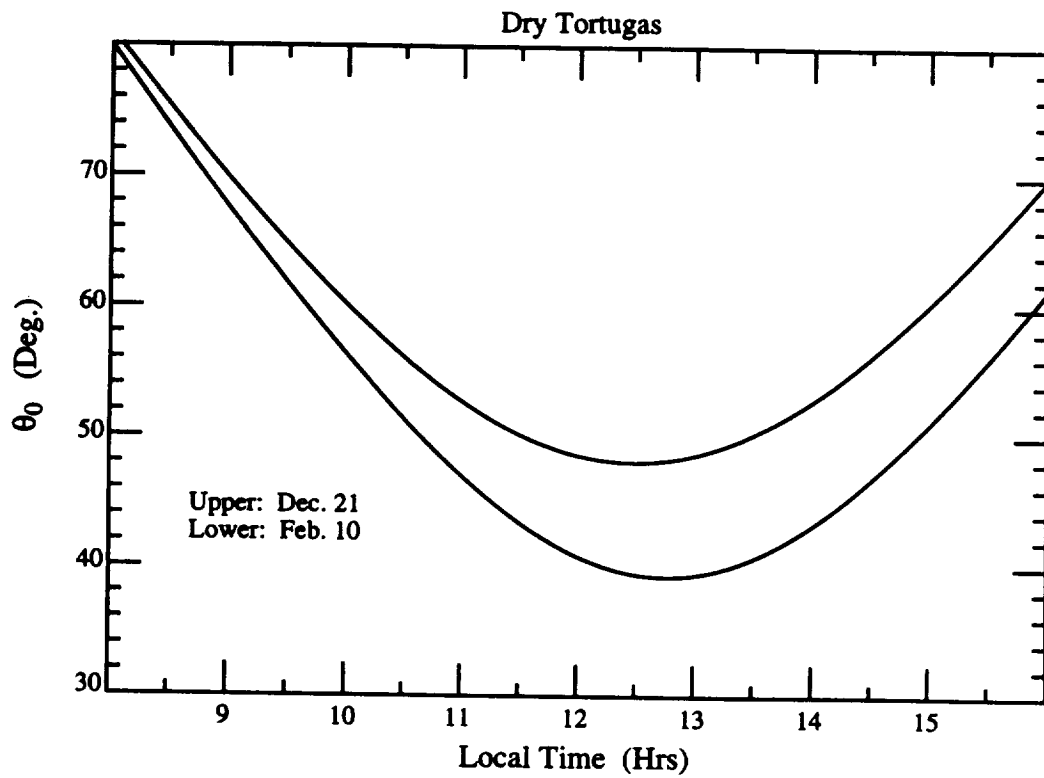


Figure 7. θ_0 as a function of local time for two days at the Dry Tortugas.

Appendix 4

Long term aerosol optical depth analysis: Program description and results. (DRAFT)

DRAFT

Long Term Maritime Aerosol Optical Depth Analysis: Program Description and Results

Ellsworth J. Welton, Kenneth J. Voss, and Joseph M. Prospero

To Be Submitted to the Journal of Geophysical Research: Spring 1997

Abstract: The radiative properties of atmospheric aerosols are an important element of the global radiation balance and in applications such as remote sensing. One of the most important radiative properties is the aerosol optical depth (AOD) and its associated wavelength dependence; characterized by the Angstrom exponent, α . Long term measurements of these aerosol features taken at various locations are necessary to track seasonal patterns of radiative behavior and to determine characteristic differences in the optical properties of different sites. An AOD measurement program was begun in August of 1993 to determine the radiative properties of aerosols over existing Atmosphere/Ocean Chemistry Experiment (AEROCE) sites in Miami, Florida, Bermuda, and Barbados. A description of the radiative program, instrumentation and calibration procedures, the methodology employed to determine the AOD and α , and the final results obtained from the measurements are presented. Analysis of the AOD and Angstrom exponents in terms of seasonal variations and unique site characteristics were performed as well.

Keywords: Aerosols, Optical Depth, Angstrom Exponent, sunphotometer, shadowband

1. INTRODUCTION

There is relatively little information on the climatology of atmospheric aerosols, particularly over the ocean. However, the radiative effects of marine aerosols directly alter terrestrial optical properties, such as the planetary albedo, and may play an important role, directly and indirectly, in the global climate [Charlson, 1992]. In addition to the terrestrial impact of marine aerosols they also affect our ability to extract surface information from satellites, in particular for ocean color remote sensing [Gordon, ???]. Knowledge of the aerosol optical properties are necessary to correct for these effects in both Global Circulation Models and in satellite correction algorithms.

The most commonly measured aerosol optical property is the aerosol optical depth (AOD), which determines how the aerosol attenuates the direct solar beam. The total optical depth, $\tau(\lambda)$, is defined by

$$\tau(\lambda) = \frac{1}{m(\vartheta_z)} \text{Ln} \left[\frac{E_o(\lambda)}{E(\lambda)} \right], \quad (1)$$

where $m(\vartheta_z)$ is the air mass at zenith angle ϑ_z , $E_o(\lambda)$ is the extra-terrestrial solar irradiance (solar constant) at wavelength λ , and $E(\lambda)$ is the direct, unscattered solar irradiance at the surface. For wavelengths that lie outside the usual atmospheric gas absorption bands, the total optical depth may also be written as the sum

$$\tau(\lambda) = \tau_r(\lambda) + \tau_o(\lambda) + \tau_w(\lambda) + \tau_a(\lambda) \quad (2)$$

where $\tau_r(\lambda)$ is the Rayleigh optical depth due to molecular scattering, $\tau_o(\lambda)$ is the Chappius band ozone optical depth, $\tau_w(\lambda)$ is the optical depth due to water vapor absorption, and $\tau_a(\lambda)$ is

the aerosol optical depth. The basic experimental method of acquiring the AOD from the total optical depth has been outlined in several papers, most notably *Shaw* [1979] and *King et al.* [1980].

The spectral variation of the AOD can be used to extract additional useful information on the aerosols. One convenient spectral parameterization uses the fact that the AOD is often proportional to some power of the wavelength [*Angstrom*, 1964], and is written as

$$\tau_a(\lambda) = \beta \lambda^{-\alpha}, \quad (3)$$

where λ is the wavelength, α is the Angstrom exponent, and β is a scale factor. In the special case of a Junge type size distribution ($dn/dr = Cr^{-(n+1)}$), the Angstrom exponent is related to the slope of the size distribution of the aerosol scatterers [*Van de Hulst*, 1981]. The exponent, α , generally varies from zero to two, with lower exponents representing a lower ratio of small to larger sized particles than in the case with a higher exponent.

Greenhouse gases are typically long-lived and diffuse, and while they are important, their effects can be modeled. Aerosols, by contrast, have short lifetimes and are highly inhomogeneous and variable. To determine the possible radiative impact of aerosols, long term studies of the optical properties of the aerosols at many locations are required. As one of our objectives is to determine the optical climatology of the aerosols over the ocean, these measurements can be performed from ships or small islands. Island locations are convenient for multi-year observational records as local observers can be used and logistical problems are reduced.

In order to obtain long term data sets of the AOD and other physical aerosol measurements, hand-held sunphotometers were used at existing AEROCE (Atmosphere/Ocean Chemistry Experiment) sites in Miami (Florida), Bermuda, and Barbados. Utilization of the AEROCE stations [*Reference ???*] for the sunphotometer measurements was advantageous because problems associated with operating long term remote sites in foreign countries were reduced. In addition,

these sites perform a variety of measurements of the chemical and physical properties of the boundary layer aerosols. The hand-held sunphotometers were replaced with Automated Multi-Filter Rotating Shadowband Radiometers [Harrison *et al.*, 1994] by the end of 1994. The shadowbands create a more complete data record as they automatically sample all day, perform a potential calibration each day (dependent on weather), and also measure diffuse irradiance. The shadowbands operated concurrently with the sunphotometers for several months during the instrument replacement process. Table 1 indicates the geographical information and time period of the sunphotometer and shadowband measurements at each site. The instrument calibration procedure, methods of data selection, aerosol optical depths, and Angstrom exponents recorded for each site are presented in this paper.

2. INSTRUMENT PROGRAM DESCRIPTION AND CALIBRATION

The sunphotometers used to generate the AOD data sets in Miami, Bermuda, and Barbados each had nine channels containing an interference filter. New filters were installed in each instrument at the beginning of the measurement period reported in the paper. Identical filters, selected from the same lot, were used in all the sunphotometers. The spectral bandwidth of each sunphotometer channel filter had a passband approximately 5 nm wide centered at wavelengths from 380.2 to 1025.9 nm (Table 2). Each shadowband had seven channels containing an interference filter, except for channel one which was a broadband channel (no spectral filter). The spectral bandwidth of shadowband filters two through seven are 10 nm wide, and are centered at wavelengths from 410 to 940 nm (Table 2). Channel seven of the shadowbands is located in a water vapor absorption band in order to obtain $\tau_w(\lambda)$. Neither water vapor analysis or broadband studies were a focus of this project, therefore data from shadowband channels one and seven was not used. The remaining filter wavelengths in each instrument were chosen to avoid strong absorption bands such as water vapor, thus simplifying equation 2 as $\tau_w(\lambda)$ was taken to be zero.

However, avoidance of the ozone Chappius band was not possible, therefore ozone absorption must be taken into account in the data reduction process.

The sunphotometers were operated by on site personnel who recorded measurements at approximately 10:00 am and 3:00 pm local time respectively. The shadowbands ran automatically, eliminating the need for an on site operator, however, on site personnel are needed in the event of instrument malfunction or equipment upgrades. The Miami shadowband sampled data every minute throughout the day, while the Bermuda and Barbados shadowbands sampled every four minutes to reduce the number of data downloads per week. As the shadowbands perform measurements continually, each day offers the potential of a Langley calibration [Shaw, 1983]. Therefore the calibrations for the shadowbands are more complete than those for the sunphotometers.

A calibration record (history) for each instrument was compiled in order to account for time shifts in the solar constants of each channel, often caused by degradation of the filter. The calibration record for an instrument refers to the plot of the date versus $E_o(\lambda)$ for the length of the entire data set. A fit to this plot allows the solar constants, on a day that did not allow a Langley calibration to be performed, to be calculated using the fitted equation. An error correction procedure was then employed for both instruments to modify the conventional Langley calibration. The sunphotometer and shadowband calibration procedures are outlined below.

2a. SUNPHOTOMETER DATA PROGRAM AND CALIBRATION

A sunphotometer was located at each site, while an additional sunphotometer was used for calibration processes during and after the measurement period. Initially the Langley method was used to perform the calibrations, for each sunphotometer, in Miami prior to deployment into the field. The instruments were then sent into the field, and operations began as indicated in Table 1. With the exception of poor weather days, the measurements continued uninterrupted for the

remainder of the sunphotometer program. Sea level Langley calibrations in these locations are difficult due to atmospheric instability and cloudiness. Thus it was not possible to perform routine Langley calibrations at the Bermuda and Barbados locations. The Miami instrument (M114) was calibrated several times during the sunphotometer program, both in Miami and in Brainard Lake, Colorado. An additional sunphotometer (M119), not tied to any location, was extensively calibrated during an oceanographic cruise, off of Hawaii, in October and November of 1994. Post-calibrations for the Bermuda and Barbados instruments were performed in Miami at the end of the sunphotometer program (through a method described below). Calibration values were obtained for days within the data set using an interpolation between the initial calibrations and the post-calibrations. Prior experience with the sunphotometer interference filters led us to use an exponential function to fit the decay of these filters for the interpolation.

It was difficult to perform full Langley calibrations on the instruments at the end of the sunphotometer program due to poor weather. The Miami instrument was calibrated several times during the initial startup, and throughout the program, and was considered to be the best calibrated of the sunphotometers. The M119 sunphotometer was well calibrated, using the Langley procedure, during October and November 1994 and was used to calibrate the Miami instrument at the end of the sunphotometer program through a cross-calibration procedure. A cross-calibration assumes that two identical sunphotometers are present, one is fully calibrated and is referred to as the reference instrument, the other is uncalibrated and referred to as the target instrument. Simultaneous direct beam measurements are made with each sunphotometer at the same location. The resulting equations for each instrument are

$$E_r(\lambda) = E_{r_0}(\lambda) \exp[-\tau(\lambda)m_r(\vartheta_z)], \quad (4)$$

$$E_t(\lambda) = E_{t_0}(\lambda) \exp[-\tau(\lambda)m_t(\vartheta_z)], \quad (5)$$

where the r subscript denotes the reference instrument, the t subscript denotes the target instrument, and $m(\vartheta_z)$ is the air mass at zenith angle, ϑ_z , computed using the formula provided by *Kasten and Young* [1989]. $E_r(\lambda)$ and $E_t(\lambda)$ are the measured direct solar irradiances in instrument counts, and $E_{r_0}(\lambda)$ and $E_{t_0}(\lambda)$ are the extraterrestrial solar irradiances in instrument counts for the reference and target instruments. As $E_{r_0}(\lambda)$ is known, the total optical depth is calculated using the calibrated instrument. Once the total optical depth is determined, $E_{t_0}(\lambda)$, can be written as

$$E_{t_0}(\lambda) = E_{r_0}(\lambda) \frac{E_t(\lambda)}{E_r(\lambda)} \exp[\tau(\lambda)(m_t(\vartheta_z) - m_r(\vartheta_z))], \quad (6)$$

for each wavelength of the sunphotometer. This cross-calibration procedure was useful as the weather need only be stable and cloud free for a small window of time, as opposed to the requirements for a Langley calibration. The total optical depth changes for different air masses, therefore the two values, $m_r(\vartheta_z)$ and $m_t(\vartheta_z)$, should be as close as possible to avoid errors in calculating $E_{t_0}(\lambda)$. If the measurements are made close to solar noon, the air mass changes very little during the measurement process and the exponential term is negligible. This procedure also assumes that the instruments have matched wavelengths ($\lambda_r = \lambda_t$), and in our case the filters were matched for all sunphotometers.

Once the Miami instrument, (M114), had been cross-calibrated against M119, the cross-calibrations were added to the calibration history for M114, and it was considered fully calibrated. M114 was then used as a reference instrument during cross-calibrations for the Bermuda and Barbados sunphotometers. These cross-calibrations were then added to the calibration history for

Bermuda and Barbados. The calibration histories for the three locations are given in Figs. 1a, 1b, and 1c. The solid line is the exponential fit to the calibrations given above.

An error correction procedure was utilized to fine tune these solar constants. This procedure assumes that there is some error, $\chi(\lambda)$, present in the solar constant, and that the aerosols above the sites, on average, obey the Angstrom spectral dependence (Eq. (3)). Redefining the solar constant in terms of this error and the true solar constant yields

$$E_o(\lambda) = \chi(\lambda)E'_o(\lambda), \quad (7)$$

where $E_o(\lambda)$ is the previously derived solar constant, $\chi(\lambda)$ is the error factor, and $E'_o(\lambda)$ is the true solar constant. The measured total optical depth is given by

$$\tau(\lambda) = \frac{1}{m(\vartheta_z)} \text{Ln} \left[\frac{E_o(\lambda)}{E(\lambda)} \right] = \frac{1}{m(\vartheta_z)} \text{Ln} \left[\frac{E'_o(\lambda)}{E(\lambda)} \right] + \frac{\text{Ln}[\chi(\lambda)]}{m(\vartheta_z)}, \quad (8)$$

using Eq. (7). The true optical depth would be

$$\tau'(\lambda) = \frac{1}{m(\vartheta_z)} \text{Ln} \left[\frac{E'_o(\lambda)}{E(\lambda)} \right] \quad (9)$$

as follows from Eq. (1). Using Eqs. (8) and (9) the following equation can be calculated

$$\text{Ln}[\chi(\lambda)] = [\tau(\lambda) - \tau'(\lambda)]m(\vartheta_z) \quad (10)$$

relating the error factor $\chi(\lambda)$, to the difference in measured and true total optical depths. The calculated Rayleigh optical depth [Hansen *et al.*, 1974] and the ozone optical depth, computed using ozone profiles provided by Klenk *et al.* [1983], are subtracted from both the measured and true total optical depths. The resulting equation

$$\text{Ln}[\chi(\lambda)] = [\tau_a(\lambda) - \tau'_a(\lambda)]m(\vartheta_z), \quad (11)$$

relates the error factor, $\chi(\lambda)$, to the difference in measured and true aerosol optical depths.

During the calibration process, a sunphotometer reading consisted of recording $E(\lambda)$ for each of the nine wavelengths. The AOD derived from $E(\lambda)$, using $E_o(\lambda)$, was then fit to Eq. (3), determining β and α , and this equation was then used to generate $\tau'_a(\lambda)$ producing the final relation

$$\text{Ln}[\chi(\lambda)] = [\tau_a(\lambda) - \beta\lambda^{-\alpha}]m(\vartheta_z). \quad (12)$$

Therefore, $\text{Ln}[\chi(\lambda)]$, is the difference between the measured AOD and the Angstrom fitted AOD for a given wavelength, times the air mass. This factor determines the variation from the Angstrom power law for that particular measurement.

The AOD, for each location's entire data set, was first calculated using the original solar constants, and the Rayleigh and ozone models cited above. For each day, the deviation of the AOD from the Angstrom power law was determined and used to generate the error factor $\chi(\lambda)$. The error factors calculated during the sunphotometer program were fit by another exponential function, yielding an equation for $\chi(\lambda)$ for each instrument. The resulting error factors were used to correct the solar constants according to Eq. (7). The error-corrected solar constant histories are

plotted in Figs. 1a, 1b, and 1c as the dotted lines. Channels one (380.2 nm) and nine (1025.9 nm) were not processed, and were not used in this paper. The 380.2 nm filter degraded rapidly in all instruments and was considered unusable. Channel nine deviated significantly from the Angstrom power law, perhaps due to the weak water vapor absorption band around 1000 nm [Shaw, 1979] which was not considered in our analysis, or the effects of sea spray [Villevaude *et. al.*, 1994]. These error corrected calibration values are not significantly different from the original values but provide a fine tuning adjustment.

2b. SHADOWBAND DATA PROGRAM AND CALIBRATION

The shadowbands began operation in the fall of 1994. The time periods of the shadowband program are indicated in Table 1. Gaps are present in all data sets due to instrument malfunctions and the subsequent time needed to repair the problems. A gap exists in the Miami data from September 1995 to November 1995. This was caused by data communication problems and poor weather. Normal operation began again in December 1995. The Bermuda data gap, also caused by data communication problems, resulted in the loss of data from July 1995 to November 1995. The communication problems were fixed in December 1995 and shadowband operation was continued. The Barbados shadowband data set only includes data from May 1995 to August 1995 due to poor phone line connections for data transfer and unstable electrical power at the site. These problems have been fixed by new phone line connections to the site and the installation of an uninterruptable power supply (UPS) for the shadowband. Barbados shadowband operation began again after the end of 1995.

All of the shadowbands collect enough data each day to perform two Langley calibrations, one in the morning and one in the afternoon, weather permitting. Therefore all that remains is to determine which of the days has weather suitable for Langley calibrations. Each shadowband's data set was analyzed using the Objective Langley Regression Algorithm (OLRA) [Harrison and Michalsky, 1994] in order to recover the solar constants for each shadowband. The OLRA rejected

a large number of the Langley calibrations for all three sites due to the variable tropical weather at each location. However, this strict criteria assures that the remaining Langley calibrations are accurate. Once the solar constants for each shadowband were determined using this technique, a calibration history was compiled in the same manner as for the sunphotometers. The calibration histories for each shadowband and interpolations are depicted in Figs. 2a, 2b, and 2c. There were few solar constant values recovered for the Barbados shadowband due to the small time period of the data set. Therefore, the solar constants for the Barbados shadowband were obtained by using the mean value of the solar constant for each channel instead of the interpolations described above.

A linear fit to the calibration histories was performed for all of the channels except channel four (610 nm) of the Miami shadowband, and channels four and five (610 and 665 nm respectively) of the Bermuda shadowband. The filters in these channels were found to stabilize after a period of time making a singular linear fit unsuitable. Instead a linear fit was performed on the first part of the calibrations, ignoring the stabilized portion, and a second linear fit was performed on the stabilized portion.

These Langley calibrations were fine tuned with another procedure. This procedure assumes that there is some error, $\mu(\lambda)$, present in the solar constant, but the assumption that the aerosol above the sites obey the Angstrom spectral dependence on average is not necessary. As more measurement samples are recorded by the shadowband than with the sunphotometer it is possible instead to analyze a month's worth of data to test for dependence of the AOD on solar zenith angle. By definition, the set of minimum aerosol optical depths should not depend on solar zenith angle (air mass), over the span of one month. A plot of the AOD versus $m(\vartheta_z)^{-1}$ for a given month should have the lowest AOD's represent a background AOD. A linear fit to the lowest AOD's in the plot described above should have zero slope and a y intercept equal to the average background AOD for that month. A slope not equal to zero would indicate that the background AOD has some dependence on the air mass that may only have been caused by error in the solar constant, $E_o(\lambda)$, [Reference ???, personal correspondence] as detailed below.

Assuming that there is some error, $\mu(\lambda)$, in the solar constants yields the following equation

$$E_o(\lambda) = \mu(\lambda)E'_o(\lambda), \quad (13)$$

where $E_o(\lambda)$ is the previously derived solar constant, $\mu(\lambda)$ is the error factor, and $E'_o(\lambda)$ is the true solar constant. Inserting Eq. (13) into Eq. (1) produces the following relation

$$\tau(\lambda) = \frac{\text{Ln}[\mu(\lambda)]}{m(\vartheta_z)} + \frac{1}{m(\vartheta_z)} \text{Ln}\left[\frac{E'_o(\lambda)}{E(\lambda)}\right] = \frac{\text{Ln}[\mu(\lambda)]}{m(\vartheta_z)} + \tau'(\lambda), \quad (14)$$

$\tau'(\lambda)$ is the true optical depth as it contains the true solar constant, $E'_o(\lambda)$. The Rayleigh and ozone optical depths are not dependent on the calibrations so they may be subtracted from both sides of Eq. (14) to produce the equation

$$\tau_a(\lambda) = \frac{1}{m(\vartheta_z)} \text{Ln}[\mu(\lambda)] + \tau'_a(\lambda). \quad (15)$$

Equation 15 may only be used when both $\tau_a(\lambda)$ and $\tau'_a(\lambda)$ represent the background (minimum) AOD, as other values of $\tau_a(\lambda)$ and $\tau'_a(\lambda)$ may have a dependence on the air mass. Therefore, the slope of the background AOD versus $m(\vartheta_z)^{-1}$ plot described above is the natural logarithm of $\mu(\lambda)$. This procedure may be used to obtain monthly values of $\mu(\lambda)$ for each shadowband channel. The shadowband error corrected solar constants were obtained by first calculating the

solar constant from the linear fit and then using the appropriate month's $\mu(\lambda)$ in Eq. (13). The error corrected solar constants are plotted in Figs. 2a, 2b, and 2c..

3. AOD AND ANGSTROM EXPONENT CALCULATIONS

The final aerosol optical depths and corresponding Angstrom exponents were calculated for Miami, Bermuda, and Barbados using both the sunphotometer and shadowband data. The uncorrected calibration fits and the error corrected calibrations described above were applied to the data sets separately in order to gauge the usefulness of the error correction procedures. Data filtering procedures were then used to remove optical data affected by atmospheric phenomena other than aerosols, such as clouds. Both data filtering procedures were similar, but due to the nature of the instruments, a different filtering procedure was employed for each instrument. The filtering procedures and comparisons between the uncorrected and error corrected results are described below.

3a. SUNPHOTOMETER DATA FILTERING PROCEDURE

The aerosol optical depths and Angstrom exponents were only calculated for channels two to eight, for the respective data sets, due to the calibration problems with channels one and nine. The sunphotometer data filter contained three levels. Level one determined the deviation of the measured $\tau_a(\lambda)$ from the power law fitted $\tau'_a(\lambda)$ for a given measurement, similar to the error factor procedure above. If the magnitude of the deviation between $\tau_a(\lambda)$ and $\tau'_a(\lambda)$ was greater than 0.1, then the measured AOD at that wavelength was rejected. This was done to screen out AOD measurements that did not resemble an Angstrom power law. The aerosol optical depths that survived this filter were then subjected to level two of the filter. It should be noted that a given measurement consists of two series of readings, $E(\lambda)$, for each of the nine channels. This was

done to ensure that the atmosphere was stable during the measurement, as the optical depth should not change appreciably during a span of five minutes (the approximate time for one measurement). The level two filter examined the difference between the first and second measured aerosol optical depths. If the magnitude of the difference was greater than 0.03, then that channel was rejected. If only one of the two dual readings survived the level one filter, then the level two filter was not performed. Finally, the level three filter determines if at least six of the seven channels (one and nine are excluded) remain, and channels two and eight are among them. If this was true then this measurement was considered usable, else the entire measurement was discarded. The tolerance settings in the filter were the result of a trade off between eliminating questionable data, and retaining enough of the data set to analyze. This filter process ensures that the atmosphere is fairly stable, the AOD roughly resembles an Angstrom power law formula, and there are enough remaining aerosol optical depths to accurately perform a fit to the Angstrom power law (for the wavelength range, 412.2 nm to 861.8 nm only). The AOD was then calculated for the surviving measurements, and used to generate Angstrom parameters from equation 3. These surviving measurements were recorded as the optical properties for that sample.

3b. SHADOWBAND DATA FILTERING PROCEDURE

The shadowbands record data throughout the day, as opposed to the sunphotometer's singular morning and afternoon measurements. Therefore, another method of filtering out bad data was employed. The filtering procedure used for the shadowband data was based on the Sliding Window Optical Depth Procedure (SWODP) [*Jim Schlemmer, personal correspondence*] developed at the Atmospheric Sciences Research Center at the State University of New York, Albany.

The University of Miami SWODP (MSWODP) used the aerosol optical depths for each sampled measurement by the shadowband. The MSWODP then analyzed one day at a time, starting with the first measurement sample. The term, "sliding window," originated because the

MSWODP analyzed a twenty minute “window” of data to determine if the window contained usable data. Three filtering levels were then applied to the resulting AOD window by the MSWODP. The first filter performed a linear least squares fit to the AOD, and then calculated the individual AOD deviations from the fit. If all of the aerosol optical depths were within 0.01 of the linear fit then the MSWODP continued on to the next filter level for that window. If the first filter test failed then the MSWODP slid the window ahead one sample measurement and applied the filter again to the new window. If the filter one test was successful then the MSWODP applied filter two. This filter level determined the mean AOD for that window. If the mean AOD was less than 1.0 then the MSWODP recorded the mean AOD and corresponding Angstrom exponent for that window. If the mean AOD was greater than or equal to 1.0 then the entire window was rejected, and no data was recorded for that window of time. Regardless of the outcome of the filter two check, the MSWODP then slid the window ahead by twenty minutes to the corresponding sample measurement, and the process was started over again from the level one filter. The MSWODP output twenty minute averages of the AOD, and the corresponding Angstrom parameters from equation 3, for each day in the data set. Each twenty minute window of data output by the MSWODP contained aerosol optical depths that did not vary too wildly and that had AOD values reasonable for atmospheric aerosol, not clouds. The surviving measurements were recorded as the optical properties for the time of day falling at the center of the window.

3c. COMPARISON OF UNCORRECTED AND ERROR CORRECTED RESULTS

The spectral variation of the aerosol optical depths for each channel of each sunphotometer and shadowband are shown in Figs. 3a, 3b, and 3c. Each figure displays the entire data set’s uncorrected and error corrected AOD results for the sunphotometers and shadowbands.

The uncorrected sunphotometer results are not much different from the error corrected results, indicating that the data was not changed significantly by the error correction procedure. However, an improvement to the Angstrom power law fit was obtained using the error corrected

sunphotometer results. The average chi-squared data fitting parameter was reduced for each data set, indicating a better power law fit. The Miami chi-squared data fitting parameter was 0.086 for the uncorrected results and 0.034 for the error corrected results. The Bermuda uncorrected and error corrected chi-squared parameters were 0.065 and 0.012 respectively. Finally, the Barbados uncorrected and error corrected chi-squared parameters were 0.744 and 0.058. The sunphotometer error correction procedure assumes that the true AOD follows the Angstrom power law. Furthermore, the sunphotometer data filter explicitly screened out days (for both uncorrected and error corrected results) that did not accurately fit the Angstrom power law. For these two reasons, a small improvement in the fits to the Angstrom power law between uncorrected and error corrected results was expected.

There were significant differences between the uncorrected and error corrected results for certain channels of each shadowband. However, all of the error corrected changes also resulted in a better average Angstrom power law fit. In particular, the clear bias in channel five of the Miami shadowband was removed after using the shadowband error correction procedure. The Miami chi-squared data fitting parameter was 0.521 for the uncorrected results and 0.122 for the error corrected results. The Bermuda uncorrected and error corrected chi-squared parameters were 0.300 and 0.131 respectively. Finally, the Barbados uncorrected and error corrected chi-squared parameters were 0.071 and 0.059. The shadowband error correction procedure and the shadowband data filter did not assume any particular spectral form of the AOD. However, results obtained using the error corrected results more accurately portrayed a power law fit compared to the uncorrected results.

Level one of the sunphotometer data filter determined the deviation of the measured AOD from the Angstrom power law. Turning off levels two and three of the sunphotometer data filter allowed the percentage of measurements rejected by only level one to be determined. The level one sunphotometer data filter rejected 3% of the Barbados measurements and 7% of the Miami and Bermuda measurements. Therefore, at all three locations, over 90% of the sunphotometer AOD measurements resembled an Angstrom power law. Also, there were significant improvements in

the Angstrom power law fits using the error corrected shadowband results compared to using the uncorrected shadowband data. This improvement indicates that the majority of shadowband AOD measurements also resembled an Angstrom power law, particularly since no spectral dependence of the AOD was assumed but the error corrected data more accurately fit the Angstrom power law. As a result of this analysis, the majority of the aerosol optical depths measured over Miami, Bermuda, and Barbados were found to accurately depict an Angstrom power law in the wavelength range 400 nm to 860 nm.

4. FINAL RESULTS AND CONCLUSION

The sunphotometer and shadowband results, obtained using the filtering procedures of the previous section, were merged together and monthly mean values of both the AOD at 500 nm and the corresponding Angstrom exponent were recorded. This was accomplished for each measurement site. The monthly mean values for Miami, Bermuda, and Barbados are depicted graphically in Figs. 4a, 4b, and 4c. Table 3 contains the monthly mean values mentioned above and the Angstrom scale factor, β , for each measurement site, as well as the total mean values.

Seasonal variability of the AOD existed for each site. Peaks in the Miami AOD occurred primarily during the May to June periods. The Barbados AOD results also indicated clear peaks from the May to August periods. The Bermuda AOD results were not as obvious, however, elevated AOD values were found during the April to June periods. Each site also has shown minimum AOD levels during the winter months. This pattern of seasonal variability in the AOD has been documented previously [*Malm et. al.*, 1994; *Smirnov et. al.*, 1995; *Husar et. al.*, Submitted *JGR* 1996]. Seasonal trends in the Angstrom exponents were not easy to deduce from the monthly mean values as the exponents vary widely from day to day, due not only to changing aerosol types but also to changing meteorological conditions. However, the Miami and Bermuda exponents did show a tendency to drop during the summer months, relative to levels during the spring and early

fall. Barbados exponents also have shown a tendency to drop relative to surrounding months, but during April to June 1994 and the summer of 1995. These seasonal trends in the optical properties for each site are due in large part to the origin [Smirnov *et. al.*, 1995] and seasonal variability in the type and concentration of the major aerosol species found at each site [Welton *et. al.*, 1997].

The high degree to which the aerosols at each site could be characterized by the Angstrom power law was greater than expected. If there had not been a strong AOD power law dependence on average, the shadowband error correction procedure would not have correlated as well with the sunphotometer results. The spectral variation of the AOD is an important parameter in determining the atmospheric path radiance, used primarily in remote sensing applications. Kaufman [1993] has shown that the path radiance over land can be derived more accurately using aerosol optical depths derived from an average Angstrom exponent rather than individual measurement exponents, except for conditions dominated by dust. The tendency of our maritime aerosol optical depth results to fit the Angstrom power law on average indicates that it may be possible to use the same condition to generate the path radiance over the ocean. Due to the sharp difference between the spectral dependence of dust dominated AOD and that of other maritime aerosols [Binenko *et. al.*, 1993; Welton *et. al.*, 1997], it is also possible that the same exclusion conditions apply to the calculation of the maritime path radiance during dusty periods.

Further analysis of the aerosol optical depth and Angstrom parameter results must take into account individual aerosol types and concentrations, as well as seasonal trends in the aerosol's transport from their points of origin. Analysis of this type may be added to the results contained in this paper to produce a characteristic description of the aerosol over a particular site. Long term data records of these aerosol properties over several different sites will also help track trends in global climate change. The measurement programs described in this paper will continue until the end of the AEROCE program (DATE??) in order to extend the data sets presented above. In addition, two more shadowbands have been installed in Tenerife, located in the Canary Islands. One is located at the mountain top weather station at Izana, a long time AEROCE site, and the other is located in La Laguna, at sea level. The Tenerife shadowbands will produce optical data close to

the primary source of north Atlantic ocean dust, the Saharan desert [*Prospero, 1995*]. Also, they will allow the comparison of optical properties taken below the aerosol boundary layer to those taken above it, as the boundary layer often lies between Izana and sea level [reference]. Finally, specific correlations between aerosol types, concentrations and optical properties are the subject of another paper by the authors [*Welton et. al., 1997*].

REFERENCES

- Angstrom, A., The Parameters of Atmospheric Turbidity, *Tellus*, 16, 64-75, 1964.
- Binenko, V.I., and H. Harshvardhan, Aerosol Effects in Radiation Transfer, Chapter in *Aerosol Effects on Climate*, Univ. of Arizona Press, Tucson, Arizona, 1993.
- Charlson, R.J., S.E. Schwartz, J.M. Hales, R.D. Cess, J.A. Coakley Jr., J.E. Hansen, D.J. Hofmann, Climate Forcing by Anthropogenic Aerosols, *Science*, 255, 423-430, 1992.
- Hansen, J.E., and L.D. Travis, Light Scattering in Planetary Atmospheres, *Space Sci. Reviews*, 16, 527-610, 1974.
- Harrison, L., J. Michalsky, and J. Berndt, The Automated Multi-Filter Rotating Shadow-band Radiometer: An Instrument for Optical Depth and Radiation Measurements, *Appl. Optics*, 33, 5118-5125, 1994.
- Harrison, L., and J. Michalsky, Objective Algorithms for the Retrieval of Optical Depths From Ground-Based Measurements, *Appl. Optics*, 33, 5126-5132, 1994.
- Husar, R.B., L. Stowe, and J. Prospero, Satellite Sensing of Tropospheric Aerosols Over the Oceans with NOAA AVHRR, *Submitted to J. Geophys. Res.*, 1996.
- Kasten, F., and A.T. Young, Revised optical air mass tables and approximation formula, *Appl. Optics*, 28, 4735-4738, 1989.
- Kaufman, Y.J., Aerosol Optical Thickness and Atmospheric Path Radiance, *J. Geophys. Res.*, 98, 2677-2692, 1993.
- King, M., D. Byrne, J. Reagan, and B. Herman, Spectral Variation of Optical Depth at Tucson Arizona Between August 1975 and December 1977, *J. Appl. Meteorol.*, 19, 16,639-16,650, 1980.
- Klenk, K., P. Bhartia, E. Hilsenrath, and A. Fleig, Standard Ozone Profiles From Balloon and Satellite Data Sets, *J. Clim. Appl. Meteorol.*, 22, 2012-2022, 1983.
- Malm, W.C., J. Sisler, D. Huffman, R. Eldred, and T. Cahill, Spatial and Seasonal Trends in Particle Concentration and Optical Extinction in the United States, *J. Geophys. Res.*, 99, 1347-1370, 1994.
- Prospero, J.M., Saharan Dust Transport Over The North Atlantic Ocean and Mediterranean, Chapter in *The Impact of Desert Dust From Northern Africa Across the Mediterranean*, Kluwer Academic Publishers, Oristano, Sardinia, 1995.
- Shaw, G., Aerosols at Mauna Loa: Optical Properties, *J. Atmos. Sci.*, 36, 862-869, 1979.
- Shaw, G., Sun Photometry, *Bulletin American Meteorol. Soc.*, 64, 4-9, 1983.
- Smirnov, A., Y. Villevalde, N. O'Neill, A. Royer, and A. Tarussov, Aerosol Optical Depth Over the Oceans: Analysis in Terms of Synoptic Air Mass Types, *J. Geophys. Res.*, 100, 16639-16650, 1995.
- Van de Hulst, H. C., *Light Scattering by Small Particles*, Dover Publications Inc., New York, NY, 1981.
- Villevalde, Y.V., A.V. Smirnov, N.T. O'Neill, S.P. Smyshlyaev, and V.V. Yakovlev, Measurement of aerosol optical depth in the Pacific Ocean and the North Atlantic, *J. Geophys. Res.*, 99, 20983-20988, 1994.
- Welton, E.J., K.J. Voss, and J.M. Prospero, Radiative Characteristics of Specific Types and Concentrations of Maritime Aerosols, *Submitted to J. Geophys. Res.*, 1997.
- Gordon, H.R., Ocean Color Correction reference.....
- AEROCE Reference.....
- Personal Correspondence: Background AOD Dependence on 1/airmass.....
- Personal Correspondence: Jim Schlemmer, Sliding Window Reference.....
- Reference for Tenerife boundary layer, etc.....

Table 1. Instrumentation Location Information

Location	Latitude	Longitude	Altitude	Sunphotometer Time Period	Shadowband Time Period
Miami, FL	25.75	80.2	Sea Level	Aug93 to Nov94	May94 to Dec95
Barbados	13.18	59.43	Sea Level	Aug93 to Sep94	Jul94 to Dec95
Bermuda	32.38	64.70	Sea Level	Aug93 to Nov94	Nov94 to Dec95

Table 2. Instrument Channel Numbers and Filter Wavelengths (nm)

Channel Number	Sunphotometer Wavelength (nm)	Shadowband Wavelength (nm)
1	380.2	Broadband
2	412.2	410
3	440.5	500
4	501.8	610
5	551.2	665
6	675.2	860
7	777.9	940
8	861.8	-
9	1025.9	-

TABLE 3a: Miami Monthly Mean Aerosol Optical Depths and Angstrom Parameters (Aug93 to Dec95)

Number of samples

Month-Year	$\bar{\tau}_{a_{500}}$	σ_{τ}	$\bar{\beta}$	σ_{β}	$\bar{\alpha}$	σ_{α}
Aug-93	-	-	-	-	-	-
Sep-93	0.114	0.024	0.070	0.022	0.734	0.228
Oct-93	0.142	0.068	0.069	0.020	0.976	0.374
Nov-93	0.142	0.020	0.080	0.011	0.833	0.001
Dec-93	0.121	0.034	0.050	0.013	1.269	0.056
Jan-94	0.121	0.030	0.071	0.005	0.740	0.398
Feb-94	0.120	0.035	0.083	0.035	0.566	0.375
Mar-94	0.151	0.073	0.069	0.030	1.063	0.240
Apr-94	0.166	0.038	0.104	0.035	0.706	0.553
May-94	0.243	0.091	0.111	0.033	1.098	0.319
Jun-94	0.163	0.058	0.128	0.057	0.217	0.457
Jul-94	0.234	0.055	0.209	0.034	0.148	0.100
Aug-94	0.075	0.013	0.059	0.011	0.347	0.319
Sep-94	0.127	0.058	0.079	0.026	0.524	0.773
Oct-94	0.119	0.054	0.056	0.027	0.987	0.509
Nov-94	0.093	0.039	0.049	0.014	0.762	0.713
Dec-94	0.097	0.041	0.093	0.019	-0.246	0.820
Jan-95	0.091	0.032	0.059	0.017	0.443	0.579
Feb-95	0.115	0.049	0.062	0.024	0.846	0.501
Mar-95	0.118	0.020	0.065	0.010	0.768	0.284
Apr-95	0.143	0.037	0.094	0.019	0.480	0.311
May-95	0.288	0.078	0.108	0.023	1.294	0.199
Jun-95	-	-	-	-	-	-
Jul-95	0.165	0.053	0.103	0.030	0.494	0.565
Aug-95	0.148	0.077	0.100	0.043	0.347	0.557
Sep-95	-	-	-	-	-	-
Oct-95	-	-	-	-	-	-
Nov-95	-	-	-	-	-	-
Dec-95	0.099	0.032	0.045	0.016	1.110	0.565
Total	0.141	0.050	0.084	0.034	0.684	0.367

TABLE 3b: Bermuda Monthly Mean Aerosol Optical Depths and Angstrom Parameters (Aug93 to Dec95)

Number of samples

Month-Year	$\bar{\tau}_{a_{500}}$	σ_{τ}	$\bar{\beta}$	σ_{β}	$\bar{\alpha}$	σ_{α}
Aug-93	-	-	-	-	-	-
Sep-93	0.161	0.043	0.104	0.015	0.603	0.290
Oct-93	0.161	0.041	0.103	0.020	0.622	0.232
Nov-93	0.117	0.025	0.081	0.018	0.540	0.214
Dec-93	0.160	0.037	0.102	0.009	0.614	0.304
Jan-94	0.099	0.012	0.069	0.011	0.531	0.298
Feb-94	0.102	0.023	0.079	0.005	0.322	0.372
Mar-94	0.157	0.041	0.099	0.026	0.666	0.268
Apr-94	0.169	0.050	0.105	0.022	0.667	0.415
May-94	0.134	0.047	0.085	0.030	0.655	0.259
Jun-94	0.270	0.125	0.170	0.072	0.599	0.233
Jul-94	0.116	0.072	0.081	0.045	0.474	0.179
Aug-94	0.126	0.131	0.097	0.125	0.424	0.334
Sep-94	0.100	0.061	0.049	0.035	1.058	0.746
Oct-94	0.075	0.041	0.060	0.015	0.288	0.663
Nov-94	0.068	0.021	0.077	0.016	-0.209	0.351
Dec-94	0.064	0.028	0.085	0.033	-0.920	0.973
Jan-95	0.081	0.035	0.075	0.023	-0.236	0.817
Feb-95	0.104	0.027	0.059	0.025	0.697	0.616
Mar-95	0.091	0.050	0.068	0.023	0.108	0.416
Apr-95	0.172	0.077	0.095	0.034	0.818	0.187
May-95	0.168	0.057	0.088	0.030	0.851	0.318
Jun-95	0.134	0.069	0.072	0.024	0.558	0.659
Jul-95	-	-	-	-	-	-
Aug-95	-	-	-	-	-	-
Sep-95	-	-	-	-	-	-
Oct-95	-	-	-	-	-	-
Nov-95	-	-	-	-	-	-
Dec-95	-	-	-	-	-	-
Total	0.129	0.047	0.086	0.025	0.442	0.433

TABLE 3c: Barbados Monthly Mean Aerosol Optical Depths and Angstrom Parameters (Aug93 to Dec95)

Number of samples

Month-Year	$\bar{\tau}_{a_{500}}$	σ_{τ}	$\bar{\beta}$	σ_{β}	$\bar{\alpha}$	σ_{α}
Aug-93	-	-	-	-	-	-
Sep-93	-	-	-	-	-	-
Oct-93	0.078	0.033	0.059	0.029	0.442	0.166
Nov-93	0.072	0.019	0.055	0.021	0.483	0.256
Dec-93	0.064	0.006	0.051	0.015	0.360	0.322
Jan-94	0.084	0.029	0.071	0.022	0.262	0.180
Feb-94	0.129	0.057	0.097	0.055	0.508	0.446
Mar-94	0.078	0.058	0.064	0.056	0.605	0.674
Apr-94	0.184	0.157	0.167	0.156	0.275	0.245
May-94	0.201	0.151	0.167	0.102	0.256	0.245
Jun-94	0.247	0.095	0.224	0.084	0.148	0.139
Jul-94	0.362	0.128	0.267	0.111	0.504	0.225
Aug-94	0.210	0.067	0.132	0.055	0.731	0.211
Sep-94	0.169	0.090	0.118	0.076	0.640	0.287
Oct-94	-	-	-	-	-	-
Nov-94	-	-	-	-	-	-
Dec-94	-	-	-	-	-	-
Jan-95	-	-	-	-	-	-
Feb-95	-	-	-	-	-	-
Mar-95	-	-	-	-	-	-
Apr-95	-	-	-	-	-	-
May-95	-	-	-	-	-	-
Jun-95	0.257	0.107	0.260	0.108	0.014	0.059
Jul-95	0.144	0.060	0.147	0.063	0.047	0.187
Aug-95	0.200	-	0.176	-	0.138	-
Sep-95	-	-	-	-	-	-
Oct-95	-	-	-	-	-	-
Nov-95	-	-	-	-	-	-
Dec-95	-	-	-	-	-	-
Total	0.165	0.085	0.137	0.073	0.361	0.220

Figure 1a.

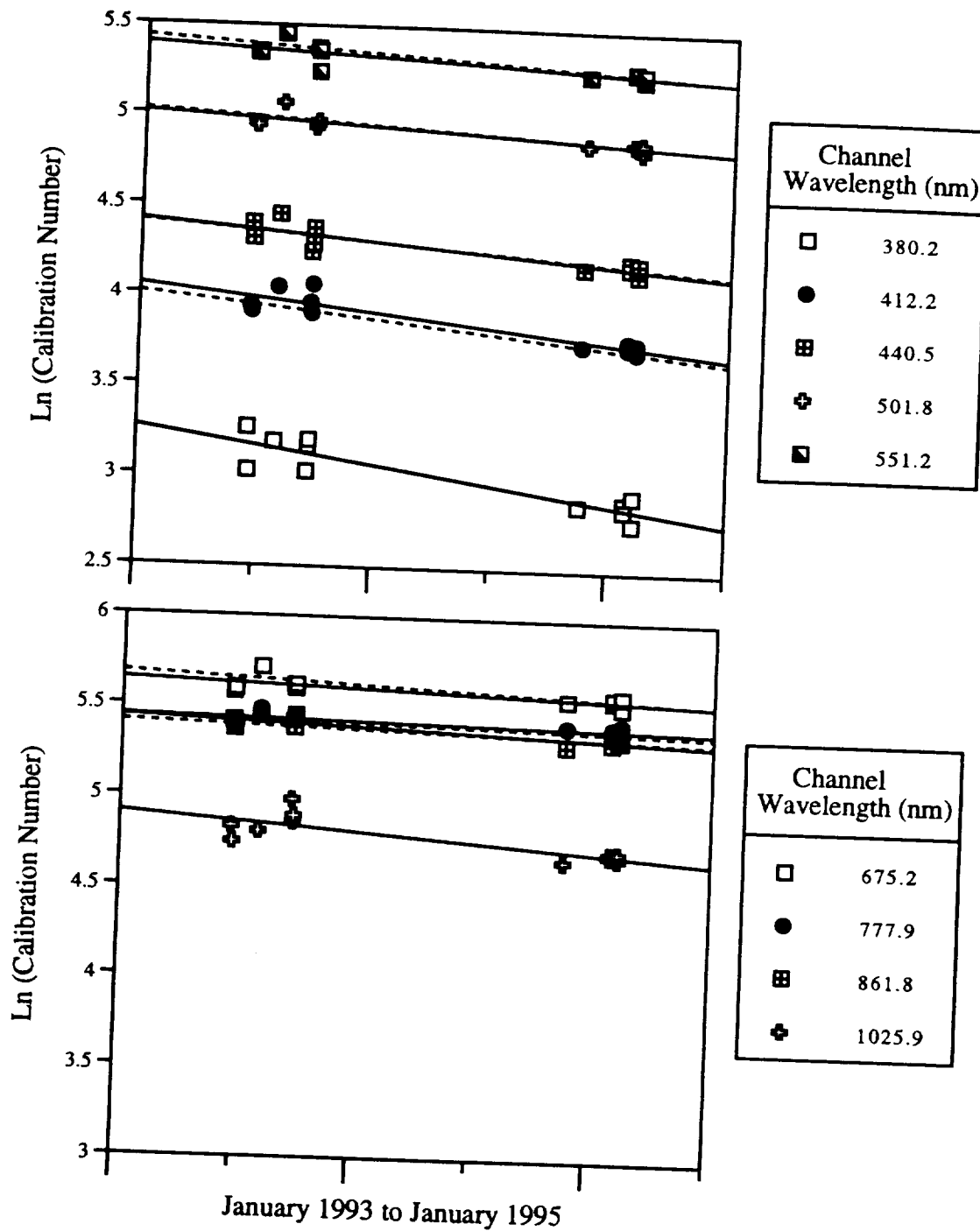


Figure 1a. Calibration history for the Miami sunphotometer. The solid line is the exponential fit to the Langley and cross-calibrations. The dotted line is the exponential fit to the error corrected Langley and cross-calibrations.

Figure 1b.

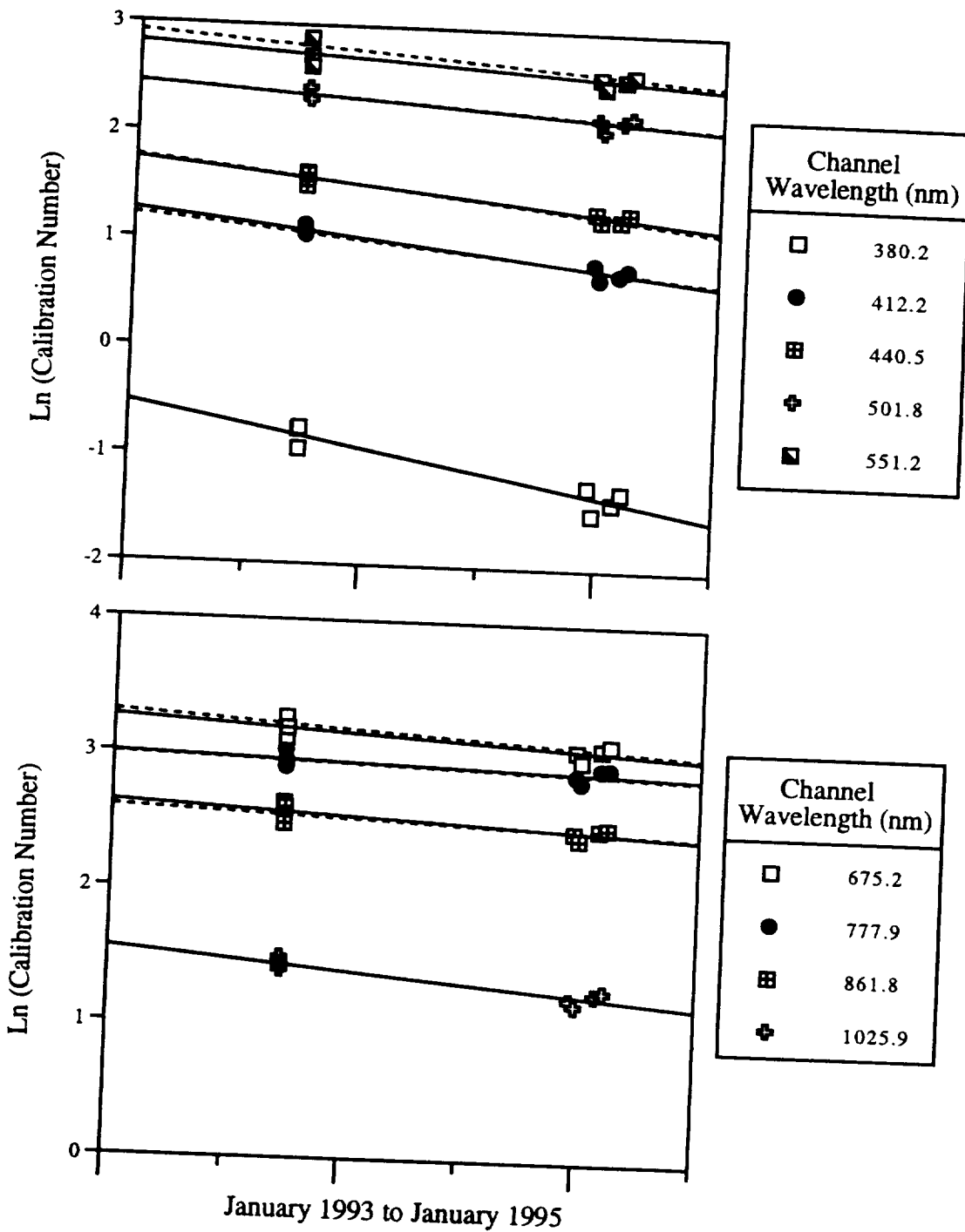


Figure 1b. Calibration history for the Barbados sunphotometer. The solid line is the exponential fit to the Langley and cross-calibrations. The dotted line is the exponential fit to the error corrected Langley and cross-calibrations.

Figure 1c.

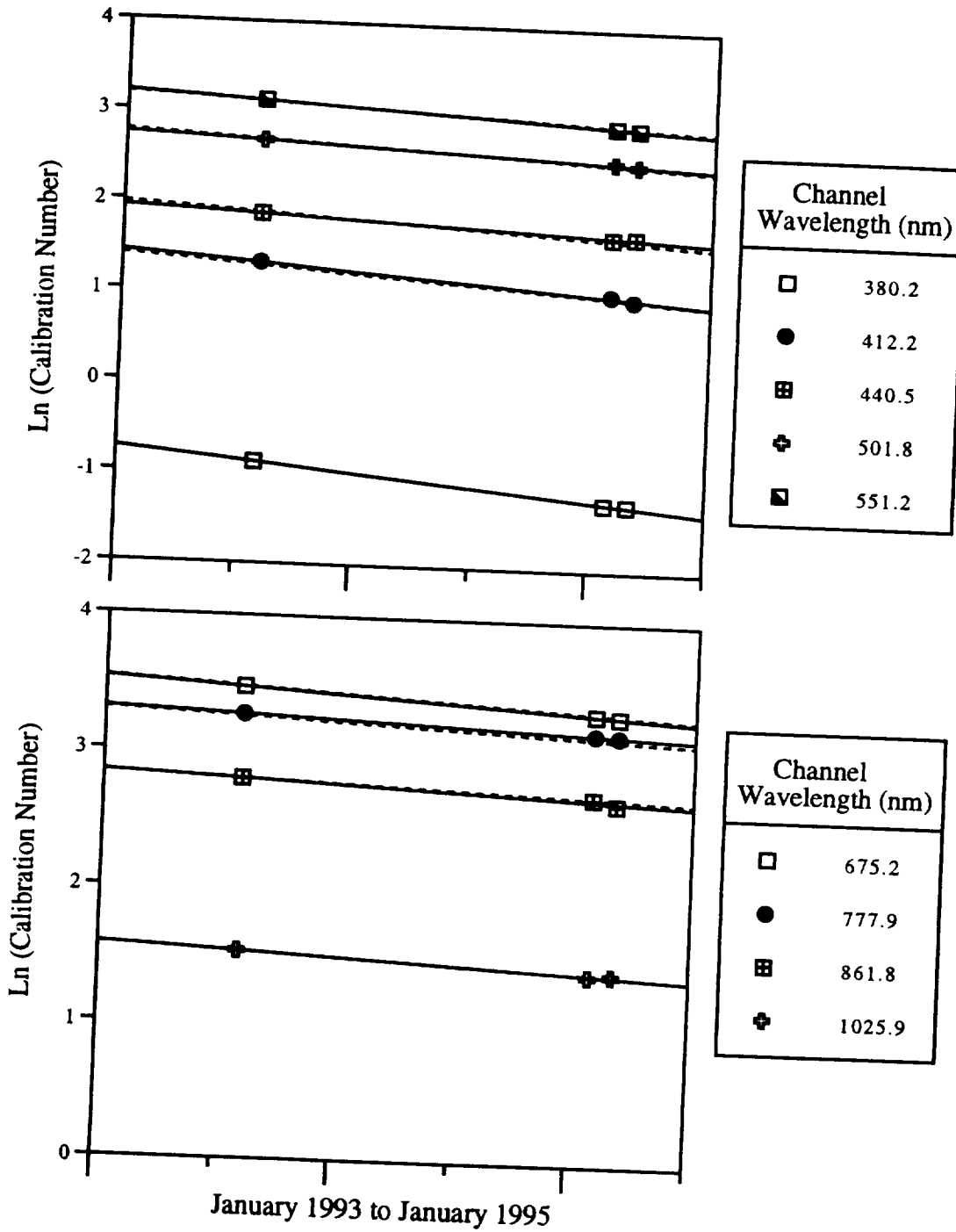


Figure 1c. Calibration history for the Bermuda sunphotometer. The solid line is the exponential fit to the Langleys and cross-calibrations. The dotted line is the exponential fit to the error corrected Langleys and cross-calibrations.

Figure 2a

Miami Shadowband Calibration History: May94 to Dec95

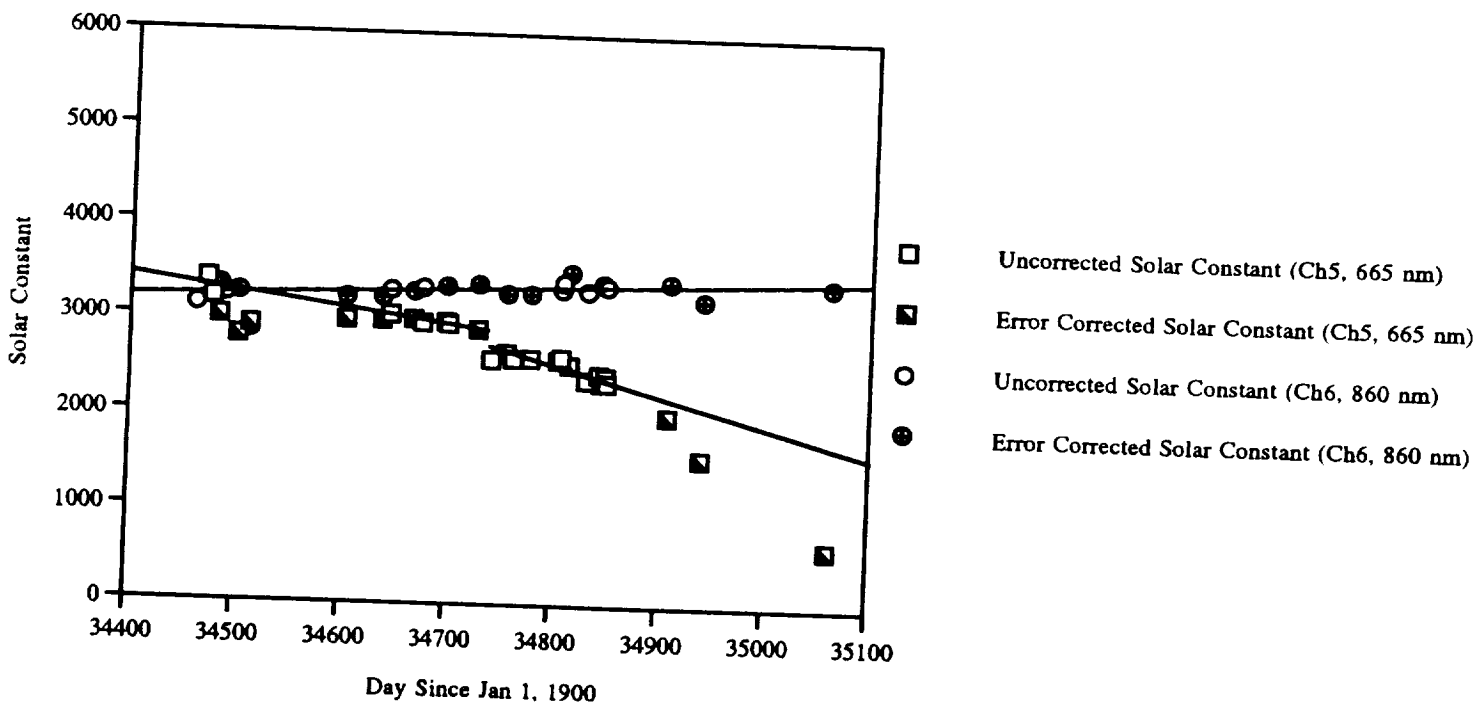
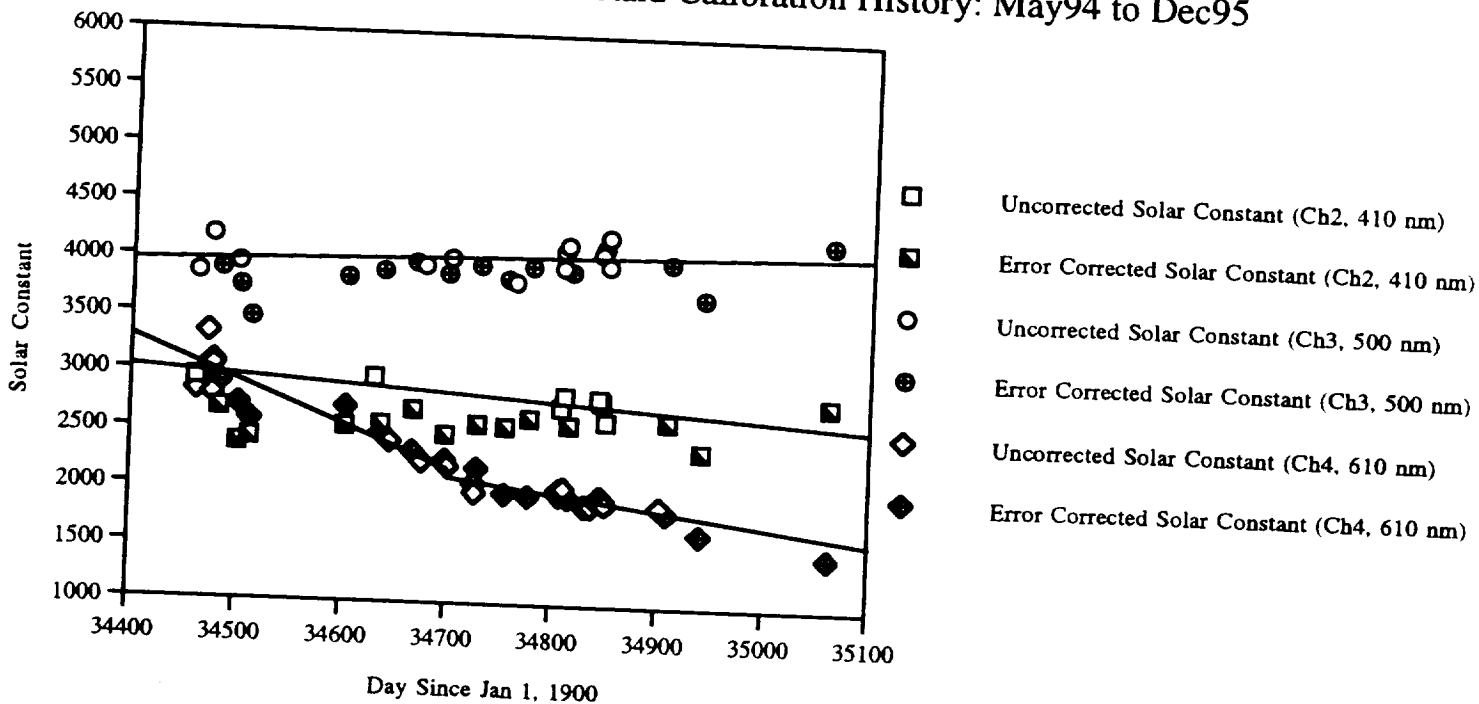


Figure 2b

Bermuda Shadowband Calibration History: May94 to Dec95

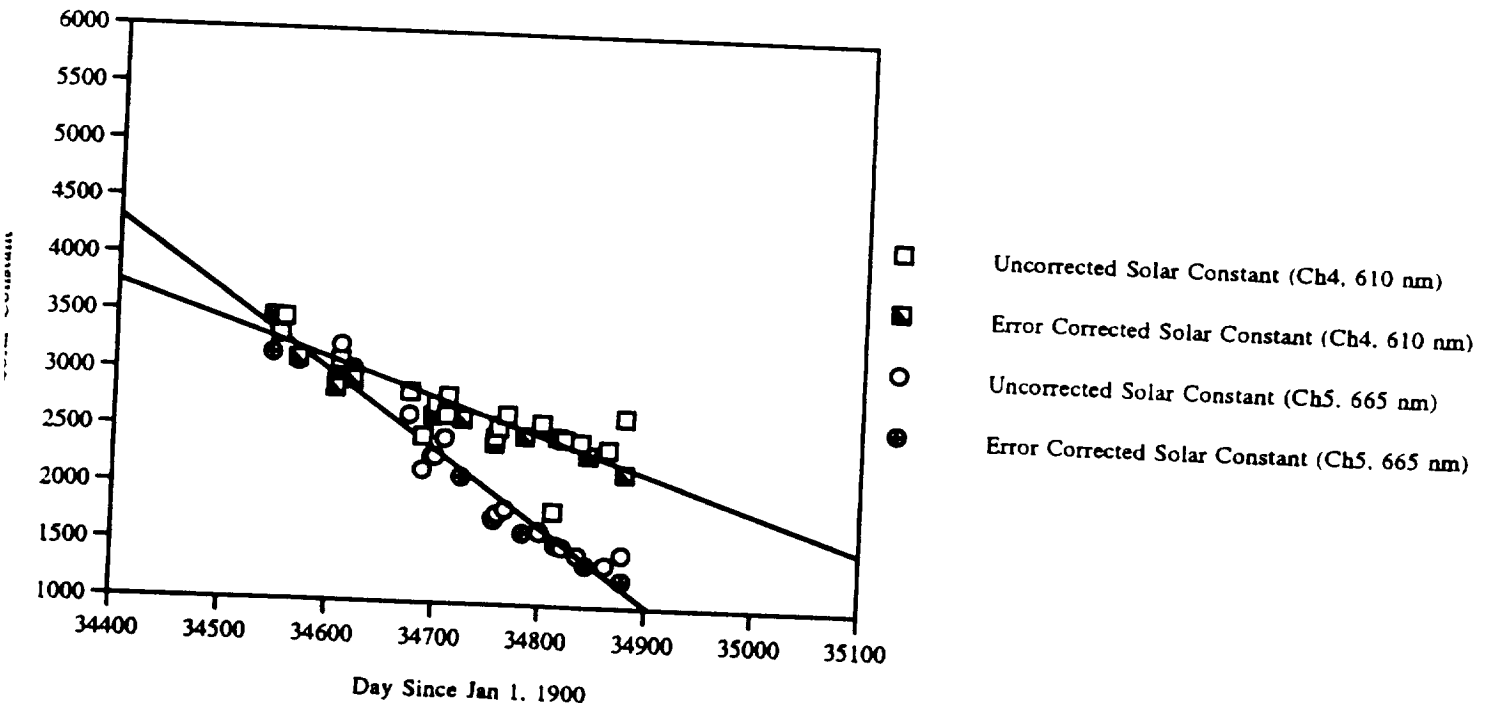
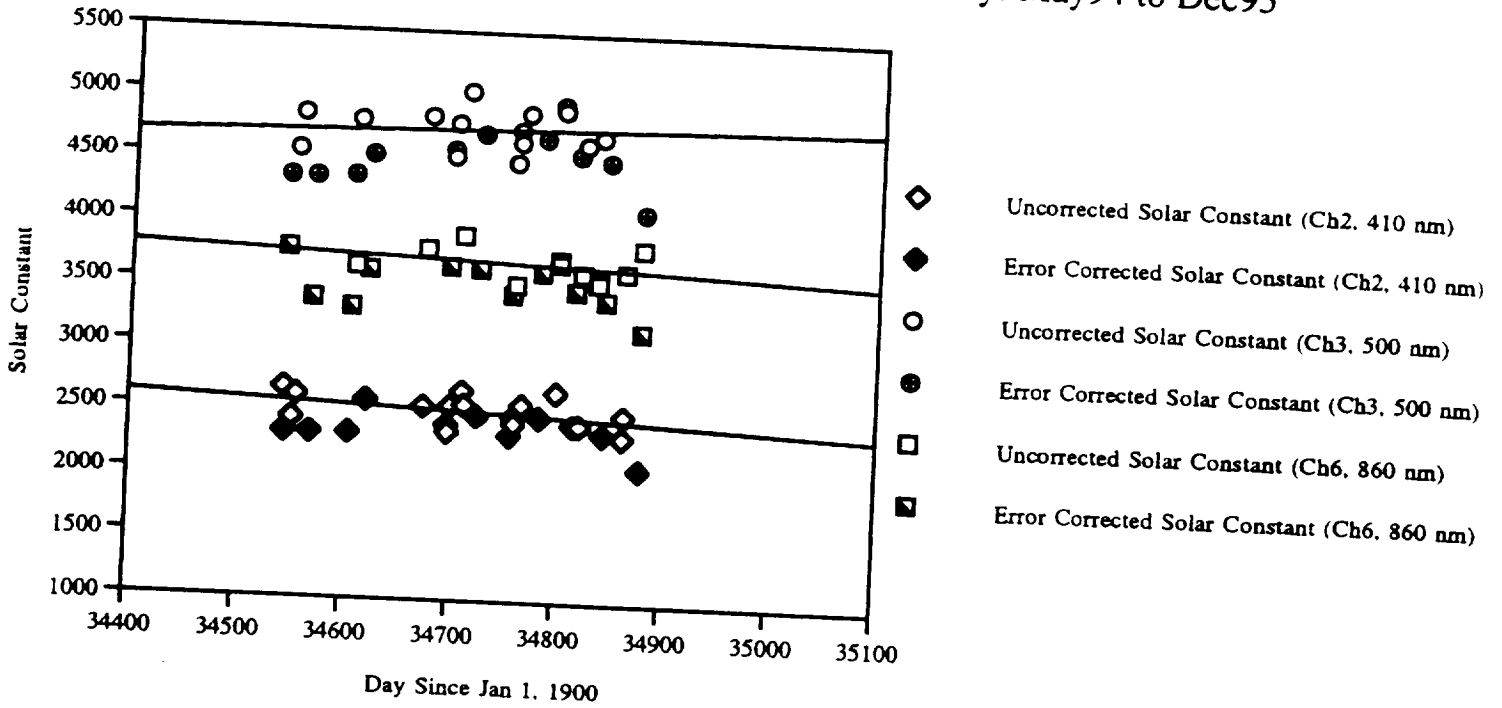


Figure 2c

Barbados Shadowband Calibration History: Jun95 to Aug95

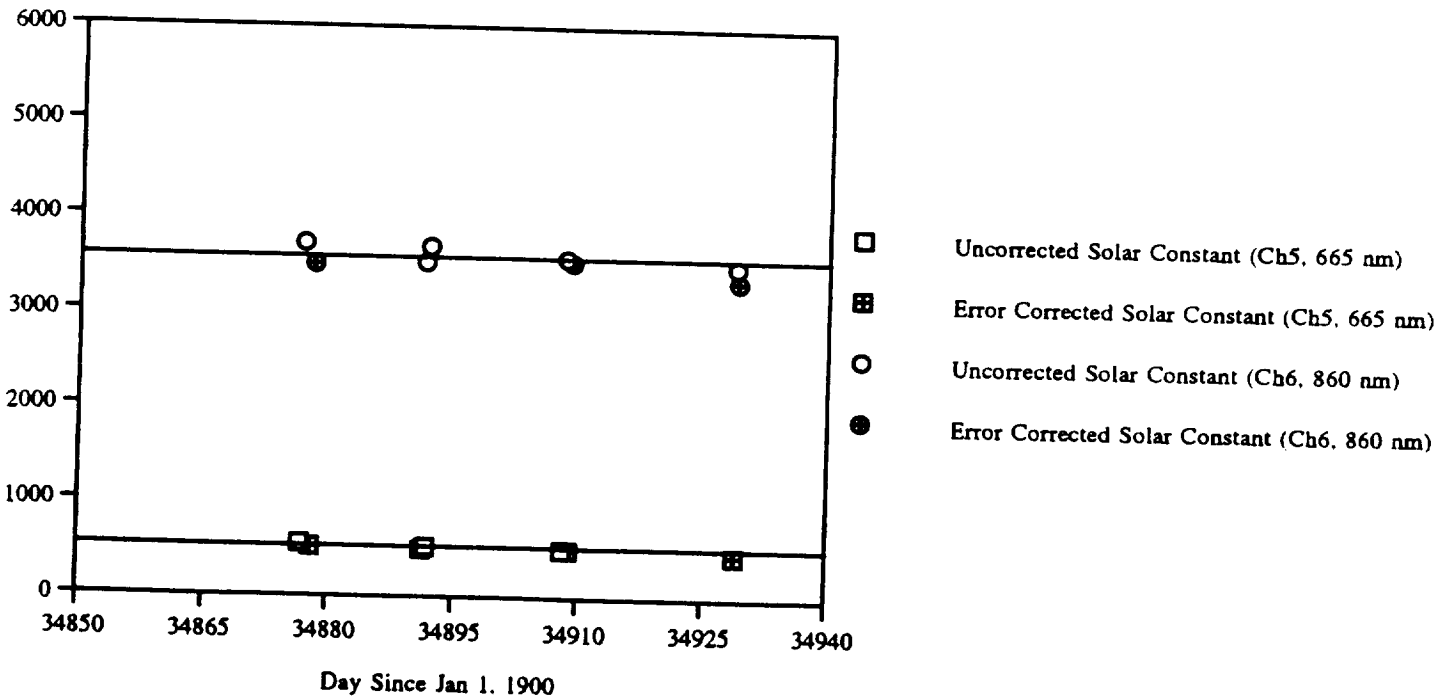
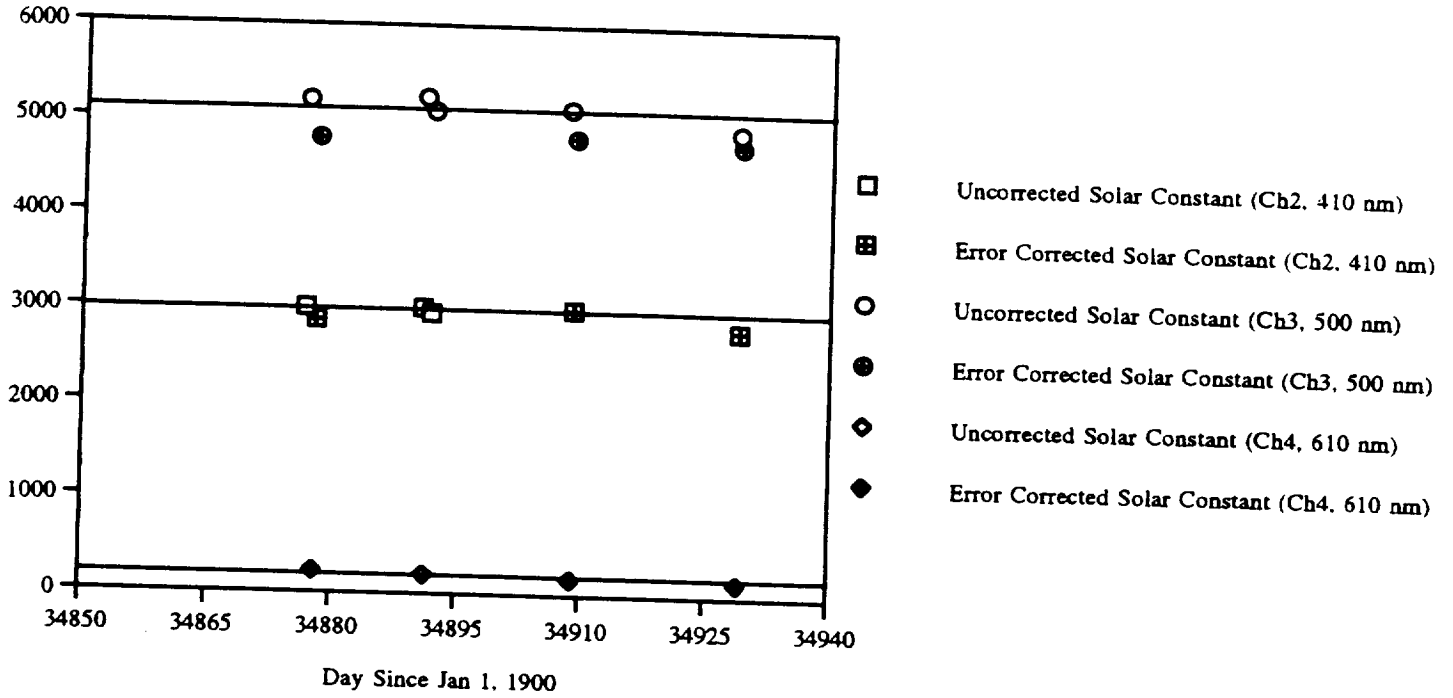
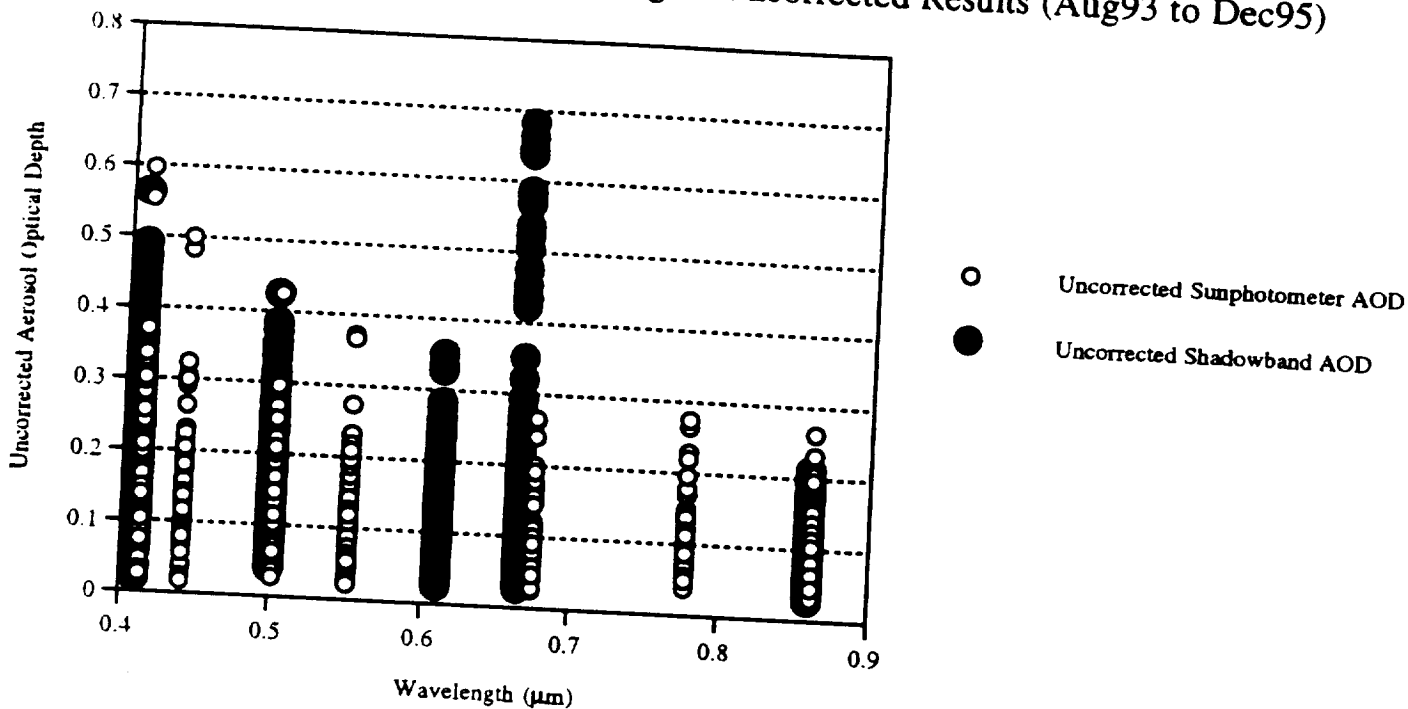


Figure 3a

Miami AOD vs. Wavelength: Uncorrected Results (Aug93 to Dec95)



Miami AOD vs. Wavelength: Error Corrected Results (Aug93 to Dec95)

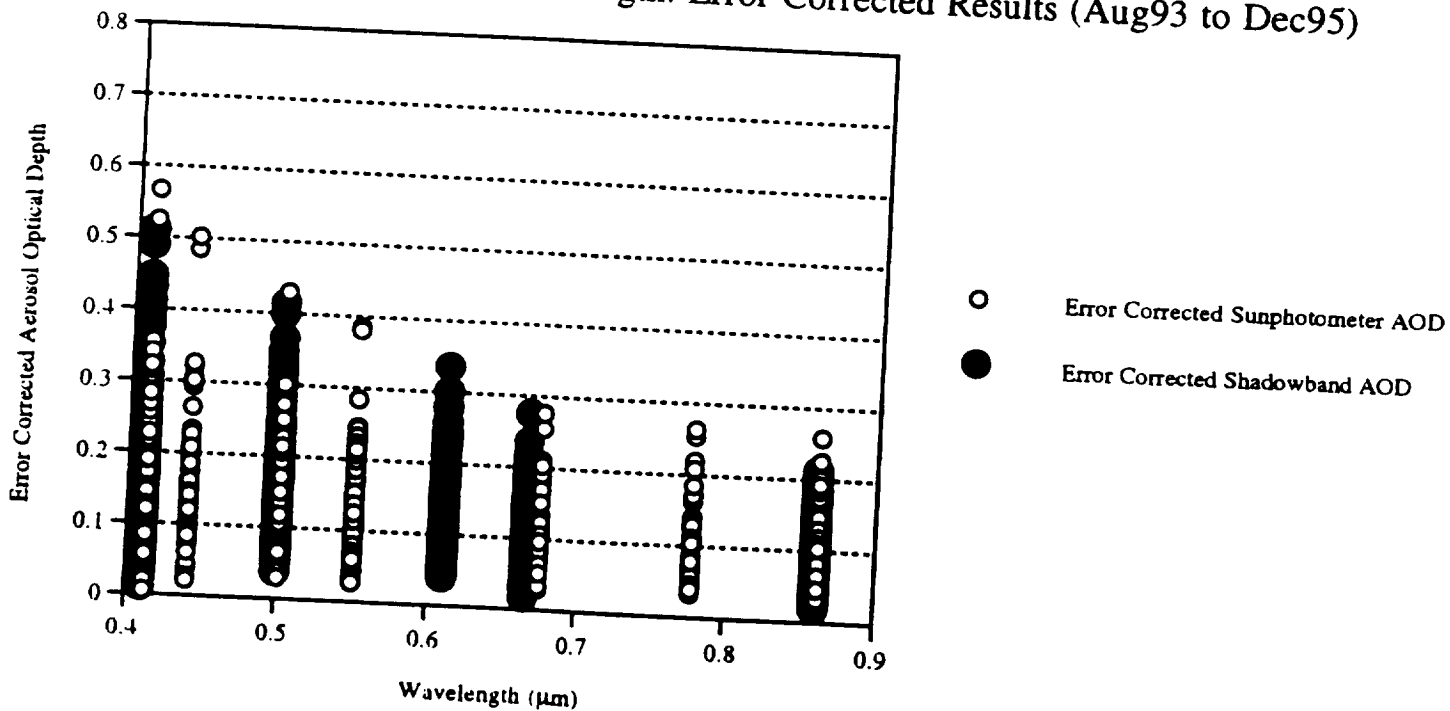
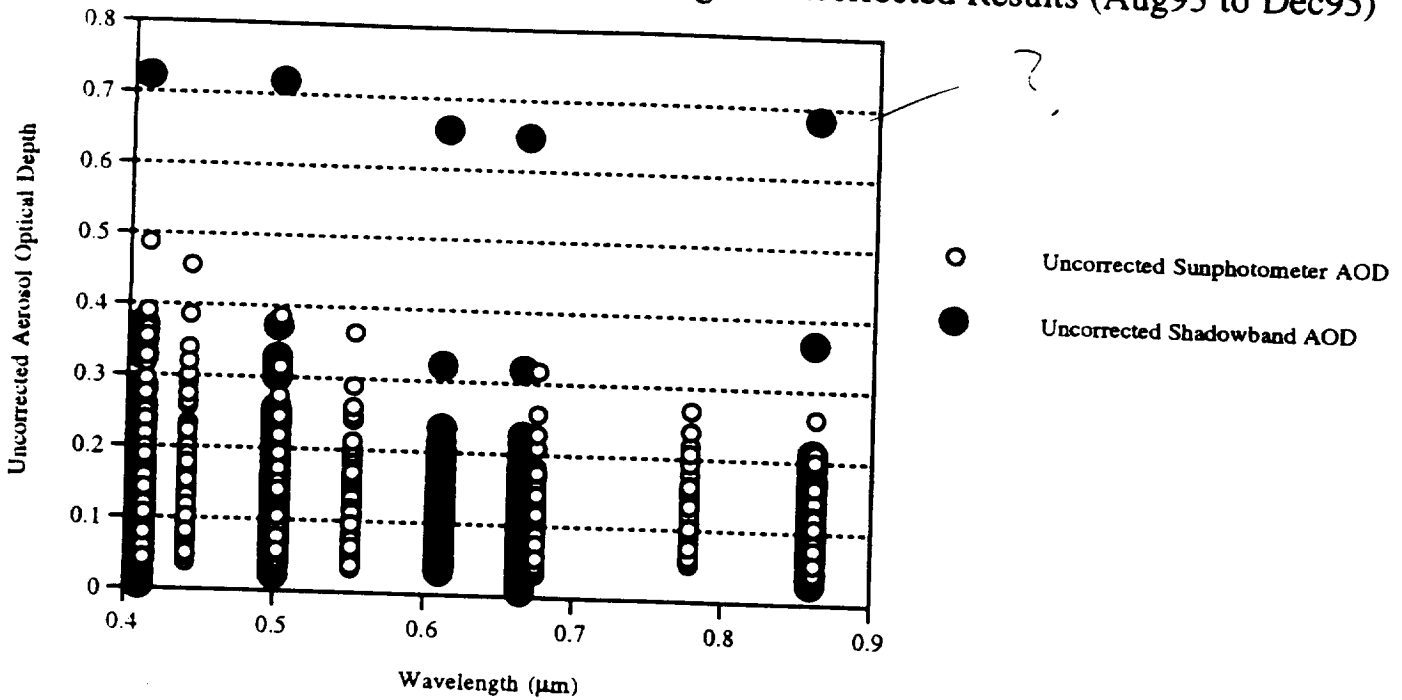


Figure 3b

Bermuda AOD vs. Wavelength: Uncorrected Results (Aug93 to Dec95)



Bermuda AOD vs. Wavelength: Error Corrected Results (Aug93 to Dec95)

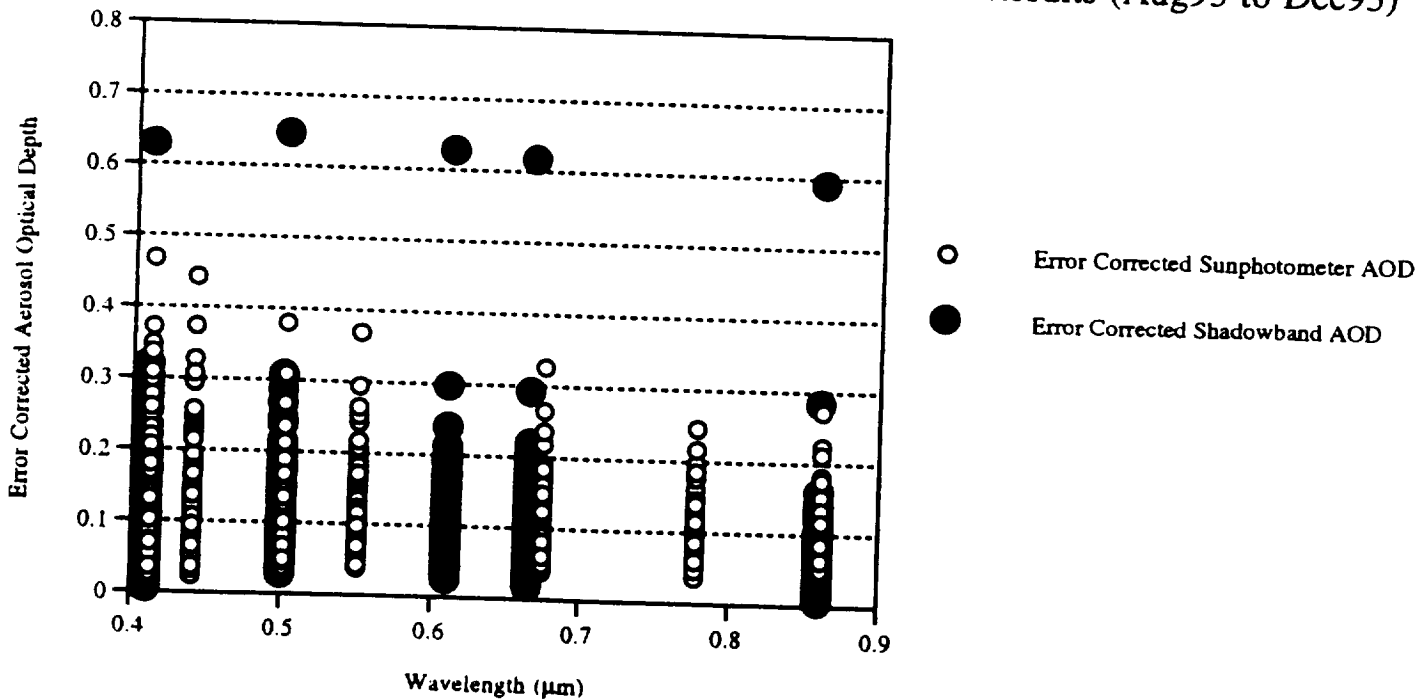
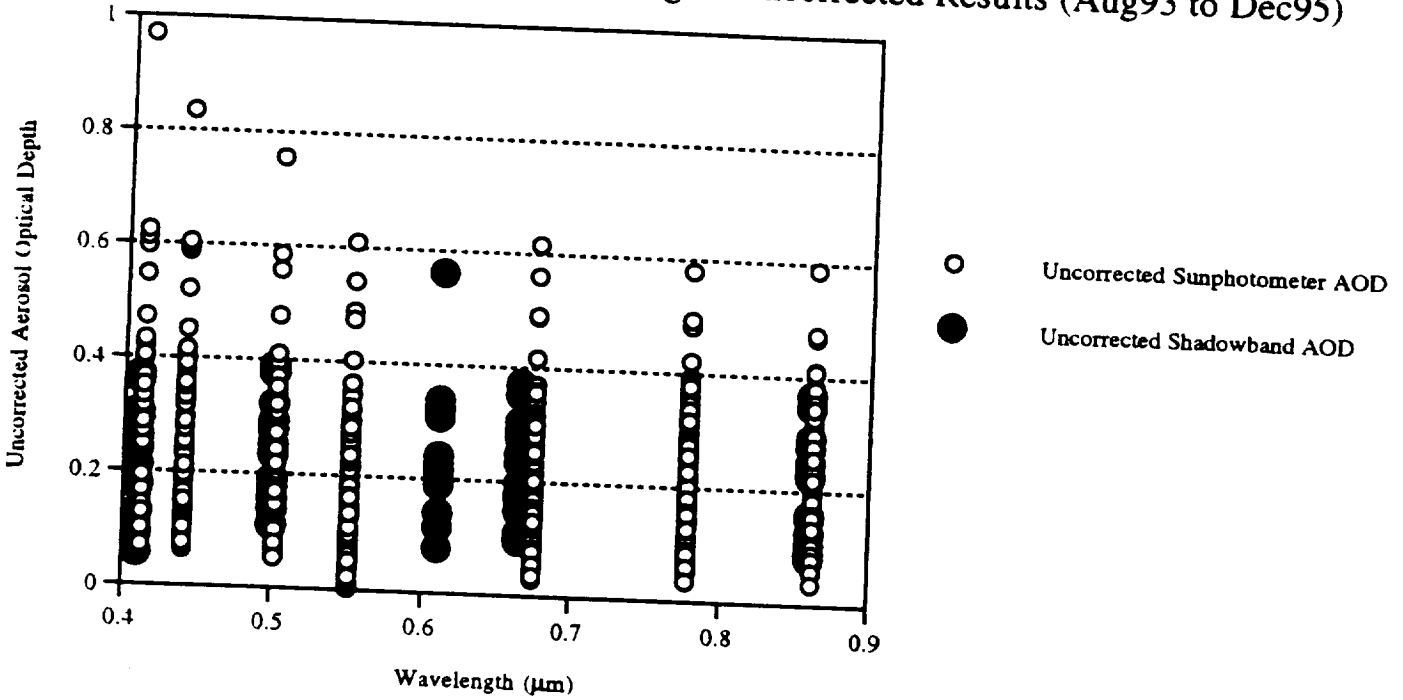


Figure 3c

Barbados AOD vs. Wavelength: Uncorrected Results (Aug93 to Dec95)



Barbados AOD vs. Wavelength: Error Corrected Results (Aug93 to Dec95)

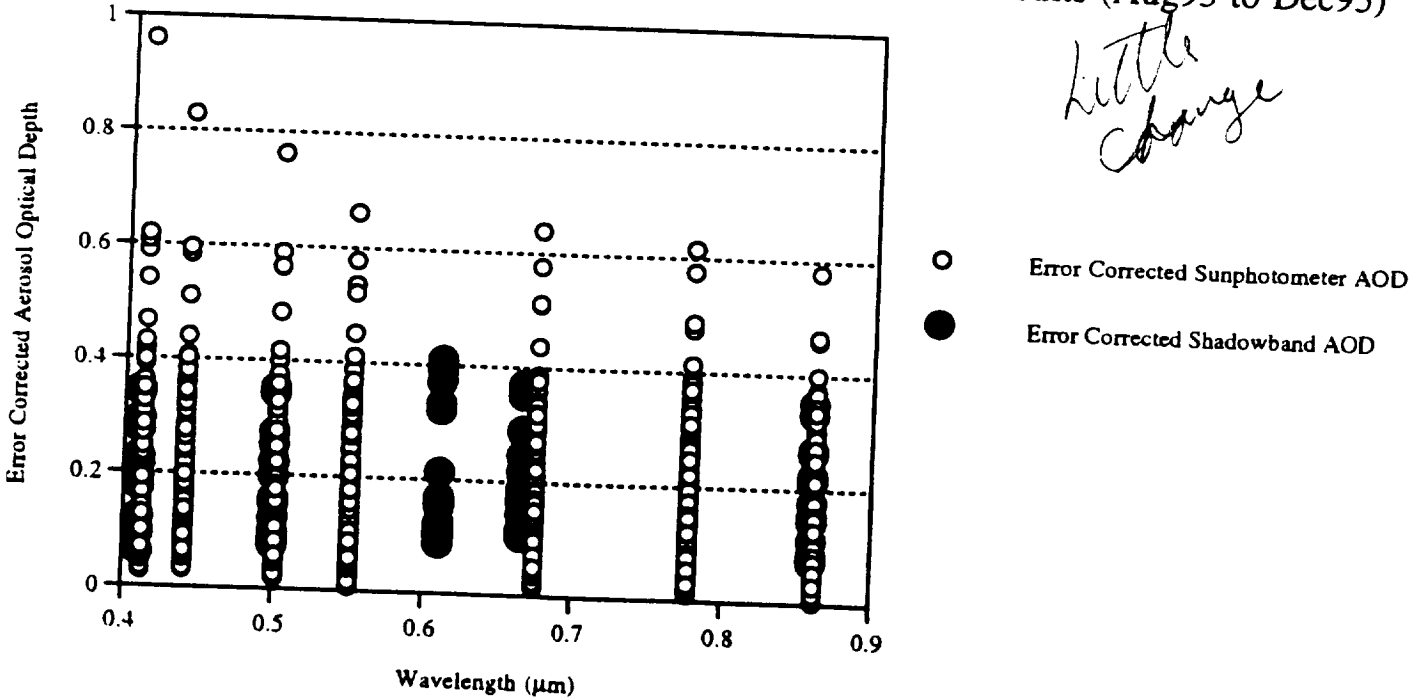


Figure 4a

Miami AOD and Angstrom Exponent Monthly Averages: Aug93 to Dec95

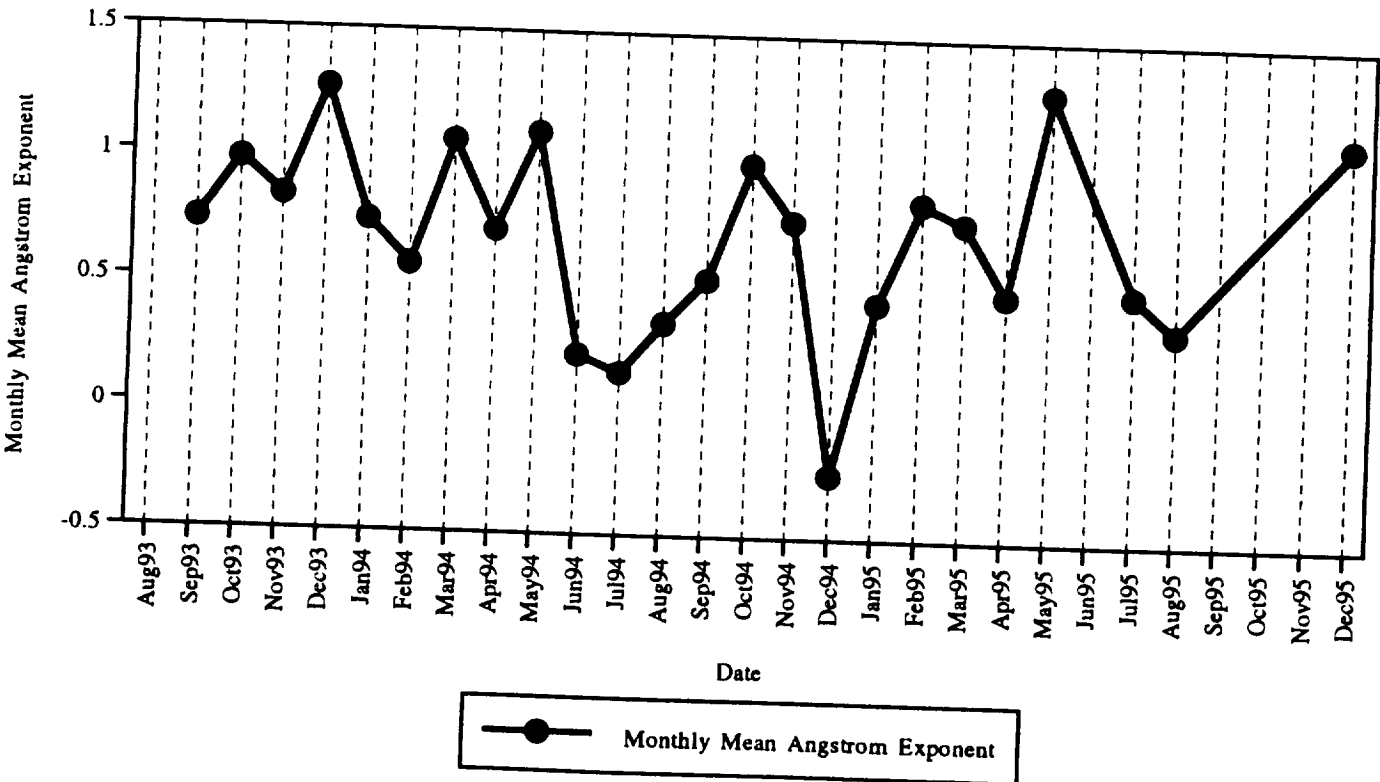
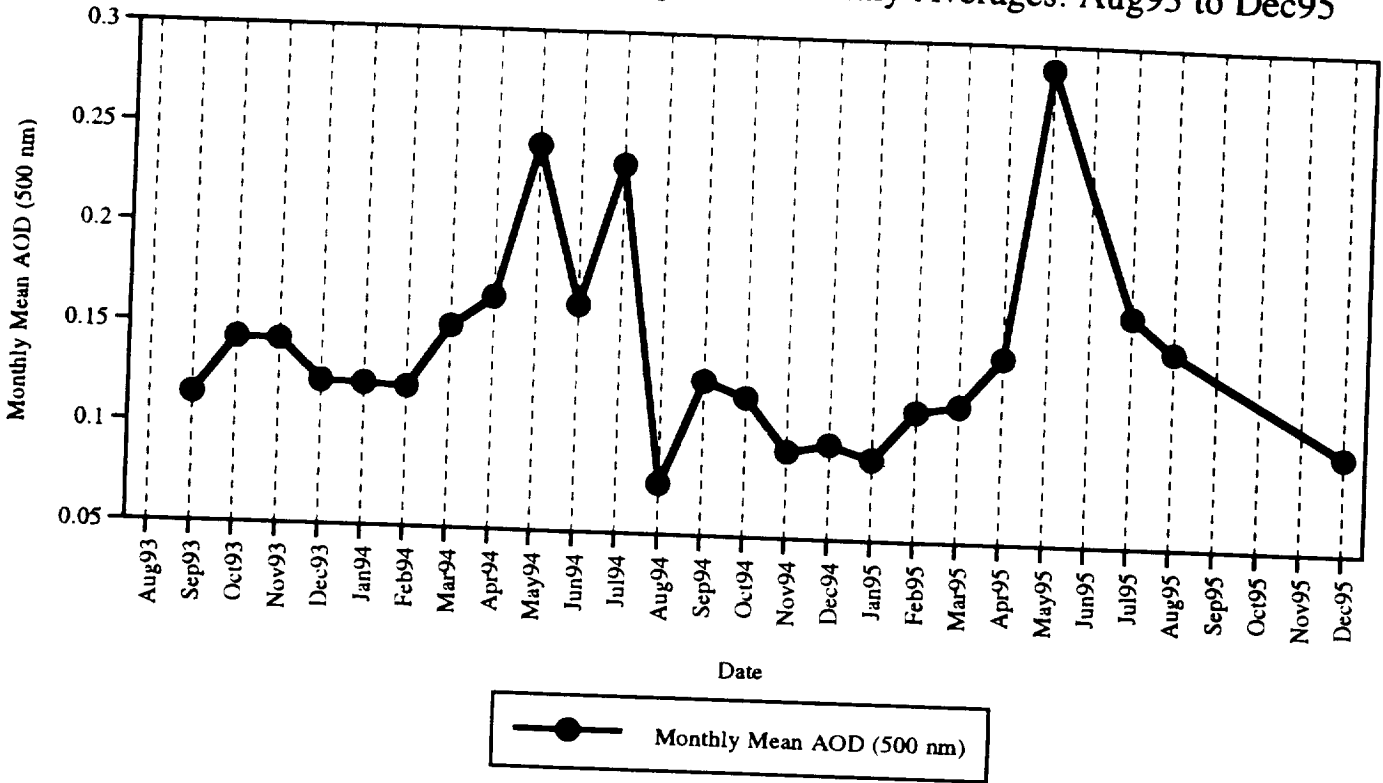


Figure 7b

Bermuda AOD and Angstrom Exponent Monthly Averages: Aug93 to Dec95

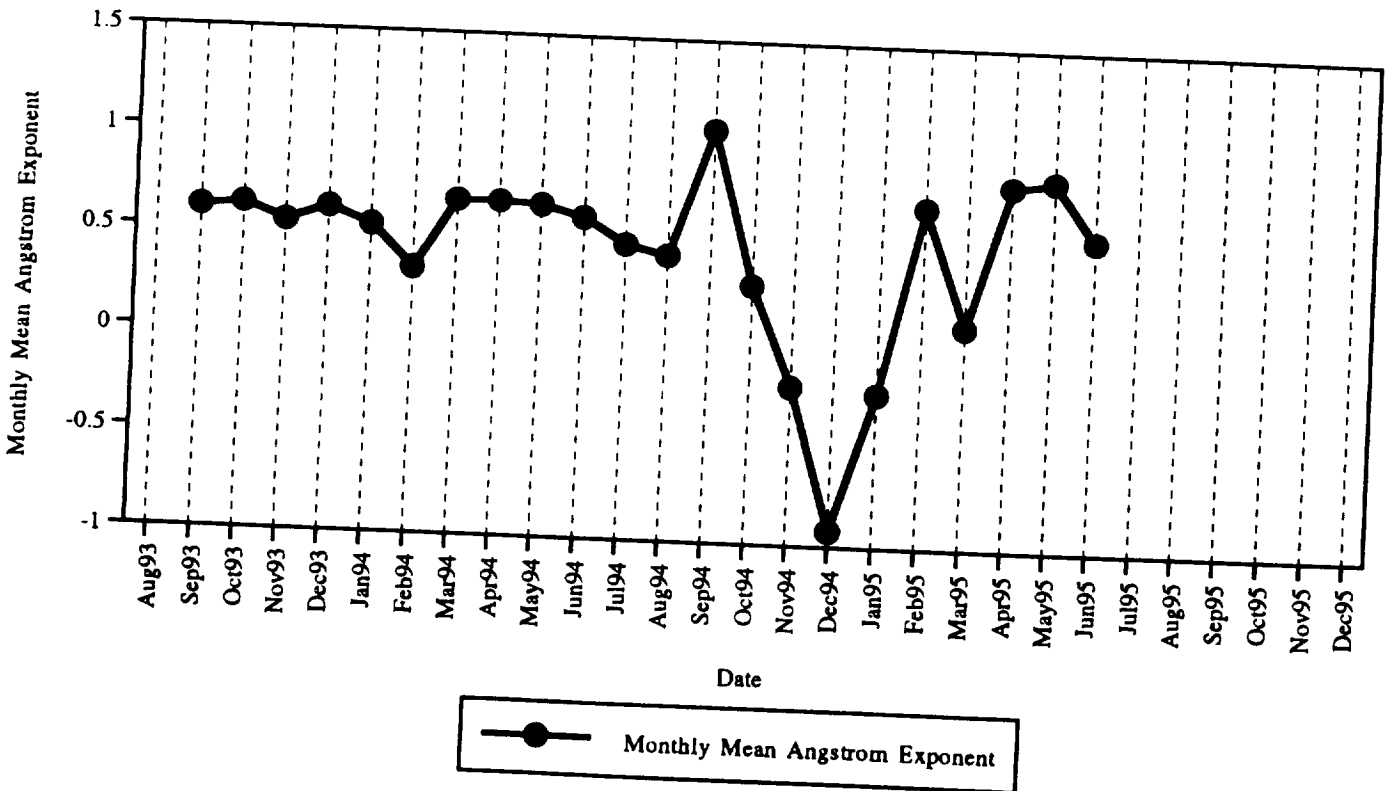
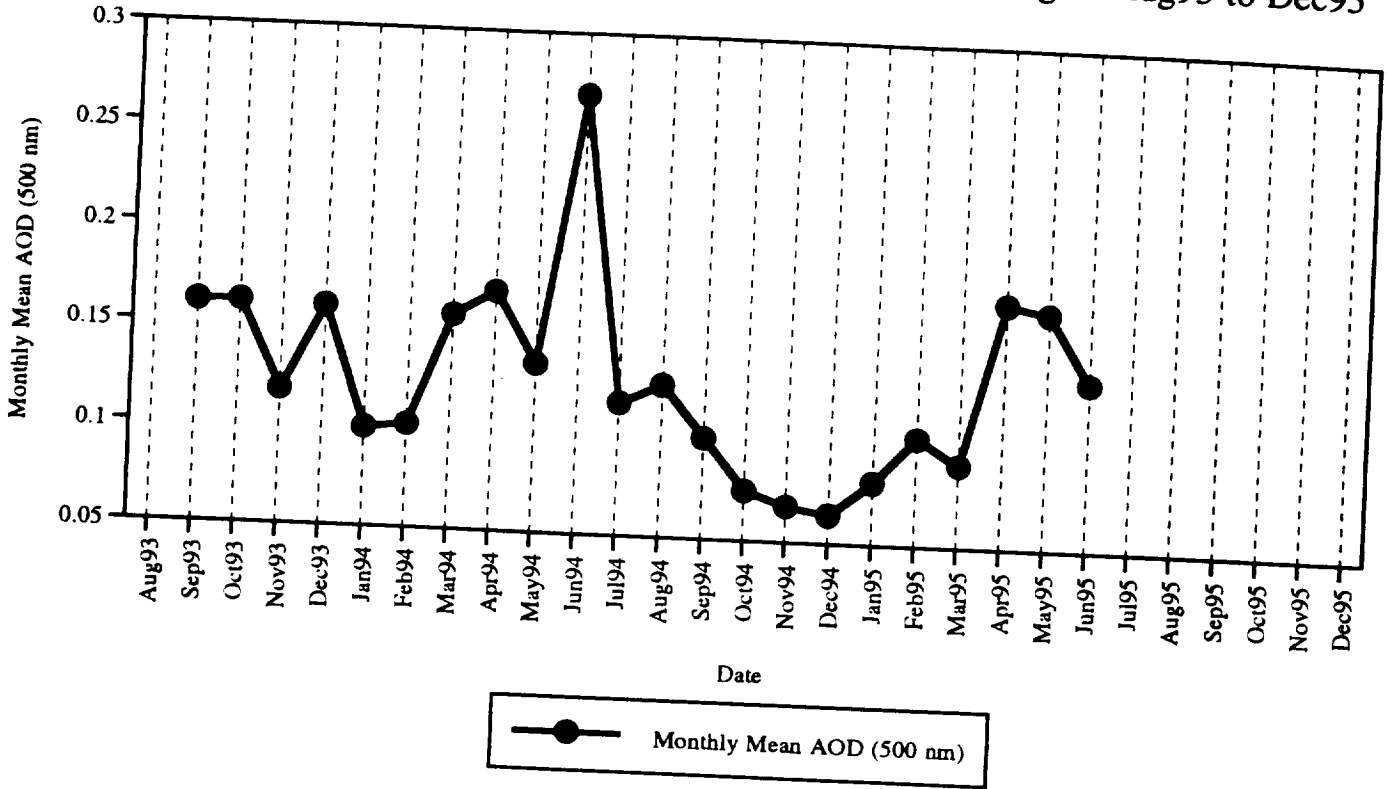
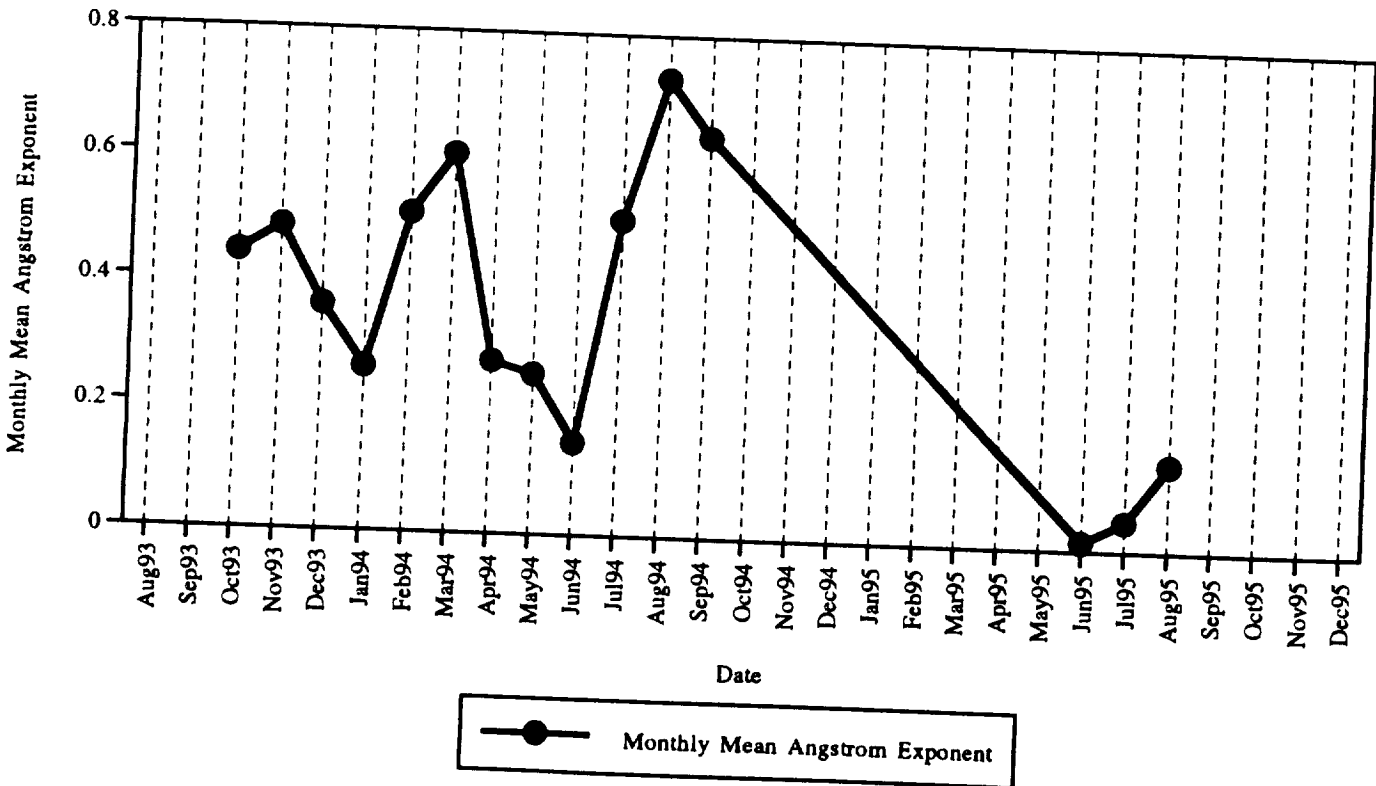
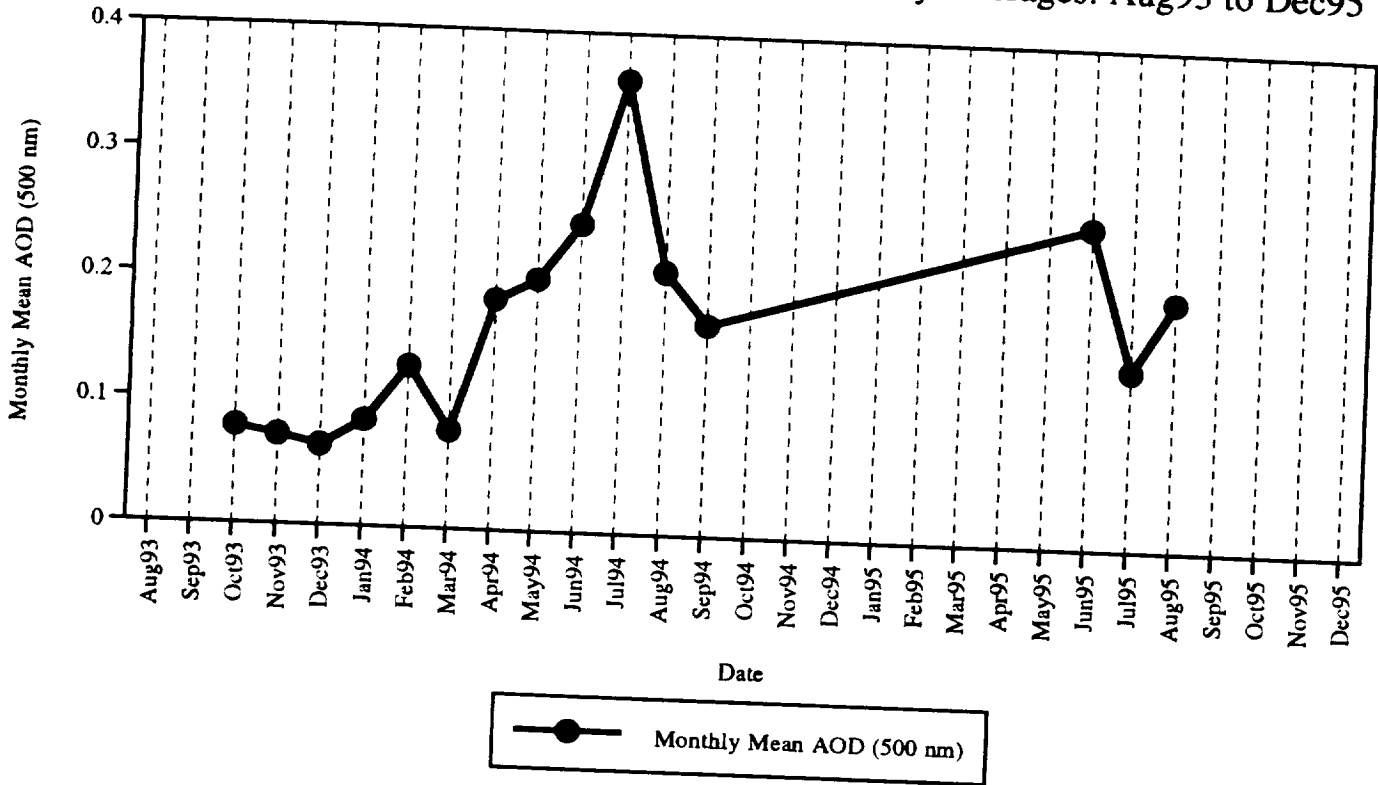


Figure 4c

Barbados AOD and Angstrom Exponent Monthly Averages: Aug93 to Dec95



Appendix 5

Polarized radiance distribution measurements of skylight: Part 1, system description and characterization

Polarized radiance distribution measurements of skylight: Part 1, system description and characterization.

Kenneth J. Voss and Yi Liu

Physics Department

University of Miami

Coral Gables, Fl. 33124

(305) 284 2323 ext 2, kvoss@umiami.miami.edu

Abstract

A new system to measure the natural sky light polarized radiance distribution has been developed. The system is based on a fisheye lens, CCD camera system, and filter changer. With this system sequences of images can be combined to determine the linear polarization components of the incident light field. In this paper calibration steps to determine the system's polarization characteristics are described. Comparisons of the radiance measurements of this system and a simple pointing radiometer were made in the field and agreed within 10% for measurements at 560 nm and 670 nm and 25% at 860 nm. Polarization tests were done in the lab. The accuracy of the intensity measurements is estimated to be 10%, while the accuracy of measurements of elements of the Mueller are estimated to be 2%.

1. Introduction

The intensity and polarization of skylight have long been studied for many reasons. Early interest involved explaining natural phenomena such as the color of the sky and rainbows.^{1,2} Since the discovery of skylight polarization by Arago in 1809, studies on the polarization of skylight and neutral points have been emphasized as these can be used as indicators of atmospheric turbidity.^{3,4}

Early measurements of skylight polarization were made mainly by visual means. As the semiconductor technology advanced, new photodetectors in conjunction with computer technology made the automatic measurements of light and its polarization possible. A large number of optical systems have been developed for observations of polarized light in various fields. Coulson¹ lists the various types of polarimeters developed for observations of the earth's atmosphere and surface. Although photomultiplier tubes have been used as detectors for most of the systems, some devices use other detectors such as silicon cells or photographic film for special purposes. Video polarimetry techniques have also been developed using three TV cameras for atmospheric science⁵ and CCD cameras for the natural light field.⁶ Imaging Stokes polarimetry using CCD image sensors⁷ has the advantage of processing data on a pixel-by-pixel basis; thus data over a wide field-of-view can be obtained. The polarimeter described in this paper takes advantage of Stokes polarimetry using a CCD image sensor and a "fisheye" lens as the input optics thus enabling measurement of Stokes parameters over the whole hemisphere.

This system is based on the RADS-II Electro-Optic "Fisheye" Camera Radiance Distribution System.⁸ This system uses a "Fisheye" camera lens, a filter changer, and a cooled CCD image sensor to measure a hemisphere of the spectral radiance distribution. With the spectral filter changer, measurement at several spectral bands can be performed in a short time (minutes). By placing dichroic sheet type polarizers in one of the filter wheels, RADS-II becomes an analyzer-type polarimeter (RADS-IIP). With proper calibration, RADS-IIP enables spectral measurement of the skylight polarized radiance distribution. The data process involves taking three data images with the polarizers in different orientations, i.e., the preferred transmission axes oriented in different directions, and these images combined to acquire three of the light field Stokes parameters.

In this paper we will discuss the overall design of the RADS-IIP system, and the calibration steps unique to the polarization system, specifically the characterization of the

instrument in Mueller matrix representation. Radiometric calibration of the RADS system without polarization has been described previously⁹ and will not be discussed in detail here; only aspects specific to this system are included and we will show results of a field comparison with a simple unpolarized radiometer. Spectral polarization radiance distribution measurements at different sites, aerosol optical thickness, and sun angles will be presented in a following paper.

2. Background information

It is useful to define the radiometric quantities that we will need. The radiance is defined as the amount of radiant power, d^2P_λ , at wavelength λ , within a wavelength interval $d\lambda$ and a differential solid angle $d\Omega$, which crosses an element of area dA and in the direction making an angle θ to the normal of dA :

$$L_\lambda(\theta, \phi) = \frac{d^2P_\lambda(\theta, \phi)}{\cos\theta dA d\Omega d\lambda}. \quad \text{Eq. (1)}$$

Implicit in the radiance is the directional dependence of the quantity. The collection of radiance information for all angles is the radiance distribution. The commonly measured quantities of upwelling and downwelling irradiance (E_u and E_d respectively) are simply defined as the cosine weighted integrals of the radiance distribution over the relevant solid angles.

To describe the polarized radiance distribution we must have a way to represent the polarization of the radiance in a given direction. A convenient representation is provided by the Stokes vector. The electric field vector \vec{E} of the light field can be decomposed into two components, E_{\parallel} and E_{\perp} , which represent the magnitude and phase of the electric field vectors parallel (\vec{I}) and perpendicular (\vec{J}) to a reference plane:

$$\vec{E} = E_{\parallel}\vec{I} + E_{\perp}\vec{J}. \quad \text{Eq. (2)}$$

The reference plane is normally defined as the plane containing the incident and scattered beams in scattering problems. Assuming that a coherent electromagnetic wave propagates in the Z direction ($\vec{r} \times \vec{l}$) with a frequency ω , and that amplitudes and phases for the electric fields of an electromagnetic wave in the \vec{l} and \vec{r} directions are a_l, a_r and δ_l, δ_r , respectively, then

$$E_l = a_l \cos(kz - \omega t + \delta_l), E_r = a_r \cos(kz - \omega t + \delta_r) \quad \text{Eq. (3)}$$

where $k = 2\pi/\lambda$ is the wave constant. In general, the tip of the electric vector described in Eqs. (2) and (3) forms an ellipse. To describe the elliptically polarized wave three independent parameters, such as those of the Stokes vector,¹⁰ (first introduced by Stokes¹¹ in 1852) are needed,

$$\begin{aligned} I &= E_l E_l^* + E_r E_r^*, \\ Q &= E_l E_l^* - E_r E_r^*, \\ U &= E_l E_r^* + E_r E_l^*, \\ V &= -i(E_l E_r^* - E_r E_l^*). \end{aligned} \quad \text{Eq. (4)}$$

For a coherent wave, $I, Q, U,$ and V are real quantities that satisfy the following equation:

$$I^2 = Q^2 + U^2 + V^2. \quad \text{Eq. (5)}$$

Assume the ellipse has a major axis (length b) and a minor axis (length c), and the major axis makes an angle χ with the \vec{l} direction. The four Stokes parameters can also be expressed in terms of $I, \chi,$ and β ($\tan \beta = c/b$) by direct analyses as:

$$\begin{aligned} I &= I_l + I_r, \\ Q &= I_l - I_r = I \cos 2\beta \cos 2\chi, \\ U &= I \cos 2\beta \sin 2\chi, \end{aligned}$$

$$V = I \sin 2\beta. \quad \text{Eq. (6)}$$

In representing the wave using Eqs. (4) or (6), we have assumed a constant amplitude and phase. However, the actual light field consists of many simple waves in very rapid succession. As a result, measurable intensities are associated with the superposition of many millions of simple waves with independent phases. In this case it is straightforward to prove that

$$I^2 \geq Q^2 + U^2 + V^2. \quad \text{Eq. (7)}$$

The degree of polarization, P_+ , and the degree of linear polarization, $P(\text{linear})$, are useful parameters and can be defined as:

$$P_+ = (Q^2 + U^2 + V^2)^{1/2} / I \quad \text{Eq. (8)}$$

$$P(\text{linear}) = (Q^2 + U^2)^{1/2} / I \quad \text{Eq. (9)}$$

The plane of polarization and the ellipticity are defined as:

$$\tan 2\chi = U / Q, \quad \text{Eq. (10)}$$

$$\sin 2\beta = V / (Q^2 + U^2 + V^2)^{1/2}. \quad \text{Eq. (11)}$$

For partially polarized light, the Stokes parameters (I, Q, U, V) can be decomposed into two vectors, a completely unpolarized component and elliptically polarized component as

$$\begin{bmatrix} I \\ Q \\ U \\ V \end{bmatrix} = \begin{bmatrix} (Q^2 + U^2 + V^2)^{1/2} \\ Q \\ U \\ V \end{bmatrix} + \begin{bmatrix} I - (Q^2 + U^2 + V^2)^{1/2} \\ 0 \\ 0 \\ 0 \end{bmatrix} \quad \text{Eq. (12)}$$

Transformation of a Stokes vector, (I_o, Q_o, U_o, V_o), into a new Stokes vector, (I, Q, U, V) by an optical process (scattering, optical elements, reflection, refraction, etc.) can be represented as a linear process with the Mueller matrix:

$$\begin{bmatrix} I \\ Q \\ U \\ V \end{bmatrix} = \begin{bmatrix} M_{11} & M_{12} & M_{13} & M_{14} \\ M_{21} & M_{22} & M_{23} & M_{24} \\ M_{31} & M_{32} & M_{33} & M_{34} \\ M_{41} & M_{42} & M_{43} & M_{44} \end{bmatrix} \begin{bmatrix} I_0 \\ Q_0 \\ U_0 \\ V_0 \end{bmatrix} \quad \text{Eq. (13)}$$

Consider an optical instrument with elements such as birefringent crystals, sheet polarizers, quarter-wave plates, imaging lenses, filters, etc. In general this instrument may cause absorption, scattering, reflection, and refraction and these actions will be represented by the system's Mueller matrix. If a polarization insensitive detector (such as a CCD array with the light at approximately normal incidence) is placed behind the optical system, then only the intensity (I) of the light exiting the system is measured. In general this intensity is due to the system's Mueller matrix and the Stokes vector of light incident on the system. If the system Mueller matrix is known and variable, it is possible that combinations of measurements may be used to measure the Stokes vector of the incoming light field. For example, when a linear polarizer is used as the optical element, its Mueller matrix can be represented as follows:

$$M_P = \begin{bmatrix} k_1 + k_2 & (k_1 - k_2) \cos 2\psi & (k_1 - k_2) \sin 2\psi & 0 \\ (k_1 - k_2) \cos 2\psi & (k_1 + k_2) \cos^2 2\psi + 2\sqrt{k_1 k_2} \sin^2 2\psi & (k_1 + k_2 - 2\sqrt{k_1 k_2}) \cos 2\psi \sin 2\psi & 0 \\ (k_1 - k_2) \sin 2\psi & (k_1 + k_2 - 2\sqrt{k_1 k_2}) \cos 2\psi \sin 2\psi & (k_1 + k_2) \sin^2 2\psi + 2\sqrt{k_1 k_2} \cos^2 2\psi & 0 \\ 0 & 0 & 0 & 2\sqrt{k_1 k_2} \end{bmatrix}$$

$$\text{Eq. (14)}$$

where k_1 and k_2 are the transmittances of the polarizer along the preferred axis and an axis 90° to this axis. ψ is the angle between the polarizer preferred transmittance plane and a reference plane. If a sequence of perfect polarizers ($k_1=1$ and $k_2=0$) with $\psi = 0^\circ, 45^\circ, 90^\circ$

are used as analyzers of an incoming Stokes vector (I_o, Q_o, U_o, V_o) then the resulting intensities measured by a detector after the polarizers would be

$$\begin{aligned}
 (\psi = 0^\circ) \quad I_1 &= I_o + Q_o \\
 (\psi = 45^\circ) \quad I_2 &= I_o + U_o \\
 (\psi = 90^\circ) \quad I_3 &= I_o - Q_o
 \end{aligned}
 \tag{15}$$

By combining these measurements three elements of the incoming stokes vector I_o, Q_o and U_o can be determined. If the circular polarization element, V_o , is required than an additional step using a circular polarizer as an analyzer is needed. In general however, light in the atmosphere is not circularly polarized, so we will not measure this quantity. In the ocean, due to the existence of water-air surface, light may undergo total reflection at the surface and return back to the ocean, this process will introduce a small amount of circularly polarized light.¹²

These equations form the basis of analyzer polarimeters, such as the RADS IIP. What must be determined, through the calibration process, are the instrumental Mueller matrix elements with each orientation of the internal polarizers. This calibration process will be discussed below.

3. Instrument description

The development of the electro-optic radiance distribution camera system (RADS) has enabled rapid and accurate measurement of the spectral radiance distribution.^{13,8} A block diagram of this system is given in Fig. 1.

The central features of RADS-II are "Fisheye" optics which allows the radiance distribution over a whole hemisphere (of spatial directions) to be imaged on the 2-D image sensor through the imaging optical system, a remotely controlled filter changer assembly which allows the spectral measurement region to be changed rapidly, and, in the case of

RADS IIP, a polarization filter wheel which allows the Mueller matrix of the instrument to be varied. The integration time of the CCD sensor is determined by an electro-mechanical shutter, which is controlled by a computer interface card. Typical image integration times are between 0.5 and 15 seconds; thus measurement takes place rapidly. The acquired image is digitized using a 16 bit A/D converter and the digital images are stored in a hard drive in the associated IBM/PC computer.

The CCD camera system uses a solid state StarScape II CCD camera from First Magnitude Corp.,¹⁴ which adopts the TC215 image sensor from Texas Instrument. The TC215 is a full-frame charged-coupled device (CCD) image sensor that provides high-resolution image acquisition for image-processing applications. The image format measures 12 mm horizontally by 12 mm vertically. The image area contains 1018 active lines with 1000 active pixels per line. Six additional dark reference lines give a total of 1024 lines in the image area, and 24 additional dark reference pixels per line give a total of 1024 pixels per horizontal line. The digitizer adds 32 more dummy lines and 32 more dummy elements each line, thus the actual size of a digital image is 1056 x 1056 pixels. The image acquiring software provides binning features and in all of our images the data were binned into 2x2 pixel samples resulting in a 528 by 528 format; thus the effective pixel size is approximately 24 μm x 24 μm .

A series of lens relay optics transfers the bundle of light rays from the fisheye converter lens, through the spectral and polarization filters, and then forms an image on the CCD array. The final image size is 10.66 mm in diameter for a maximum full angle field of view of 178°, which guarantees the image is well within the 12 mm by 12 mm CCD array. The maximum deviation of light rays from the instrument optical axis, at the position of the spectral interference filters, is 12°. This angular dispersion of the light rays is taken into account in the spectral calibration of the instrument system.

A. Dark Noise Analysis

In the CCD sensor, dark noise (signal with no light flux incident) of the whole camera system can be generated by three processes: (a) thermal generation of electrons inside the sensor array, which depends on sensor temperature and is by nature random, (b) readout noise, which depends on readout circuitry, and (c) signal processing noise, which depends on the signal processing (A/D converter) circuitry. In normal operation the thermoelectrically cooled TC215 image sensor temperature ranges from -30° to -40° to reduce the thermal generation of electrons.

Dark images were obtained by keeping the shutter closed while the CCD was integrating. Fig. 2 is the typical dark count pattern along a row and column of the same image. Inactive and dummy pixels on the edges of the image manifest themselves in both graphs on the left and right sides. As shown, the dark current in an image is far from uniform. Figure 3 is the variation in the average dark current of a central area of 10 by 10 pixels on the image as a function of time and sensor temperature. This shows that the dark current increases linearly as we increase the integration time and increases exponentially as the sensor temperature increases, as expected.¹⁵ In all experiments, dark images were measured immediately after data images, keeping the same integration time and temperature. These dark images are subtracted from the data images during data processing.

Careful investigation of a series of dark images shows that there is also random noise after the subtraction. In order to reduce this random noise, a series of dark images were taken under the same conditions. Images were then added, and the standard deviation of the whole image was calculated as each image was added. Application of a 3 x 3 averaging filter to the subtracted image is sufficient to maximize the reduction of this random noise.

B. Crosstalk Effect

Pixel crosstalk can be defined as the interaction between the individual detector elements of an array detector. Blooming is a particular form of spatial crosstalk that affects most array detectors. This phenomenon arises when a pixel or a localized group of pixels is over exposed to light. Blooming has appeared while using TC215 imager and manifests itself as spilling of charge from saturated pixels into neighboring unsaturated pixels on the same column. Thus the information content of neighboring pixels is destroyed. This effect can limit the accuracy and dynamic range of the sensor and is avoided by adjusting the neutral density filter or exposure time to prevent saturation. In the sky radiance distribution measurements, an occulter has been adopted to block the direct solar radiation in all field experiments to avoid this effect and to avoid camera lens "flaring".

The row-column crosstalk phenomenon¹⁶ was also found on the TC215 image sensor. The existence of this effect requires a correction algorithm be applied in image processing programs in order to offset this interaction between pixels. Row-column crosstalk means that the signal in a single pixel will affect another pixel on the same row. Investigations were made to gain qualitative and quantitative characterization of the phenomenon. An experiment was performed which illuminated only the central portion of the array. A typical result is shown in Fig. 4. In this figure, there are two lines; one line is the signal from the pixels of the selected row after the pixels in the illuminated region were exposed to light (peak between 300 and 400), the other line is the same row in a corresponding dark image. While counts in the illuminated pixels increased substantially, the counts from pixels in the nonilluminated region decreased significantly with respect to dark counts. This decrease is due to row-column crosstalk effect and is proportional to the counts in the illuminated region. A row-column crosstalk correction can be accomplished by determining the crosstalk signal for all pixels located on a given row and subtracting this from the net signal of each pixel on that same row. The crosstalk signals for all rows in an image are determined by the signals in a single column in the dark area of the data image;

this single column then is duplicated to form a crosstalk signal image in which every column has the exact same information. The correction for the entire data image can be achieved by subtracting this crosstalk signal image from the data image.

C. Shutter control

An experiment was performed to test the shutter-controlling signals and the accuracy of the exposure timing. The period of the signal opening the shutter was measured for a series of specified integration times. The result was that all input times agree with measured times within 0.2% in a range of 100ms to 50s. Due to the reaction time of the shutter and the finite opening and closing times, a maximum 5 ms absolute error may still exist; thus in the field we use integration times longer than 0.5 seconds, which makes the maximum error from this source approximately 1%.

4. Calibration

The objective of the RADS-IIP calibration is to obtain a functional relationship between the incident flux and polarization, and the instrument output. The calibration of the instrument requires a functional set of data concerning the spectral, spatial, and polarization characteristics of the instrument.¹⁷ Voss and Zibordi⁹ discussed the steps required for radiometric scalar (non-polarized) calibration of a fisheye camera system. Calibration of the system linearity, spectral response, camera system rolloff, and absolute system response were performed by these methods. Only the results of these steps will be discussed.

A. Linearity and Spectral Calibration

Figure 5 shows the result of a test of the system linearity. In the experimental setup a barium sulfate reflectance plaque was illuminated in the normal direction by a stable 1000W lamp providing source of stable radiance for the camera. The camera viewed the plaque at a direction 45 degrees to the normal. The light intensity incident on the array was controlled

by changing the integration time, and an average of 3 by 3 pixels in the center of the image was obtained. This result shows that the camera output is not exactly linear but can be defined accurately over three orders of magnitude by a simple power function, with an exponent of 1.04.

Interference filters are used in the RADS system to select the spectral band of interest. A calibration was performed to determine the spectral response of the camera system by illuminating the system with light from a monochromator and measuring the system response. Spectral filters 1-4 were found to be centered at 439 nm, 560 nm, 667 nm, and 860 nm, with full width at half maximum of 10.5 nm, 10.0 nm, 11.0 nm, and 13.5 nm respectively.

Figure 6 is a typical system rolloff curve determined in the calibration process; the method is described in Voss and Zibordi.⁹ This curve was found to be rotationally symmetric around the optic axis of the camera system, so the regression curve shown was used in the data reduction process. An absolute calibration of the system response was also done using a 1000 W lamp (FEL standard lamp traceable to NIST) and a Spectralon reflectance plaque.

B. Polarimetric Calibration

The Mueller matrix of the camera optical system can be represented as a single 4 x 4 matrix. Although in theory this Mueller matrix of the optical system can be decomposed into a chain of matrices that are representations of the individual optical components, it is better to calibrate the system as one unit using prepared sources of partially polarized light. Since the CCD array only measures intensity, only the first row of the total system Mueller matrix must be determined. In this case we input known sets of I_0 , Q_0 , U_0 , and V_0 , I is measured,

and $M11$, $M12$, $M13$, and $M14$ can be determined. A convenient set of Stokes vectors to use as input beams are:¹⁸

$$A = \begin{bmatrix} I_0 \\ I_0 \\ 0 \\ 0 \end{bmatrix}, B = \begin{bmatrix} I_0 \\ -I_0 \\ 0 \\ 0 \end{bmatrix}, C = \begin{bmatrix} I_0 \\ 0 \\ I_0 \\ 0 \end{bmatrix}, \text{ and } D = \begin{bmatrix} I_0 \\ 0 \\ 0 \\ I_0 \end{bmatrix}. \quad \text{Eq. (16)}$$

where A is horizontally polarized light, B is vertically polarized light, C is +45° polarized light, and D is right-handed circularly polarized light. These beams are sequentially input into the optical system and the output light intensity recorded in each case. This provides four linear equations, the solution of which determines the required elements of the system Mueller matrix.

Since we produce the linear polarization states with a dichroic sheet polarizer (Gray polarizing film, Edmund Scientific)¹⁹ we need to measure the spectral polarization and transmission properties of this polarizer. The principal transmittances of the dichroic polarizers used were measured and are shown as functions of wavelength in Fig. 7. The extinction ratios, i.e., the fraction of light transmitted through a closed pair of polarizers, were found to be less than 1% for visible light. Transmission for a single dichroic polarizer acting alone, ranges from 5% to 50% for visible light. Thus using sheet polarizers and an unpolarized light source, one can generate the following light beams as input light:

$$A = \begin{bmatrix} 1 \\ \frac{k_1 - k_2}{k_1 + k_2} \\ 0 \\ 0 \end{bmatrix}, B = \begin{bmatrix} 1 \\ \frac{-k_1 + k_2}{k_1 + k_2} \\ 0 \\ 0 \end{bmatrix}, C = \begin{bmatrix} 1 \\ 0 \\ \frac{k_1 - k_2}{k_1 + k_2} \\ 0 \end{bmatrix}. \quad \text{Eq. (17)}$$

In general the ingoing light undergoes interactions with various optical components of the RADS. If we number each individual optical element in the order of their presence,

then the Mueller matrix can be described by the Mueller matrix of a chain of total number of optical components as follows:

$$M = \dots M_3 M_2 M_1, \quad \text{Eq. (18)}$$

where M_i is the Mueller matrix of the i -th optical component. For our RADS-II system, these optical components are lenses, polarizers, interference color filters, and absorption neutral density filters. For the convenience of our analysis, let us denote the Mueller matrix of the polarizer as M_p . Light interacting with the surfaces of optical components undergoes refraction for lenses, reflection and refraction for interference filters, absorption and refraction for neutral density filters.

The Mueller matrix for an isotropic absorption process is the unity matrix (note that below all Mueller matrices are normalized to M_{11} , and therefore we use the term of reduced Mueller matrix). The reduced Mueller matrix for reflection and refraction processes has been derived by Kattawar and Adams²⁰ and has the following form:

$$\begin{bmatrix} 1 & \frac{\alpha - \eta}{\alpha + \eta} & 0 & 0 \\ \frac{\alpha - \eta}{\alpha + \eta} & 1 & 0 & 0 \\ 0 & 0 & \frac{\gamma}{\alpha + \eta} & 0 \\ 0 & 0 & 0 & \frac{\gamma}{\alpha + \eta} \end{bmatrix} \quad \text{Eq. (19)}$$

where α , η , and γ depend on incident and refracted angles. These matrix elements are plotted in Fig. 8 as a function of incident angle assuming light entering glass (relative index of refraction, 1.5).

The product of a chain of matrices with the form of Eq. (19) has the same symmetry as Eq. (19), and this allows us to write the total Mueller matrix as the product of the polarizer Mueller matrix and the Mueller matrix for all other optical components. In doing so we have made an assumption that all the contributions to the camera's Mueller matrix due to

optical components other than polarizers are from optical components before the polarizer, mainly due to the fish-eye input optics. This is reasonable because only at the input stage are large refraction angles involved. Even for the interference filter, every transmitted ray undergoes two refractions and pairs of reflections. The reduced Mueller matrix for double reflections at small angles is close to unity and therefore the reduced Mueller matrix for an interference filter is nothing but double refraction at small angles, which is also close to a unity matrix. The validity of these assumptions will be tested by experiment. Let M_o be the Mueller matrix due to optical components other than the polarizer, then we can write the total Mueller matrix as:

$$M = M_p M_o \quad \text{Eq. (20)}$$

Once k_1 and k_2 for polarizers are known, the Mueller matrix, M_p , can be calculated. Thus it is only necessary to measure the Mueller matrix for the camera without a polarizer and the orientation of the polarizer.

In the following discussions, we use the notation $m_{12}(W1)$, $m_{13}(W1)$ and $m_{14}(W1)$ to denote the reduced Mueller matrix elements for the polarization filter wheel in position 1 and $m_{12}(W2)$, $m_{13}(W2)$ and $m_{14}(W2)$ for reduced Mueller matrix elements for the second position. Similar notations will be used to describe the Mueller matrix elements for the third and fourth polarizer positions. There is no polarizer in position 1, but the polarizers in positions 2, 3, and 4 are oriented at 0° , 45° , 90° relative to an arbitrary axis.

Figure 9 shows that the measured m_{14} values for the four filter wheel locations are close to zero as expected from the form of Eq. (19). The deviations from zero are caused by the imperfect quarter-wave plate employed in the experiment. As we used a quarter-wave plate (at 550nm, Melles Griot 02WRM009) made of mica, it can only approximate a quarter-wave plate at the wavelengths of the RADS-II. The Mueller matrix elements m_{12} and m_{13} are shown in Figs. 10 and 11. It can be seen that $m_{13}(W1)$ and $m_{14}(W1)$ are

close to zero. These are the Mueller matrix elements of the camera without a polarizer. But $m_{12}(W_1)$ is not zero and varies with incidence angle as T_{12}/T_{11} of Fig. 8. These results show that the total Mueller matrix of the camera (without polarizers) is similar to Eq. (19).

Experimentally $m_{12}(W_1)$ and $m_{13}(W_1)$ were found to be rotationally symmetric around the optical axis. Similar experiments were also performed to test for spectral dependence, and it was found that the Mueller matrix is independent of wavelength within experimental error. In each of these cases the system was found to be rotationally symmetric, and spectrally constant within 1%.

With this method we have the following reduced Mueller matrix elements: $m_{12}(W_1)$, $m_{13}(W_1) = m_{14}(W_1) = 0$. Applying symmetry principles to the Mueller matrix and considering there are only reflections and refractions involved in the camera case (without polarizer), the overall Mueller matrix has the same form as Eq. (19). Thus we can assume $m_{33}(W_1) = m_{44}(W_1) = 1$, $m_{23}(W_1) = m_{24}(W_1) = m_{34}(W_1) = 0$, and the Mueller matrix for the camera (in Eq. (20)) is known. Since the Mueller matrix for a sheet polarizer is known, we are able to generate the Mueller matrix of the RADS-II for any direction of view once the preferred transmission axis of the polarizer is known.

5. Calibration tests

To confirm the accuracy of the scalar (non-polarized) calibration procedures, an experiment was performed in April 1994 in Key West, Florida in conjunction with the Hand Held Contrast Reduction Meter (HHCRM).²¹ Measurements of the sky radiance distribution using RADS-II (without polarizers in place) were obtained at 3 wavelengths common to both instruments, 558, 673, and 866 nm. The measurement site was located at the edge of Key West, Florida.

While the RADS-II measurement was obtained quickly (typical integration time was 1 second), the HHCRM measurement had to be taken successively one point at a time. Only

principal plane and almucantor data were taken using the HHCRM. The almucantor corresponds to directions with the same sun-zenith angle but varying azimuthal angles from the sun. The principal plane is composed of directions in the plane containing the sun and the zenith. The HHCRM measurement sequence took about three minutes for each wavelength. In the RADS-II measurements an occulter was used to block the direct solar radiation due to the dynamic range limitation of CCD sensor and to prevent flare from the direct solar beam in the camera optics. Thus no data is available within 20 degrees of the sun in the radiance image.

Figures 12 and 13 compare the RADS-II data with the HHCRM data for three channels at wavelengths of 560 nm, 667 nm and 860 nm. It should be noted that the HHCRM has an approximate pointing inaccuracy of 2 degrees. Figure 14 shows the relative difference of the data in the principal plane for three channels. The difference is computed as:

$$\% \text{ difference} = 100 \times \frac{HHCRM - RADS}{(HHCRM + RADS)/2} \quad \text{Eq. (21)}$$

The Principal plane is a more difficult comparison because of pointing inaccuracies in the HHCRM and because the rolloff calibration in the RADS system enters strongly into the RADS data set.

For 560 and 670 nm all the data shown have less than a 10 percent difference. The agreement between RADS-II data and HHCRM data for 860 nm is poor, the difference can reach as big as 25% when the radiance value is small, with RADS-II data always higher. The gain of the HHCRM is very sensitive to temperature at this wavelength; thus, the HHCRM data may not be as accurate at this wavelength.

To test the polarization calibration method (separation of polarizer and camera Mueller matrices) an experiment was performed to measure the Mueller matrix elements directly and compare with those same elements obtained by matrix transformation (Eq. (20)). The experimental setup is similar to the absolute calibration method in the way the camera was

placed and light source arranged. An additional device prepared light beams A, B and C as in Eq. (17) and the camera viewed a reflectance plaque, illuminated by a 1000W lamp, through this device. This device is basically a hollow cylinder painted black with a sheet polarizer placed on a polarizer holder in front of the cylinder. The polarizer can be rotated around the cylinder's axis precisely. The aperture of the polarizer allowed a 4 degree field of view. While tests were done for all three wavelengths, Fig. 15 and 16 show the comparisons between experimental results and matrix transformation results for 560 nm. The transformed values differ from the directly measured values only by 1 to 2 %. The development of the matrix transformation technique for RADS-II polarimetric calibration allows the Mueller matrix elements to be computed relatively quickly for the whole hemisphere.

VI) Camera System Mueller Matrix Elements for the Whole Hemisphere

So far we have illustrated the polarimetric calibration procedures for the RADS-II CCD camera system. Since the Mueller matrix elements depend on the coordinate system, it is necessary to define the coordinate system used.

Consider an x-y coordinate system on the CCD array with z pointing normal to the array. All the Mueller matrix elements are represented in this x-y-z coordinate system for the RADS-II optical system and in describing the radiative transfer process. For the optical system of RADS-IIP, each pixel on the array corresponds to a zenith and azimuth angle. The *l* axis of the system is in the plane defined by the specific look direction and the optic axis of the system. The zenith and azimuth angles determine the Mueller matrix elements and therefore determine the polarization signature of the camera system. In the previous discussions, we have shown that Mueller matrix of the camera does not depend on azimuth angle (rotationally symmetric around the optic axis). Since we know the geometric mapping of spatial direction to individual pixel on the array, it is possible to express the spatial Mueller matrix in an image format.

The following figures (Figs. 17 - 18) are example contour plots of the Mueller matrix element images for M12 and different configurations of polarizers, all generated by using Eq. (20). The rotational symmetry is evident in those images. M12(W1) only slowly varies with off-axis zenith angle. M12(W2) varies strongly with zenith angle as the incoming l axis is oriented parallel and perpendicular to the transmission axis of the polarizers orientation, shown in Fig. 17. M12(W3) (shown in Fig. 18) and M12(W4) are similar only rotated at 45° azimuthally to follow the rotation of the polarizer. With these (effectively) images of the Mueller matrix elements, the Mueller matrix of the camera system is defined exactly. These images then provide a convenient way to store this information and operate on data acquired in the field.

7) Conclusion

We have described the RADS-IIP instrument and have shown through experiment that the system performs well. We expect that the absolute calibration of the system is accurate with 10% for most channels. Polarization measurements are accurate within approximately 2%. With the images resulting from the polarimetric calibration we can process sets of sky radiance distribution data to obtain polarized spectral radiance distributions accurately and quickly (< 2 min.) for all directions. Because all directions are taken simultaneously the system is well adapted to operate in a changing environment or on a less stable platform, such as a ship. In a companion paper we will present data obtained with the instrument and investigate aspects of the sky light polarization.

8) Acknowledgments

The authors would like to acknowledge the support of the Ocean Optics Program at ONR, under grant N000149510309 and NASA under NAS5-31363. Also we would like to thank Albert Chapin for his help during the calibrations.

References

- 1) K. L. Coulson, *Polarization and intensity of light in the atmosphere*, A. Deepak publishing, Hampton Va. USA (1988).
- 2) A. T. Young, "Rayleigh Scattering", *Physics Today*, Jan 1982, 42-48.
- 3) K. L. Coulson, "Characteristics of skylight at the zenith during twilight as indicators of atmospheric turbidity, I: Degree of Polarization", *Appl. Opt.*, 19, 3469 - 3480 (1980).
- 4) H. H. Kimball, "The effect of the atmospheric turbidity of 1912 on solar radiation intensities and skylight polarization," *Bul. Mt. Weather Observatory*, 5, 295 - 312 (1913).
- 5) T. Prosch, D. Hennongs, and E. Raschke, "Video polarimetry: a new imaging technique in atmospheric science", *Appl. Opt.*, 22, 1360 - 1363 (1983).
- 6) T. W. Cronin, N. Shashar, and L. Wolff, "Portable imaging polarimeters" in *IEEE Proc of the 12th IAPR International conference on pattern recognition*, (IEEE Computer Society, Los Alamitos, Ca., 1994), pp. 606- 609
- 7) H. Povel, "Imaging stokes polarimetry with modulators and charge coupled-device image sensors", *Optical Engineering*, 34, 1870 - 1878 (1995).
- 8) K. J. Voss and A. L. Chapin, "Next generation in-water radiance distribution camera system", *SPIE Vol. 1750, Ocean optics XI*, 384 -387 (1992).
- 9) K. J. Voss and G. Zibordi, "Radiometric and geometric calibration of a visible spectral electro-optic 'fish-eye' camera radiance distribution system, *J. Atmos. Ocean. Tech.*, 6, 652 -662 (1989).
- 10) H. C. Van de Hulst, *Light Scattering by Small Particles*, Dover Publications, Inc. (1981).
- 11) G. G. Stokes, "On the composition and resolution of streams of polarized light from different sources", *Trans. Cambridge Phil. Soc.*, 9, 399 (1852).

- 12) G. W. Kattawar and X. Xu, "Detecting Raman scattering in the ocean by use of polarimetry", SPIE Vol. 2258, Ocean Optics XII, 222 - 233 (1994).
- 13) K. J. Voss, "Electro- optic camera system for measurement of the underwater radiance distribution," Opt. Engineering, 28, 241 -247 (1989).
- 14) P. J. Johnson, "Manual on Starscape II CCD cameras", First Magnitude Inc., Laramie, Wy. (1992).
- 15) J. S. Campbell, "TC271 Characterization Report", Area array image sensor products, Data book, Texas Instruments, Dallas, Tx.(1994).
- 16) G. R. Sims and M. B Denton, "Spatial pixel crosstalk in a charge-injection device", Opt. Eng., 26, 999 - 1007 (1987).
- 17) C. L. Wyatt, *Radiometric calibration: Theory and Methods*, Academic Press, New York (1978).
- 18) B. J. Howell, "Measurement of the polarization effects of an instrument using partially polarized light", Appl. Opt., 18, 809 -812 (1979).
- 19) E. H. Land, "Some aspects of the development of sheet polarizers", J. Opt. Soc. Am., 41, 957 - 963 (1951).
- 20) G. W. Kattawar and C. N. Adams, "Stokes vector calculations of the submarine light field in an atmosphere-ocean with scattering according to a Rayleigh phase matrix: effect of interface refractive index on radiance and polarization", Limnol. Oceanogr., 34, 1453-1472 (1989).
- 21) W. H. Wilson, "Measurements of atmospheric transmittance in a maritime environment", in Proceedings of the Society of Photo-Optical Instrumentation Engineering, Atmospheric Effects on Radiative Transfer, Vol 195, Sand Diego, 29-30 August, 1979.

Figures

Fig. 1) Block diagram of RADS-IIP instrument.

Fig 2) Dark counts (row) and (column). Illustrates the non-uniformity of the dark signal on the detector. Integration time was 1 s, sensor temperature was $-34.5\text{ }^{\circ}\text{C}$.

Fig 3) Dark counts as a function of integration time and sensor temperature. Illustrates linear relation of dark counts with integration time and exponential relation with sensor temperature.

Fig 4) Cross talk experiment which illustrates the suppression of counts from pixels in the same row as a bright pixel.

Fig 5) Linearity calibration. Line is a power fit to the data and fits well over three order of magnitude of light intensity (exponent is 1.04).

Fig 6) Typical rolloff curve found through calibration process.

Fig 7) Measured principal transmittances for the dichroic polarizer used as a function of wavelength.

Fig 8) Non-zero matrix elements for the reflected and transmitted light due to interaction with a glass (index of refraction = 1.5) surface.

Fig 9) Reduced matrix element M14 as a function of off-axis angle and polarization filter position.

Fig 10) Reduced matrix element M12 as a function of off-axis angle and polarization filter position.

Fig 11) Reduced matrix element M13 as a function of off-axis angle and polarization filter position.

Fig 12) Almucantor comparison of HHCRM and RADS.

Fig 13) Principal plane comparison of HHCRM and RADS.

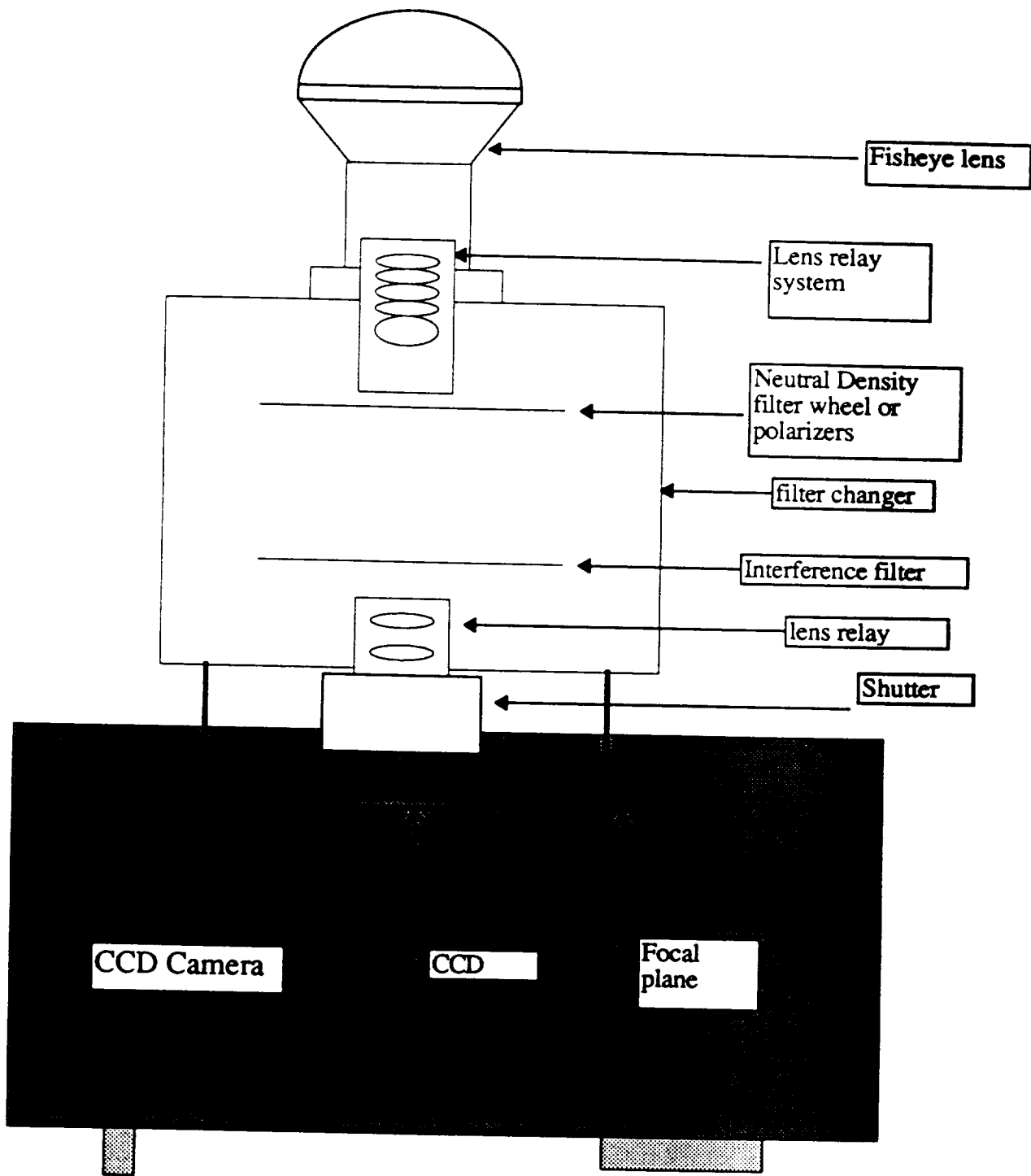
Fig 14) Relative difference between HHCRM and RADS measurements in the principal plane at each wavelength.

Fig 15) M12 direct measurement and matrix transformation method, illustrating how well the matrix transformation method works to estimate the system Mueller matrix.. Measurements performed at 560 nm.

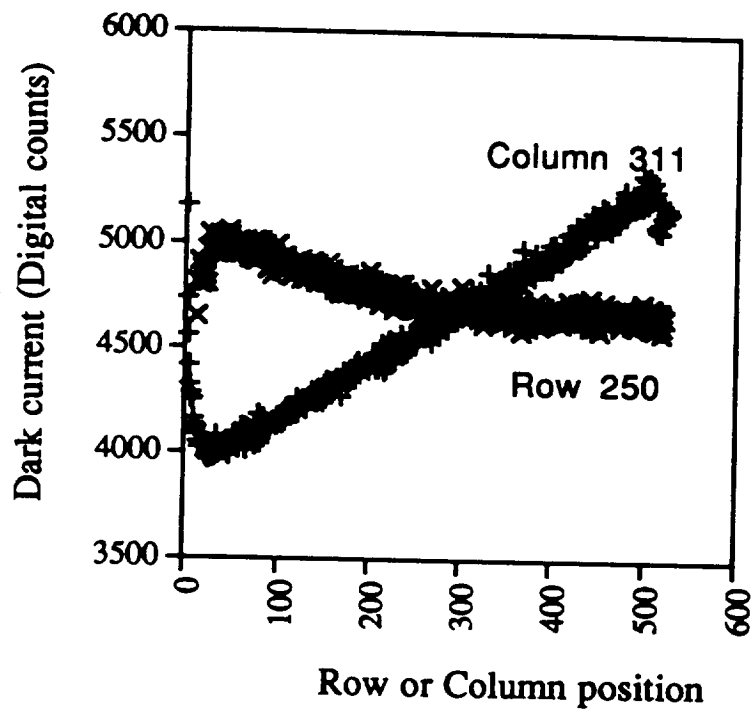
Fig 16) M13 direct measurement and matrix transformation method, illustrating how well the matrix transformation method works to estimate the system Mueller matrix. Measurements performed at 560 nm.

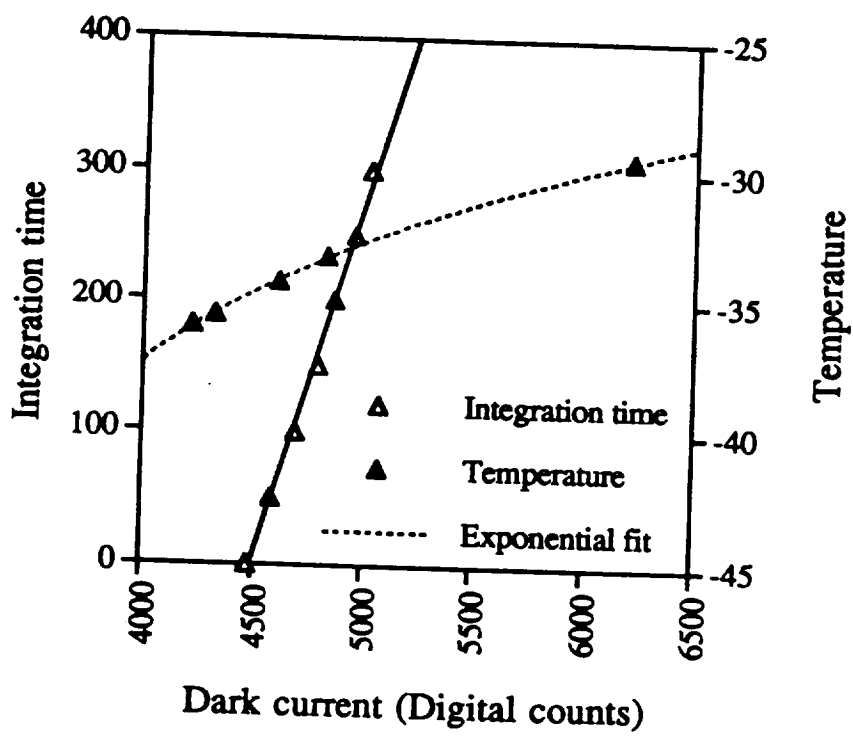
Fig 17) M12(W2)

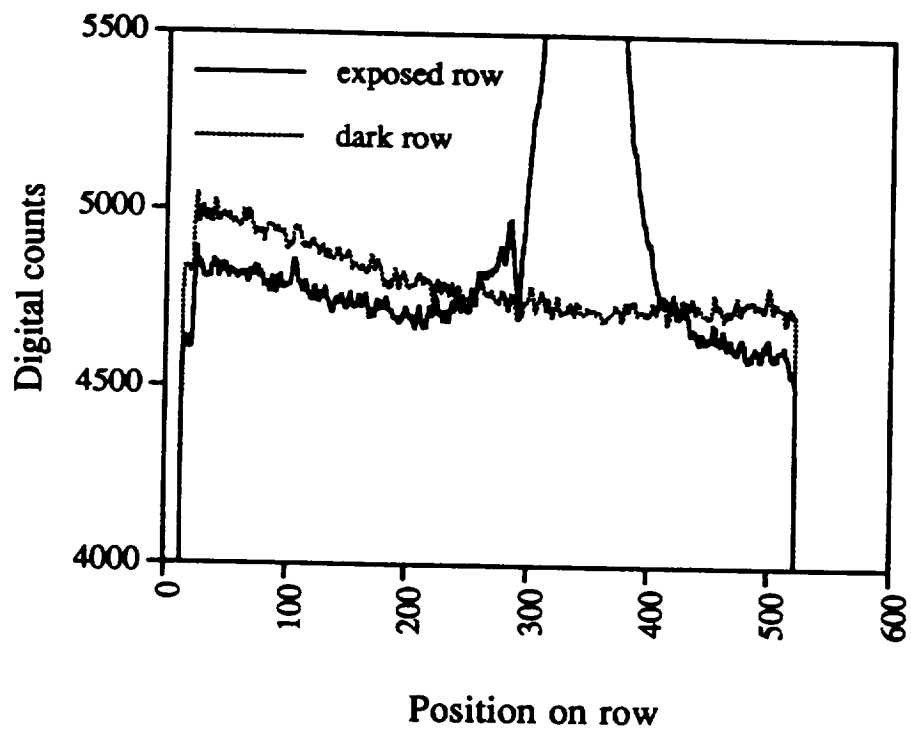
Fig 18) M12(W3)

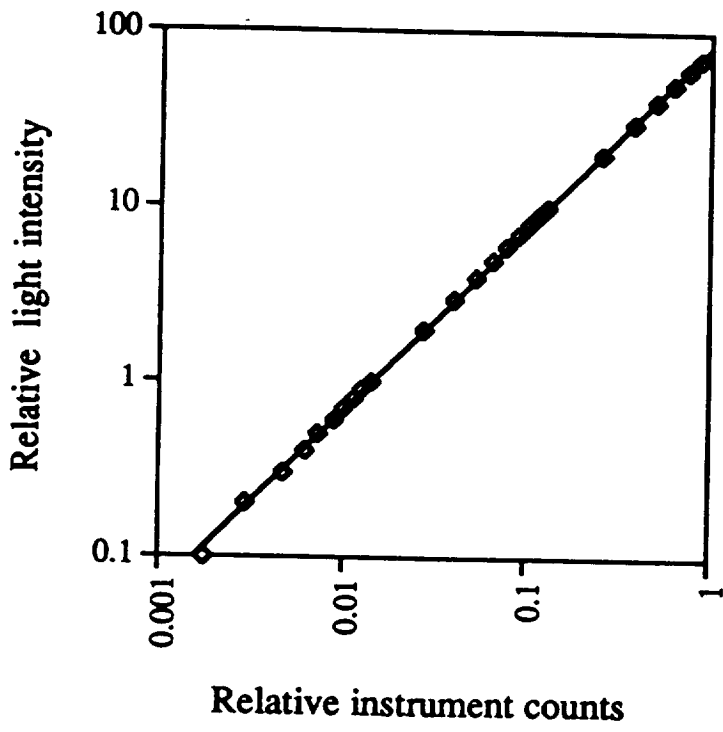


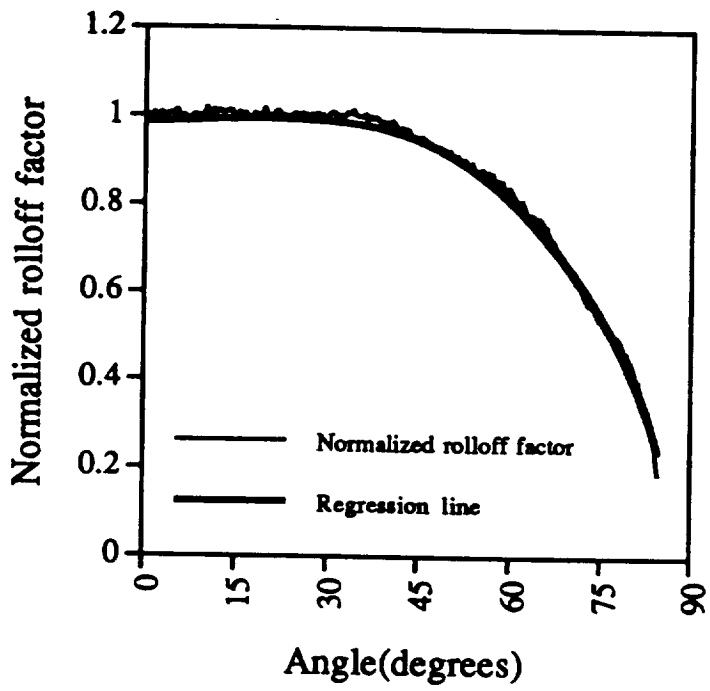
Wang and Lin, Fig 1

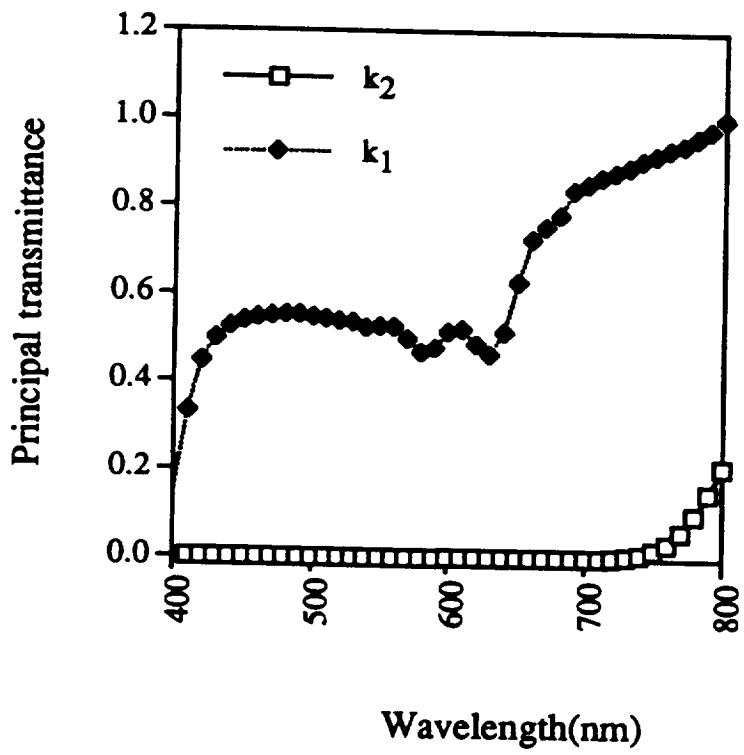


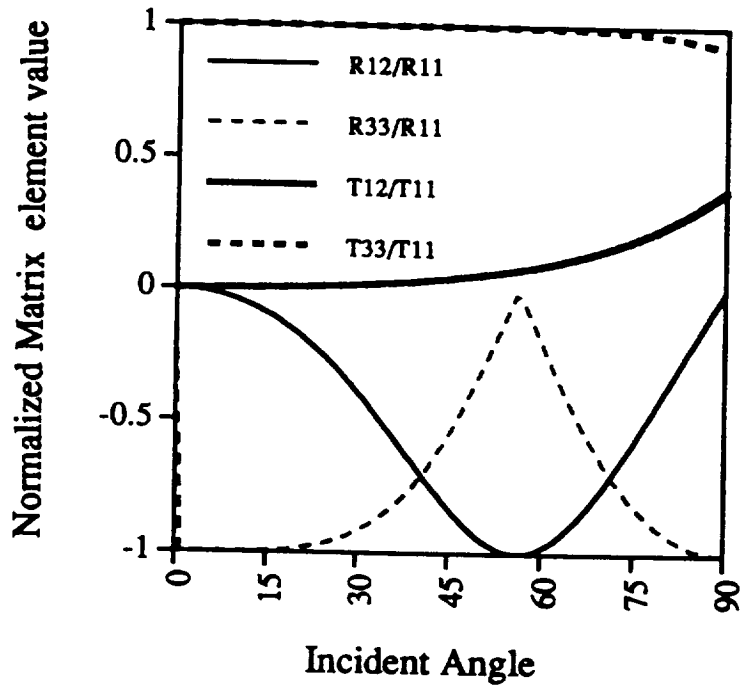


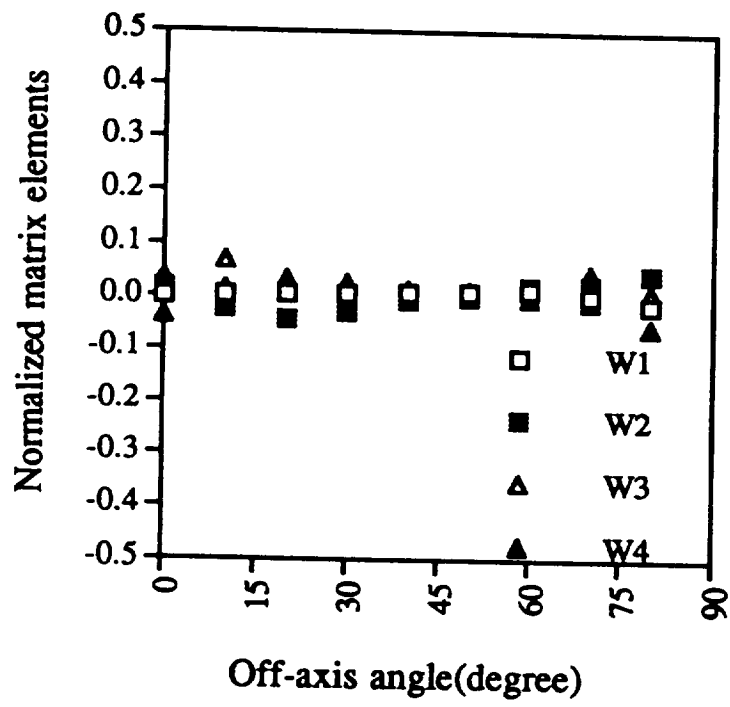


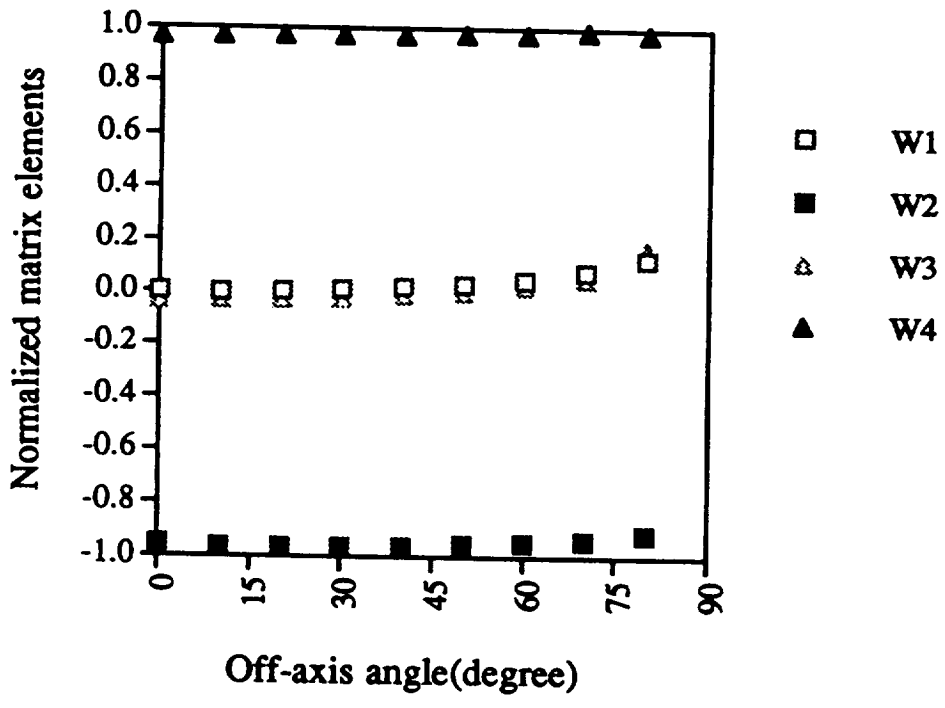


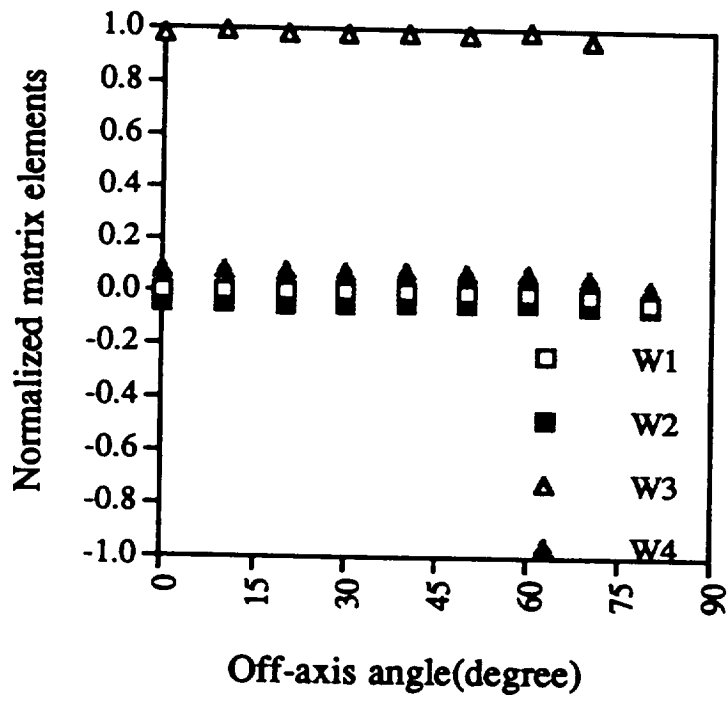


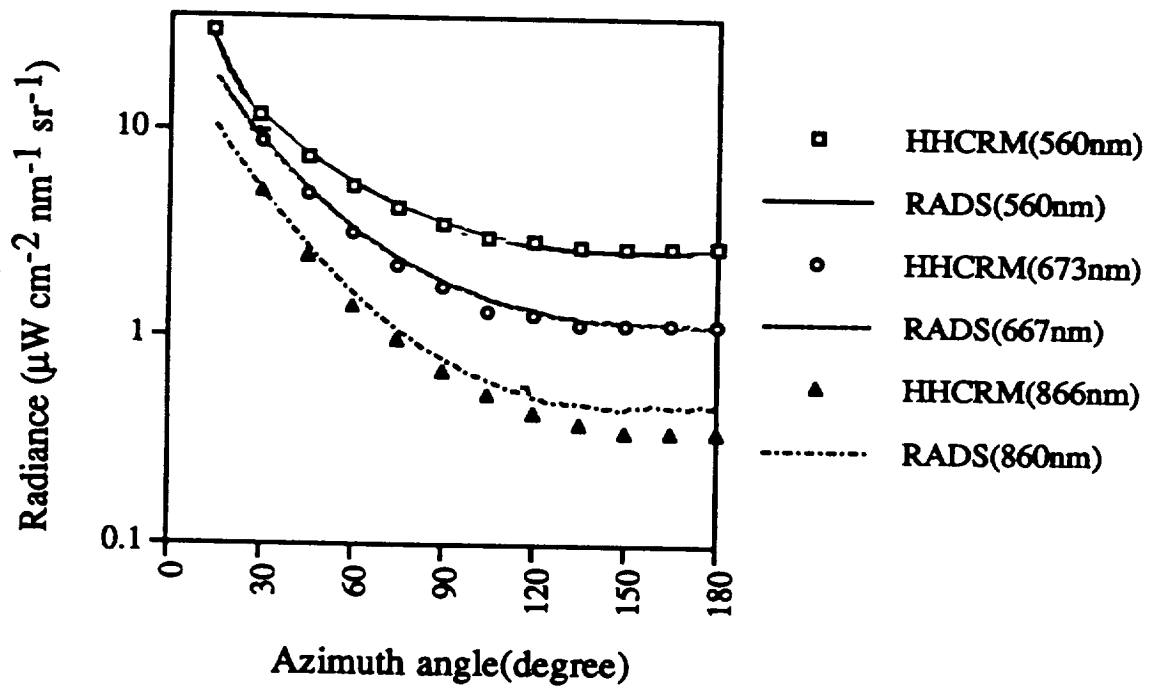


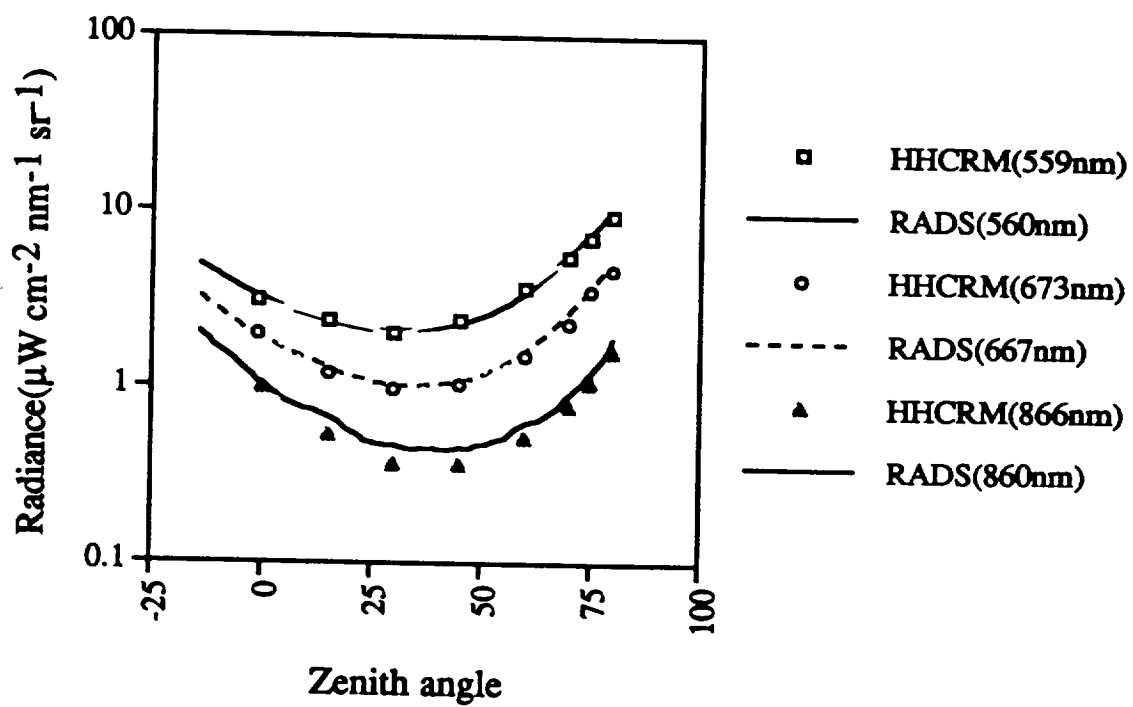


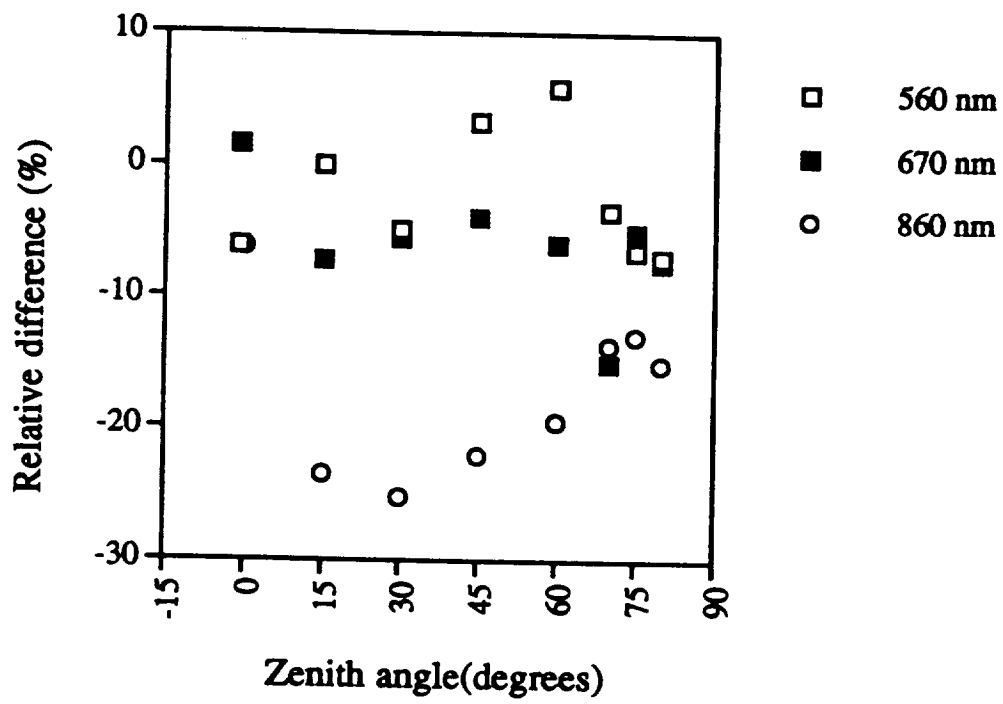


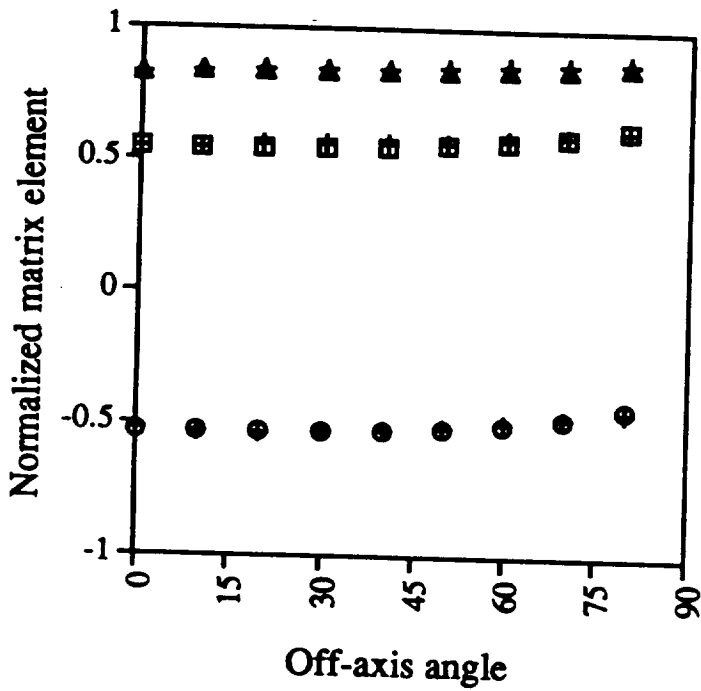




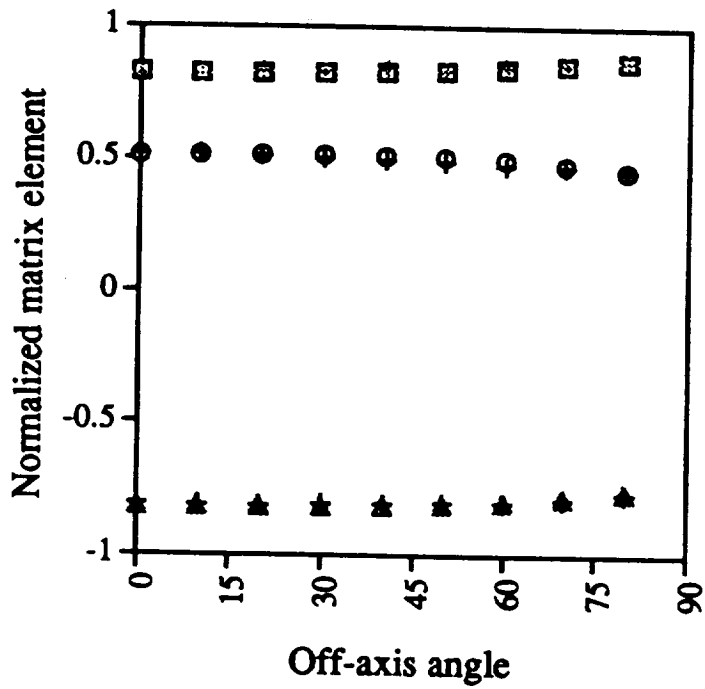




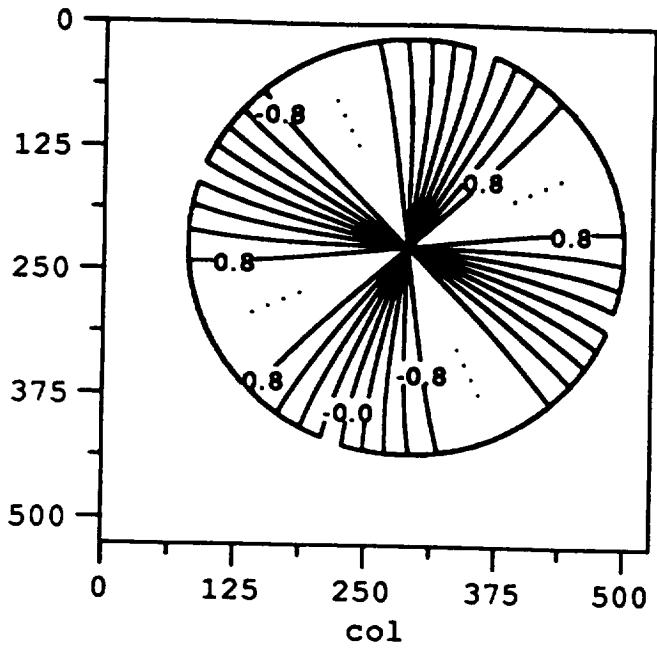


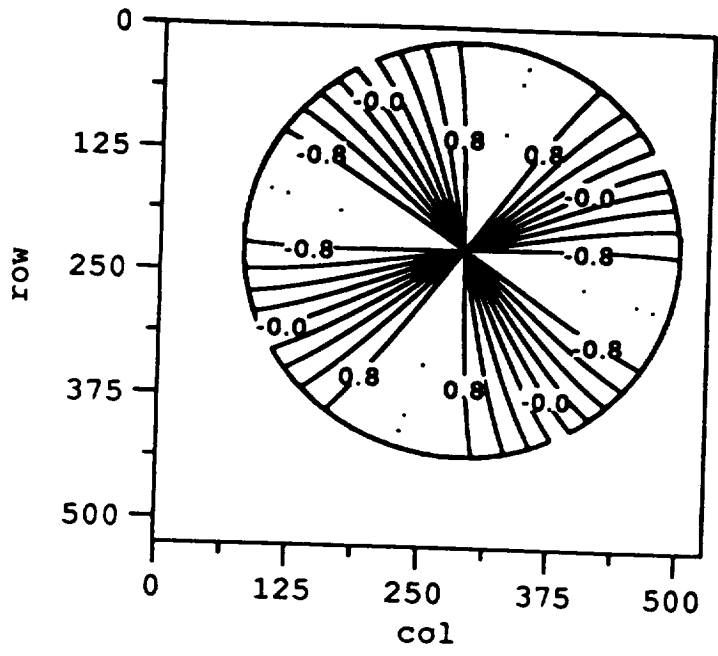


- + m12(W2) matrix transformation
- o m12(W2) direct measurement
- + m12(W3) direct measurement
- Δ m12(W3) matrix transformation
- + m12(W4) direct measurement
- m12(W4) matrix transformation



- + m13(W2) matrix transformation
- m13(W2) direct measurement
- + m13(W3) direct measurement
- m13(W3) matrix transformation
- + m13(W4) direct measurement
- △ m13(W4) matrix transformation





Appendix 6

Polarized radiance distribution measurements of skylight: Part 2, experiment and data

Polarized Radiance Distribution Measurement of Skylight: Part 2, Experiment and Data

Yi Liu

Research and Data System Corporation
7833 Walker Drive Suite 550
Greenbelt, MD 20770

and Kenneth Voss,
Physics Department
University of Miami
P. O. Box 248046
Coral Gables, FL 33124

ABSTRACT

Measurements of the skylight polarized radiance distribution were performed at different measurement sites, atmospheric conditions, and three wavelengths using our newly developed Stokes polarimeter (RADS-IIP). Three Stokes parameters of skylight (I, Q, U), the degree of polarization, and the plane of polarization are presented in image format. The Arago point and neutral lines have been observed using RADS-IIP. Qualitatively the dependence of the intensity and polarization data on wavelength, solar zenith angle, and surface albedo is in agreement with the results from computations based on a plane parallel Rayleigh atmospheric model.

Key words: Stokes polarimeter, degree of polarization, neutral point, skylight

1. Introduction

Polarization is an intrinsic property of the light field. Solar radiation as a natural light source is not polarized before it enters the atmosphere. The natural light field is polarized

through scattering interactions^{1,2} with the atmospheric constituents, such as the permanent gases (N₂, O₂, etc.), gases with variable concentration (O₃, SO₂, etc.), and various solid and liquid particles (aerosols, water, and ice crystals). The pattern of sky-light polarization³ is related to the sun's position, the distribution of various components of the atmosphere, and the under-lying surface properties. Since the discovery of sky-light polarization by Arago in 1809, observations of sky-light polarization have been related to the studies of atmospheric turbidity^{4,5,6} and surface properties.⁷ The recent development of the Polarization Radiance Distribution Camera System^{8,9} provides a new method to observe the sky-light polarization and can provide the spectral polarized radiance distribution over the whole hemisphere quickly and accurately.

It has been generally recognized that the principal features of the brightness and polarization of the sunlit sky can be explained in terms of Rayleigh scattering by molecules in the atmosphere.³ Modern radiative transfer theory investigating polarization^{1,2,10} has been applied to studies on planetary atmospheres^{11,12} as well as the earth-ocean system.^{13,14,15} Understanding the intensity and polarization of light in the atmosphere is also important in atmospheric correction of the remotely sensed data. The atmospheric correction algorithm developed for the Coastal-Zone Color Scanner (CZCS) imagery^{16,17} is most easily understood by first considering only single scattering, including contributions arising from Rayleigh scattering and aerosol scattering. The analysis of multiple scattering effects was based on scalar radiative transfer computations in model atmospheres.¹⁸ Recent advancements^{19,20} solved the exact (vector) radiative transfer equation to compute the scalar radiance. Neglecting the polarization in radiance calculations in an atmosphere-ocean system will introduce errors as large as 30%.²¹ Measurements of the total sky polarized radiance distribution can be used to test the validity of vector radiative transfer models. Through inversion techniques it can also be used in the determination of physical and optical properties such as the absorption and scattering phase function of aerosols²² which

can not be done directly because of the difficulty in measuring the scattering phase function²³ and the single-scattering albedo.²⁴

2. Background

Although scattering in the real atmosphere is more complicated than Rayleigh scattering, knowledge of the intensity and polarization of light in a plane parallel Rayleigh atmosphere is very important for discussion of the skylight. While quantitatively different, radiance distributions resulting from Rayleigh and Rayleigh-aerosol conditions exhibit similar variation with sun elevation, atmospheric turbidity and other parameters.³

A. Intensity of Skylight in a Model Atmosphere

To illustrate the dependence of the intensity of light in a model atmosphere on the surface properties, computations using Gordon's successive order approximation¹⁹ (including polarization) in a Rayleigh atmosphere with a Fresnel reflecting surface was performed at a sun zenith angle of 53.1 degrees and at optical depths of 0.05, and 0.25. Light intensities on the principle plane are shown in Fig. 1 and compared with results from Coulson et al.¹¹ for the same atmosphere with a lambertian reflecting surface. The surface reflectances, R , are displayed on the graph. As can be seen, a Fresnel surface will increase the skylight intensity only slightly above a totally absorbing surface ($R=0$). A lambertian surface reflectance of 0.25 affects the radiance distribution much more, as will be seen in our experimental data.

In Fig. 1, the radiance has been normalized to the solar constant. It can be seen that the normalized radiance increases as the reflectance increases due to light being reflected from the surface. The normalized radiance also increases as the optical thickness increases. At this point it is worth noting that the separation between lines with different surface reflectances becomes larger as the optical thickness increases.

Since the skylight radiance for a clear atmosphere is dependent on both atmospheric turbidity and surface albedo, it is useful to look at the skylight measurements that have been made at various geographic locations and times. We have chosen cases in which cloud interference was absent or minimum.

B. Polarization of Skylight in a Model Atmosphere

The principal interest in measurements of skylight polarization is its sensitivity to dust, haze, and pollution in the atmosphere.^{25,26} The maximum degree of polarization is diminished by the effects of aerosol scattering, and at the same time the neutral points ($Q=0, U=0$, defined below) of the polarization field are shifted from their normal positions. To illustrate how the degree of polarization and its maximum varies with surface properties and optical thickness, we will first look at computational results of a Rayleigh atmosphere using the plane parallel model.³ These changes will be investigated with experimental data in next section.

Figure 2 illustrates the degree of polarization in the principal plane (azimuth angle 180 degrees) with a sun zenith angle of 53.1 degrees. The data were taken from tables computed by Coulson et al.¹¹ As can be seen, the degree of polarization has a strong dependence on surface properties and optical thickness. As the surface reflectance or optical thickness increases, the degree of polarization decreases accordingly. The Fresnel reflecting surface case was not shown, as the degree of polarization over a Fresnel reflecting surface is only slightly larger than that over a totally absorbing surface.

A convenient representation of the polarization of a light beam is the Stokes vector.² The four components of this vector, labeled I, Q, U, and V, are defined in terms of the electric field.^{8,9} Simply these may be defined as:

$$\begin{aligned} I &= I_1 + I_r \\ Q &= I_1 - I_r \\ U &= I_{45} - I_{135} \end{aligned}$$

$$V = I_{rc} - I_{lc}$$

where I_r is the intensity of light polarized in a reference plane, I_l is the intensity of light polarized perpendicular to this reference plane, I_{45} and I_{135} is the intensity of light polarized in a plane 45 and 135 degrees to the reference plane, and finally I_{rc} and I_{lc} are the right and left circularly polarized intensities. Other parameters, used to describe the polarized light field, will be defined. The linear degree of polarization is defined as $\sqrt{(Q^2 + U^2)} / I$. The importance of the Stokes parameters Q and U in the atmosphere is that they define the polarization state of the atmosphere.

The neutral points are points where the degree of polarization is zero. Neutral points are then characterized by the double requirement $Q=0$ and $U=0$. For a lambertian surface these requirements are only met simultaneously at points on the principal plane. The Arago point is located above the anti-solar point. Two other points, the Babinet and Brewster points are located above and below the sun. Since the RADS-IIP instrument can not measure the part of the sky in which the Babinet and Brewster points occur due to an occulter, we will restrict our discussions to the Arago point. Neutral points can be outside the principal plane over a still water surface due to Fresnel reflections from the air-water interface.^{27,28} Neutral points can also depart from their normal observed positions due to light scattering by dust, haze, and other aerosols²⁵, which suggest that neutral point positions are sensitive indicators of atmospheric turbidity.³

The lines which separate the regions of positive Q from the regions of negative Q are called neutral lines. Another parameter which can be deduced from the polarization field is the angle of the plane of polarization χ . χ , defined by $U = Q \tan(2\chi)$, is the angle between the plane of polarization and the vertical plane at the relevant azimuth. By symmetry, χ must be ± 90 degrees on the principal plane, depending on whether Q is positive or

negative, in either case $U = 0$. Also, when χ is zero, U is zero. Neutral lines, lines of $U=0$, and χ are particularly important to the examination of radiative transfer models.

3. Experiment and Data

A. Method of Measurement

The measurements of the polarization radiance distribution were all made with the Polarization Radiance Distribution Camera System (RADS-IIP)^{8,9} at the following wavelengths: 439, 560, 667 nm. In normal operation, the analyzer is at each of three polarizer positions and an image obtained. The resulting data images, plus a dark count image taken with the shutter closed, constitute the basic data of one measurement. The overall time period for one complete measurement is 2 minutes. After correction for dark counts, the three data images are analyzed, and values of the Stokes vectors are computed and saved in image format. The degree of polarization and angle of the plane of polarization can also be calculated and displayed in image format. Measurement errors arise from errors in the recorded light intensity and the calibrated Mueller matrix elements. The uncertainties in recorded light intensities are due to (1) measurements taken in a series that extends about 1.5 minutes, ideally we should take measurements at the same time, and (2) unavoidable stray light and noise in the optical and electronic system. Normally skylight does not change significantly in 1.5 minutes especially when the sun elevation is high. Stray light and noise has been accounted for to the best of our abilities and as shown in comparisons with other instrument.⁸ An analytical estimate shows the error in determination of the Mueller matrix elements can reach a maximum of 2%. To minimize the blooming effect caused by the direct solar radiation and the limited dynamic range of the system, a sun occulter has been adopted in our system to block the direct solar radiation.

This occulter also blocks a portion of the sky, as a result, there is a portion of the data not available on all data images on the sun's half of the atmosphere.

B. Description of Measurement Sites

The RADS-IP polarimeter was deployed on top of JLK physics building on the main campus of University of Miami on Feb. 12, 1996 and on the top of the Science and Administration building (SLAB) at Rosenstiel School of Marine and Atmospheric Sciences (RSMAS) on Feb. 5, 1996 (at approximately 25° 43' N and 80° 16' W). The aerosol optical depths (AOD) for these days are shown in Fig. 3. The AOD measurements were made with a shadowband radiometer.²⁹ It can be seen that AOD varies with wavelength and time.

Feb. 12 was a very clear day and the surrounding area corresponds to a typical urban area. Buildings, vegetation, and surfaces of varied reflectances surround the site. Measurements taken on Feb. 5 have different features (Fig. 4), southeast of the site is water and northwest is land (including buildings, vegetation, and sand). On that day, there were clouds early in the morning and late in the afternoon, clear sky conditions occurred between 10:00 AM to 2:00 PM.

C. Radiance Distribution of Skylight

The data taken on Feb. 12 are shown first. In these cases, measurements of the sky radiance distribution were taken at 3 wavelengths (439, 560 and 667 nm) and typical data are shown in contour plots. Only 439 nm and 667 nm are shown for brevity. Figures 5a, 5b, and 5c are contour plots of radiance distribution at 439 nm (solar zenith angle 45.3°), 667 nm (solar zenith angle 47.2°), and 439 nm (solar zenith angle 77°) respectively. In these images the center is the zenith direction, the zenith angle is directly proportional to radius from the center. The bold circular lines are at 30 and 60 degree zenith angles. The units are $10^{-2} \mu\text{W} / (\text{nm cm}^2 \text{sr})$. On the solar half of the hemisphere the rectangular area on the right of the image is the sun occulter, used to block the direct solar radiation.⁸ In

general, for all three wavelengths, the minimum radiances appear on the antisolar half of the hemisphere. As the wavelength increases, the absolute values of the minimum region decreases. This reflects the wavelength dependence of Rayleigh scattering and explains the blue sky. It is important to note that the symmetry to the sun's principal plane exists in these images due to being over an approximately uniform reflectance background. One can also note the increase in radiance at the horizon due to the increased effective atmospheric path length at the horizon. As the sun-zenith angle increases, the absolute radiances decrease at all wavelength bands and the minimum regions shift with the sun.

Measurements were also performed on Feb. 5 on top of the Science and Administration (SLAB) building at RSMAS to investigate the effect of surface inhomogenities on the measurement. The major features are similar to the Feb. 12 data set. The area southeast of the measurement site at RSMAS is water and northwest is land. Feb. 5 was immediately after a cold front passed through Miami and the optical depths were higher than those on Feb. 12. It was cloudy early in the morning and late in the afternoon. Skylight intensity is significantly higher due to higher optical depth. Figure 6a is a contour plot of light intensity at 439 nm (solar zenith angle 46.3°) and figure 6b is at 667 nm (solar zenith angle 44.7°). On both graphs, the minimum intensity regions are shifted toward the direction over the water and thus destroy the symmetry to the principal plane. This shift from the principal plane decreases as the wavelength increases. The shift can be explained since a Fresnel reflecting surface (water) only increases the skylight intensity slightly but a surface with $R=0.25$ (approximates land) has a large effect (Fig. 1).

D. Stokes Parameter Q and Neutral Lines

Figures 7a -7c show the contour plots of the Stokes parameter Q for the images shown in Figs. 5a-5c. These demonstrate how Q changes with wavelength and sun angle. The numbers shown on the graphs are first normalized to the intensity and multiplied by 1000. They all show good symmetry to the principal plane as expected from a plane parallel

model and the uniform surface. The deviation from this symmetry mainly appears on the sun's half of the atmosphere. Neutral lines (designated with number 0) are formed clearly on the hemisphere opposite to the sun. Parts of neutral lines are also formed on sun's half of the atmosphere but large parts of these lines have been blocked due to the sun occulter. The minimum Q (negative number) appears on the principal plane and 90 degrees from the solar position. Tables 1 and 2 list the minimum Q's on the principal plane. Q is negative inside the neutral lines but positive outside and the maximum contours are symmetric to the principal plane and expand with the increasing solar zenith angle. As the solar zenith angle increases, neutral lines shrink significantly but still keep the similar shape and form a closed line. The contours crossing the principal plane seem to be dragged towards the zenith and their shapes change significantly.

E. Stokes Parameter U and Lines of $U=0$

Figures 8a - 8c show the contour plots of the Stokes parameter U for the images shown in Figs. 5a-5c. These demonstrate the change in U with wavelength and sun angle. The numbers shown on the graphs are first normalized to the intensity and multiplied by 1000. The Stokes parameter U is anti-symmetric to the principal plane, $U=0$ lines only appear on the principal plane and on the sun's half of the atmosphere. This is in agreement with the computation results using a plane parallel Rayleigh atmosphere model.³ In the contour plots shown, since the sky in the vicinity of the sun has been blocked, a closed $U=0$ lines are not shown but the parts of lines shown suggest this trend. Again the deviation from anti-symmetry seems to occur on sun's side of the atmosphere. The maximum regions (both negative and positive) occur on the half of the atmosphere opposite the sun. As the solar zenith angle increases, these contours displace towards the zenith and their shapes are deformed. As the wavelength increases, for constant solar zenith angle, the maximum region expands, which implies larger degrees of polarization at longer wavelength. Table 3 lists the maximum U's. Notice that when the sun is low, the $U=0$ line on the principal

plane has deflected from a straight line and bends close to the horizon. This phenomenon is not seen in a Rayleigh scattering plane parallel model with a uniform surface. A possible explanation could be that water is southeast of the measurement site. As the sun was setting (west, azimuth angle around 247 degrees from true north for graphs shown) the $U=0$ lines shift towards the part of the atmosphere where the polarization is influenced by reflection from water. When the sun was high, the water body was under the sun's half of the atmosphere and had a negligible effect.

F. Degree of Polarization and Neutral Points

Figures 9a - 9c show the contour plots of the degree of polarization, P , for the images shown in Figs. 5a-5c. These demonstrate how P changes with wavelength and sun angle. The numbers shown on the graphs have been normalized to the radiances and then multiplied by a factor of 1000. The degree of polarization shows very good symmetry to the principal plane. Starting from the position of the sun (figure 9), the degree of polarization increases as the primary scattering angle increases. The maximum values occur in the region where the primary scattering angle is 90 degrees from the sun, this is in agreement with our earlier discussion using a plane parallel model. Following the maximum region, the degree of polarization decreases as scattering angle increases. The maximum degree of polarization is larger for longer wavelength. Since the Rayleigh optical thickness is smaller for longer wavelengths, light in the longer wavelengths suffers less multiple scattering thus a larger maximum degree of polarization.

Tables 4 and 5 lists the maximum P on the principal plane. As in the real atmosphere, light interacts with aerosol particles as well as molecules, the degree of polarization deviates from the predictions of a simple Rayleigh atmosphere model. As the solar zenith angle increases, while the maximum degree of polarization moves with the sun to maintain a scattering angle of 90 degrees, new contours are formed around a point on the principal plane at which a minimum value in degree of polarization is shown. This point is the

Arago point described later. As the solar zenith angle increases, the degree of polarization also increases for all three wavelengths in accord with the theoretical expectations.¹¹ Another feature of the contour plot at lower sun elevation is the deviation from symmetry, this could be caused by light reflected by the water and then scattered into the measurement site as compared with light reflected by land, as discussed earlier.

Figure 10 plots all Arago points observed at various sun angles and at three wavelength bands. The position of the neutral points are measured in angular distance from the antisolar point. It can be seen that this angular distance increases as the solar elevation increases. The observed neutral points are at larger angles than the positions computed using a Rayleigh atmosphere with a totally absorbing surface. In Fig. 10, the total optical depths are listed for each channel. The difference between the observed value and the computed value is due to light scattering by aerosols and surface reflections.

G. Plane of Polarization

Figures 11a - 11 c show the contour plots of the angle of plane of polarization, χ , for the images shown in Figs. 5a-5c. The numbers shown on the graphs have been multiplied by a factor of 100. These contour plots can be best understood when compared with the corresponding Q and U plots shown. At first let us point out that the heavy lines on the principal plane are an artifact of the contour program. χ is antisymmetric to the principal plane thus on each side of the principal plane χ approaches either 90 degrees or -90 degrees. The contour program sees an abrupt change of 180 degrees when crossing the principal plane and adds many lines close to the principal plane. χ is ± 45 degrees at the neutral lines and zero at lines of $U=0$ except in the principal plane. As the wavelength changes, χ changes according to the changes of Q and U. As the sun's elevation decreases, the contour on the half of the hemisphere opposite the sun shrinks significantly

while the contour on the sun's side expands. When the sun is low, the Arago point appears and some contours will go into the neutral point.

H. Degree of Polarization Influenced by Measurement Site and Aerosols

As mentioned previously, the measurement site at RSMAS is special because the southeast is water but the northwest is land (Fig. 4). This results in a change in the skylight distribution (Figs. 6a, 6b). To illustrate how these factors affect the polarization, contour plots of the degree of polarization have been chosen at 439 (Fig. 12a), and 667 nm (Fig. 12b). Though the region where the maximum degree of polarization occurs is 90 degrees from the sun in general, the maximum in the region most likely affected by water has higher values than the region most likely affected by land. This deviation from symmetry is because the degree of polarization over a Fresnel reflecting surface is much higher than the degree of polarization over a Lambertian reflecting surface. As the wavelength increases, the degree of polarization increases also. Comparing Figs. 9a and 9b with Figs. 12a and 12b, the degree of polarization is much lower on Feb. 5 (Figs. 12a and 12b) than on Feb. 12 (Figs. 9a and 9b) due to the higher aerosol optical thickness. Light scattered by aerosols is not as highly polarized as in the case of Rayleigh scattering and adding aerosols will result in a higher chance of multiple scattering. Table 6 lists the maximum degree of polarization (P).

4. Conclusions

Although various aspects of the intensity and polarization in the sunlit atmosphere have been studied in the past, rapid measurements of the absolute skylight polarization radiance distribution over the whole hemisphere have not been possible previously. In this paper, measurements of skylight polarized radiance distribution were performed at different measurement sites, different atmospheric conditions, and three different wavelengths.

Qualitatively the radiance and polarization data are in agreement with the results from computations based on a plane parallel Rayleigh atmosphere model.

The ability of RADS-IIP to give polarization radiance distributions has great application potential in studies of atmospheric aerosols as well as radiative transfer problems in the earth-ocean system due to the fact that data can be taken in a short time thus changes in the atmosphere during measurement can be avoided. The neutral point (Arago point) appearing in the data suggests the potential to detect other neutral points if a smaller sun occulter is adopted. Since anomalous neutral point positions²⁸ have been predicted to occur over a still water surface, RADS-IIP can also be used to detect this effect. In the future, data will be compared with computed data based on realistic atmospheric models (including aerosols and surfaces) and used to validate the models and investigate the optical properties of aerosols.

Acknowledgments

The authors would like to acknowledge the support of the Ocean Optics Program at ONR, under grant N000149510309 and NASA under NAS5-31363. Also we would like to thank Dr. H. R. Gordon's support in computation and Mr. Judd Welton's support in optical depths' measurement. One of the authors, Yi Liu, would like to acknowledge University of Miami for providing University fellowship during the course of this work.

References

1. K. N. Liou, *An Introduction to Atmospheric Radiation*, Academic Press, Inc. (1980).
2. H. C. Van de Hulst, *Light Scattering by Small Particles*, Dover Publications, Inc. (1981).
3. K. L. Coulson, *Polarization and Intensity of Light in the Atmosphere*, A. DEEPAK publishing, Hampton, Virginia, USA. (1988).
4. H. H. Kimball, "The effect of the atmospheric turbidity of 1912 on solar radiation intensities and skylight polarization," *Bul. Mt. Weather Observatory*, **5**, 295-312 (1913).
5. T. Takashima, H. S. Chen, and C. R. N. Rao, "Polarimetric investigations of the turbidity of the atmosphere over Los Angeles," in T. Gehrels (ed.), *Planets, Stars, and Nebulae Studied with Photopolarimetry*, Univ. of Arizona Press, 500-509 (1974).
6. K. L. Coulson, "Characteristics of skylight at the zenith during twilight as indicators of atmospheric turbidity: I: Degree of Polarization," *Appl. Opt.*, **19**, 3469-3480 (1980).
7. K. L. Coulson, "The polarization of light in the environment," in T. Gehrels (ed.), *Planets, Stars, and Nebulae Studied with Photopolarimetry*, Univ. of Arizona Press, 444-471 (1974).
8. Y. Liu, "Measurement of the intensity and polarization of light in the atmosphere", Ph. D. dissertation, University of Miami (1996).
9. K. J. Voss and Y. Liu, "Polarized Radiance Distribution of Skylight: Part 1, System Description and Characterization," submitted to *Applied Optics*. (1997).
10. S. Chandrasekhar, *Radiative Transfer*, Clarendon Press, Oxford (1950).
11. K. L. Coulson, J. V. Dave, and Z. Sekera, *Tables Related to Radiation Emerging From a Planetary Atmosphere with Rayleigh Scattering*, University of California Press, Berkeley and Los Angeles (1960).

12. J. W. Chamberlain, *Theory of Planetary Atmospheres*, 22, Int. Geophys. Series, Academic Press, New York (1978).
13. G. N. Plass and G. W. Kattawar, "Polarization of the radiation reflected and transmitted by the earth's atmosphere," *Appl. Opt.*, 9, 1122-1130 (1970).
14. G. W. Kattawar, G. N. Plass, and J. A. Guinn, Jr. "Monte Carlo calculations of the polarization of radiation in the earth's atmosphere-ocean system," *J. Phys. Oceanogr.* 3, 353-372 (1973).
15. G. W. Kattawar and C. N. Adams, "Stokes vector calculations of the submarine light field in an atmosphere-ocean with scattering according to a Rayleigh phase matrix: effect of interface refractive index on radiance and polarization," *Limnol. Oceanogr.*, 34, 1453-1472 (1989).
16. H. R. Gordon, "Removal of atmospheric effects from satellite imagery of the oceans," *Appl. Opt.*, 17, 1631-1636 (1978).
17. H. R. Gordon, J. L. Mueller, and R. C. Wrigley, "Atmospheric correction of Nimbus-7 Coastal Zone Color Scanner imagery," in *Remote Sensing of Atmospheres and Oceans*, A. Deepak, Ed. (Academic, New York), 457-483 (1980).
18. H. R. Gordon and D. J. Castano, "Coastal Zone Color Scanner atmospheric correction algorithm: multiple scattering effects," *Appl. Opt.*, 26, 2111-2122 (1987).
19. H. R. Gordon and M. Wang, "Surface-roughness considerations for atmospheric correction of ocean color sensors. I: The Rayleigh scattering component," *Appl. Opt.*, 31, 4247-4260 (1992).
20. H. R. Gordon and M. Wang, "Surface-roughness considerations for atmospheric correction of ocean color sensors. II: Error in the retrieved water-leaving radiance," *Appl. Opt.*, 31, 4261-4267 (1992).

21. C. N. Adams and G. W. Kattawar, "Effect of volume-Scattering function on the errors induced when polarization is neglected in radiance calculations in an atmosphere-ocean system," *Appl. Opt.*, **32**, 4610-4617 (1993).
22. M. Wang and H. R. Gordon, "Retrieval of the columnar aerosol phase function and single-scattering albedo from sky radiance over the ocean: simulations," *Appl. Opt.*, **32**, 4598-4609 (1993).
23. M. Nakajima, M. Tanaka, M. Yamano, M. Shiobara, K. Arao, and Y. Nakanishi, "Aerosol optical characteristics in the yellow sand events observed in May 1982 at Nagasaki--Part II Models," *J. Meteor. Soc. Jpn*, **67**, 279-291 (1989).
24. H. E. Gerber and E. E. Hindman, eds., *Light Absorption by Aerosol Particles*, Spectrum, Hampton (1982).
25. Z. Sekera, "Recent developments in the study of the polarization of skylight," *Adv. in Geophys.*, **3**, 43-104, Academic Press, New York (1956).
26. K. Bullrich, "Scattered radiation in the atmosphere and the natural aerosol," *Adv. in Geophys.*, **10**, 99-260, Academic Press (1964).
27. R. S. Fraser, "Atmospheric neutral points over water," *J. Opt. Soc. Am.*, **58**, 1029-1031 (1968).
28. R. S. Fraser, "Atmospheric neutral points outside of the principal plane," *Contrib. Am. Phys.*, **54**, 286-297 (1981).
29. J. J. Michalsky, R. Perez, and R. Stewart, "Design and development of a rotating shadowband radiometer solar radiation/daylight network," *Solar Energy*, **41**, 577-581. (1988)

Figure Captions

Figure 1. Normalized radiance on the principal plane with an azimuth angle of $\phi=180^\circ$ and solar zenith angle of 53.1° . Data are shown for two optical depths, 0.05 and 0.25. Data with Lambertian surface are from Coulson et al.¹¹

Figure 2. Degree of polarization at various optical depths, from Coulson et al.¹¹

Figure 3. Aerosol optical depth (AOD) as a function of time on Feb. 5 and Feb. 12, 1996.

Figure 4. Illustration of the measurement site at RSMAS, used on Feb. 5, 1996.

Figure 5. Contour plots of skylight radiance. The data shown were taken on top of the JLK physics building at University of Miami on Feb. 12, 1996. The origin of the coordinate shown corresponds to the zenith and the inner and outer circles to 30° and 60° zenith angles respectively. (a) Measurement wavelength is 439 nm, solar zenith angle is 45.3 degrees, AOD(410 nm) is 0.17. (b) Measurement wavelength is 667 nm, solar zenith angle is 47.2 degrees, and AOD(410 nm) is 0.20. (c) Measurement wavelength is 439 nm, solar zenith angle is 77 degrees, and AOD(410 nm) is 0.14.

Figure 6. Contour plots of skylight radiance. The data shown were taken on top of the Science/Administration building at RSMAS on Feb. 5, 1996. (a) Measurement wavelength is 439 nm, solar zenith angle is 46.3 degrees, and AOD(410 nm) is 0.35. (b) Measurement wavelength is 667 nm, solar zenith angle is 44.7 degrees, and the AOD(410 nm) is 0.30.

Figure 7. Contour plots of the Stokes parameter Q. The measurement descriptions for a, b, and c correspond to 5a, 5b, and 5c respectively.

Figure 8. Contour plot of the Stokes parameter U. The measurement descriptions for a, b, and c correspond to 5a, 5b, and 5c respectively.

Figure 9. Contour plots of the degree of polarization. . The measurement descriptions for a, b, and c correspond to 5a, 5b, and 5c respectively.

Figure 10. The observed angular distance of the Arago point from the antisolar point versus solar elevation. Data obtained on Feb. 12, 1996.

Figure 11. Contour plots of the plane of polarization. The measurement descriptions for a, b, and c correspond to 5a, 5b, and 5c respectively.

Figure 12. Contour plots of the degree of polarization. The measurement descriptions for a and b correspond to 6a and 6b, respectively.

Table 1 The minimum Q/I (x1000) on the principal plane as a function of solar-zenith angle, θ_0 , at 439 nm.

θ_0	40°	42.5°	44.5°	45.3°	52.6°	64.8°	69.3°	73.9°	77.1°
Q/I	406	438	467	535	546	564	570	569	592

Table 2 The minimum Q/I (x1000) on the principal plane.

solar zenith Angle(θ_0)	Q/I for 439 nm	Q/I for 560 nm	Q/I for 667 nm
45°	-535	-578	-584
75°	-592	-646	-638

Table 3 List of the maximum U/I (x1000).

solar zenith angle (θ_0)	U/I for 439 nm	U/I for 560 nm	U/I for 667 nm
45°	540	594	610
75°	580	640	630

Table 4 The maximum P (x1000) on the principal plane as a function of solar -zenith angle, θ_0 , at 560 nm.

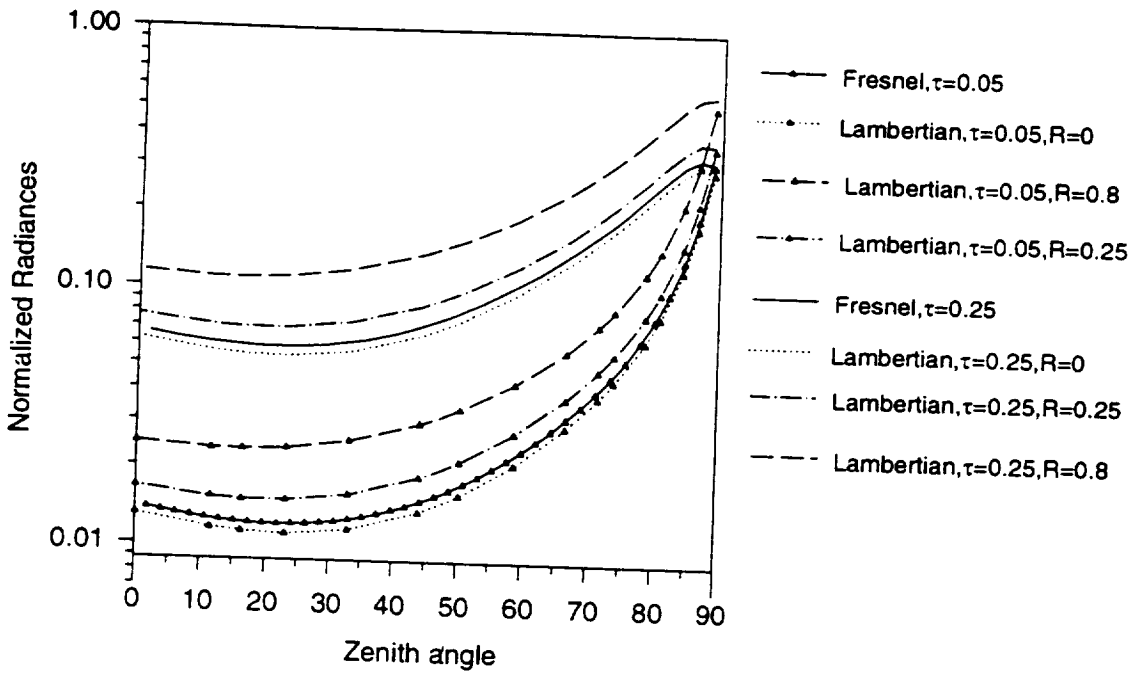
θ_0	40°	41.8°	43.9°	46.4°	53.5°	66°	70.1°	74.5°	77°
P	494	468	460	578	624	630	647	633	646

Table 5 List of the maximum P (x1000) on the principal plane.

solar zenith angle (θ_0)	P for 439 nm	P for 560 nm	P for 667 nm
44°	535	578	584
75°	592	646	638

Table 6 Illustration of the maximum degree of polarization ($\theta_0=45^\circ$). PP represents principal plane, MP represents the maximum P in the image.

Date, region	AOD at 410 nm	P at 439 nm	P at 560 nm	P at 667 nm
Feb. 12, PP	0.20	535	578	584
Feb. 5, PP	0.35	301	355	420
Feb. 5, MP	0.35	400	456	510



lis & Voss Figure 1

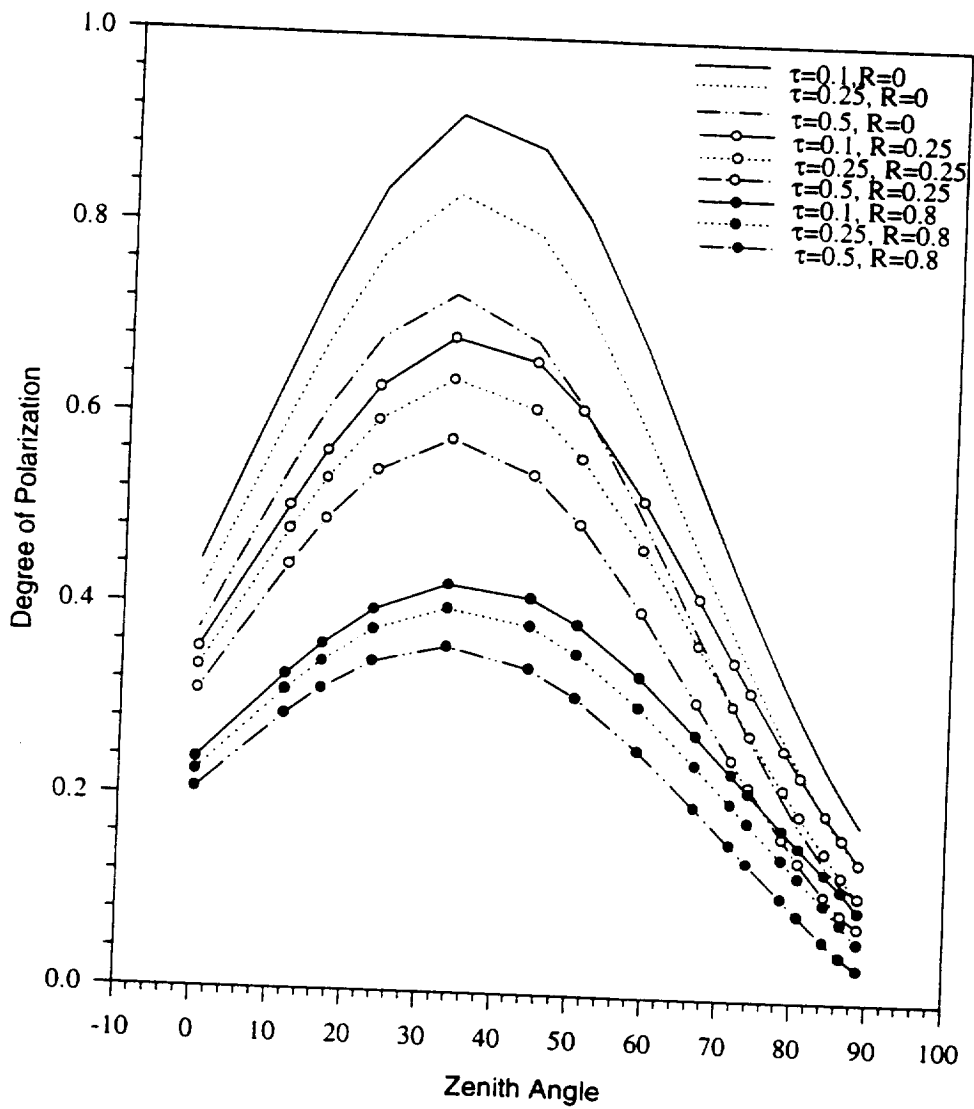
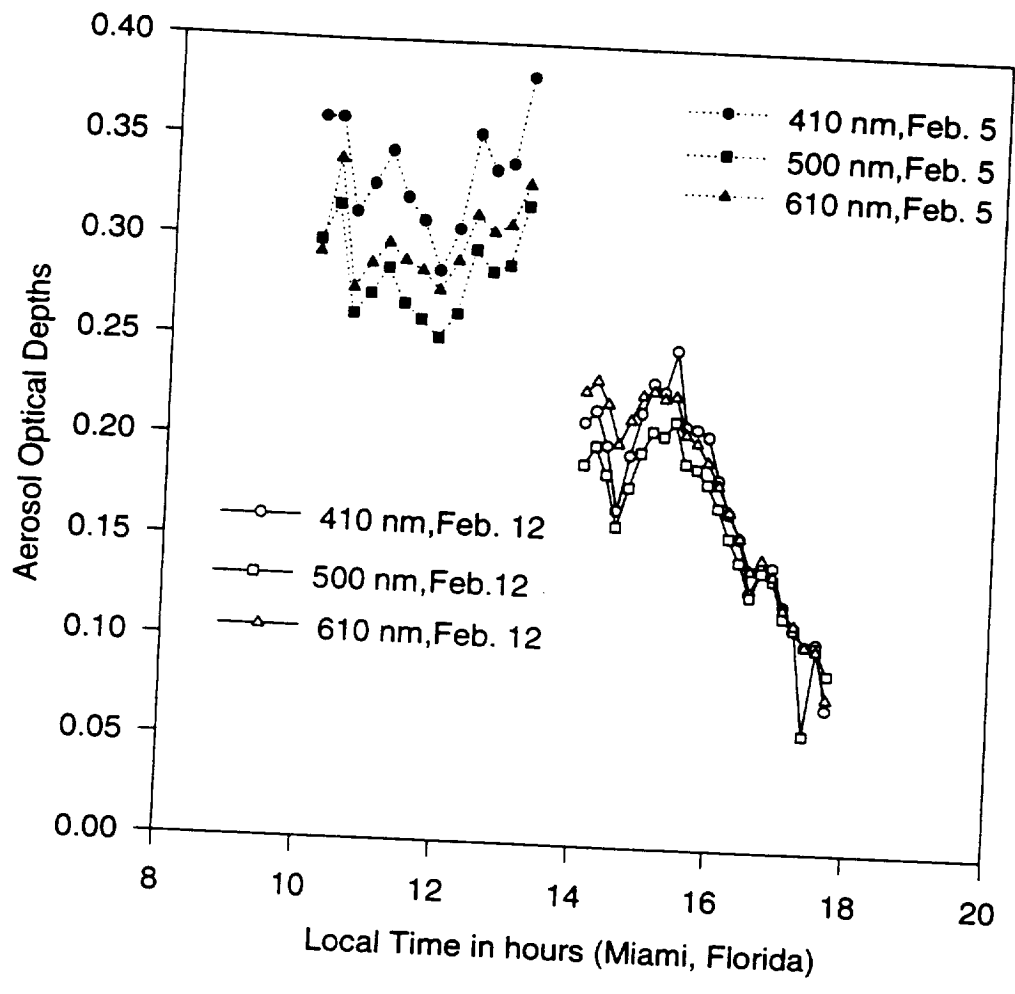
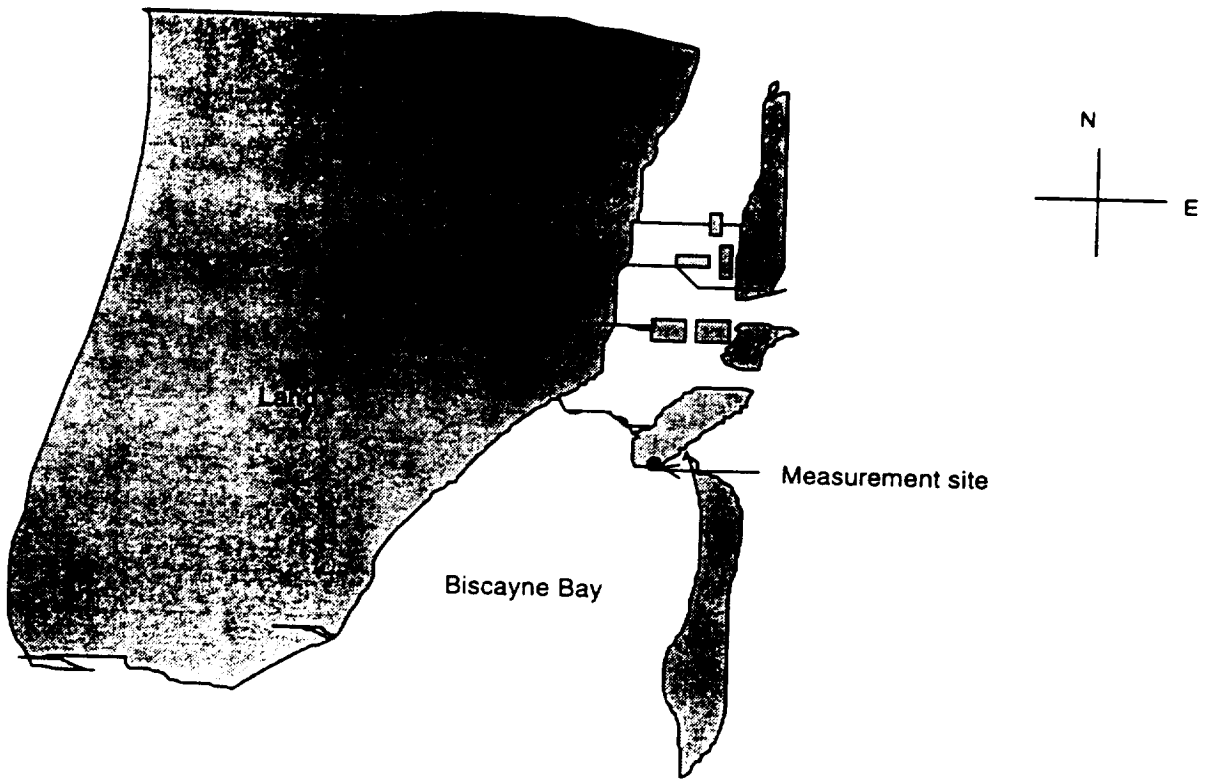
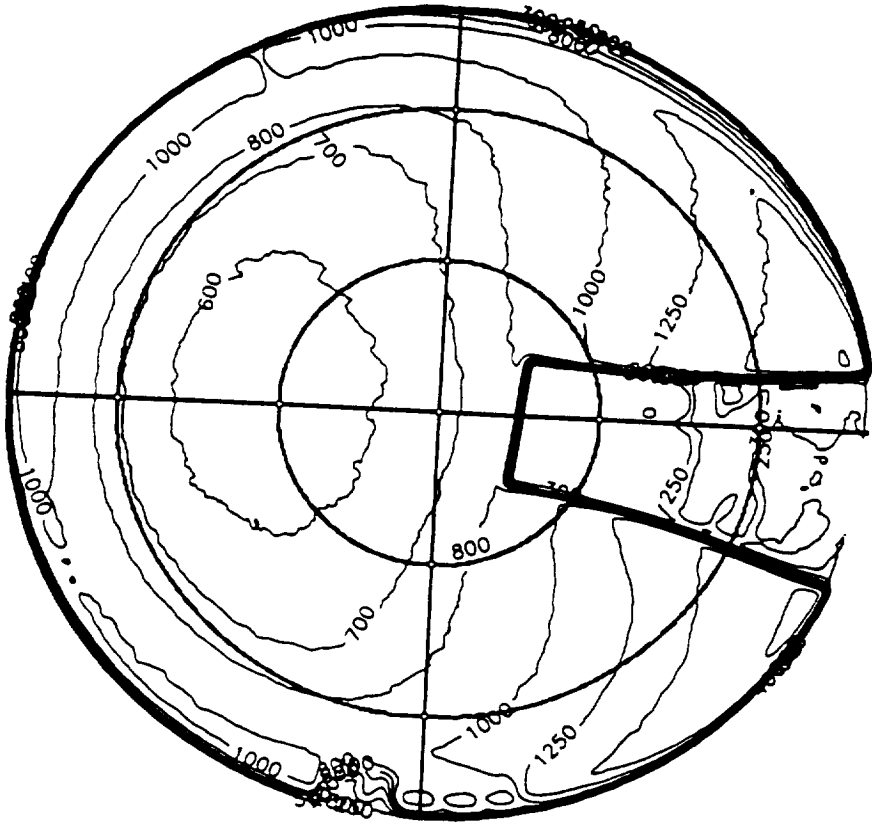


Fig. 6.7 Degree of polarization at various optical depths.

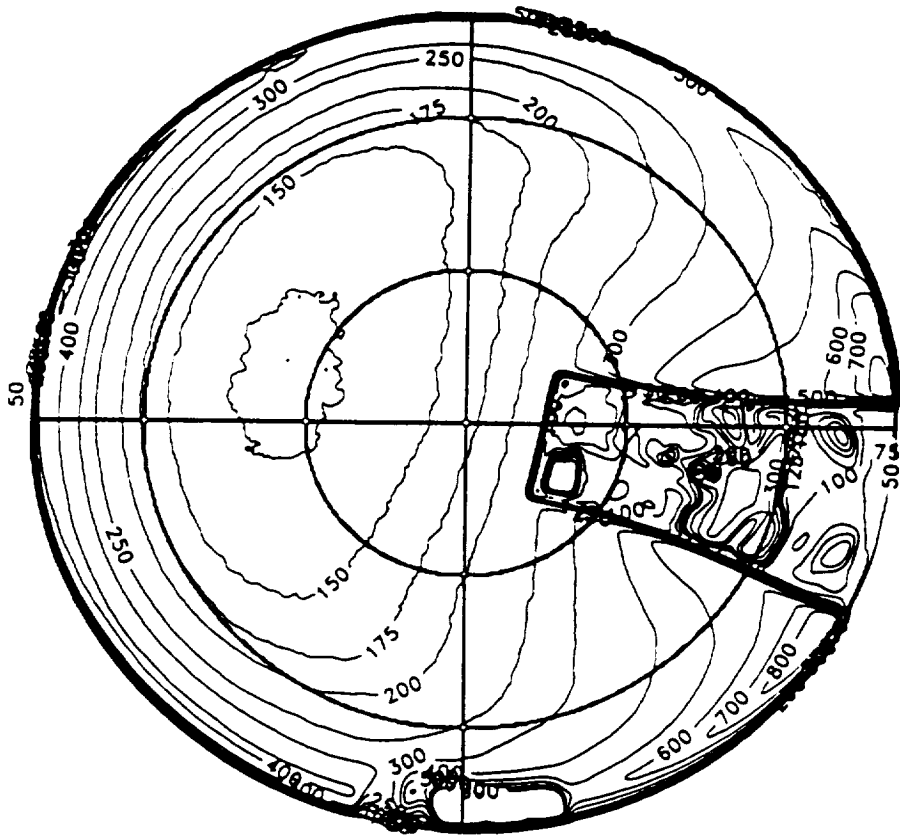


Liv & Voss Figure 3

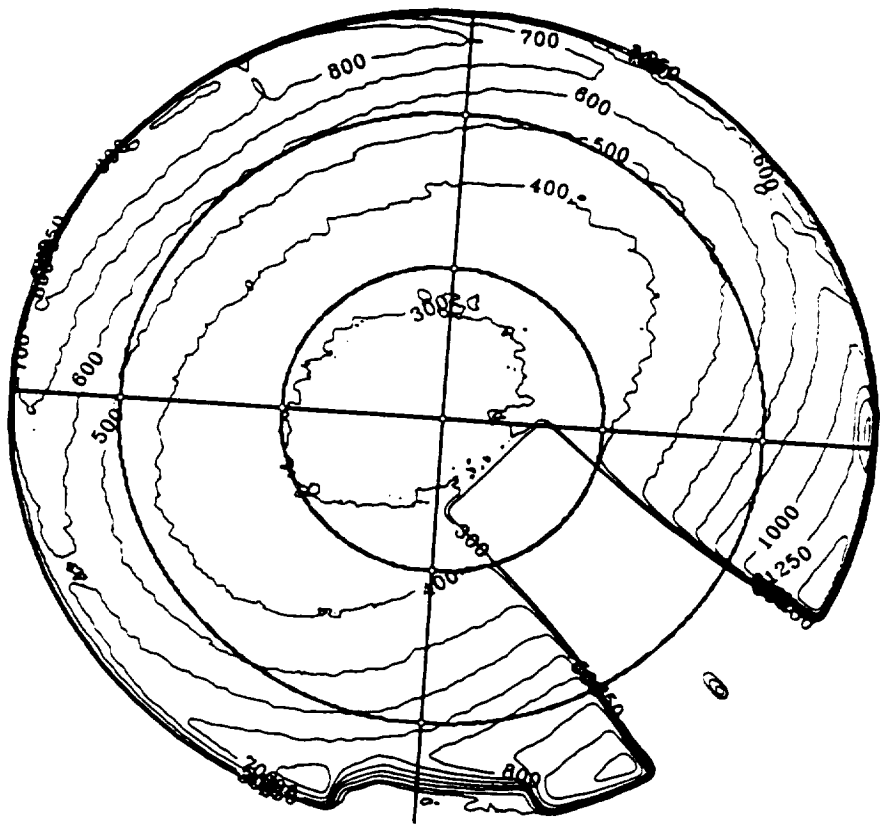




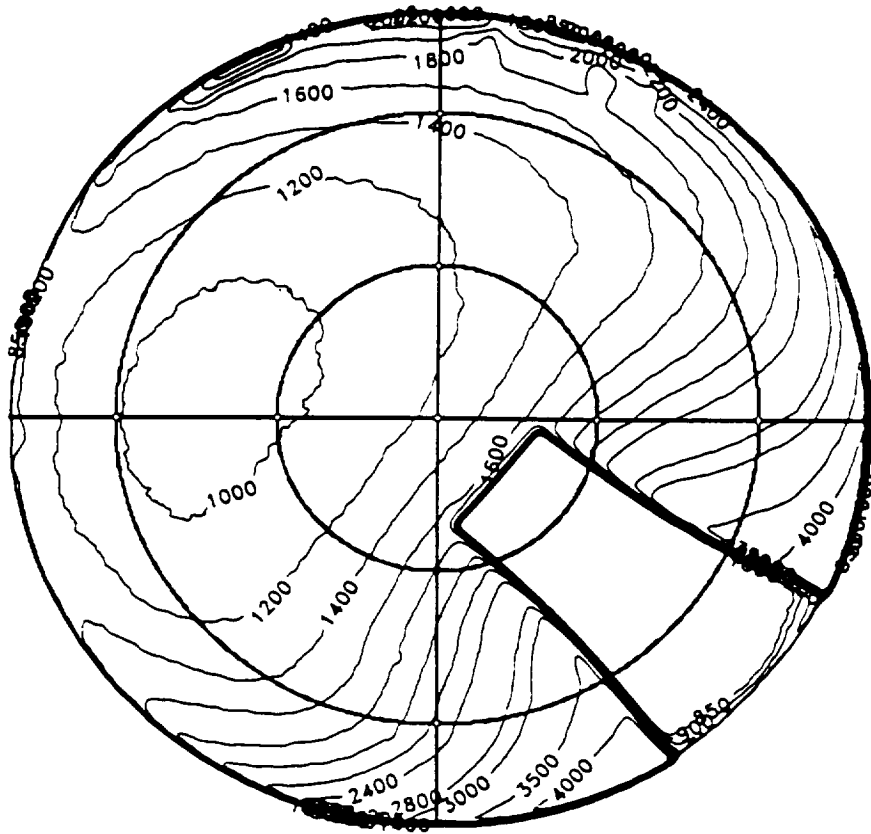
Liu & Voss Fig. 5a



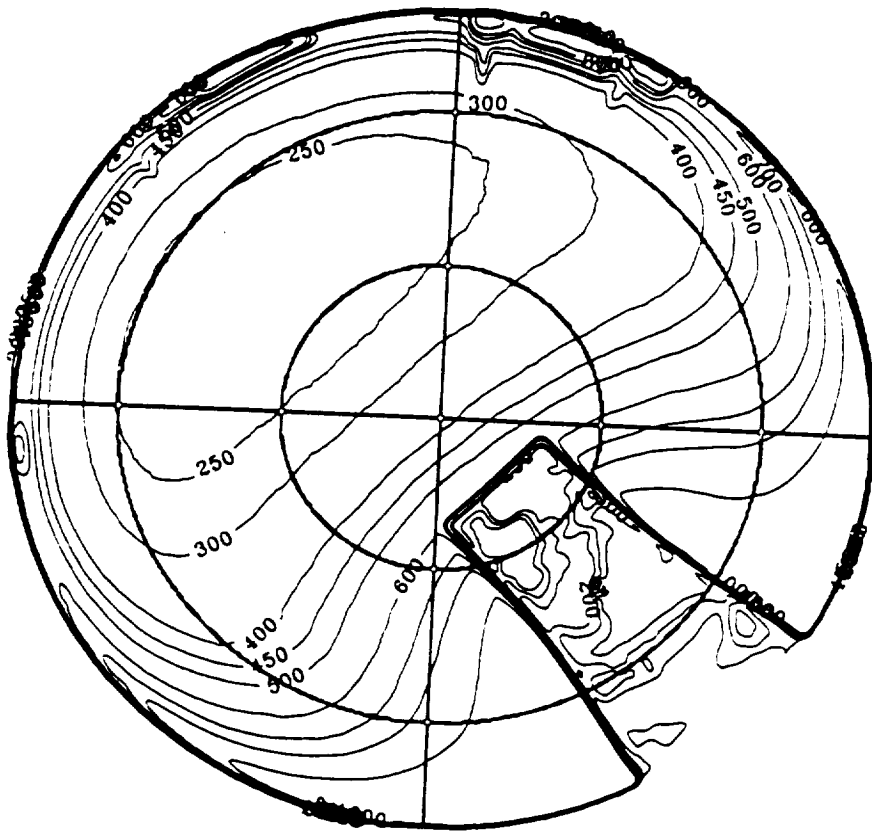
Liu X Voss Eio ^{sb} ~~ph~~



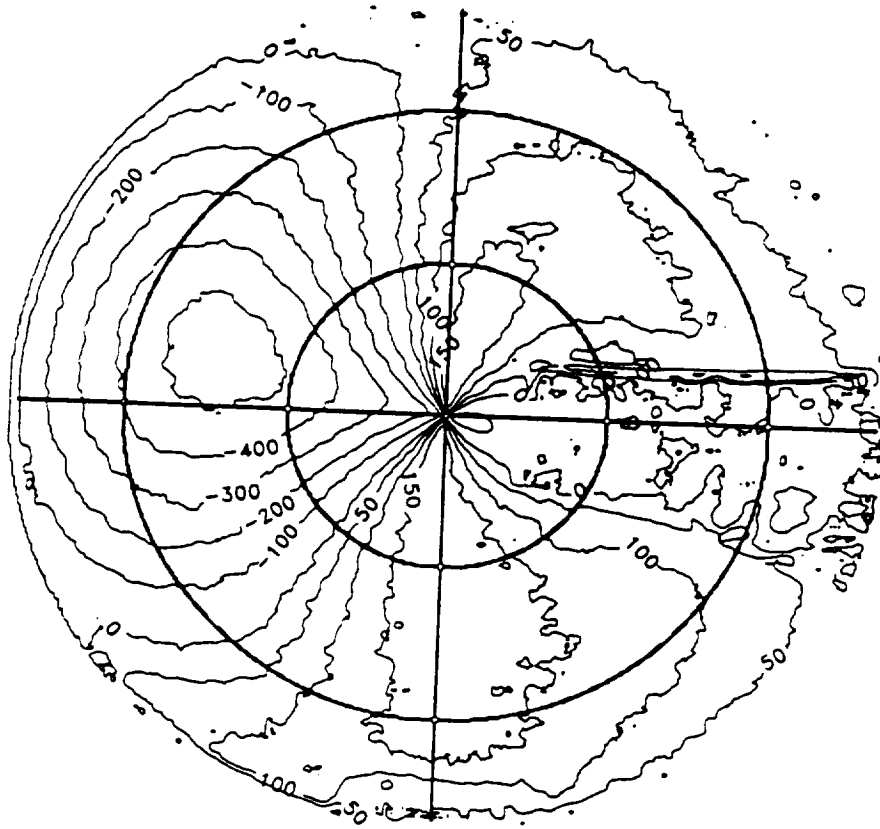
1. 2. 11. 50
H



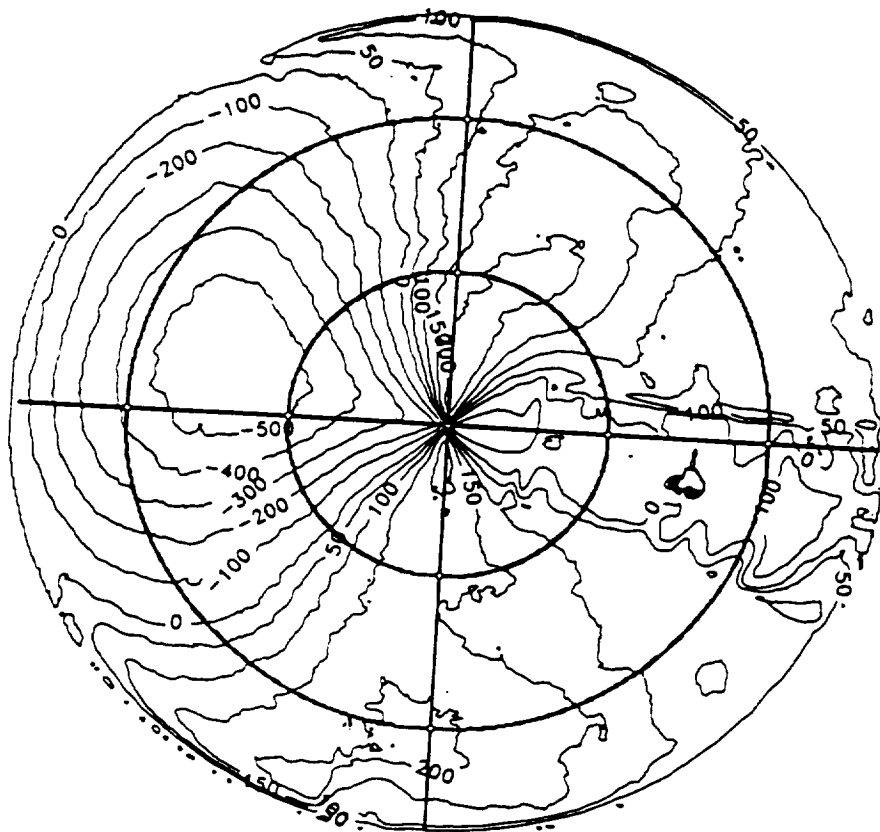
Liu R Vess Fig. 79 ^{6a}



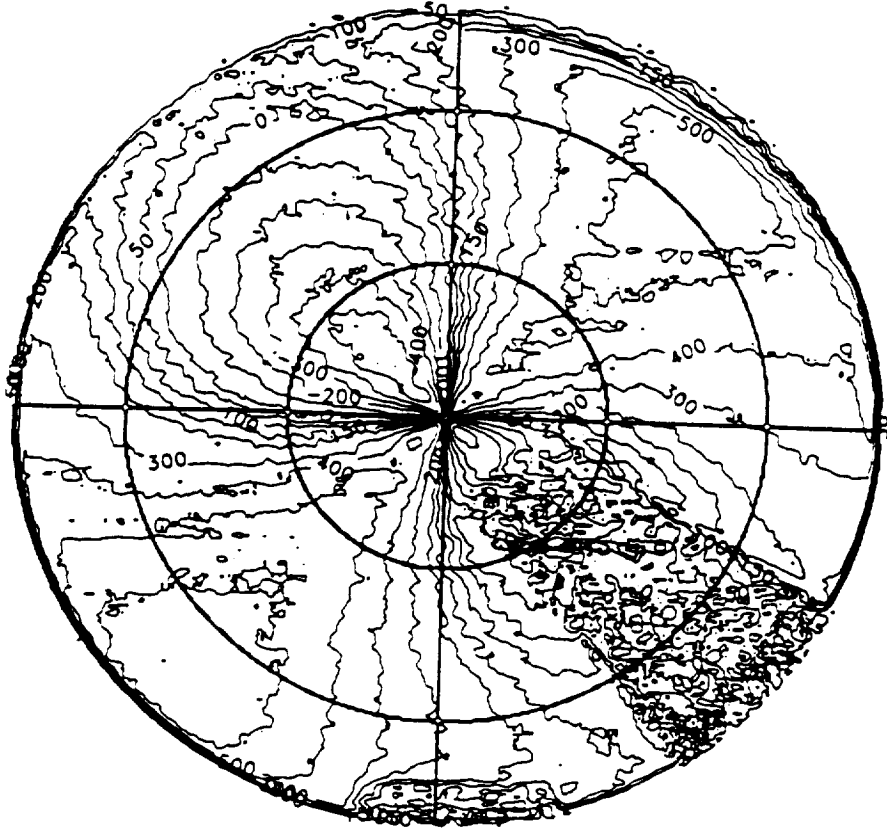
Liu & Voss Fig. 6b



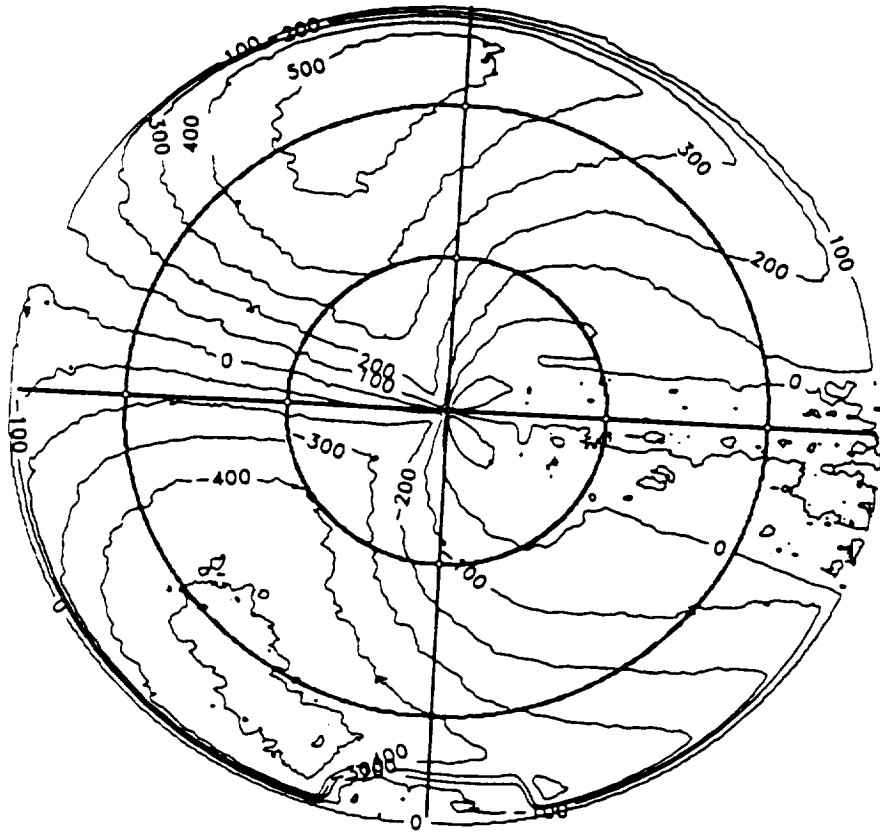
Liu & Voss Fig. 7a



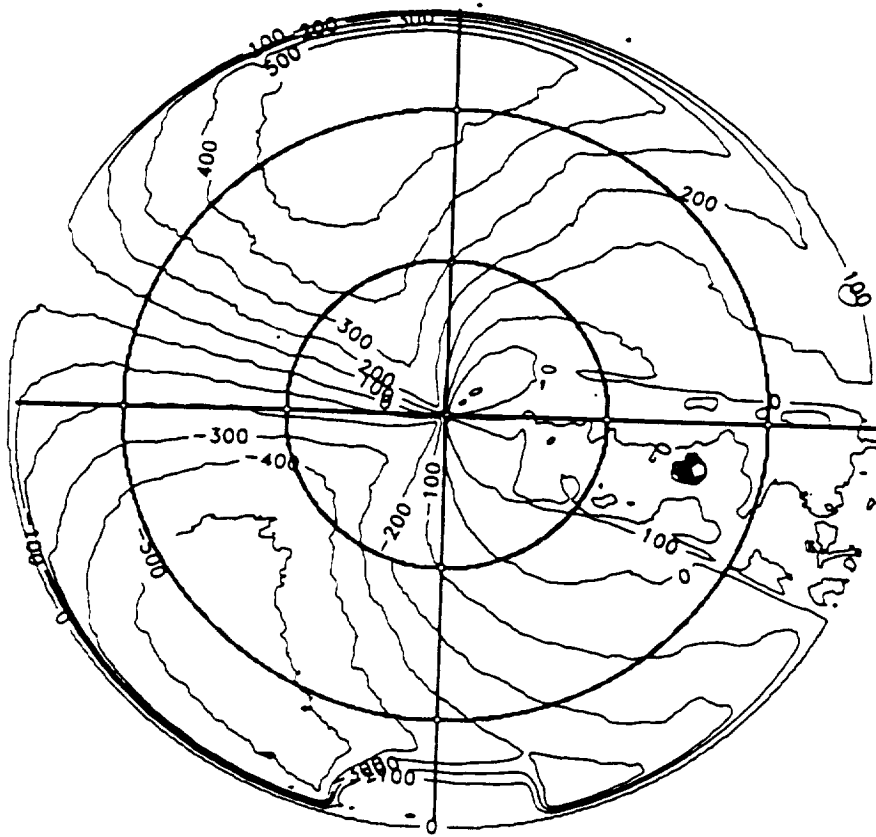
Liu & Voss Fig 7b



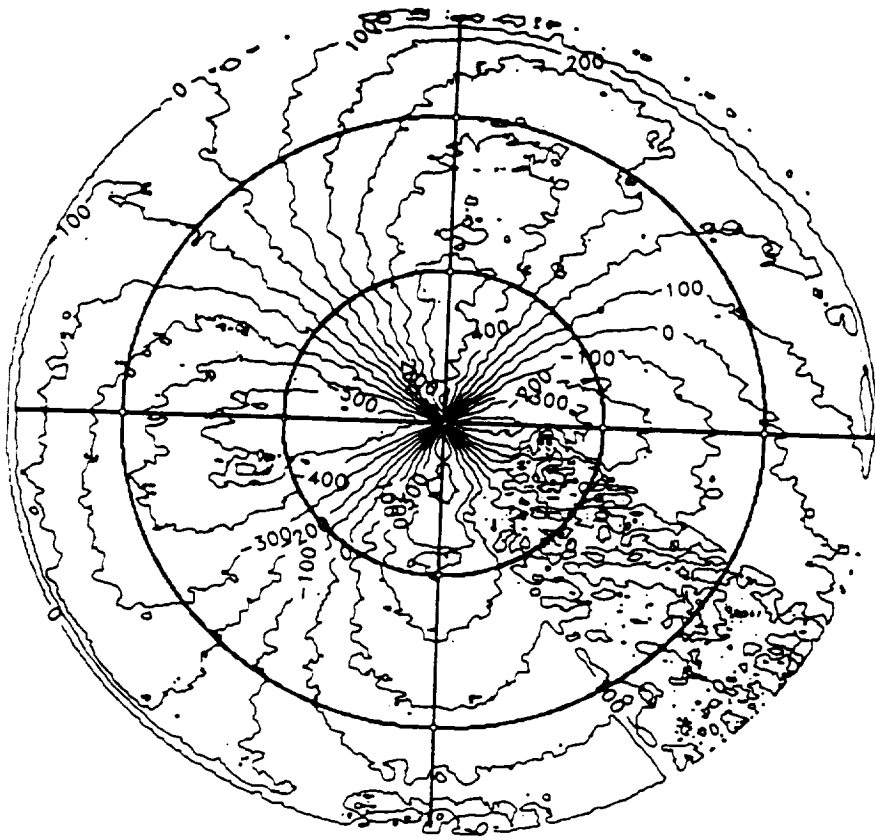
Liu & Voss Fig. 84^{7c}



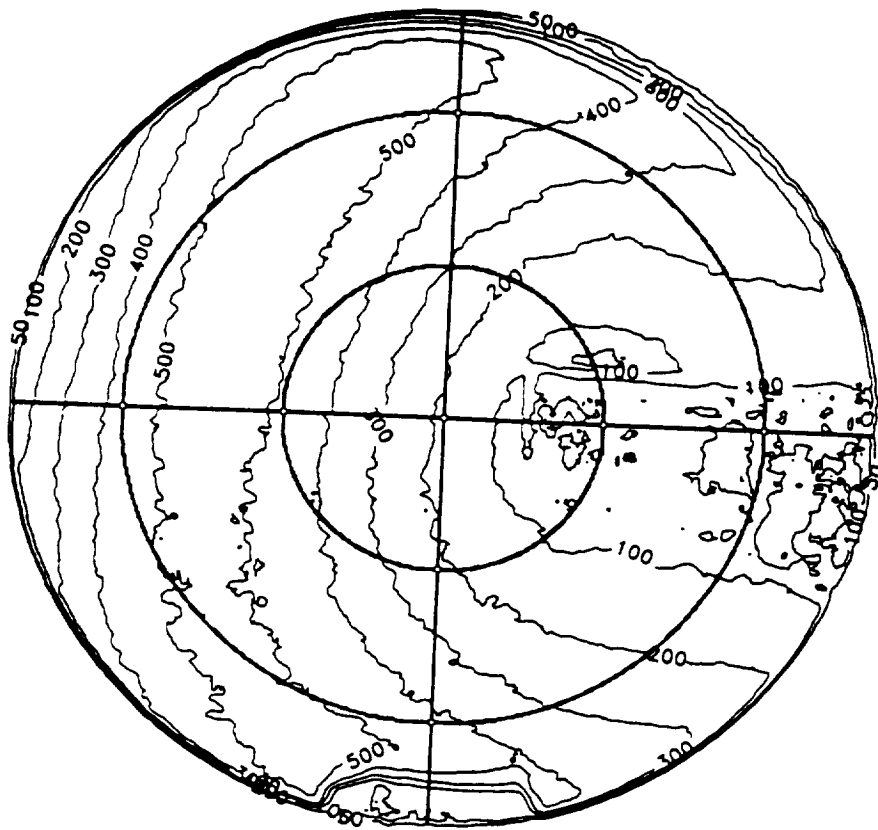
Liu & Voss Fig. 8a



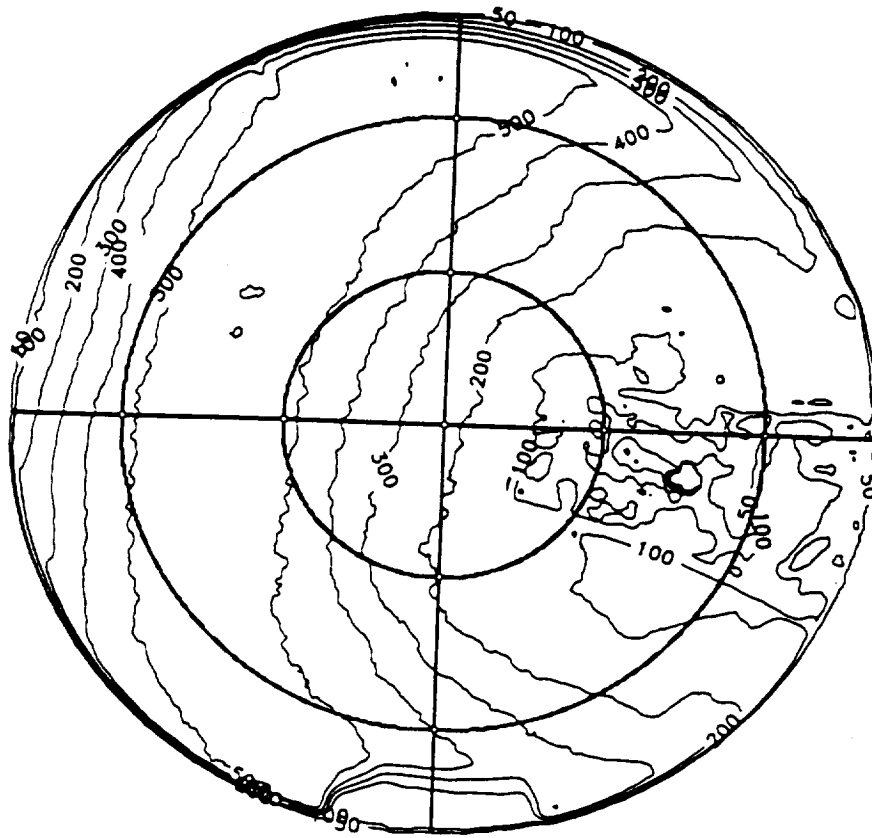
Liu & Voss Fig. 8b



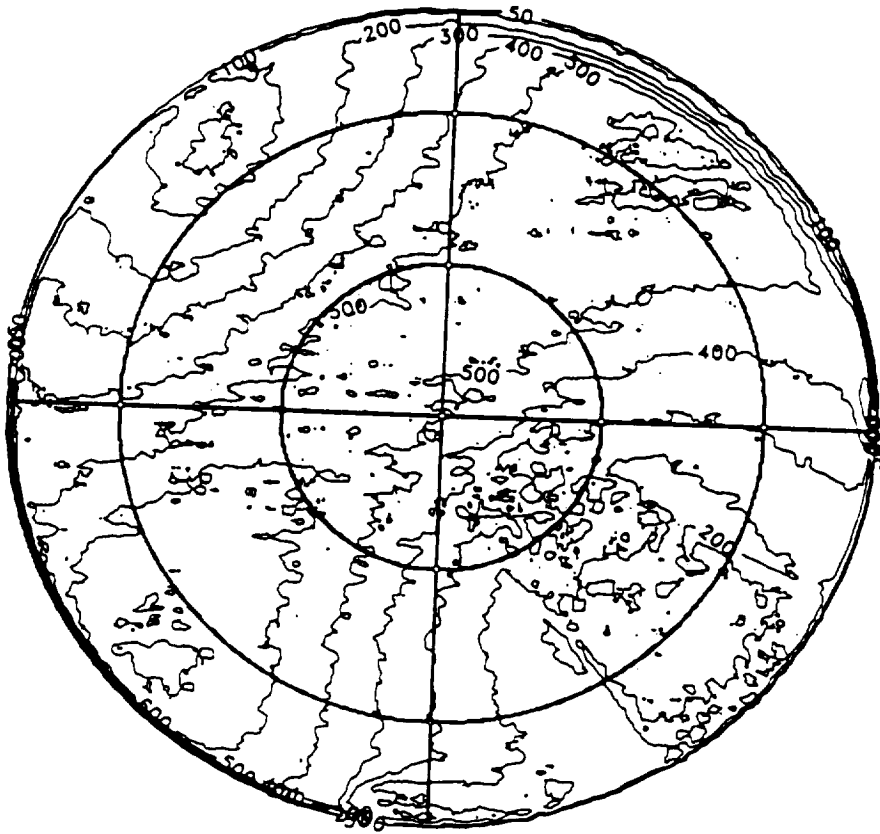
Liu & Voss ~~Fig. 8a~~ 8c



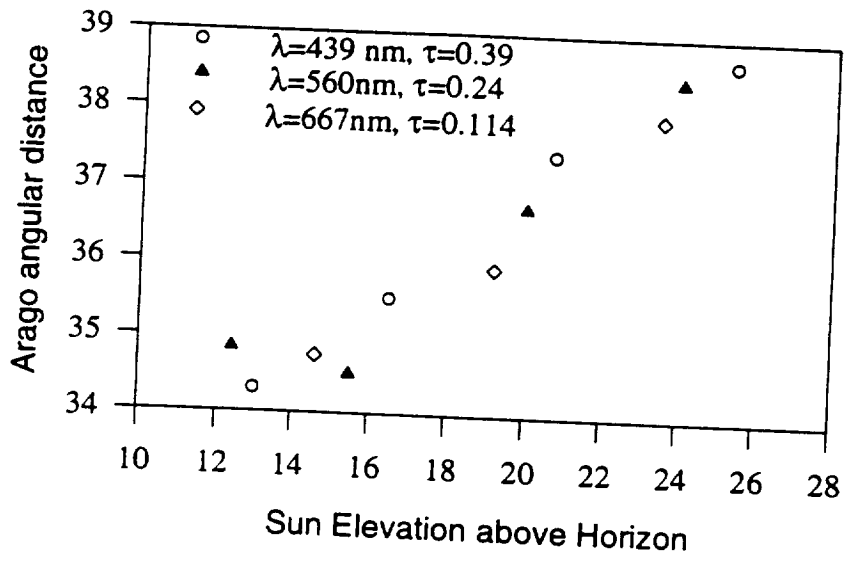
Liu & Voss Fig. 9a
100

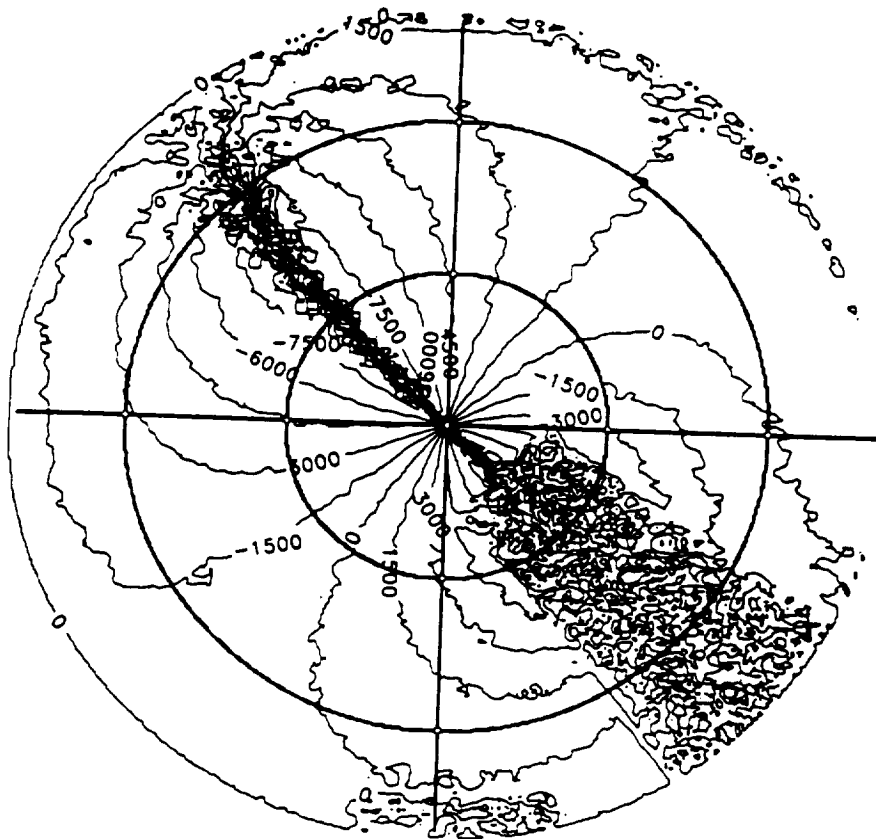


Liu & Voss Fig. ^{9b} ~~100~~

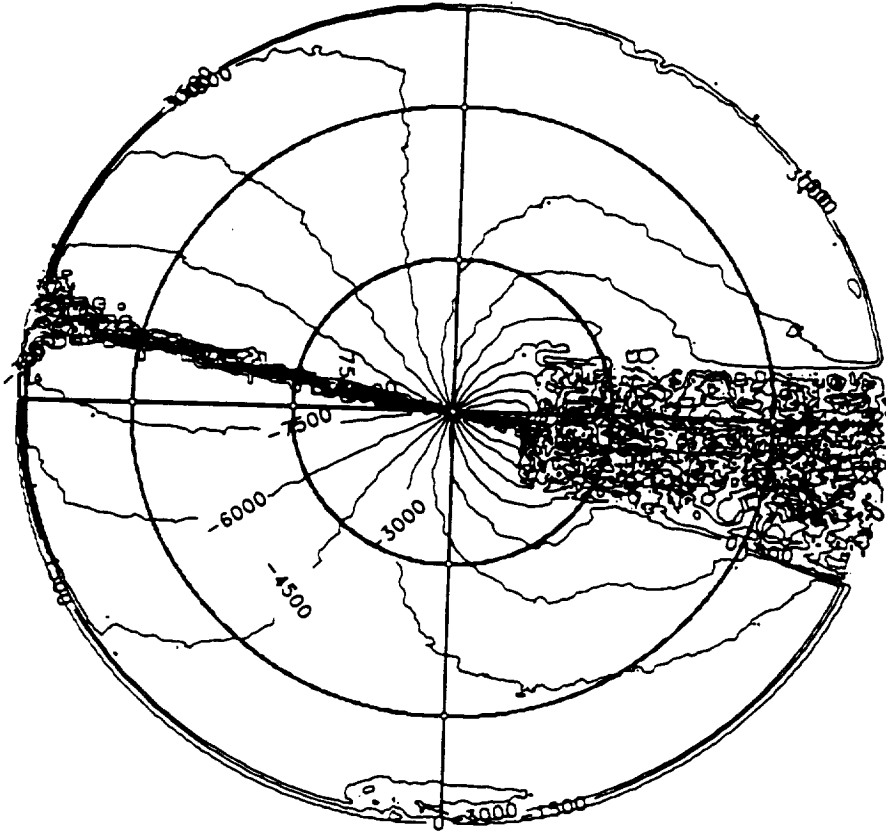


Liu & Voss Fig. 95

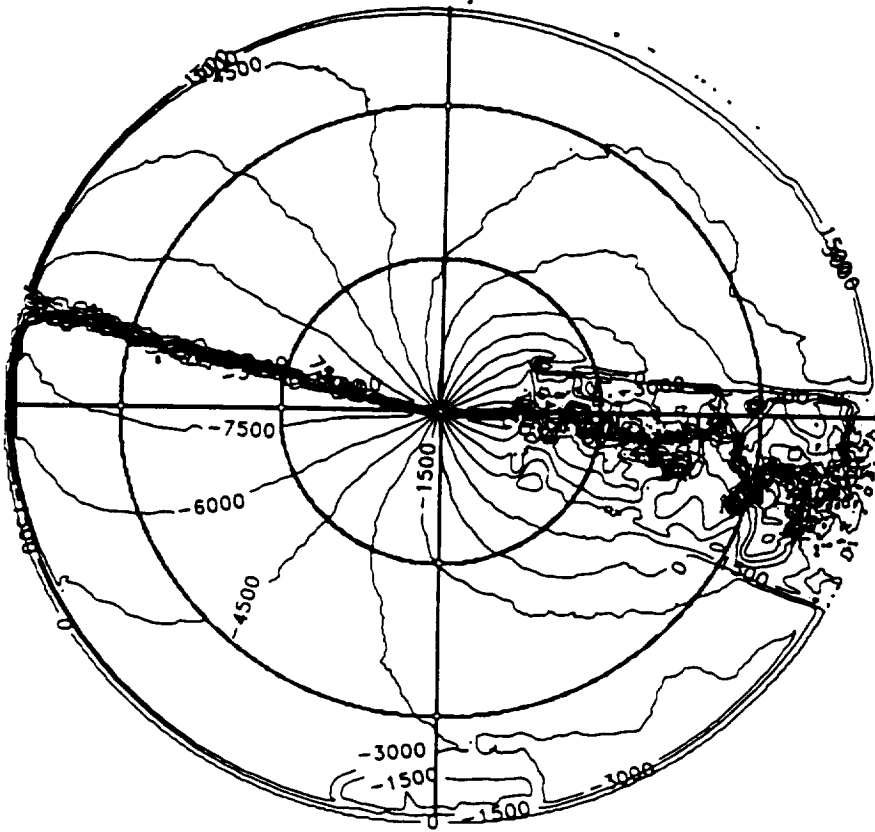




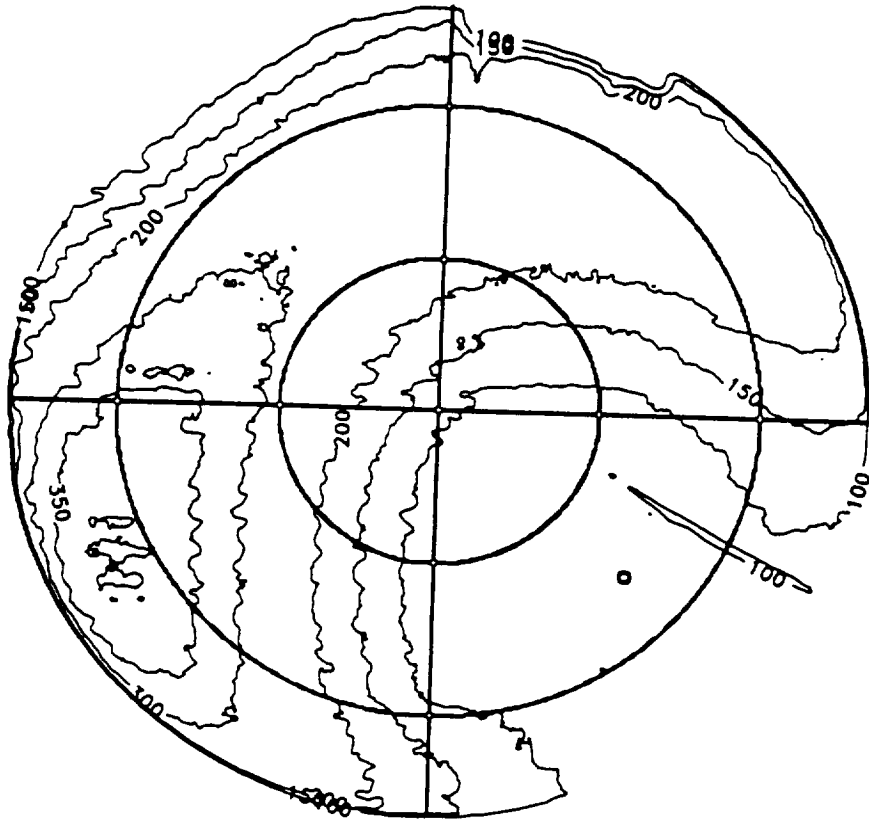
Lin & Voss Fig 11^c



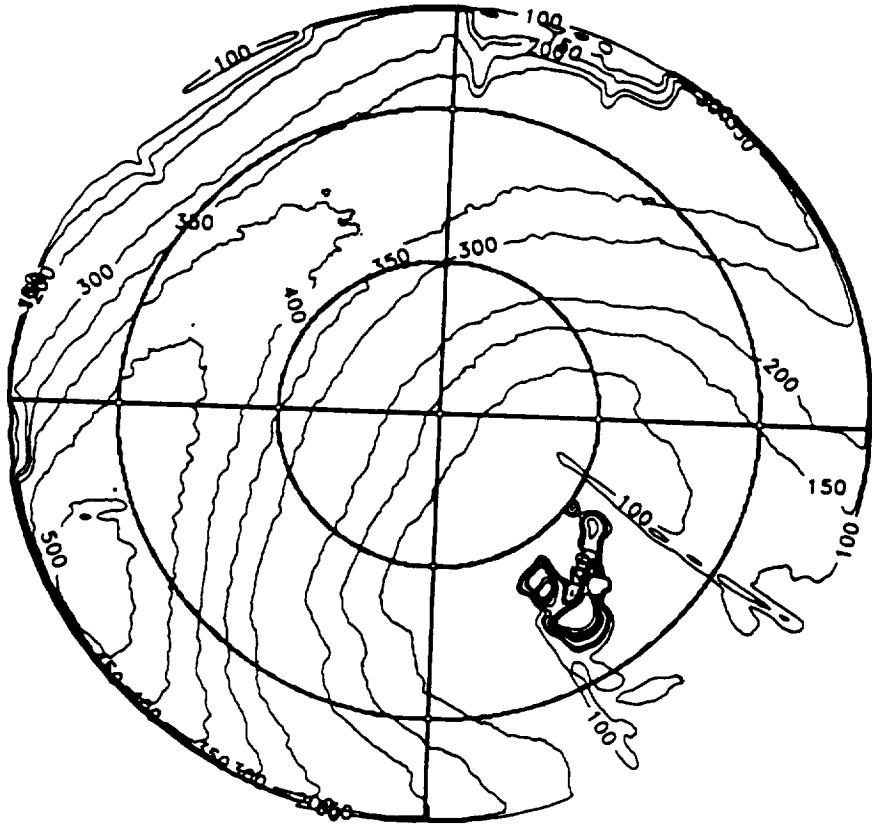
119
Liu & Voss Fig. 12a



Liu & Voss Fig. ~~122~~ 11b



Liu & Voss Fig. 12^a



Liu & Voo Fig 12b

Appendix 7

Scattering and attenuation properties of *Emiliana huxleyi* cells and their detached coccoliths

Scattering and attenuation properties of Emiliana huxleyi cells and their detached coccoliths

Kenneth J. Voss

Department of Physics, University of Miami, Coral Gables, FL 33124

William M. Balch

Bigelow Laboratory for Ocean Sciences, McKown Point, West Boothbay Harbor, Me.
04575

Katherine A. Kilpatrick

Division of Meteorology and Physical Oceanography, Rosenstiel School for Marine
and Atmospheric Science, University of Miami, 4600 Rickenbacker Causeway, Miami, FL.
33149.

Abstract

Measurements of the spectral scattering and attenuation properties of coccolithophores (E. huxleyi; clone 88E) and their associated coccoliths were made for three growth phases as well as for acidified cultures. These measurements allow a clean separation and determination of the optical effects of the various components. The specific beam attenuation coefficients, $m^2(\text{particle})^{-1}$, were found to be $5.17E-12$, $7.43E-10$, and $7.88E-11$ for coccoliths, plated cells and naked cells respectively at 440 nm. The spectral dependence of these factors followed a power law dependence, with a wavelength exponent of -3.7, -0.28, and -0.38 for the coccoliths, plated cells and naked cells respectively. The volume scattering functions for all appeared similar, however the specific backscattering coefficients ($m^2(\text{particle})^{-1}$) at 456 nm were $1.37E-13$, $6.72E-12$, and $9.90E-13$ for coccoliths, plated cells, and naked cells, respectively. The wavelength dependence of this parameter also followed a power law and was -1.4, -1.2 and -1.0 for the coccoliths, plated cells and naked cells. Overall these results show that optical properties of

a coccolithophore bloom are sensitive to the coccolith/cell ratio and can vary between and within blooms.

Introduction

The coccolithophore Emiliana huxleyi (Lohm.) Hay and Moler, strain 88E, is a ubiquitous species in the world's oceans, common in both bloom and nonbloom conditions (Green and Leadbeater, 1994). It has a major effect on carbon flux in the oceanic system and, through effects on the optical properties of the water column, on remote sensing. E. huxleyi produces calcite coccoliths which cover the cell, increasing its effective index of refraction changing its scattering properties. It can also release these coccoliths, adding free coccoliths to the water column and, growing more, continue to release these, until the optical effects of free coccoliths in the water column become significant. Finally, as with other phytoplankton, the cells themselves, quite apart from coccoliths, will add to the water column attenuation and scattering. To determine the relative optical effect of free coccoliths and plated or naked cells, these optical properties must be determined separately in some manner. In field experiments, optical effects of calcite coccoliths have been isolated by bubbling with CO₂ or adding acid (Kilpatrick et al, 1994). However in this process both coccoliths attached to cells and detached in the medium are dissolved, thus separating components is difficult. Laboratory cultures of E. huxleyi can be grown which allow easier manipulation, cleaner interpretation, and separation of the optical signatures of the various components of this species. The measurements reported in this paper are the first separate determinations of the optical properties of spectral backscattering, b_b , and spectral beam attenuation, c , for coccoliths, plated cells, and naked cells.

Methods

Experimental Design - In this experiment, volume scattering and attenuation were measured for cultures of E. huxleyi in three distinct growth phases. We also measured these optical parameters in acidified samples of the same cultures, which allowed resolution of the scattering and attenuation properties of pure suspensions of naked (unplated) cells.

In the first growth phase, cells were in stationary growth (henceforth referred to as “stationary phase” cells). In this phase the cells were predominately (95%) naked and in the sample along with free coccoliths. When this sample is acidified the free coccoliths from the sample are dissolved. Many studies have been performed which have shown that optical properties such as b_b of the cells are not changed during the acidification process (Balch et al, 1992, 1996a, 1996b; Balch and Kilpatrick, 1996). As such, measurement of attenuation or scattering before and after acidification allowed the distinct determination of the optical signature of unplated cells combined with free coccoliths, unplated cells separately, and by difference, free coccoliths.

In the second experiment, a culture was used which was in log phase growth (henceforth referred to as “log”). In this case, most of the cells were plated (80%) and there were also free coccoliths. Optical measurement of the total sample then yielded a combination of plated cells, free coccoliths, and a few naked cells. The acidified sample allowed measurement of the optical properties of unplated cells. Hence, the optical properties of particle types could be resolved with these two samples in their two phases (log and stationary, acidified and non-acidified).

A third independent sample, an older culture (where 50% of the cells had lost their coccoliths) was measured (referred to as “senescent”). In this case only scattering measurements were performed. In this sample the values derived from the other two growth phases were combined with cell and coccolith count information to find an estimate of the relevant optical properties, and these modeled values compared with the values obtained by direct measurement.

More details on the measurement procedures follows.

Cultures - Three cultures of *E. huxleyi* (clone 88e) were grown in 10 liters of K media (Keller et al. 1987). Cultures were grown in an incubator at 19° C and a 12:12 light:dark cycle at a PAR (photosynthetically available radiation) illumination of $51 \mu\text{E m}^{-2} \text{s}^{-1}$. Cell

and coccolith counts were made daily to follow the growth of the culture and extent of platedness. Aliquots of the culture were removed for optical measurements when the cells were in log, stationary, and senescent growth phases. Cell sizes (diameters) were previously measured to be: 6.4 μm for cells with coccoliths, 5.2 μm for cells without coccoliths. The free coccoliths were approximately 3 μm in length and 2.4 μm in width, the surface area was 13 μm^2 (Fritz, 1997). All measurements were performed at the same time each day to avoid possible problems with diel variability.

Microscope counts - Cells and free coccoliths were counted in a Palmer Maloney chamber using an Olympus BH-2 epi-fluorescence microscope with polarization optics. Cells were examined under both polarization and epi-fluorescence to determine the ratio of plated and naked cells in culture. The free coccoliths in solution were counted under polarization only. Microscopic particle counts were made daily on the original cultures and during the optical experiments after each addition of culture to the experimental tank.

Tank preparation - A blackened 210 liter drum was filled with fresh seawater taken from Bear Cut, off the RSMAS, Univ. of Miami dock and filtered overnight by recirculating the water through a 0.2 μm poresize Gelman pleated filter cartridge attached to a Mini-Giant submersible pump. The filter cartridge was removed before each experiment and the Mini-Giant remained in the drum to re-circulate the seawater during measurements. The temperature in the drum was maintained at 19 $^{\circ}\text{C}$ by a cooling coil made from tygon tubing which was attached to a re-circulating water bath chiller.

Optical measurements - Spectral attenuation of the stationary and log phase cultures were made with the Vislab Spectral Transmissometer (VLST). (Petzold and Austin 1968) These measurements were done at 5 wavelengths: 440 nm, 490 nm, 520 nm, 550 nm, and 670 nm. Light scattering measurements were done with the General Angle Scattering Meter (GASM) (Petzold 1972) at 6 wavelengths: 440, 490, 520, 550, 610, and 670 nm.

The volume scattering function (*VSF*) was measured with this instrument at every degree between 10 and 170 degrees from the incident beam. Light scattering was also measured using a Brice Phoenix (BP) scattering photometer at three angles, 45, 90 and 135 degrees, and at two wavelengths, 436 nm and 546 nm. The VLST and GASM are designed to be in-situ devices, hence they require a large enough sample to immerse the instrument. This immersion was done by placing the instruments in the tank of 0.2 μm filtered seawater and sequentially adding culture aliquots. The BP measures a much smaller sample (beam size = 4 x 15 mm) which allowed much more sample manipulation (e.g. acidification).

The procedure followed for each instrument was as follows. GASM and VLST were placed in the tank filled with filtered seawater. The spectral attenuation, *c*, and *VSF*, of the background seawater were measured, and a sample removed for the BP measurement. The BP measured the *VSF* for this sample, and the sample was acidified by adding 6.4 ml of 1.2% glacial acetic acid per liter seawater to the cuvette and the *VSF* measured again. There was no significant difference between the measured *VSF* for the acidified and non-acidified cases in this background seawater sample. At this point an aliquot of the culture sample was added to the water, and the barrel was stirred with an electric pump until the transmissometer readings stabilized. A subsample of this container was removed for measurement by the BP and particle counts, then GASM and VLST measurements were performed. Following the BP measurement the aliquot was acidified and the *VSF* remeasured. *E. huxleyi* culture was added to the tank to achieve three concentrations and measurements performed at each stage. The maximum optical pathlength (*c** geometric pathlength) measured was approximately 0.2, thus multiple scattering effects were not significant. After the last culture addition the entire tank was acidified to dissolve all calcite coccoliths by adding 6.4 ml of 1.2% glacial acetic acid per liter seawater bringing the pH to 5.5, whereupon measurements were performed both in the drum and with the BP. At this point the BP sample was acidified again to confirm that the coccoliths had been totally dissolved in the first case. This procedure was followed for each of the three cultures,

however for the senescent case the VLST was malfunctioning so no spectral attenuation measurements were available.

The VLST directly measures the spectral transmission over a 1 meter path, $T(\lambda)$, which is converted to the spectral beam attenuation, $c(\lambda)$, by the equation:

$$c(\lambda) = -\ln(T(\lambda)) .$$

No correction was made for the finite (about 1.5 degree) acceptance angle of the transmissometer. This effect is estimated to cause a 10% underestimate of c (Voss and Austin, 1993).

The backscattering coefficient, b_b , was calculated with the measurements of the VSF in two ways. Since the GASM measurements only extend to 170 degrees, the data was extrapolated to 180 degrees by assuming $VSF(\theta)$ for 170 to 180 degrees is constant. The data was then integrated directly to obtain b_b through the equation:

$$b_b = 2\pi \int_{90^\circ}^{180^\circ} VSF(\theta) \sin(\theta) d\theta$$

While more sophisticated extrapolation methods might be hypothesized, because the solid angle between 170° and 180° is such a small part of the total hemisphere and $VSF(\theta)$ is approximately flat in this region, the portion of b_b from 170 to 180 degrees only contains 1% of the total b_b . Thus this is probably only a +-1% error in the calculation of b_b .

For the BP, data was only obtained at three angles (45, 90, and 135). To interpolate and extrapolate these measurements to obtain the VSF from 90-180 degrees, these data were used to fit the equation (Beardsley and Zaneveld, 1969; Gordon, 1976):

$$VSF(\theta) = \frac{f}{(1 - g \cos(\theta))^4 (1 + h \cos(\theta))^4} .$$

Once the coefficients for this equation (f , g , and h) were determined, the equation was numerically integrated to obtain b_b . A test of this method was performed in which the GASM data was directly integrated to obtain b_b and the values of the VSF at the three angles used to derive a b_b through the analytical fit. This was done for all the GASM measurements and the results can be seen in Figure 1. As can be seen this technique works well (the standard deviation was 6%), indicating that the b_b derived from the fitted analytic equation is accurate.

Results

Spectral beam attenuation - As previously introduced, we made two types of measurements for beam attenuation, the stationary cell case and the log case which provided three independent variables, concentrations of 1) naked cells, 2) plated cells, and 3) free coccoliths. The dependent variable is the measured beam attenuation. We also examined three concentrations of each growth phase (stationary and log), and the acidified sample. In total, for the beam attenuation, we have 8 measurements of beam attenuation, with associated cell and coccolith counts. A linear, multivariable, least squares analysis (Natrella, 1963) was performed, fitting the experimentally measured beam attenuation data to the equation:

$$c(\lambda) = x(\lambda) X + y(\lambda) Y + z(\lambda) Z,$$

where X was the concentration of naked cells (cell m^{-3}), Y was the concentration of plated cells (cell m^{-3}), and Z was the concentration of coccoliths (coccolith m^{-3}). The parameters determined in the fit were $x(\lambda)$, $y(\lambda)$, and $z(\lambda)$, the beam attenuation per naked cell, plated cell, and coccolith concentrations, respectively. In this way the relative contribution to the beam attenuation for each component could be determined. The resulting specific beam attenuation coefficients, and their standard deviations, for the different wavelengths are shown in Table 1 and in Figure 2. The error for the free coccoliths is fairly large, mainly because we had few samples (relative to the b_b measurements) to work with. These still are

informative as they give a qualitative view of the relative magnitude of these coefficients. A typical result of how well the above equation fits the data is shown in Figure 3. This is the experimentally measured $c(440 \text{ nm})$ vs the modeled c values, using the empirically determined coefficients from the above equation. The average absolute error in the predicted c values was 25%. In all cases the worst prediction was for the acidified sample for the log case, when this point is excluded the average absolute error is less than 20%. The cell coefficients can be compared to the measurements of Bricaud and Morel (1986). By using their Table III the specific beam attenuation coefficient of *E. huxleyi* can be derived as $1.94\text{E-}10$ (cells m^2) (435 nm) and $1.72\text{E-}10$ (cells m^2) (550 nm). There is no information in this paper as to the state of the coccolithophores, however these values fall between our values for naked and plated cells.

The first important point to note in this data is the wavelength dependence of the factors. Each of these factors can be fit to a power law wavelength dependence (λ^α). The plated cell and naked cell factors are spectrally flat, with wavelength exponents of -0.3 and -0.4 respectively. This agrees well with the value derived from the Bricaud and Morel (1986) measurements (-0.5). The coccolith specific beam attenuation coefficients are strongly wavelength dependent (a wavelength exponent of -3.7), but this is strongly influenced by the 670 nm data point. Without this point the wavelength exponent is -2.4, still strong but significantly less than -3.7. Secondly it is important to note the relative magnitude of the factors, increasing by roughly an order of magnitude between the coccolith, naked cell and plated cell. The specific beam attenuation coefficient for the plated cells were more than 100 times greater than free coccoliths, this factor was greater than the number of coccoliths plating each cell (~ 30; Fig. 3).

Spectral light scattering - The normalized *VSF* for all of the samples showed no significant spectral dependence (as reported for field measurements during *E. huxleyi* blooms, Balch et al 1991). The normalized *VSF* at each wavelength is shown in Figure 4. As can be seen there was also no marked difference in the normalized *VSF* between the

various samples. Because we have no measure of the *VSF* between 0 and 10 degrees it is not possible to comment on the total scattering coefficient, b . However b_b , the backscattering coefficient is perhaps a more important parameter because of its impact on remote sensing reflectance and diffuse attenuation.

As mentioned above we can derive b_b from both the GASM and BP measurements. The b_b measured for each sample, for the blue (440 nm for GASM, 436 for BP), and green (550 nm for GASM and 546 for BP) are shown in Figure 5. As can be seen from these figures, for the most part, the measurements with BP and with GASM agree well, but there are some deviations. Each instrument has specific advantages. GASM allows measurement of much more of the *VSF* (10-170 degrees) and more wavelengths (6), but BP allows more manipulation of the sample. This is primarily because GASM requires immersion, thus we did not logistically have enough culture to repeatedly bring the 210 liter tank to a given cell and coccolith concentration, acidify and then start again. The BP allowed us to acidify each sample, thus gaining more information in each case.

As with the spectral c case, we performed a multiple linear fit to b_b which isolated the specific b_b coefficients (b_b^*) for coccolith, plated cells and naked cells. Because b_b is an additive property, the linear, multivariable, least squares fit took the following form:

$$b_b(\lambda) = x(\lambda)X + y(\lambda) Y + z(\lambda) Z,$$

where once again X , Y , and Z were the coccolith, plated cell, and naked cell concentrations. Hence $x(\lambda)$, $y(\lambda)$ and $z(\lambda)$ represented the b_b^* for coccoliths, plated cells, and naked cells. Table 2 shows the BP derived coefficients and the GASM derived coefficients. Figure 6 shows the same data graphically. Note the 520 nm measurement with GASM was probably an overestimate as it was anomalously high in all the measurements with this instrument (but no reason has been found for this problem, so the measurements are reported "as is"). First we note that the GASM coefficients are somewhat larger than the BP coefficients (but within the standard error), particularly in the

blue. The BP derived coefficients have lower standard error than the GASM derived coefficients. This is because the acidified measurements could be performed on every sample, versus the end points for GASM, as discussed above. The previous work by Bricaud and Morel (1986) have no experimental measurements of b_b for *E. huxleyi*, however they do show theoretical Mie scattering calculations for this parameter. These calculations predict a positive exponent for the wavelength dependence of b_b , however the wavelength dependence determined from the GASM measurements leads to a power law dependence on wavelength with an exponent of -1.4, -1.2, and -1.0 for the coccolith, plated cell and naked cell component respectively. Naked cells should be similar to typical phytoplankton cells, which have a relatively low average relative index of refraction (1.05 or less, relative to water (Mobley, 1994)). A wavelength dependence -1 is what is commonly assumed for the wavelength dependence of the total scattering coefficient (Gordon and Morel, 1983). Plated cells will have a higher relative index of refraction because of the calcite coccoliths, and in this case show a larger wavelength dependence. Free coccoliths, with their high relative index of refraction and small size have the largest wavelength dependence, which could cause a signature in remotely sensed images if differences in the visible bands are viewed.

While in field cases it is not possible to get a separate number for the b_b^* of plated cells and naked cells, some estimates of the b_b^* due to coccoliths have been made. The $b_b^*_{\text{coccolith}}$ from the BP measurements (1.37E-13 and 1.27E-13 m² coccolith⁻¹) are close to the field measurements reported in Balch et al.(1991) of 1.41E-13 and 1.29E-13 m² coccolith⁻¹ for the 436 and 546 nm respectively. Field measurements of $b_b^*_{\text{coccolith}}$ should be an overestimate due to neglecting the contribution of plated cells, but this does not appear to have been the case in this situation. Note that in the Balch et al. data set, the ratio of free coccoliths to cells reached values of 400 or more, thus the free coccoliths dominated the optical properties, the contribution by plated cells was negligible (as will be discussed below).

Besides the wavelength dependence of these factors it is useful to look at the absolute magnitude of the b_b^* . As can be seen, it varies between components by less than the beam attenuation coefficients. This is because small particles (in this case coccoliths) tend to direct more of the scattered light in the backward direction causing them to be more efficient backscatterers. Thus the ratio of b_b^* coccolith to the b_b^* plated cell is on the order of 40 rather than 100 as in the case of c .

If these b_b^* coefficients are relevant for field samples we can use them to look at the relative importance of free coccoliths to plated cells in determining the optical signature of the ocean for bloom conditions. To test these coefficients a data set obtained during a coccolithophore bloom off of Iceland (Holligan et. al. 1993; Balch et. al. 1996a and b) was used. This data set had counts of live cells and free coccoliths along with b_b measurements. Figure 7 illustrates the fit to the measurements, using the specific bb coefficients derived above and the cell count data from the cruise, for the blue and green wavelengths of BP. The value shown in Figure 7, bb' , is the acid labile b_b , which is b_b total minus b_b acidified and is effectively the b_b for the calcite in the sample. The coefficients used in the model were from the ones derived from the BP measurements of the laboratory cultures. The 1:1 line is shown along with a line representing the best fit. There seems to be an overestimate of the field data by 20%, but overall the model seems to do a reasonable job of estimating the field data. The importance of this work is in showing the relative importance of the components in determining the optical properties. With counts of the separate components, we can determine the relative contribution of the plated cells and coccoliths to the total b_b in this situation. Figure 8 illustrates the portion of b_b due to plated cells versus b_b' . b_b' should include contributions from plated cells and free liths. It appears that in this data set b_b' is dominated by plated cells. If one looks at the ratio of free coccoliths to plated cells, it is obvious that in this study the high b_b' cases are those dominated by cells (i.e. low detached coccolith to plated cell ratio). Since the ratio of free coccoliths/cells can vary from bloom to bloom, the importance of free coccoliths versus

cells in determining the optical properties can vary. For example, Balch et al. (1991) reported coccolith/cell ratios for blooms occurring in the Gulf of Maine for two years, 1988 and 1989. In the first case the highest free coccolith/cell reported were about 50, indicating that coccoliths would have had approximately equal importance as cells in determining the backscattering. In the 1989 bloom, the coccolith/cell ratio reached values over 400, and in this case the free coccoliths would have been the dominate constituent. The coccolith/cell ratio can vary within blooms and non-bloom waters which makes this an important ratio to understand in interpretation of remote sensing reflectance.

Conclusions

We have found the specific backscattering and spectral beam attenuation coefficients for the separate components of coccoliths, plated cells, and naked cells. These show that the plated cell contribution to the optical properties can be greater than the sum of the coccoliths coating them. Thus the optical properties of a coccolithophore bloom are sensitive to the ratio of free coccoliths to plated cells. Since the spectral variation of b_b^* is different for these coefficients, the remote sensing reflectance will vary with this ratio, with the stronger spectral variation when free liths dominate the upper water column. This ma be the reason that blooms with a high ratio free liths are most evident in satellite images based on color differences techniques.

Acknowledgments

This work was supported by the Ocean Optics program of the Office of Naval Research under contracts #N00014-95-10309 (KV). WMP was supported by the ONR Ocean Optics program (N00014-91-J-1048), NASA (NAS5-31363 and NAGW 2426) and NSF(OCE90-22227 and OCE-9596167). We would also like to thank Al Chapin for his help in making these measurements.

References

- Balch, W. M., P. M. Holligan, S. G. Ackleson, and K. J. Voss. 1991. Biological and optical properties of mesoscale coccolithophore blooms in the Gulf of Maine. *Limnol. Oceanogr.* **36**: 629 - 643.
- Balch, W. M., P. M. Holligan and K. A. Kilpatrick. 1992. Calcification, photosynthesis and growth of the bloom-forming coccolithophore, *Emiliana huxleyi*. *Cont. Shelf Res.* **12**: 1353-1374.
- _____ and K. A. Kilpatrick. 1996. Calcification rates in the equatorial Pacific along 140W. *Deep Sea Research.* **43**:971-993.
- _____, _____, P. M. Holligan, and C. Trees. 1996a. The 1991 coccolithophore bloom in the central north Atlantic I - Optical properties and factors affecting their distribution. *Limnology and Oceanography.* **41**: 1669-1683.
- _____, _____, _____, D. Harbour, and E. Fernandez. 1996b. The 1991 coccolithophore bloom in the central north Atlantic II - Relating optics to coccolith concentration. *Limnology and Oceanography.* **41**: 1684-1696.
- Beardsley, G. F. and J. R. V. Zaneveld. 1969. Theoretical dependence of the near-asymptotic apparent optical properties on the inherent optical properties of sea water. *J. Opt. Soc. Am.* **59**: 373-377.
- Fritz, J. J. 1997. Growth dependence of coccolith detachment, carbon fixation, and other associated processes by the coccolithophore *Emiliana huxleyi*. Univ. Miami. Ph.D. Thesis, Rosenstiel School for Marine and Atmospheric Sciences, Miami, Fl. 179 pp.
- Gordon, H. R.. Radiative transfer in the ocean: A method of determination of absorption and scattering properties. *Appl. Opt.* **15**: 2611 - 2613.
- Gordon, H. R. and A. Morel. 1983. Remote Assessment of Ocean Color for Interpretation of Satellite Visible Imagery, a Review; Lecture Notes on Coastal and Estuarine Studies, Volume 4. Springer Verlag.

- Green, J. C. and B. S. C. Leadbeater. 1994. *The Haptophyte Algae*. Oxford Science Publications, The Systematics Association Special Volume No 51. Clarendon Press: Oxford. 446 pp.
- Holligan, P. M., E. Fernandez, J. Aiken, W. M. Balch, P. Boyd and others. 1993. A geochemical study of the coccolithophore *Emiliana huxleyi*. In the North Atlantic Global Biogeochemical Cycles. **7**: 879-900.
- Keller, M. D., R. C. Selvin, W. Claus, and R. R. L. Guillard. 1987. Media for the culture of oceanic ultraphytoplankton. *J. Phycol.* **23**: 633-638.
- Kilpatrick, K. A., Y. Ge, W. M. Balch, and K. J. Voss. 1994. A photometer for the continuous measurement of Calcite-dependent light scatter in seawater. *Proc. Soc. Photo-Optical Instrumentation*, 1994: 512 - 521.
- Mobley, C. D.. 1994. *Light and Water, Radiative Transfer in Natural Waters*. Academic Press.
- Natrella, M. G. 1963. *Experimental Statistics*. National Bureau of Standards Handbook 91. U. S. Government Printing Office, Washington.
- Petzold, T. J.. 1972. Volume scattering functions for selected ocean waters. Univ. Calif. Scripps Inst. Oceanogr. Tech. Rep. 72-78.
- Petzold, T. J. and R. W. Austin. 1968. An underwater transmissometer for ocean survey work. Univ. Calif. Scripps Inst. Oceanogr. Tech. Rep. 68-9.
- Voss, K. J. and R. W. Austin. 1993. Beam-Attenuation measurement error due to small-angle scattering acceptance. *J. Atmospheric and Oceanic Techn.* **10**: 113-121.

Table 1) Specific beam attenuation coefficients. Standard error of the coefficients are shown in parenthesis.

wavelength	$c^*_{\text{coccolith}}$ $\text{m}^2 (\text{lith})^{-1} \times 10^{12}$	$c^*_{\text{plated cell}}$ $\text{m}^2 (\text{plated cell})^{-1} \times 10^{10}$	$c^*_{\text{naked cell}}$ $\text{m}^2 (\text{naked cell})^{-1} \times 10^{11}$
440	5.2(3.9)	7.4(3.4)	7.9(3.8)
490	4.1(3.4)	5.9(3.0)	7.3(3.3)
520	3.6(3.3)	5.5(2.9)	7.4(3.3)
550	3.0(3.3)	5.7(3.0)	7.3(3.2)
670	1.1(3.5)	6.3(3.0)	6.6(3.4)

Table 2)

BP derived spectral backscattering coefficients. Standard error of the coefficients are shown in parenthesis.

wavelength	b_b^* coccolith $\text{m}^2 (\text{lith})^{-1} \times 10^{13}$	b_b^* plated cell $\text{m}^2 (\text{plated cell})^{-1} \times 10^{12}$	b_b^* naked cell $\text{m}^2 (\text{naked cell})^{-1} \times 10^{13}$
456	1.4(0.2)	6.7(1.3)	9.9(2.3)
546	1.3(0.2)	5.8(1.2)	9.5(2.0)

GASM derived spectral backscattering coefficients. Standard error of the coefficients are shown in parenthesis.

wavelength	b_b^* coccolith $\text{m}^2 (\text{lith})^{-1} \times 10^{13}$	b_b^* plated cell $\text{m}^2 (\text{plated cell})^{-1} \times 10^{12}$	b_b^* naked cell $\text{m}^2 (\text{naked cell})^{-1} \times 10^{13}$
440	2.1(0.2)	8.8(2.4)	1.7(1.7)
490	1.8(0.1)	9.3(1.9)	1.3(1.0)
520	2.2(0.2)	13(2.6)	1.8(1.4)
550	1.6(0.1)	6.6(1.5)	1.1(0.8)
610	1.4(0.1)	5.1(2.3)	1.7(1.2)
670	1.2(0.1)	6.5(1.3)	0.84(0.72)

FIGURE CAPTIONS

Figure 1) Comparison of the b_b derived from the numerical fit to the Beardsly and Zaneveld (1969) equation and b_b found by directly integrating the VSF data.

Figure 2) Specific beam attenuation coefficients as a function of wavelength. Also shown is the power law fit to each component, discussed in the text. The exponent found for each component was -3.7, -0.28 and -0.38 for coccoliths, plated cells, and naked cells respectively.

Figure 3) The measured c is compared with the reconstruction of c using cell counts and the specific attenuation coefficients of the model.

Figure 4) Example VSF(490 nm) for each growth phase (stationary, log and senescent).

Figure 5) Comparison of the BP measurements and GASM measurements of b_b for the same samples.

Figure 6) Specific b_b coefficients (b_b^*) as a function of wavelength for both the BP derived and GASM derived measurements. Also shown is the power law fit to each component, discussed in the text. The exponent found for each component was -1.4, -1.2 and -1.0 for coccoliths, plated cells, and naked cells respectively.

Figure 7) Fit of empirical model to data obtained in coccolithophore bloom off of Iceland. b_b' is the acid labile b_b , derived from the $b_{b_{total}} - b_{b_{acidified}}$ for the field samples. Shown are the 1:1 line and a line showing the best fit between the measured and predicted values.

Figure 8) Relative contribution of the b_b due to plated cells to the acid labile b_b (b_b').

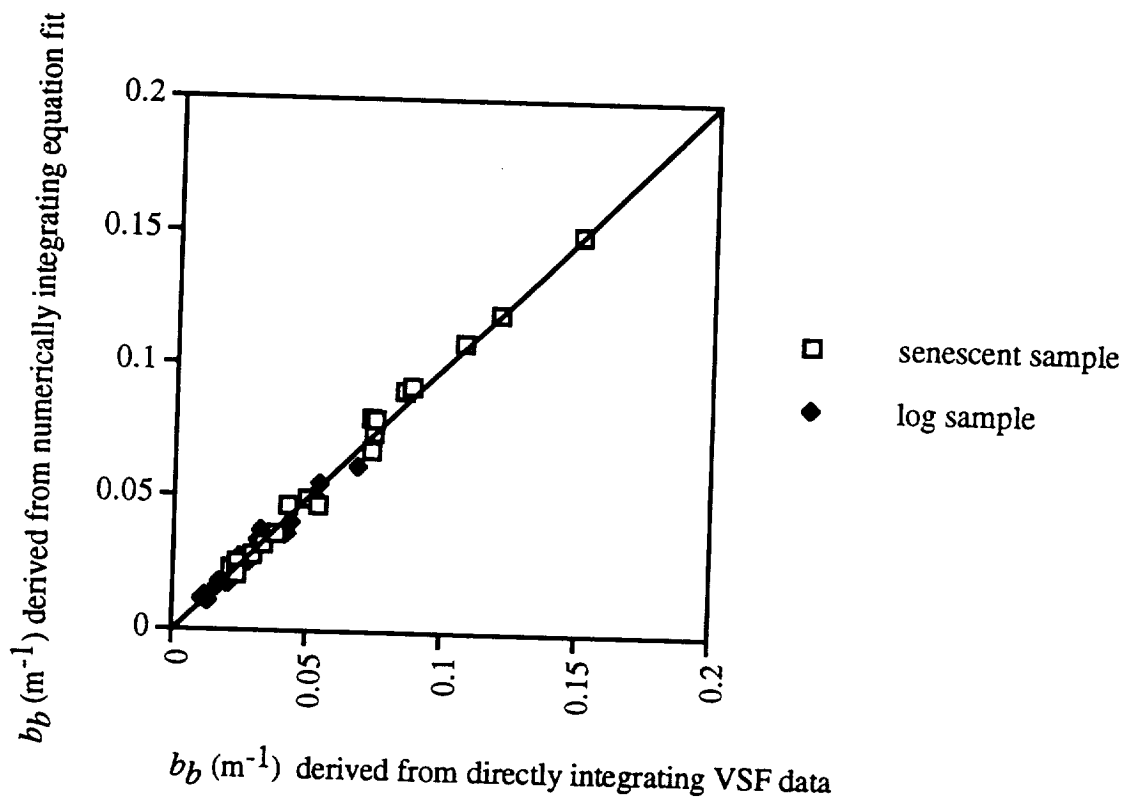


FIGURE 1

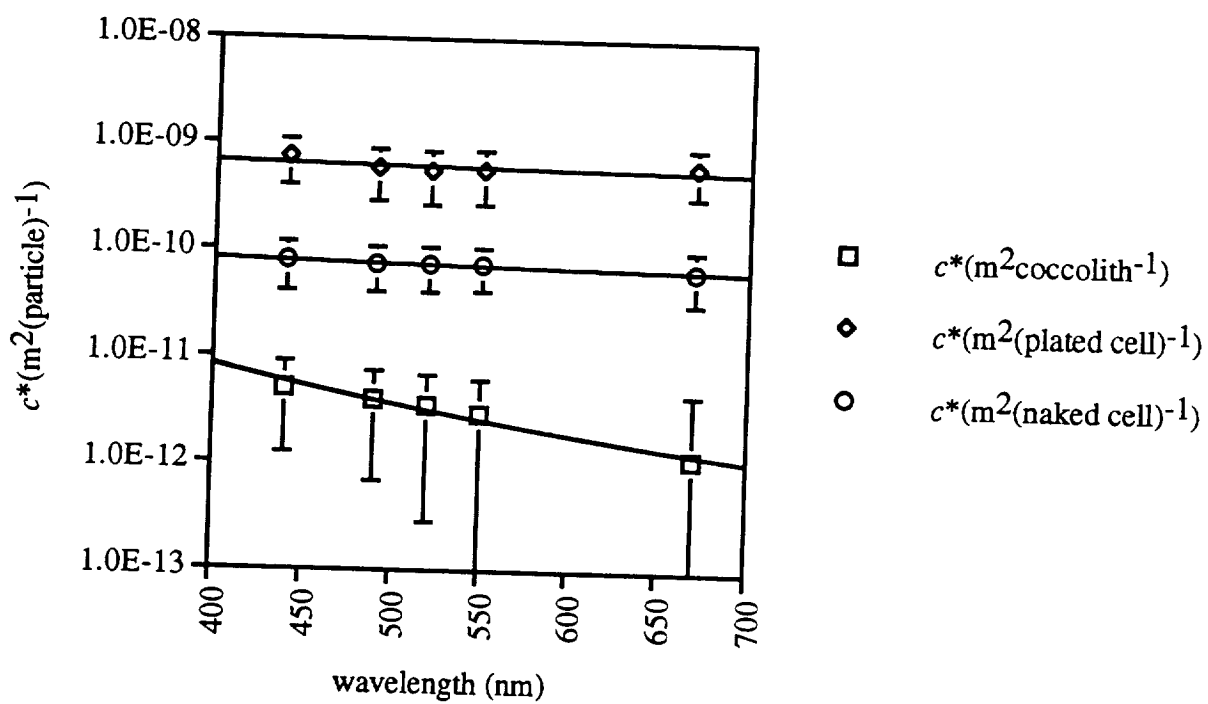


Figure 2

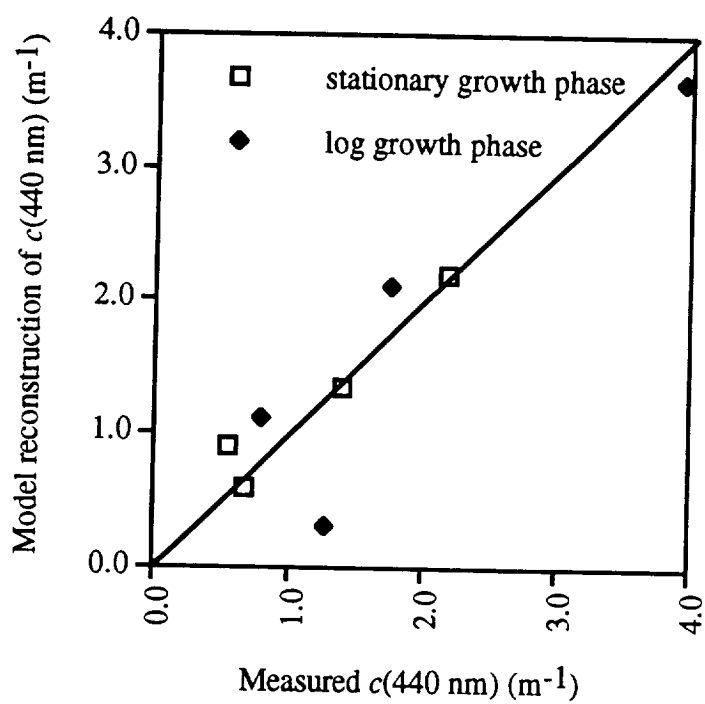


Figure 3

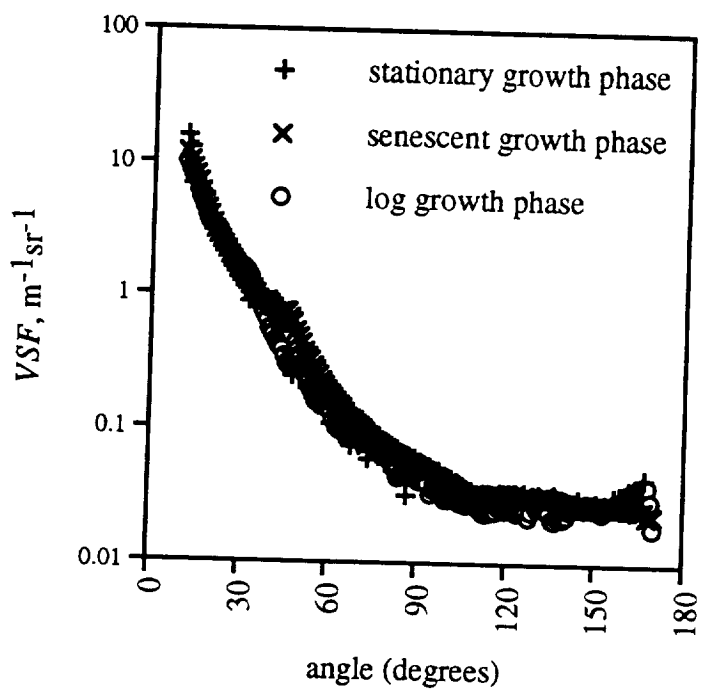


Figure 4

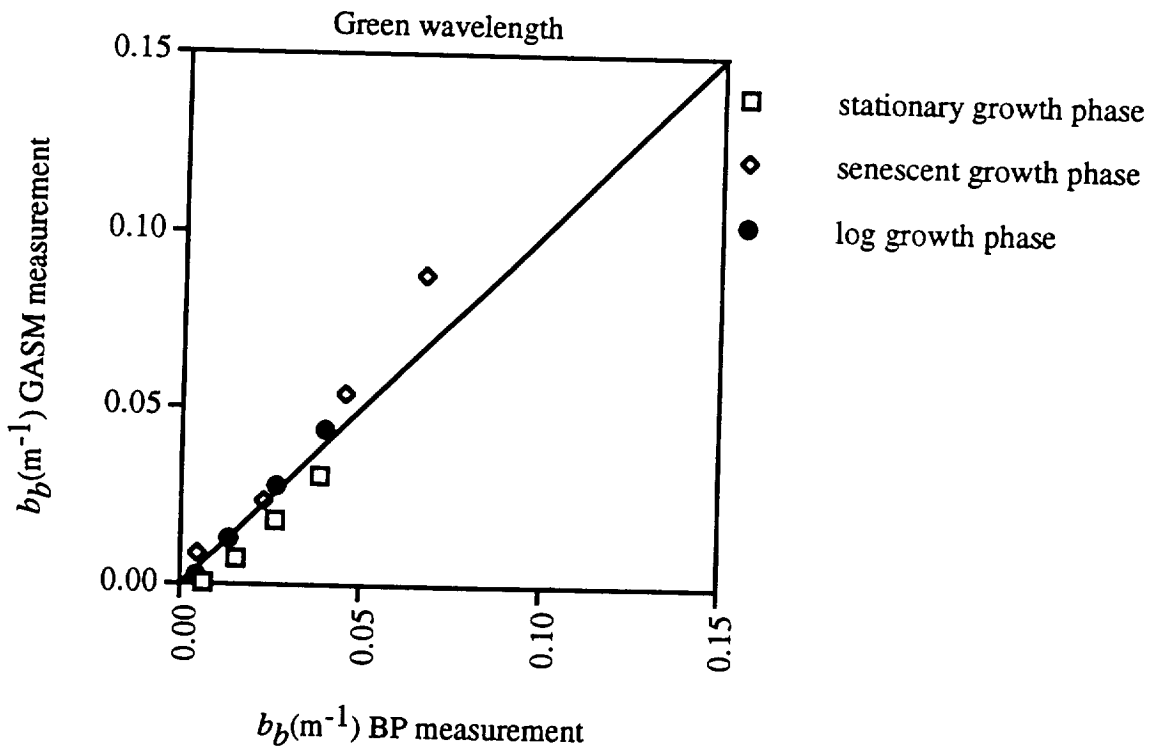
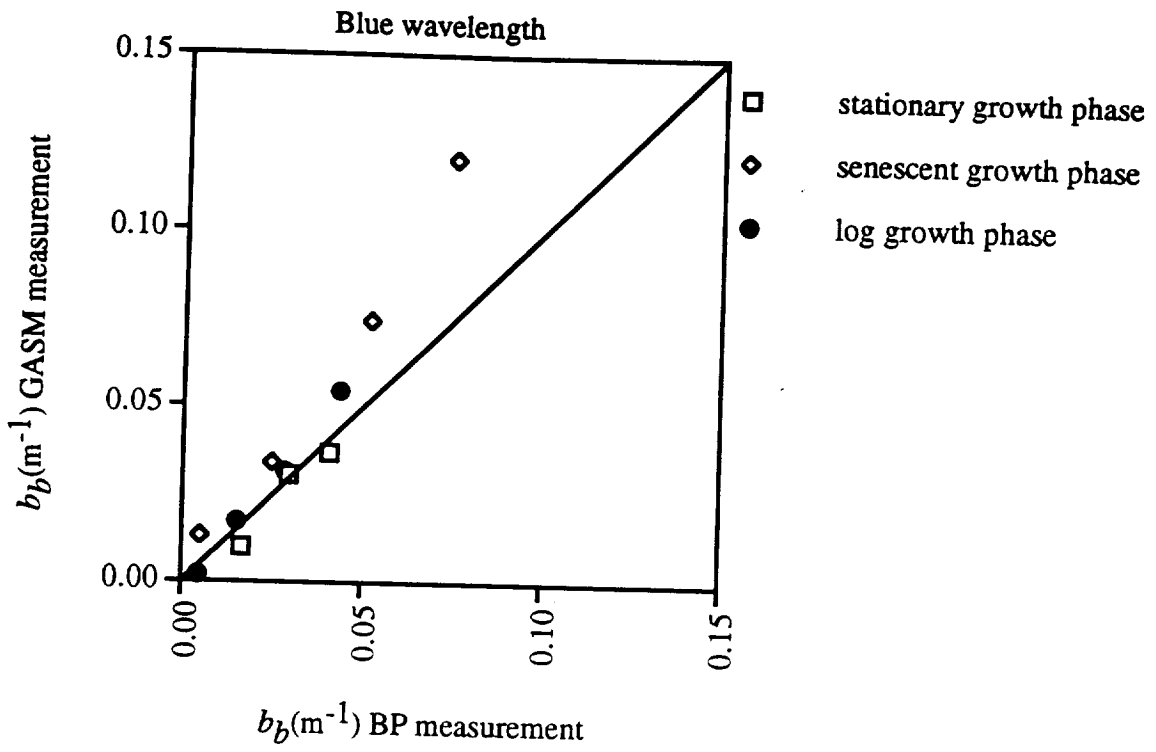


Figure 5

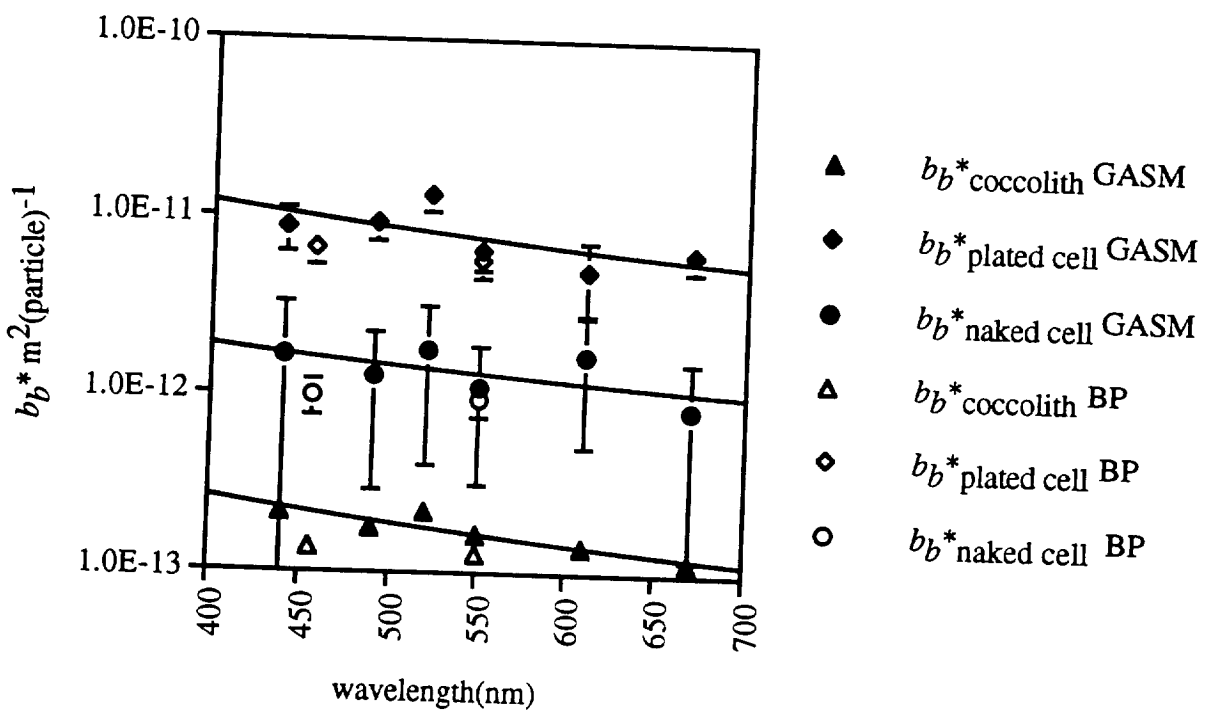


Figure 6

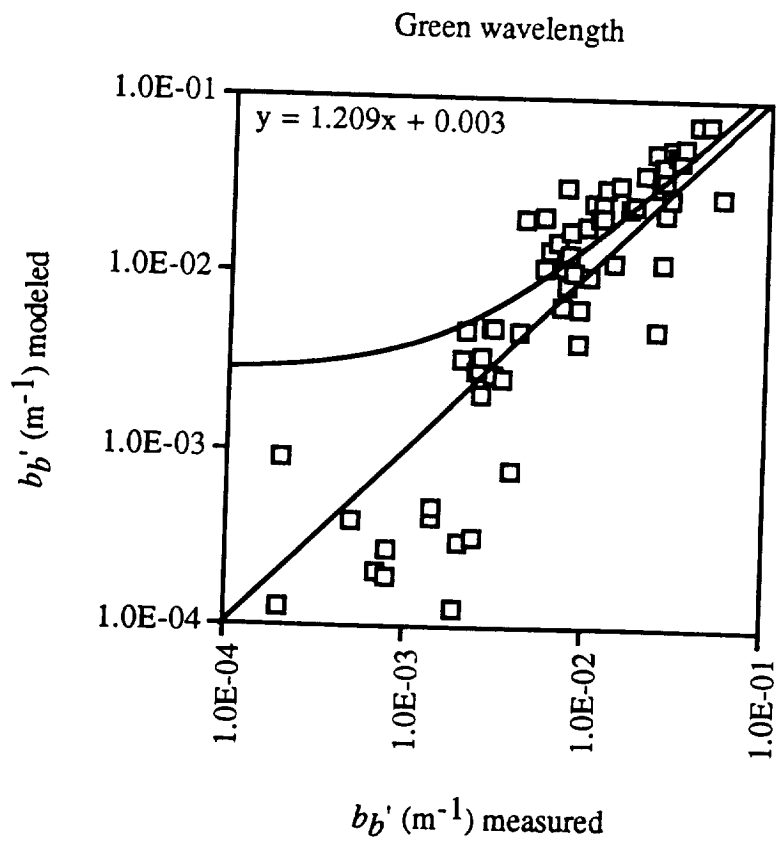
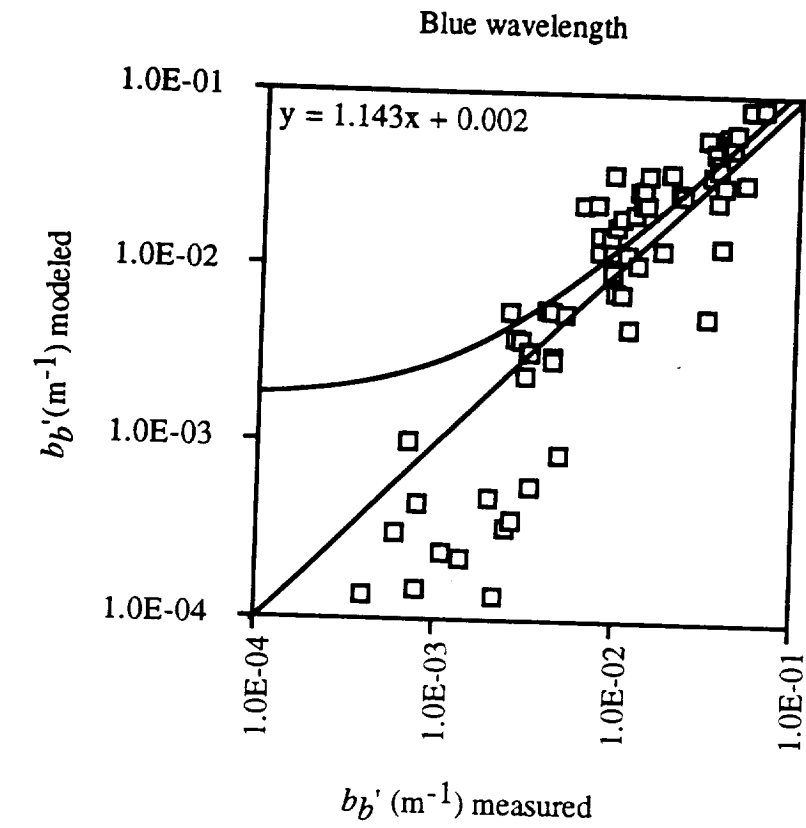


Figure 7

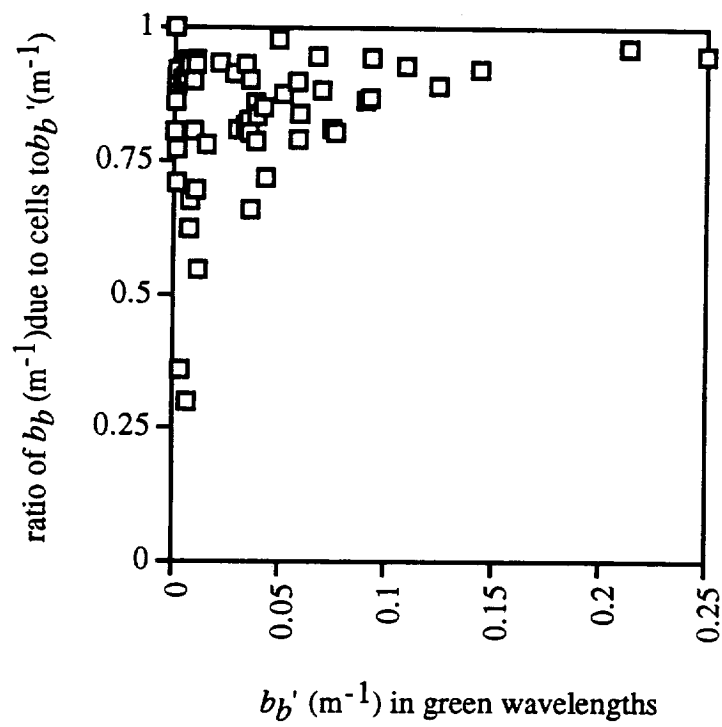


Figure 8